Author:
Oliver, Sam

Title:
Residual Stresses in Clad Nuclear Pressure Vessels and Their Interaction with Thermal and Mechanical Load

Residual Stresses in Clad Nuclear Pressure Vessels and Their Interaction with Thermal and Mechanical Load

Sam J. Oliver

A dissertation submitted to the University of Bristol in accordance with the requirements for award of the degree of Doctor of Philosophy in the Faculty of Engineering.

Department of Mechanical Engineering

September 2018

c. 49,500 words

ABSTRACT

Nuclear reactor pressure vessels are clad on their internal surface to provide resistance to corrosion. However, cladding also introduces residual stresses. The residual stresses combine with mechanical stress caused by internal pressure and thermal stress caused by rapid cooling known as thermal shock. The combination of stress from different sources may pose a threat to structural integrity. This work characterises the residual stress in reactor pressure vessel steel clad with nickel-alloy, and investigates how residual stresses interact with thermal and mechanical stresses.

Residual stress measurements were made on two steel plates clad with nickel-alloy using mechanical strain relaxation methods and synchrotron X-ray diffraction. One plate was as-welded, the other was post-weld heat-treated. The post-weld heat-treated plate was subjected to thermal shock and the residual stress was measured again afterwards. The cladding yielded during thermal shock which caused the residual stresses to redistribute. The results demonstrate that yielding should be accounted for when combining thermal and residual stresses in structural integrity analysis of thermal shock.

Measurements of stress were also made in the clad plate under transient conditions during thermal shock using in-situ synchrotron X-ray diffraction. It was demonstrated that the most severe thermal and residual stresses occurred during thermal shock, rather than before or after.

A new experimental technique was developed which represents residual stress in fracture specimens using fixed-displacement four-point bending, whilst allowing simultaneous application of mechanical stress. The technique was used to study the role of residual stress in failure of pressure vessel steel and high strength aluminium alloy. The results demonstrate that the initial level of residual stress has no effect on the fracture load if the material is sufficiently tough.

ACKNOWLEDGEMENTS

I am grateful to my academic supervisors, Professor Martyn Pavier, the late Professor David Smith, and Dr Mahmoud Mostafavi, for their generous advice, support, and encouragement. I also thank my industry supervisors from Wood, Dr Peter James and John Sharples, for providing valuable technical guidance and arranging funding for this work.

The experimental work presented in this thesis was facilitated by contributions from numerous people and organisations. Rolls-Royce supplied the two clad plates. The incremental centre hole drilling measurements were carried out by Veqter Ltd. Dr Karim Serasli from Veqter provided advice on the deep hole drilling measurements. Dr Foroogh Hosseinzadeh from the Open University arranged the contour measurement.

I acknowledge the tremendous support provided by the Faculty of Engineering technicians at the University of Bristol. Ricky Billingham, Rich Bragg, Mike Bracey, Ian Plummer, John Byles, and Lee Winter manufactured many of the specimens and apparatus used in this work. Steve Harding, Guy Pearn, and Peter Whereat helped to set up numerous tests. Steve Harding also assisted with the deep hole drilling measurements. Mark Fitzgerald, David Alonso, and Mike Penney helped to design and manufacture the control box for the thermal shock apparatus used in the diffraction experiment.

I am grateful to the team who assisted with running the synchrotron X-ray diffraction experiment over the 72 hour period allocated at Diamond Light Source: Dr Mahmoud Mostafavi, Dr Chris Simpson, Andrew James, and Megan Taylor from the University of Bristol; Dr David Collins from the University of Birmingham; and Dr Christina Reinhard from Diamond Light Source. In addition, Christina Reinhard advised on the design of the thermal shock apparatus, Chris Simpson analysed the raw diffraction data, and Andrew James measured the grain size in the clad material. Chris Simpson provided generous amounts of guidance at all stages of this experiment. Access to the I12 beamline was provided by Diamond Light Source under proposal number 16096.

My colleagues in the Solid Mechanics Research Group at the University of Bristol helped to create a unique and supportive research environment. The collective experience of the group is vast and diverse and has greatly contributed to this work.

Funding for this project was provided by the Engineering and Physical Science Research Council (EPSRC) and Wood.

AUTHOR'S DECLARATION

I declare that the work in this dissertation was carried out in accordance with the requirements of the University's Regulations and Code of Practice for Research Degree Programmes and that it has not been submitted for any other academic award. Except where indicated by specific reference in the text, the work is the candidate's own work. Work done in collaboration with, or with the assistance of, others, is indicated as such. Any views expressed in the dissertation are those of the author.

SIGNED: ..... DATE:.....

PUBLICATIONS

JOURNAL

S.J. Oliver, M. Mostafavi, F. Hosseinzadeh, M.J. Pavier, "Redistribution of residual stress by thermal shock in reactor pressure vessel steel clad with nickel alloy", International Journal of Pressure Vessels and Piping, vol. 169, pp. 37-47, 2019. https://doi.org/10.1016/j.ijpvp.2018.11.007

CONFERENCE

S. Oliver, M. Pavier, M. Mostafavi, "Applying fracture mechanics to cracked components subjected to unloading", Proceedings of the ASME Pressure Vessels and Piping Conference, 2016, PVP2016-63575. https://doi.org/10.1115/PVP2016-63575 *

H.E. Coules, G.C.M. Horne, M.J. Peel, S.J. Oliver, D.G.A. Van Gelderen, T. Connolley, "Direct observation of elastic and plastic strain fields during ductile tearing of a ferritic steel", Proceedings of the ASME Pressure Vessels and Piping Conference, 2016, PVP2016-63345. https://doi.org/10.1115/PVP2016-63345

S. Oliver, M. Mostafavi, M. Pavier, "Studying the effect of residual stress on fracture using fixed displacement four-point bending", Proceedings of the 14th International Conference on Fracture (ICF 14), 2017.

S. Oliver, C. Simpson, A. James, C. Reinhard, D. Collins, M. Pavier, M. Mostafavi, "Measurements of stress during thermal shock in clad reactor pressure vessel material using time-resolved in-situ synchrotron X-ray diffraction", Proceedings of the ASME Pressure Vessels and Piping Conference, 2018, PVP2018-84676.

*This paper was selected as the First Runner-Up Student Paper (PhD Category) in the Rudy Scavuzzo Student Paper Symposium and 24th Annual Student Paper Competition at the 2016 ASME Pressure Vessels and Piping Conference.

CONTENTS

LIST OF FIGURES

LIST OF TABLES

ACRONYMS

DHD	Deep hole drilling
EDM	Electro-discharge machining
ICHD	Incremental centre hole drilling
LOCA	Loss of coolant accident
PTS	Pressurised thermal shock
PWR	Pressurised water reactor
RPV	Reactor pressure vessel
XRD	X-ray diffraction

1 Introduction

1.1 Background

Of the various broad designs of nuclear power plants, pressurised water reactors (PWRs) are the most common. As of the end of 2017, 70% of nuclear power worldwide was generated by pressurised water reactors (PWRs), and 83% of nuclear plants under construction were PWRs [1]. The moderator in a PWR is water, which slows down neutrons produced by decay to speeds which enable sustained fission. The water in a PWR also acts as the primary coolant by transferring energy from the reactor to a steam generator via the primary coolant circuit. The reactor in a PWR plant is contained in the reactor pressure vessel (RPV). RPVs are made out of nuclear-grade low-alloy steel, which is typically a variant of ASTM A508 [2] in modern Western-built plants. RPVs are manufactured out of large, thick forgings, which are welded together. For example, Figure 1.1 shows a simplified diagram of an RPV. The dimensions are typical of an RPV designed by Westinghouse in the 1980s, similar to the one in operation at the 'Sizewell B' PWR in the UK [3]. Under normal operating conditions, RPVs typically contain internal pressure of around 16 MPa and operate at 288 – 327°C [3]. Using standard calculations for elastic thick-walled pressure vessels [4], a normal operating pressure of 16 MPa gives rise to a hoop stress of 170 MPa at the cylindrical part of the vessel shown in Figure 1.1.

It is important that sufficient measures are taken to avoid the catastrophic brittle fracture of an RPV because the consequences of failure would be severe. Therefore, structural integrity must be demonstrated under the most severe loading conditions. One such severe loading condition occurs during a loss of coolant accident (LOCA), which is a faulted condition referring to the loss of primary coolant [3]. For example, this could be caused by a break in a pipe in the primary coolant circuit. In such a scenario, the pressure rapidly falls to zero and emergency cooling water is injected into the RPV to prevent residual

decay heat from fission products causing a core meltdown. The effect is to rapidly cool the internal surface of the vessel whilst the bulk of the material remains at high temperature. The resulting thermal mismatch causes large tensile stresses at the internal surface, a scenario known as thermal shock [5].

Modern RPVs are clad on the inside surface with corrosion-resistant material, which is typically stainless steel [6]. The primary purpose of the cladding is to prevent the base metal from corroding and contaminating the primary coolant. The cladding is deposited by overlay-welding, in which the raw cladding material is melted onto the surface of the parent material. The cladding is deposited as long strips of weld metal which are laid side by side until the whole of the inside of the RPV is covered. The cladding is built up in layers of weld until the correct thickness is achieved. One of the structural integrity challenges of cladding is that it introduces high tensile residual stresses [7]. There is a concern that the cladding residual stresses could significantly contribute to drive a surface defect to fracture.

Thermal shock experienced by an RPV during a LOCA poses a risk to structural integrity, because the combination of cladding residual stresses and thermal shock stresses may cause surface defects to fracture. This is of particular concern in RPVs near the end of their service lives, because the fracture toughness of RPV steel degrades as its cumulative exposure to radiation from the reactor core increases [8, 9]. It is therefore important to understand how the different sources of stress interact. At the inner wall of the RPV the thermal shock stresses and cladding residual stresses are both tensile and of high-magnitude, approximately equal to or greater than the yield strength of the cladding. For reference, the room temperature yield strength of typical stainless steel cladding is 268 - 299 MPa [10]. If it assumed that the stresses simply superimpose, then tensile stresses of the order of twice the yield strength are predicted, which is clearly unrealistic. Some improved analytic methods for combining different sources of stress account for inelastic interaction caused by plasticity [11, 12], but there is limited direct experimental validation. These methods are also focussed on the relaxation of secondary sources of stress (i.e. thermal and residual) with primary sources (i.e. internal pressure and other applied load). The interaction between different sources of secondary stress, such as thermal shock stress and cladding residual stress, has received little attention and is poorly understood.

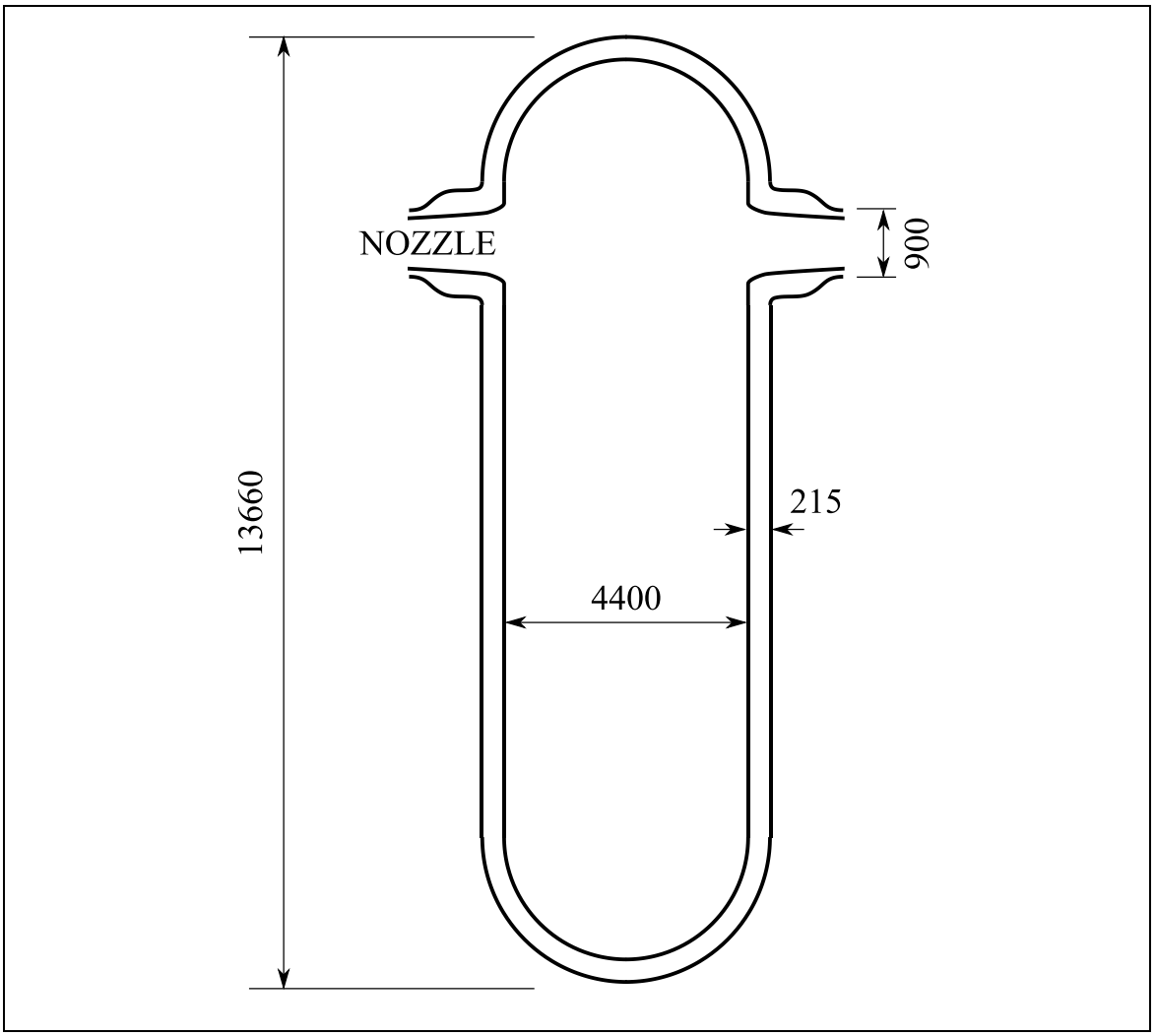

Figure 1.1 Schematic showing the overall geometry of a typical RPV. Dimensions [3] are approximate and are in mm.

1.2 Objectives

There were two broad aims of this project. The first aim was to characterise the residual stress in low-alloy RPV steel clad with nickel alloy instead of the more conventional and well-studied cladding material, stainless steel. The second aim was to investigate the interaction between cladding residual stress and other sources of stress. Three experimental studies were carried out to achieve these aims.

The first experimental study addresses both aims of the project. The first aim was addressed by measuring the residual stresses in two plates of SA508 Grade 4N nuclear pressure vessel steel, clad with Alloy 82 nickel-base alloy. One plate was as-welded, the other post-weld heat-treated. The second aim was addressed by measuring the redistribution of cladding residual stress caused by thermal shock. This was achieved by subjecting the post-weld heat-treated plate to thermal shock, and measuring the residual stress again afterwards. It was expected that significant residual stress redistribution would occur by thermal shock, thereby providing experimental validation to the prediction that it is pessimistic to combine residual and thermal stresses by elastic superposition. A finite element simulation was made to investigate the physical mechanisms causing residual stress redistribution during thermal shock.

The second experimental study addresses the second aim of the project by measuring the combined residual and thermal stresses during thermal shock. This was achieved using in-situ synchrotron X-ray diffraction. A test rig was designed to subject specimens to thermal shock, whilst simultaneously enabling time-resolved measurement of stress by X-ray diffraction at high temporal resolution. Six specimens were extracted from some of the clad material used in the first experiment which had not been subjected to thermal shock, and surface cracks were machined in the cladding. The specimens were subjected to thermal shock on beamline I12 at Diamond Light Source [13], the UK's national synchrotron facility. Time-resolved stress was measured during thermal shock at a single point close to the crack tip at a sample rate of 30 Hz. In addition, the stress around the crack tip was mapped under steady-state conditions at room temperature (before and after thermal shock) and at ~360°C (before thermal shock).

The third experimental study addresses the second aim of this project by investigating the interaction between residual and applied stresses. A novel method for applying residual stress to a test specimen was developed, which aimed to represent residual stress in a rectangular beam specimen as a fixed-displacement four-point bend. The specimen could then be loaded simultaneously under tension, representing applied load. A finite element study was carried out to fully understand the interaction between the tension and fixed-displacement bending. A unique test rig was designed and manufactured to enable specimens to be tested under this combined loading system. This test rig enables residual stress to be easily monitored in-situ using a load cell as the magnitude of applied load increases, and so the magnitude of both the applied and residual stresses are known at

every point during the test. The test rig was used to experimentally study the interaction of residual stress with applied load and the effect of residual stress on fracture in two materials: P355 pressure vessel steel, which has a high ratio of toughness to yield strength; and 7075 T7351 aluminium alloy, which has a relatively low ratio of toughness to yield strength.

1.3 Thesis structure

Chapter 2 presents a review of the literature which the author considers most relevant to the objectives stated in Section 1.2. The topics reviewed are: the role of residual stress in failure, methods for imparting residual stress on test specimens, residual stress in clad pressure vessel material, and thermal shock in RPVs.

Chapter 3 presents the first of the three experimental studies outlined in Section 1.2, in which residual stress measurements were made on clad RPV material before and after it was subjected to thermal shock.

Chapter 4 presents the second experimental study, in which measurements of stress were made on clad RPV material in-situ during thermal shock using synchrotron X-ray diffraction.

Chapter 5 presented the third experimental study, in which a novel experimental method for investigating the role of residual stress on failure was designed and tested.

Finally, Chapter 6 summarises the key findings of this project and makes recommendations for future work.

2 Literature Review

2.1 Introduction

This chapter presents a review of previous work in topics which are most relevant to the objectives stated in Section 1.2. First, the role of residual stress in the failure of components is discussed in Section 2.2. Methods for accounting for residual stress in fracture analyses are presented, as well as the results of experimental investigations into the effects of residual stress on fracture and the redistribution of residual stress with applied load. Section 2.3 reviews experimental methods used in previous work for imparting residual stress in test specimens, to inform the development of an improved experimental technique for studying the role of residual stress in failure. Section 2.4 describes the residual stresses induced by weld-overlay cladding onto pressure vessel steel. Finally, the concept of thermal shock in reactor pressure vessels is introduced in Section 2.5. The mechanism by which thermal shock generates high tensile thermal stresses is illustrated with a simple example. A review of thermal shock analysis methods and some large-scale thermal shock experiments follows.

2.2 The role of residual stress in failure

The load-bearing capacity of a component can be significantly affected by residual stress. In linear-elastic fracture mechanics, the total stress intensity factor can be calculated by adding together stress intensity factors calculated individually for different loading systems [14]. If a cracked component containing residual stress is subjected to externally applied load, the total stress intensity factor, K, can be calculated using:

$$K = K_{app} + K_{RS} \tag{2.1}$$

where K_{app} and K_{RS} are the stress intensity factors due to applied load and residual stress. The component fails when:

$$K \geq K_c \tag{2.2}$$

where K_c is the fracture toughness. Handbook solutions for K_{app} exist for extensive combinations of geometry and load [14]. Calculating K_{RS} tends to be more difficult because residual stress is often non-uniform, especially when generated by welding. One approach is the weight function method, in which the solution for K from a pair of splitting loads is integrated over the crack face [15]. Another approach is to use elastic finite element analysis in conjunction with a contour integral or domain integral calculation of K which accounts for residual stress [16]. In general, if the crack exists entirely within a region of tensile residual stress, K_{RS} is positive and so the load bearing capacity of the component, which is proportional to K_{app}, decreases. Alternatively, if the residual stress is compressive, the load bearing capacity of the component increases. It is for this reason that components are often subjected to treatments to induce compressive residual stress in regions where cracks typically form. For example, compressive residual stresses can be induced around holes using cold expansion [17] with a view to improving the fatigue life of a component.

Equation (2.1) is strictly valid for linearly-elastic materials, whereas real materials are elastic-plastic. For example, if the combined magnitude of residual and applied stresses exceeds yield, then the residual stress redistributes [18, 19], and so K_{RS} varies with applied load. R6 [20], a structural integrity assessment procedure widely used in the nuclear industry in the UK, accounts for inelastic interaction between primary load (externally applied load) and secondary load (residual and thermal stresses) using the V factor:

$$K = K_P + V \cdot K_S \tag{2.3}$$

where K_P and K_S are the stress intensity factors due to primary and secondary stresses. The calculations of K_P and K_S are the by the same method as K_{app} and K_{RS} in Equation (2.1), i.e. carried out separately using linear-elastic analysis. The V factor is calculated using:

$$V = \xi \frac{K_{J,S}}{K_S} \tag{2.4}$$

where $K_{J,S}$ is the stress intensity factor due to residual stress calculated using elastic-plastic analysis, and ξ is tabulated in R6 as a function of $K_{J,S}$, the yield strength of the material, and the magnitude of applied load. The calculation of ξ is based on the analytic calculation of combined primary and secondary stress presented by Ainsworth [11]. In this context the primary stress is the applied stress and the secondary stress is the residual stress. An alternative, more involved, analysis method is to calculate the *J* integral due to combined loading using finite element analysis with fully elastic-plastic material properties. There are numerous difficulties with this approach. First, calculating the *J* integral in finite element analysis when there are residual or thermal stresses present is outside the capabilities of typical commercial finite element codes and typically requires post-processing of the results [21]. Second, elastic plastic fracture mechanics requires that the *J* integral characterises the near-tip stresses. This is true for a non-linearly elastic material, in which near-tip stresses have been described by Hutchinson, Rice, and Rosengren for a power-law hardening stress-strain curve [22-24]. This is only true in an elastic-plastic material when no unloading occurs, which has been demonstrated in previous work by the author of this thesis [25]. It is not always clear whether unloading has occurred in complex simulations involving residual stress, and simply being able to calculate the *J* integral (i.e. convergence with increasing domain size) does not guarantee its validity.

Many experiments have been carried out to investigate the effects of residual stress on the failure load of components containing cracks. The experimental methods are discussed in the following section, and so only the key results are summarised here. Under conditions of limited yielding (low plasticity), where failure occurs by unstable cleavage fracture, it has been shown that the presence of significant residual stresses severely affects the failure load [26-31]. The load-bearing capacity (i.e. maximum applied load) of a test specimen is typically reduced under tensile residual stresses [26-29, 31] and increased under compressive residual stresses [30]. The effect of residual stress is smaller when there is more yielding (high plasticity) [26, 28, 32]. In the extreme case, when failure occurs by plastic collapse before fracture, a number of studies have shown the effect of residual stress to be insignificant [26, 28, 32].

The experiments summarised in the previous paragraph aimed to quantify the effect of residual stresses by comparing the ultimate failure loads of cracked specimens containing different amounts of residual stress. A full appreciation of the role of residual stress in failure requires an understanding of how residual stresses redistribute with other sources of stress. Comparatively few experimental studies have focussed on monitoring residual stresses during application of other loads. Turnbull et al [19] measured the surface residual stresses induced by shot peening in steel tensile specimens subjected to different amounts of applied tensile load. Horne [18] induced residual stresses in aluminium sheets by friction stir welding, and then measured redistribution under increasing applied tension using synchrotron X-ray diffraction. Both experiments showed that the magnitude of residual stress reduced with increasing applied load. Smith et al [33] generated residual stress by locking an initial misfit into a novel three-bar structure, and then measured the response of the whole structure to applied load. It was demonstrated that residual stress relaxation only occurs on the onset of yielding, and that the amount of relaxation increases with increasing plastic strain.

The following section reviews methods used to investigate the role of residual stress on failure, to provide background to the development of an improved experimental method.

2.3 Methods for imparting residual stress on test specimens

A typical experimental investigation into the role of residual stress on failure involves imparting different magnitudes of residual stress on geometrically identical test specimens and then loading the specimens to failure. This section reviews methods used in previous work to generate different magnitudes of residual stress in test specimens.

Applying heat to a small region of material in a component causes non-uniform temperatures which can give rise to thermal stresses. If the thermal stresses exceed yield, then residual stress is generated. This method was used in early work by Nishimura and

Tokimasa [34], who investigated the role of residual stress induced by drag-braking in train wheels. Different amounts of residual stress were imparted by subjecting the wheels to varying amounts of on-tread drag-braking, simulating conditions experienced during a long descent. The drag-braking caused localised regions of raised temperature, giving rise to tensile residual stress on the tread of the wheel. The wheels were then loaded to failure by subjecting them to repeated severe braking, causing cracks to gradually form and propagate until reaching a critical size where brittle fracture occurred. Another method of localised heating was used by Formby and Griffiths [26] who performed fracture tests on large centre-cracked plate specimens constructed out of pressure vessel steel. Residual stress was imparted on some of the plates by sandwiching a small region between copper cylinders heated to 600°C. Approximately 300 MPa tensile residual stress was measured in the heated region where cracks were introduced for subsequent fracture testing.

Other researchers have used mechanical rather than thermal load to generate residual stresses due to local yielding. Mirzaee-Sisan et al [35], James et al [36], and Bolinder and Faleskog [32] carried out fracture tests on steel SEN(B) specimens which were modified with a notch on one edge, using a method called in-plane compression. A schematic of the method is shown in Figure 2.1 (a). Before the crack is introduced, the specimen is loaded under compression to cause localised yielding near the edge of the notch. The compression load is carried out in the same loading plane as the subsequent fracture loading. A typical trace of the resulting residual stress is shown in Figure 2.1 (a). The approximate magnitude is shown relative to the yield strength, σ_y. Finally, the crack is inserted for subsequent fracture testing. Another method, called out-of-plane mechanical loading or side-punching, has been used to generate residual stress in SEN(B) [29, 31] and CT [30, 37] specimens. This method is illustrated in Figure 2.1 (b). Specimens are loaded in compression between cylindrical punches until yielding occurs, leaving an impression. The cylindrical punches are loaded in the x_3 direction in Figure 2.1 (b). The residual stress in the region of the crack can be made either tensile or compressive by adjusting the number and position of the side-punches. A typical trace of the residual stress field generated by a single pair of punches is shown in Figure 2.1 (b). The benefit of this method is that standard fracture specimen geometries can be used, and so it is straightforward to perform fracture tests to standard specifications such as ASTM E1820 [38].

It is well-known that welding introduces residual stresses [39] due to a combination of thermally-induced plastic deformation, phase transformation effects, and the difference in thermal expansion coefficient between the filler and parent material. Therefore, welding has been investigated by some researchers as a method of imparting residual stress on fracture specimens. Mirzaee-Sisan et al [40] used autogenous welding to generate residual stresses in stainless steel beam specimens. A tungsten inert gas (TIG) welding electrode was dragged over one edge of some of the specimens without the use of any filler material, resulting in up to 300 MPa tensile residual stress within 10 mm of the welded edge, and lower magnitude compressive stress beneath. The cracks imparted in the specimens for subsequent fracture tests were barely affected by the presence of residual stress because the contribution from the tensile and compressive regions virtually cancelled out. Wu [27] performed fracture tests on butt-welded steel plates with semi-elliptical and through cracks inserted at the weld. Tests were carried out in the as-welded condition, in which 350 MPa tensile stress was estimated in the weld, and after post-weld heat-treatment which was expected to provide significant stress relief. A similar approach of testing welded specimens before and after heat-treatment was presented (amongst other experiments) by Ainsworth et al [28], in which fracture specimens were machined out of a large butt-welded steel plate.

In summary, three broad approaches have been used to apply residual stress to test specimens in previous work. They are: localised heating, mechanical load, and welding. Localised heating was used in earlier work, although the approach of Formby and Griffiths [26] is currently being re-investigated in other work at the University of Bristol. More recent studies have used either welding or mechanical load. Both methods induce non-uniform residual stress fields which must be characterised by a combination of modelling and measurement techniques. Measuring residual stresses can be complex and time-consuming, particularly when using methods capable of measuring through-thickness stresses such as deep hole drilling [41] or neutron diffraction [42]. Both welding and mechanical methods of introducing residual stress also induce changes in material properties which must be accounted for when interpreting the test results. Welding methods introduce filler material (except in autogenous welding) and heat-affected zones (HAZ), in which material is harder [43] and the resistance to fracture could be different to the bulk material [44]. Mechanical methods rely on local plastic deformation, which causes material hardening. Finally, with mechanical and welding methods, it is typically

only feasible to compare specimens with two different amounts of residual stress. It is difficult to tune the magnitude of residual stress induced by welding, and so studies are typically limited to two cases: one with residual stress (as welded), and one either with no residual stress (no welding) or reduced residual stress (stress-relieved). In theory, it is possible to tune the residual stresses induced by mechanical methods by changing the geometry and magnitude of the mechanical load used to induce plastic deformation [30]. In practice, each new residual stress state would need to be characterised, and so studies are usually limited to two types of specimens: those with residual stress, and those without. There is significant scope for improving experimental studies on the role of residual stress in failure by investigating alternative methods for imparting residual stress on test specimens which do not suffer from some of these limitations.

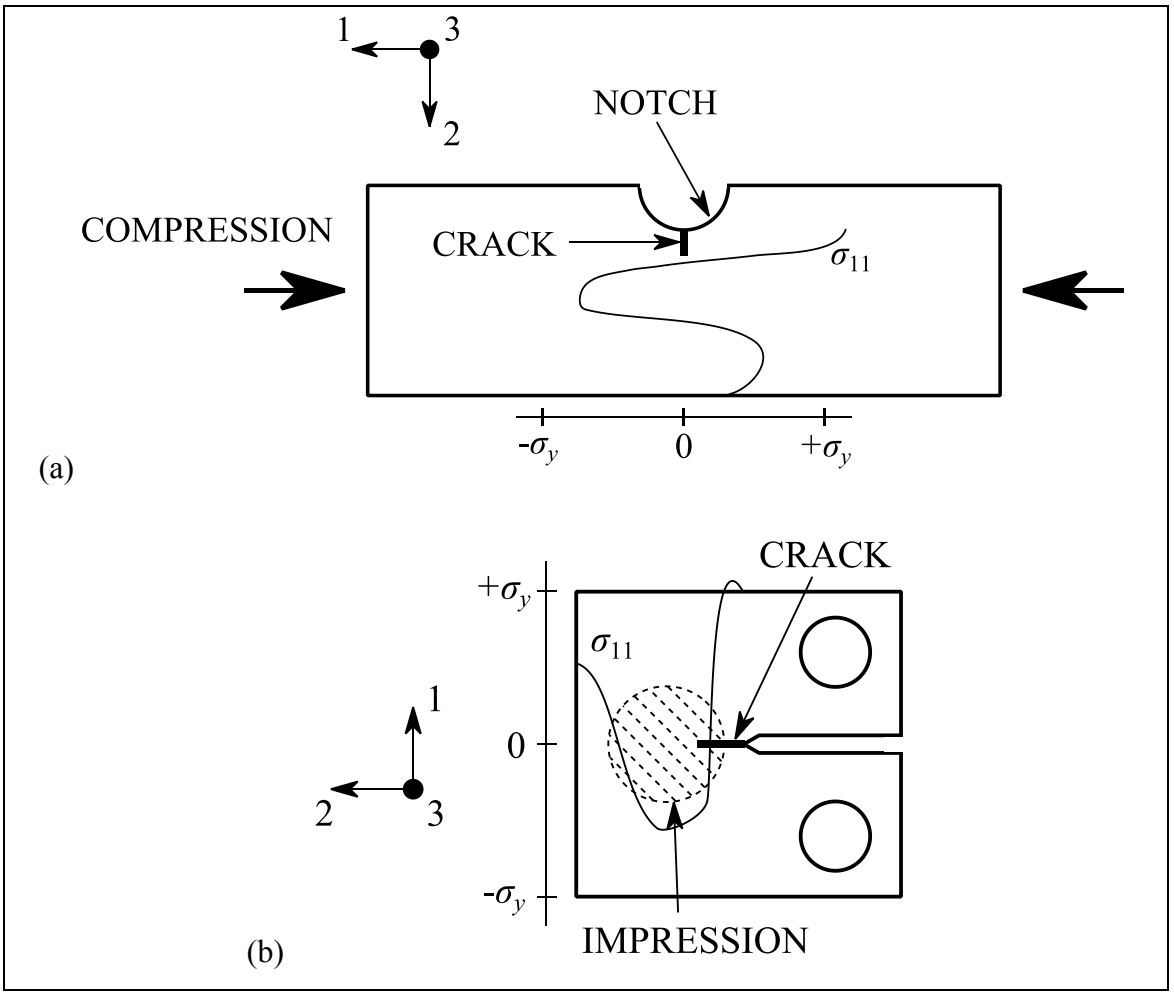

Figure 2.1 Schematic representations of the shape of the residual stress fields imposed by two different mechanical methods: in-plane compression (a), and out-of-plane compression (b). Representative residual stress fields were traced from ref. [45].

2.4 Residual stresses in clad pressure vessel material

The residual stress in pressure vessel material clad by overlay-welding with stainless steel has been extensively characterised in previous work using experimental measurements [7, 46-55] and modelling techniques [7, 48, 52, 56]. In the as-welded condition, high tensile stresses exist in the cladding and also typically in the parent close to the interface between the two materials [46, 47, 54]. In practice, reactor pressure vessels are subjected to a post-weld heat treatment in which the material is held at high temperature, typically between 538-621°C [7, 49, 50, 52, 55], in order to partially relax the residual stress by creep. However, significant residual stress remains after post-weld heat-treatment. This is partly because creep occurring at high temperature during the heat treatment does not cause the residual stresses to completely relax [48]. Furthermore, additional stresses are generated upon cooling due to the difference in thermal expansion coefficient between the cladding and parent materials. In general, clad material which has been post-weld heat-treated contains high tensile residual stresses in the cladding of around 200 – 400 MPa [7, 47, 49, 50, 55], which is close to the yield strength of 268 – 299 MPa measured in typical stainless steel cladding at room temperature [10]. The parent contains lower-magnitude tensile or compressive stresses [7, 47, 49, 50, 55]. More precisely, the residual stress is influenced by the welding process and the number of layers in which the cladding is deposited [50]. Measurements by Kume et al [46] have also shown that the residual stress in the same clad plate can vary in different parts of the weld bead, even after post-weld heat-treatment.

For example, Figure 2.2 shows a schematic of a representative piece of clad material and Figure 2.3 summarises the results of some recent residual stress measurements on stainless steel-clad RPV material which has been post-weld heat-treated. The depth is normalised by the thickness of the cladding, and the stress is the component longitudinal to the weld direction shown in Figure 2.2. Results are presented for cladding which was deposited using two different welding processes: mechanised tungsten inert gas welding (TIG), and submerged arc welding (SAW). The TIG measurements were carried out on a 50 mm thick plate of SA508 steel clad with one layer of type 309 stainless steel and then two final layers of type 308 stainless steel [55]. The SAW measurements were carried out

on two 150 mm thick plates of A533B steel, one plate clad with a single 5 mm thick layer of type 304 stainless steel, the other clad with two layers [50]. All measurements were made using the deep hole drilling method. The results collated in Figure 2.3 demonstrate that the cladding residual stresses are broadly similar with high magnitude tensile stresses in the cladding. However, the precise magnitude and through-thickness distribution can vary between specimens manufactured using different methods.

Nickel-alloy is an alternative cladding material which is considerably more expensive than stainless steel [57] but may offer some benefits including having a lower thermal expansion coefficient [58] which is closer to that of the ferritic base metal. The number of residual stress measurements reported in the open literature on nickel-alloy cladding is comparatively limited. One study by Jones et al [49] reported measurements using a layer removal technique on various pieces of low-alloy pressure vessel steel clad with Alloy 600 nickel-base alloy. In one piece which was extracted from a 143 mm thick pressure vessel, up to 250 MPa tensile stress was measured in the cladding and lower-magnitude compressive stress in the parent, although the vessel was previously subjected to hydraulic loading which could have caused some residual stress redistribution. Measurements were also made on four 38 mm thick plates, two clad with type 308/309L stainless steel and two clad with Alloy 600. The choice of cladding material did not appear to significantly affect the measured residual stress. Measurements on a plate of low alloy steel clad with Alloy 82 nickel-base alloy have also been reported [59], although the residual stress was obtained using lab-based X-ray diffraction which is only capable of measuring near-surface stresses.

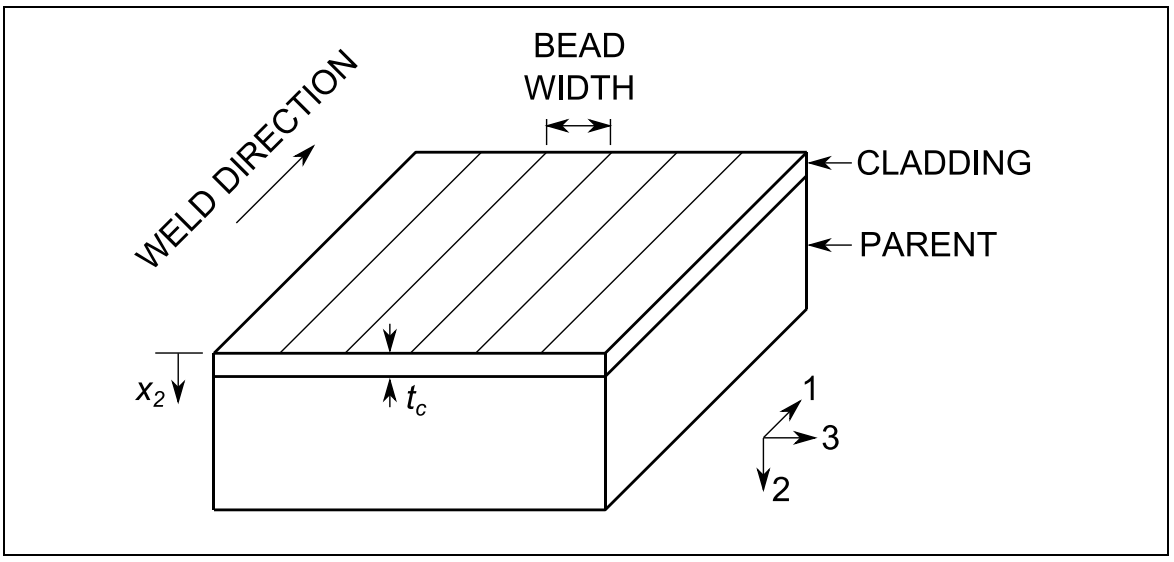

Figure 2.2 Schematic of clad material.

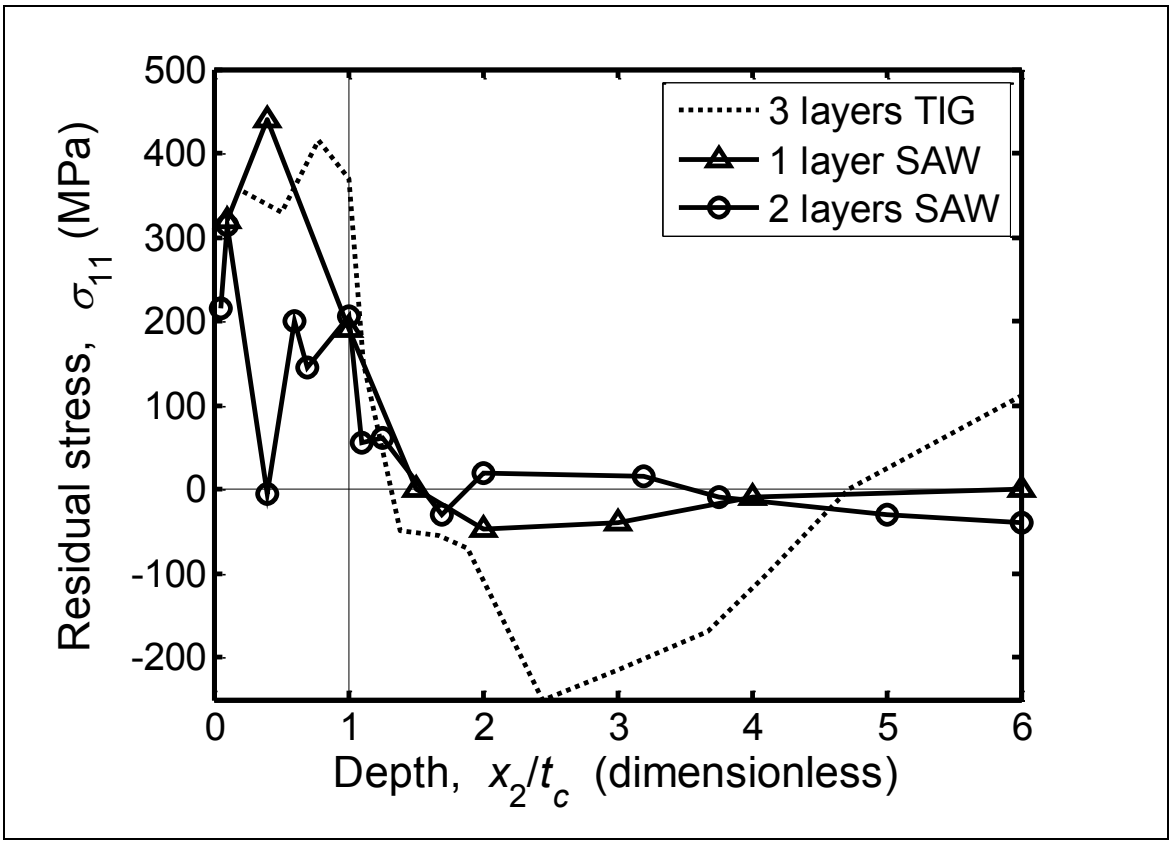

Figure 2.3 Residual stress in stainless steel-clad RPV material which has been post-weld heat-treated. Data have been reproduced from work by Serasli [55] (TIG) and Kingston et al [50] (SAW).

2.5 Thermal shock in reactor pressure vessels

Thermal shock could occur in RPVs under faulted or emergency conditions which cause the temperature of the primary coolant to rapidly fall. The effect is to rapidly cool the internal surface of the vessel whilst the bulk of the material remains at high temperature, causing high tensile stress at the inside wall. Thermal shock could arise from various scenarios [3, 60]. One scenario is a break in a steam pipe which transports steam from the steam generator to the turbines, in which case the RPV may retain internal pressure whilst concurrently experiencing rapid cooling. Another particularly severe scenario is a loss-of-coolant accident (LOCA) caused by a large break in the primary coolant circuit, in which case the pressure rapidly drops to zero and emergency cooling water is injected into the RPV, causing a severe thermal shock.

A basic thermal shock analysis is presented here to estimate the thermal stresses occurring during thermal shock, following a similar example presented by Knott [61]. Figure 2.4 shows a two-dimensional representation of an RPV wall undergoing thermal shock. The inside wall is cooled from a normal operating temperature of 300°C using 20°C water. It is crudely assumed here that a layer of material adjacent to the water immediately cools to the water temperature whilst the bulk of the vessel remains hot. If it is also assumed that thermal contraction of the cold layer is constrained by the bulk material, then the biaxial thermal stresses in the cladding are:

$$\sigma_{11} = \sigma_{33} = \frac{E \cdot \alpha \cdot \Delta T}{1 - \nu} \tag{2.5}$$

where: σ_{11} and σ_{33} are the thermal stresses (refer to Figure 2.2 for directions); E is the Young's modulus; α is the linear thermal expansion coefficient; ν is Poisson's ratio; and ΔT is the reduction in temperature in the cold layer. If typical material properties of stainless steel cladding are assumed (E = 150 GPa, α = 15.7 μm/mK, ν = 0.28 [62]) and ΔT is 280°C, then Equation (2.5) predicts 920 MPa tensile stress in the cladding. This analysis is simplistic for various reasons. First, the temperatures through the vessel wall are not constant but vary with time. The time-dependant temperatures can be accurately calculated using either analytic [5] or finite element methods [62]. Either method requires calculating a film heat transfer coefficient, h, which describes the heat flux via convection from the inner wall of the RPV to the emergency coolant fluid [63]:

$$q = h(T_w - T_f) \tag{2.6}$$

where q is the heat flux per unit area in W/m^2, h is the film heat transfer coefficient in W/m^{2}K, T_w is the temperature at the inner wall in °C, and T_f is the bulk temperature of the coolant in °C. The film heat transfer coefficient depends on the temperature difference between the vessel wall and the bulk of the coolant, and so is also time-dependant [64, 65]. In practice a single value is usually specified, typically 9000 – 21,500 W/m^{2}K [60, 62]. The use of a film heat transfer coefficient simplifies the complex interactions between hot and cold fluids during emergency cooling. Alternatively, the temperatures throughout the coolant and RPV during thermal shock can be calculated using computational fluid dynamics [66].

Since the temperatures in the RPV during thermal shock vary with time, so do the thermal stresses. Once the temperatures are known, the resulting time-dependent stress can be calculated using analytical methods if the material is assumed linearly-elastic [5]. Fully elastic-plastic thermal stress analyses are typically carried out using numerical methods such as finite element analysis. For example, Udagawa et al [60] calculated approximately 900 MPa thermal stress in the cladding at the most severe point in time during a LOCA using an elastic finite element analysis, compared with 400 MPa using elastic-plastic analysis.

Such high tensile stresses could pose a threat to structural integrity by driving pre-existing surface defects to propagate and cause fracture. This is of particular concern in RPVs near the end of their service lives, because the fracture toughness of RPV steel degrades as its cumulative exposure to radiation from the reactor core increases [8, 9]. Therefore, a series of large-scale experiments were carried out to investigate the structural integrity of RPVs during thermal shock. In one series of experiments reported by Cheverton et al [67], four large, internally clad cylinders were subjected to conditions intended to represent thermal shock by heating them up to 93°C, and then submerging them in liquid nitrogen (-196°C). Various surface defects were inserted in the cylinders prior to testing, including sub-cladding and through-cladding (surface-breaking) flaws. Another experiment was carried out as part of the NESC-I spinning cylinder project, a major international project running from 1993-2001 [62, 68]. A seven ton, internally clad steel cylinder was manufactured and eighteen sub-clad and through-clad defects were introduced. The cylinder was subjected to pressurised thermal shock conditions by heating it up to 293°C and then spraying the inside surface with 5°C water, whilst simultaneously being spun about its rotational axis to represent pressure-induced stress. In both the Cheverton and NESC-I experiments, the test cylinders were subjected to non-standard heat treatments to artificially reduce the fracture toughness, thereby representing the state of the radiation-embrittled material in an RPV. The Cheverton experiments took the extra step of using liquid nitrogen to subject the cylinders to thermal shock at cryogenic temperatures. Liquid nitrogen is a poor quenchant compared to water, and so the resulting thermal transient was much less severe (i.e. lower rate of cooling) than real thermal shock conditions. For example, the film heat transfer coefficient measured in 20°C steel cooled by liquid nitrogen is 85-540 W/m^2K [69], whereas hot steel quenched in water experiences up to 20,000 W/m^2K [64]. Therefore, the NESC-I experiment was a more realistic

representation of thermal shock experienced in a real RPV. In both studies, crack propagation and arrest was observed in some defects, and the results were used to validate fracture mechanics predictions. In the NESC I project, which provided more realistic thermal shock conditions, some crack extension was observed in large (~75 mm deep) through-clad and sub-clad defects but there was no catastrophic failure. These defects were significantly larger than the limiting defect sizes of 1-9 mm deep predicted by six different assessment codes [68], which demonstrates that the codes tend to be over-conservative when used to assess structural integrity under thermal shock.

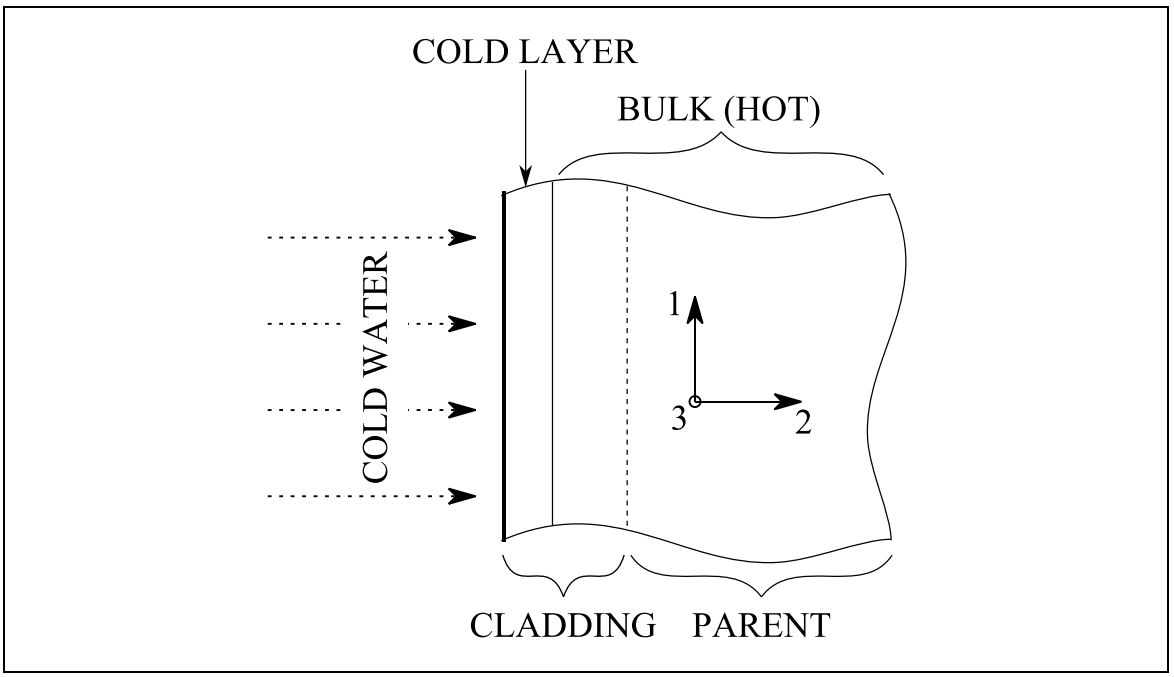

Figure 2.4 Schematic of the inner wall of an RPV undergoing thermal shock.

2.6 Chapter summary

Section 2.2 discussed the role of residual stress in the failure of components. Many experimental studies have focussed on the effect of residual stress on fracture, whereas comparatively few have measured the redistribution of residual stress with applied load. The methods used by these experimental studies to impart residual stress on test specimens were reviewed in Section 2.3. These existing methods share some limitations

which restrict the insight gained by the experiments which employ them. There is significant scope for improving experimental studies on the role of residual stress in failure by investigating alternative methods for imparting residual stress on test specimens which do not suffer from some of these limitations. One such alternative method is introduced in Chapter 5 of this thesis.

In Section 2.4 it was shown that only a limited number of residual stress measurements have been reported on nickel-alloy cladding compared with the more conventional austenitic stainless steel. Chapter 3 addresses this with a comprehensive program of measurements on Alloy 82 cladding (a nickel-base alloy) in both as-welded and post-weld heat-treated conditions.

In Sections 2.4 and 2.5, it was demonstrated that thermal shock stresses and cladding residual stress are both typically tensile and of high magnitude at the inner wall of the RPV. An understanding of how these two sources of stress combine is required to accurately assess the integrity of an RPV containing surface defects. For example, using upper-bound values from the literature of 400 MPa for the elastic-plastic thermal shock stresses [60] and 400 MPa for the cladding residual stresses [50], the elastically combined stress is 800 MPa, which is well in excess of the yield strength of typical cladding material (268 - 299 MPa for unirradiated stainless steel cladding at room temperature [10]).

Whereas inelastic interaction between residual stress and applied load has been previously demonstrated [18, 19] and incorporated into analysis methods [11], the interaction between residual and thermal stresses (i.e. two sources of secondary stress) has not received similar attention. This is addressed in Chapter 3, by measuring residual stress redistribution before and after thermal shock, and in Chapter 4, by measuring the total stress during thermal shock. Stresses during thermal shock have previously only been predicted by analytic studies, and thermal shock experiments have mainly focussed on observing fracture events by analysing test specimens after testing. Therefore, the experiment presented in Chapter 4 aims to measure for the first time the combined thermal and residual stresses in-situ during thermal shock.

3 Measurements of Cladding Residual Stress Before and After Thermal Shock

3.1 Introduction

The aim of the work presented in this chapter was to measure the residual stress in low alloy RPV steel clad with nickel alloy, and to measure the redistribution of residual stress caused by thermal shock. Residual stress measurements were made in two clad plates, one as-welded and one post-weld heat-treated, using mechanical strain relaxation methods. The post-weld heat-treated plate was subjected to thermal shock and the residual stresses were measured again afterwards.

The two clad plates used in this work are described in Section 3.2. In both plates, the parent material is SA508 Grade 4N, a modern RPV steel, and the cladding is Alloy 82, a nickel-base alloy. A preliminary finite element study is presented in Section 3.3 with the aim to evaluate the accuracy of the deep hole drilling method when measuring high stress gradients, which were expected near the interface between the cladding and parent materials. Section 3.4 outlines the experimental method. Residual stress measurements were made in the two clad plates using three methods: deep hole drilling, centre hole drilling, and the contour method. These measurements provide important data on residual stress in RPVs clad with nickel-base alloy, on which there are currently very few measurements reported in the open literature. The post-weld heat-treated plate was subjected to thermal shock by heating it up and then spraying the surface of the cladding with cold water. The residual stress was measured again afterwards. Section 3.5 presents a finite element simulation, which was made to investigate the physical mechanisms

causing residual stress redistribution during thermal shock. The results from the experiment and finite element model are presented in Section 3.6. The results are discussed in Section 3.7, which includes stress intensity factor calculations from the measured residual stresses and a study on the effect of plate thickness on cladding residual stress. It is shown that thermal shock causes the cladding residual stresses to redistribute, which demonstrates that the thermal shock stresses and residual stresses interacted in an inelastic manner.

All work reported in this section was undertaken by the author, except the Contour measurement which was arranged by Dr Foroogh Hosseinzadeh at the Open University, and the incremental centre hole drilling measurements which were carried out by Veqter Ltd.

3.2 The clad plates

Figure 3.1 shows a schematic of the two clad plates which were provided for this work by Rolls-Royce. In both plates, the parent material is SA508 Grade 4N, a modern high-strength nuclear pressure vessel steel, and the cladding is Alloy 82, a nickel-base alloy. The cladding is a weld-overlay deposited by gas metal arc welding (GMAW). One plate is in the as-welded condition, and one has been post-weld heat-treated. The as-welded plate is clad on two opposite sides, each side with two layers of weld. The weld bead is laid in the same direction on both sides. Note that RPVs are usually only clad on a single side (the internal surface), but single-side clad material in the as-welded condition was unavailable for this project. The post-weld heat-treated plate is clad on a single side with three layers of weld. The weld bead is laid in a different direction on each half of the plate. The cladding on both plates has been machined down to a uniform thickness using face milling. The cutter travelled in the x_1 direction on both plates, referring to the co-ordinate system in Figure 3.1. The thickness of the cladding as shown in Figure 3.1 is nominally 4.25 mm on each side of the as-welded plate and 6 mm on the post-weld heat-treated plate, although in practice the cladding is slightly thicker on both plates due to

melting and redistribution of material during welding. The interface is well defined and is simple to locate by visual inspection after sectioning. Residual stress measurements were made on both plates, and part of the post-weld heat-treated plate was subjected to thermal shock. The post-weld heat-treated plate was also used to provide material for specimens tested in the X-ray diffraction experiment reported in Chapter 4.

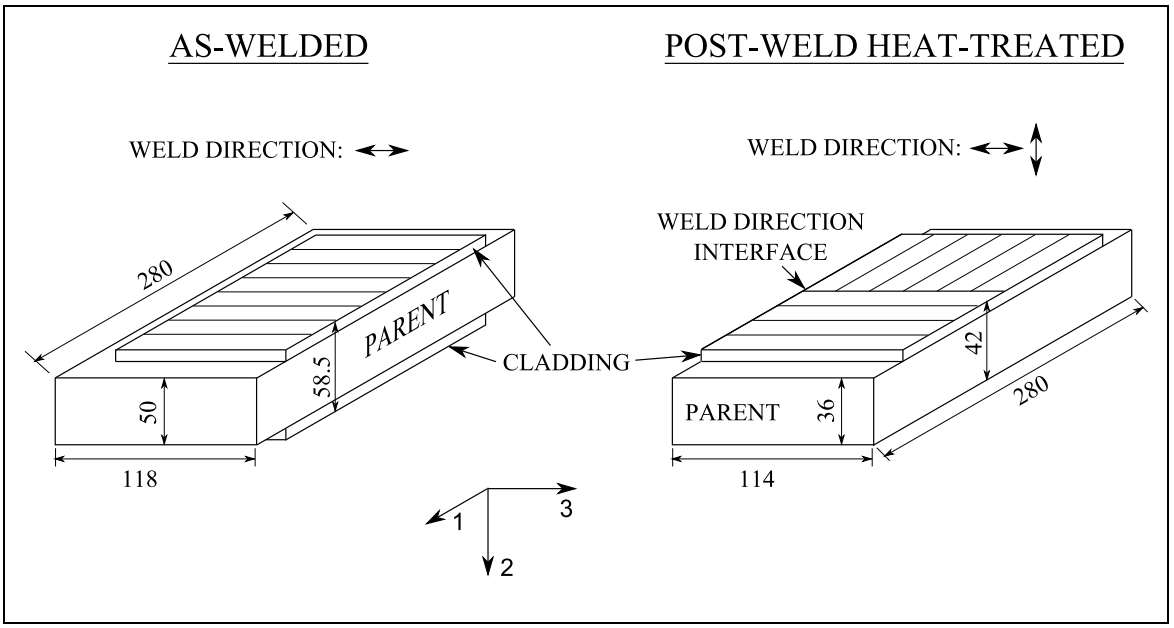

Figure 3.1 The two clad plates used for this work. Both are Alloy 82 cladding on SA508 Grade 4N parent. The lines on the cladding surface indicate the direction of travel of the welding electrode. Dimensions are in millimetres.

3.3 Finite element simulation of measurement of high stress gradients by deep hole drilling

The deep hole drilling (DHD) method can measure residual stresses in thick components. For example, a 435 mm thick DHD measurement has been previously demonstrated in a forged steel roll [70]. Therefore, the method is well-suited for measuring the through-thickness residual stresses in the clad plates described in Section 3.2. The DHD method has been thoroughly described elsewhere [41, 71-73]. Briefly, a reference hole is drilled into the specimen using a gun drill. The diameter of the gun drill is typically 1.5 or 3 mm.

The diameter of the hole is accurately measured after drilling using an air probe. An annulus is then machined around the reference hole in a process called trepanning. The trepan relaxes the residual stresses around the reference hole, thereby causing the hole to deform. The deformed diameter of the hole is accurately measured again after trepanning. Elastic analysis relates the distortion of the hole caused by trepanning to the residual stresses which existed before drilling the reference hole [72]:

$$\frac{(r_{ref,B} - r_{ref,A})}{r_{ref,B}} = \frac{1}{E}\left[\sigma_{xx}(1 + 2\cos 2\theta) + \sigma_{yy}(1 - 2\cos 2\theta) + 4\sigma_{xy}\sin 2\theta\right] \quad (3.1)$$

where: $r_{ref,B}$ and $r_{ref,A}$ are the radii of the reference hole before (B) and after (A) trepanning; E is the Young's modulus; σ_{xx}, σ_{yy}, and σ_{xy} are the pre-existing stresses in the plane normal to the reference hole; and θ is the angle of measurement around the axis of the reference hole.

It has been demonstrated in previous work on clad pressure vessel steel that high stress gradients tend to exist near the interface between the cladding and parent materials [7, 47]. See, for example, Figure 2.3. Previous work by Daniel George [74] showed that the DHD method may be inaccurate when measuring high stress gradients, and that the accuracy could be improved by reducing the diameter of the core without changing the diameter of the reference hole. A finite element study has therefore been conducted to investigate the accuracy of measuring high stress gradients using the DHD method with different core and reference hole diameters. The results were then used to inform the selection of the size of the reference hole and trepan used in the DHD measurements on the clad plates.

Figure 3.2 shows the geometry of the finite element model, which was generated and analysed using the finite element code, Abaqus 6.14 [75]. The model simulates the DHD measurement of a severe stress gradient in a cylinder. The model is axisymmetric with an overall radius which is large compared to the radii of the DHD reference hole and trepan. The radius of the reference hole is r_{ref} and the inner and outer trepan radii are $r_{t,i}$ and $r_{t,o}$. The material is linearly-elastic.

The simulation procedure was as follows. The model initially contained zero stress, and was then subjected to a uniform change in temperature, ΔT, of -300°C. The two halves of

the cylinder were assigned different thermal expansion coefficients (α_1 and α_2) so that this uniform cooling generated thermal stress with an infinite stress gradient at the interface between the two materials. Then the DHD measurement was simulated, first by removing all elements in the region labelled 'reference hole' in Figure 3.2 (simulating the drilling of the reference hole), and then by removing all elements in the region labelled 'trepan' (simulating the trepanning). The stress obtained by the simulated DHD method was calculated using:

$$\sigma_{rr} = \frac{\left(r_{ref,B} - r_{ref,A}\right)}{r_{ref,B}} \cdot \frac{E}{2} \tag{3.2}$$

where: σ_{rr} is the component of stress in the radial direction; and $r_{ref,B}$ and $r_{ref,A}$ are the radii of the reference hole before (B) and after (A) trepanning. For this simple model, Equation (3.2) is equivalent to the DHD analysis and can be derived by substituting $\sigma_{xx} = \sigma_{yy} = \sigma_{rr}$ and $\theta = 0$ into Equation (3.1).

A total of three models were made, each with a different reference hole radius (r_{ref} = 0.75, 2.5, and 5 mm). In each model, the inner and outer trepan radii, $r_{t,i}$ and $r_{t,o}$, were set to $r_{t,i} = 3r_{ref}$ and $r_{t,o} = 4r_{ref}$, which are representative of typical ratios of trepan radius to reference hole radius used in DHD measurements. The element size was the same in all three models. Quadrilateral elements were used with a side length of 0.25 mm in the DHD region. For convenience when constructing the mesh, the overall radius of the model does not scale with the reference hole radius. However, for all reference hole sizes considered the overall radius is much larger than the radii of the hole and trepan (>200 times r_{ref}), and so any size effect caused by not scaling the overall radius is considered negligible. The material properties used are shown in Table 3.1.

Figure 3.3 shows the stress in each model calculated using Equation (3.2) and the actual stress which was calculated at the axisymmetry line before the DHD method was simulated (i.e. before removing the elements in the reference hole and trepan regions). The actual stress undergoes a step change at the interface between the two materials. The simulated DHD measurements are inaccurate near the interface, but accurate far away. The distance from the interface at which the DHD method becomes accurate reduces with the size of the reference hole. In other words, the smaller the size of the DHD measurement, the greater the maximum possible stress gradient that the method can physically measure. This effect occurs because the core (i.e. the material bounded by the

trepan and reference hole in Figure 3.2) is not completely stress-free near the interface, whereas the DHD analysis assumes that all stresses acting on the reference hole are completely relaxed by trepanning. If the core thickness, $r_{t,i} - r_{ref}$, was infinitesimal, then the core would be perfectly stress-free because of the introduction of free surfaces at $r_{t,i}$ and r_{ref}. In practice, the core has a finite thickness and retains some residual stress near the interface. The retained residual stress in the core is small at distances from the interface, z, which are large compared to the core thickness, and so the error is only significant near the interface. In this model, the thickness of the trepan core, $r_{t,i} - r_{ref}$, increases proportionally with the radius of the reference hole. Therefore, at a given absolute position, z, the value of z relative to the core thickness is different in models with different reference hole radii. For example, suppose the value of z is chosen to be sufficiently far from the interface so that there is negligible residual stress retained in the core. For the same value of z in a model with a thicker core, the relative proximity of z to the interface would be smaller and therefore the amount of error-causing residual stress retained in the core would increase. This effect occurs in real DHD measurements. For example, a typical DHD measurement with a 1.5 mm diameter reference hole uses a 5 mm trepan, making the trepan core 1.75 mm thick. A typical DHD measurement with a 3.175 mm diameter reference hole uses a 10 mm trepan, making the trepan core 3.4125 mm thick, which is approximately twice as thick.

The results have been normalised and re-plotted in Figure 3.4. On the y-axis, the $\Delta\alpha$ term is the difference in thermal expansion coefficient between the two halves of the cylinder, equal to $\alpha_1 - \alpha_2$. When the x-axis is normalised by the radius of the reference hole (which is proportional to the trepan core thickness), the results for the different DHD sizes converge to the same gradient at the interface between the two materials. This demonstrates that the maximum stress gradient which can be physically measured by DHD is inversely proportional to the radius of the reference hole. The dimensionless stress on the y-axis in Figure 3.4 diverges as the distance from the interface increases because the actual stress in the model is non-uniform in each half of the cylinder.

As a result of the analysis presented in this section, the smallest practical DHD size was chosen for residual stress measurements on the clad plates described in Section 3.2. The diameter of the reference hole is 1.5 mm for the smallest DHD size, and the trepan diameter is 5 mm.

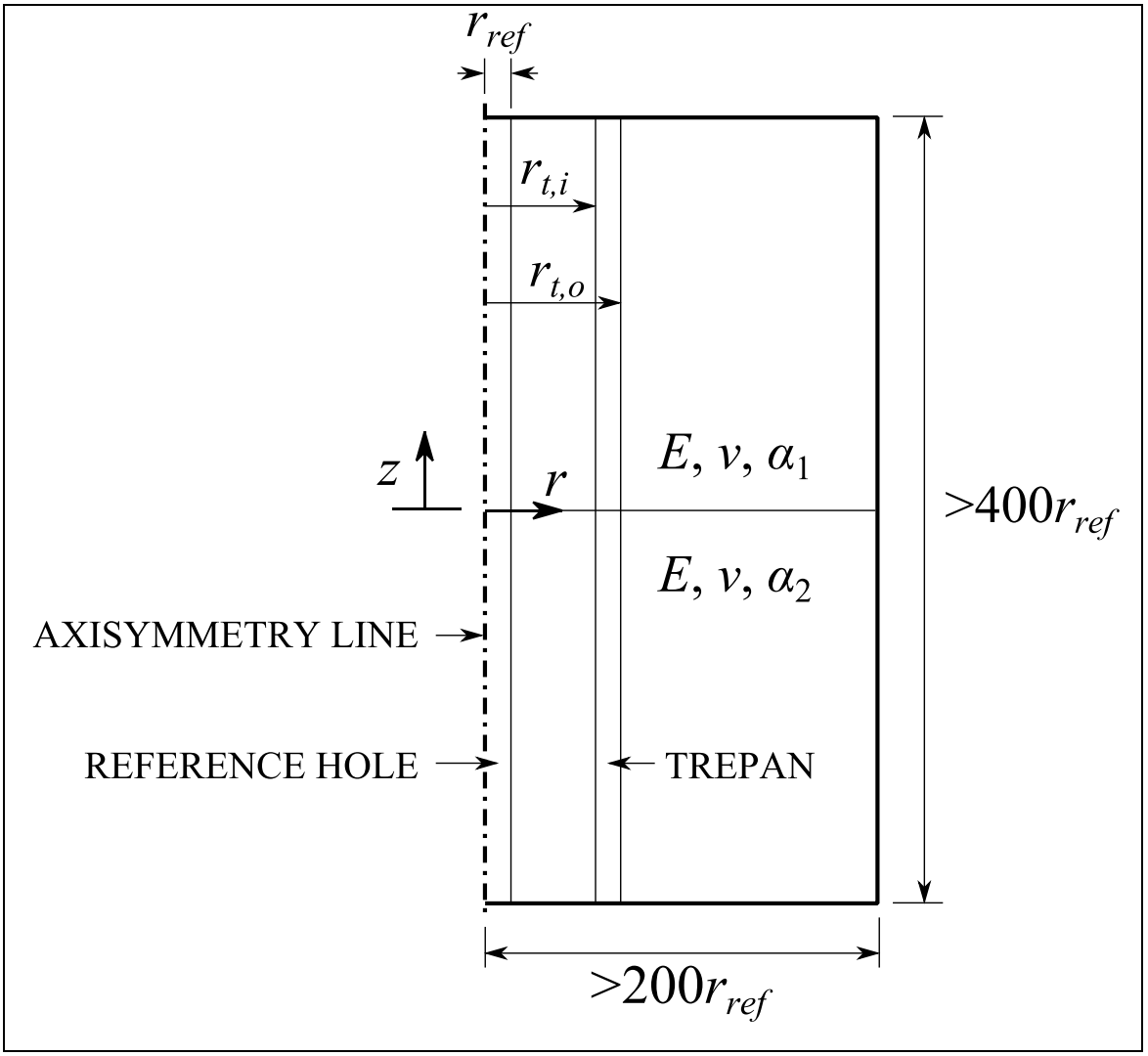

Figure 3.2 Diagram of the finite element model for simulating the measurement of severe stress gradients using deep hole drilling.

Table 3.1 Material properties used in the finite element simulation of deep hole drilling.

Young's modulus, E (GPa)	Poisson's ratio, ν	Coefficient of thermal expansion, α_1 (μm/m°C)	Coefficient of thermal expansion, α_2 (μm/m°C)
210	0.3	14	11

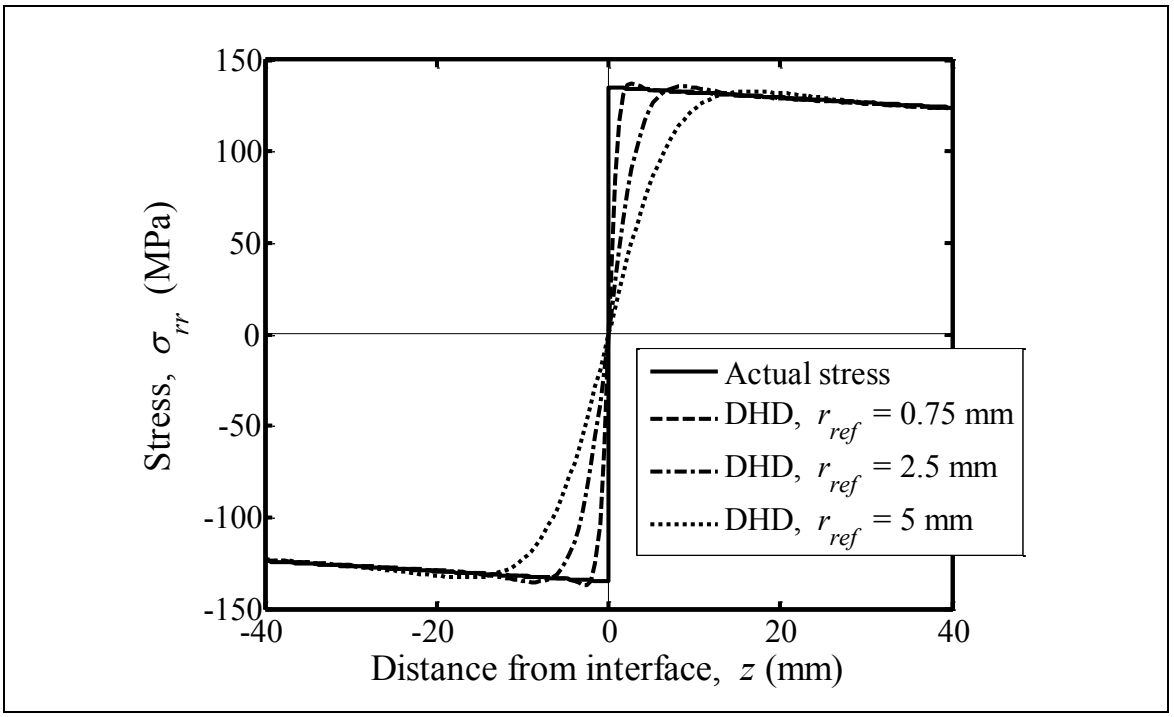

Figure 3.3 A comparison of actual stress with the stresses calculated using the simulated DHD measurement with different reference hole radii (r_{ref} = 0.75, 2.5, 5 mm).

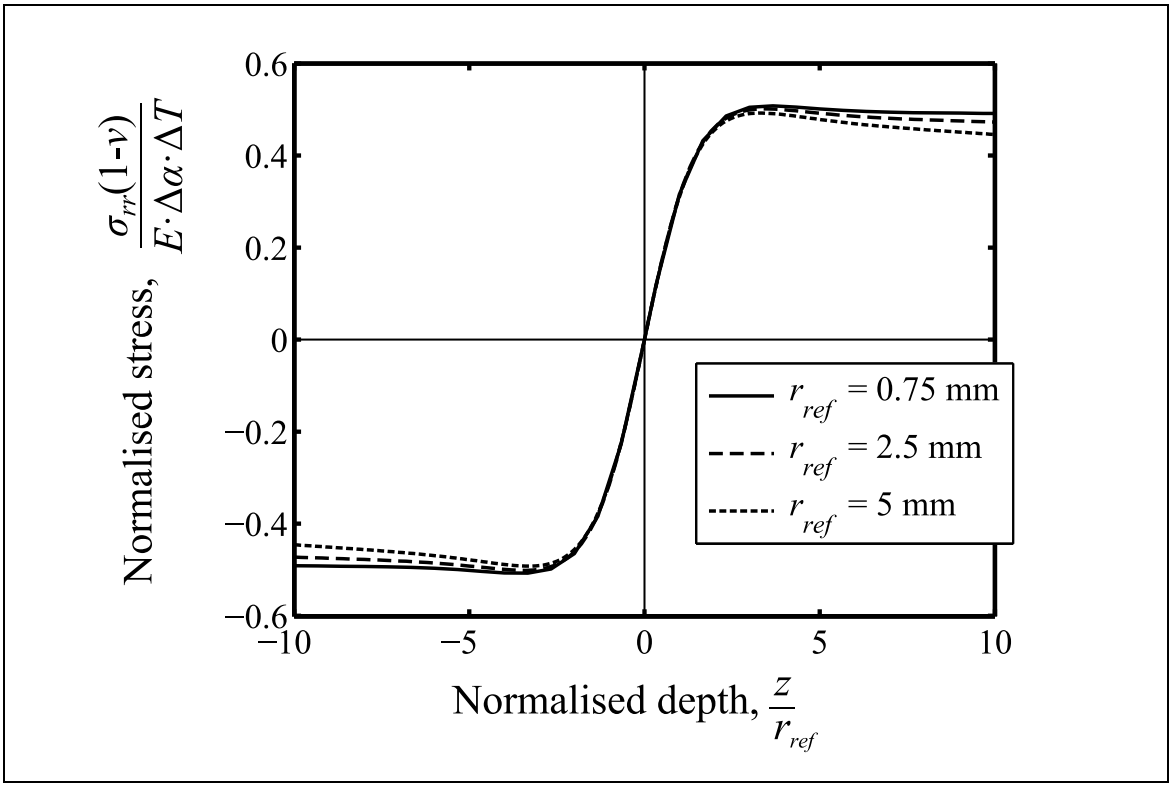

Figure 3.4 Normalised stresses calculated by simulated DHD measurement using different reference hole radii (r_{ref} = 0.75, 2.5, 5 mm).

3.4 Experimental method

3.4.1 Tensile tests

Tensile tests were carried out on specimens extracted from the parent and cladding materials in the clad plates (Figure 3.1) to determine material properties used throughout the work described in this thesis. For example, the residual stress measurements described in this chapter were all mechanical strain relaxation techniques which require a value for the Young's modulus. Also, stress-strain curves were required to determine elastic-plastic behaviour for use in finite element analyses presented in this chapter and in Chapter 4. All tests were carried out under displacement control at 20°C, and all tensile specimens were extracted after residual stress measurements were made, so that the residual stresses were not redistributed by material removal before they were measured.

CLADDING

Four specimens were extracted from the cladding on one side of the as-welded plate using wire electro-discharge machining (EDM). Two were aligned longitudinally to the weld direction, and two were transverse. The specimen geometries conformed to specifications for rectangular specimens given in ASTM E8/E8M [76], where the longitudinal specimens were subsize (25 mm gauge length) and the transverse specimens were sheet-type (50 mm gauge length). All specimens were 3.4 mm thick and contained only cladding. The specimen dimensions are shown in Figure 3.5 (a) and the positions from which they were extracted from the cladding are shown in Figure 3.5 (b). The specimen extension was measured using extensometers. One of each specimen type was subjected to several load-unload cycles up to 0.07% strain to enable accurate measurement of the Young's modulus. The remaining two specimens were tested to failure.

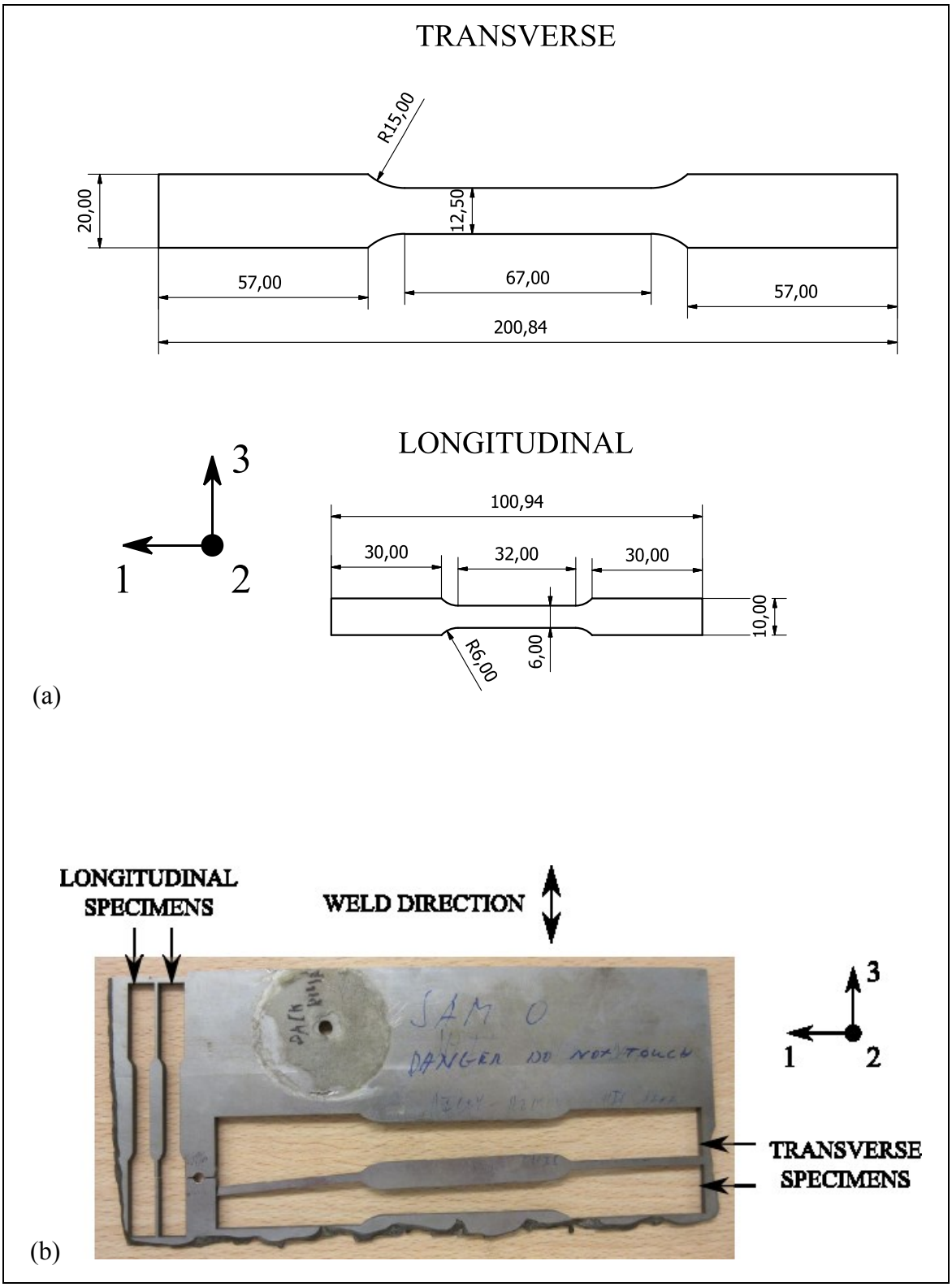

Figure 3.5 **Geometry of the transverse and longitudinal tensile specimens (a), and a picture of the cladding after it was removed from the as-welded plate and tensile specimens were extracted (b). Dimensions are in millimetres.**

PARENT

Three specimens were extracted from the parent material in the post-weld heat-treated plate. The geometry of the specimens is shown in Figure 3.6 (a). The geometry was similar to the sub-size rectangular specimens described in ASTM E8/8M [76], although the length of the grip section was smaller than standard because only limited material was available. Each specimen was extracted at a different depth beneath the interface between the cladding and the parent. It was expected that the yield strength of the material in the heat-affected zone directly beneath the cladding would be higher than the value for the bulk material, based on previous work in which enhanced hardness was measured in SA508 Grade 4N steel up to 3 mm beneath the interface with an Alloy 82 weld [43]. The depth beneath the cladding at which each specimen was extracted is shown in Figure 3.6 (b). Specimen P1 was extracted in the bulk material, far away from the cladding. Specimen P2 was extracted 3 mm beneath the cladding, and Specimen P3 was extracted as close to the cladding as possible whilst comprising entirely parent material. Specimens P2 and P3 were nominally 1.5 mm thick, and P1 was 4 mm thick. The actual machined dimensions were accurately measured prior to testing using a micrometer. The specimen extension was measured using an extensometer. Prior to testing to failure, Specimen P1 was subjected to several load-unload cycles up to 0.03% strain to enable accurate measurement of the Young's modulus.

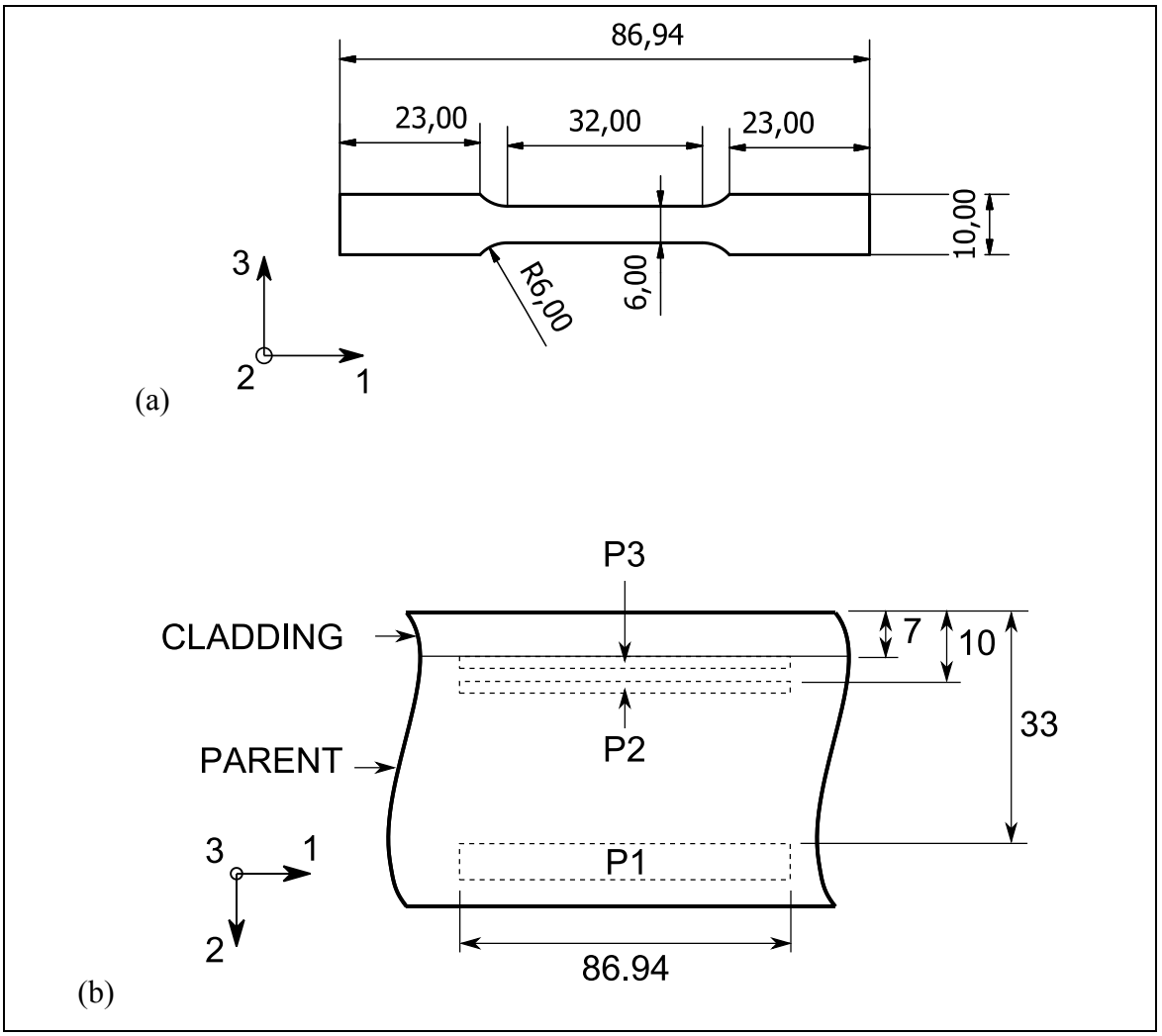

Figure 3.6 Geometry of the rectangular tensile specimens extracted from the parent material in the post-weld heat-treated plate (a), and a schematic of the positions from which the specimens were extracted relative to the interface (b). Dimensions are in mm.

RESULTS

Figure 3.7 shows the engineering stress-strain curves of the cladding (a) and the parent (b), and Table 3.2 summarises some commonly reported material properties calculated from the engineering stress-strain curves.

The stress-strain curves for the cladding in Figure 3.7 (a) only extend to fracture for the transverse specimen. Results for the longitudinal specimen are only available up to 18% strain because the extensometer reached its maximum travel at this point. The cladding specimen orientation did not significantly affect the stress-strain curve or the modulus,

and so the cladding properties shown in Table 3.2 are average values from the different tests. The cladding Young's modulus lies within the range of 160 – 234 GPa measured in overlay-welded Alloy 82 in previous work [77], and the yield strength is within the range of 295 – 351 MPa measured in specimens extracted from Alloy 82 butt welds in previous work [78].

The stress-strain curves for the parent shown in Figure 3.7 (b) do not extend to fracture because the travel of the extensometer was limited to 10% strain. The stress-strain curve of specimen P3 has been omitted beyond a point at which some slip between the extensometer and the specimen was observed. The results for specimen P2 are only available up to 0.7% strain because the thickness of the specimen varied by 5% along its length, and necking therefore occurred at the thinnest region which was at the end of the gauge length near region of the specimen which was clamped in the jaws of the test machine. The extensometer had a small gauge length relative to the gauge length of the specimen (10 vs 25 mm) and was located outside the region where significant plastic strain accumulated. The ultimate tensile strength of specimen P2 has been omitted from Table 3.2 for this reason. However, the 0.2% proof stress for specimen P2 is reported because the thickness in the region bound by the extensometer was accurately measured before testing. The Young's modulus is only reported for specimen P1 on which accurate measurements were made. The 0.2% proof stress of the bulk material (P1) lies within the range of 600 – 755 MPa measured in SA508 Grade 4N steel in previous work [79]. The 0.2% proof stress of the material directly beneath the cladding (P3) is 34% greater than the bulk value (P1).

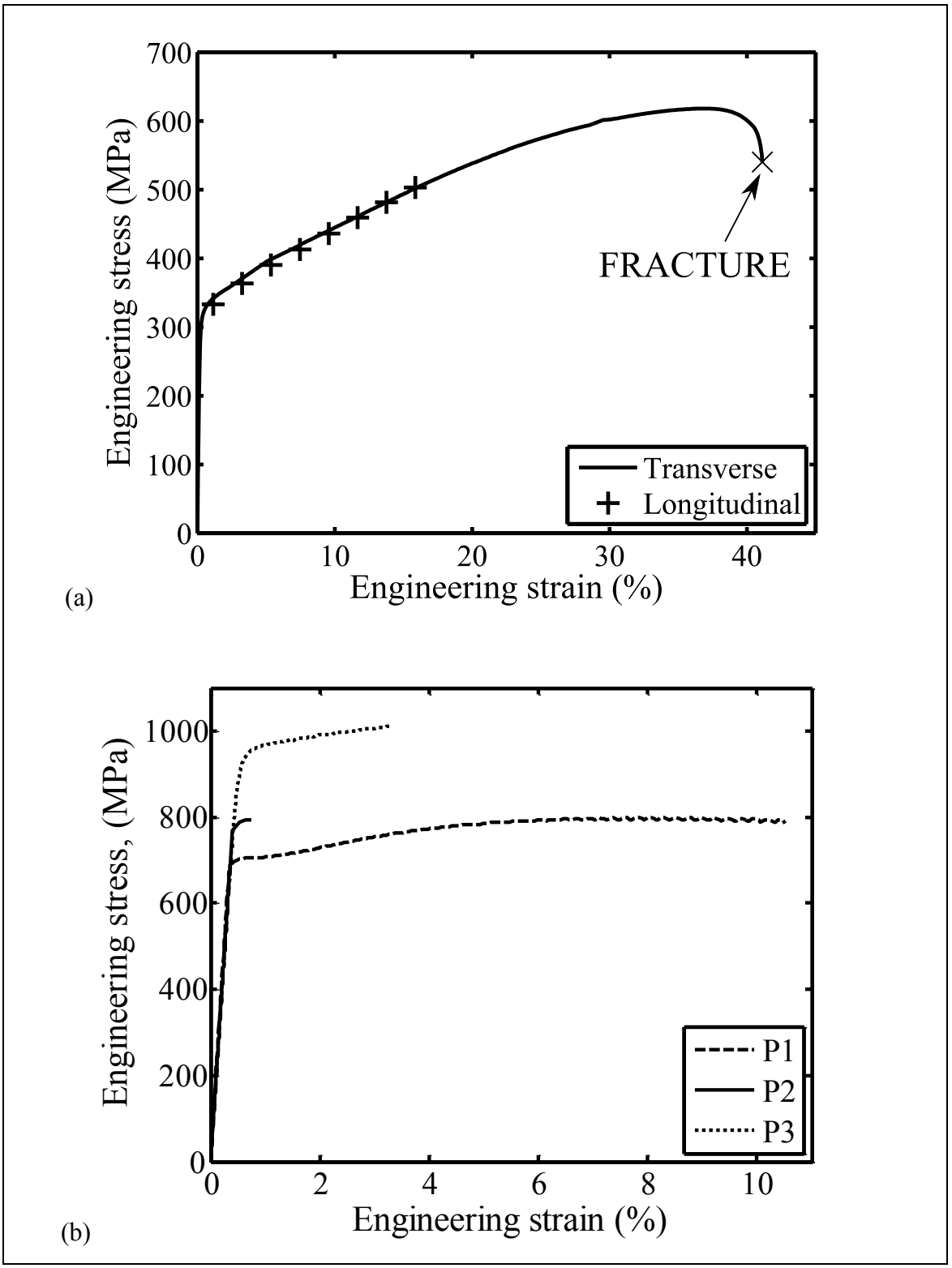

Figure 3.7 Engineering stress-strain curves of the Alloy 82 cladding (a) and the SA508 4N parent (b). Results for the cladding (a) include two different specimen orientations: transverse and longitudinal. Results for the parent (b) are for specimens P1, P2 and P3, which were extracted at the positions shown in Figure 3.6 (b).

Table 3.2 Material properties of the cladding and parent materials measured by tensile testing.

Material	Young's modulus, E (GPa)	0.2% proof stress, $\sigma_{0.2\%}$ (MPa)	Ultimate tensile strength, σ_{UTS} (MPa)
Cladding	172	310	618
Parent (P1)	203	703	799
Parent (P2)	-	783	-
Parent (P3)	-	945	1030

3.4.2 Residual stress measurements

A range of residual stress measurement techniques were used, each with specific capabilities. Near-surface residual stress measurements were carried out using incremental centre hole drilling (ICHD) [80, 81], which measures to a depth of half the hole diameter, usually 1 or 2 mm deep. Deep hole drilling (DHD) [41, 71-73] was used to measure residual stresses deep inside the specimens, although accuracy is reduced within approximately 1 mm of the surface. The contour method [82] was also used, which provides an area map of the residual stress to validate whether the line measurements obtained from DHD and ICHD are representative of the residual stresses throughout the clad plates. Table 3.3 summarises the components of stress and region measured by each measurement method. Measurements of σ_{22} were not made using the techniques reported in this chapter, although the σ_{22} component must equal zero at the surface of the cladding and previous through-thickness measurements of weld-clad pressure vessel material found that the components of stress normal to the cladding surface were small compared to the in-plane components [55]. Some measurements of σ_{22} in the post-weld heat-treated material are reported in Chapter 4, which were made using synchrotron X-ray diffraction.

Figure 3.8 shows a map of measurements and operations carried out on each block. Figure 3.8 (a) shows the as-welded block on which a single DHD measurement was made. This measurement was performed prior to the tensile specimens being extracted, so that the cladding was intact. Figure 3.8 (b) shows the measurements and cuts made on the post-weld heat-treated block. The number in brackets before each measurement label indicates the order. For example, (3) ICHD3 was carried out before (4) DHD1. The block was eventually cut into three segments, labelled A, B, and C as shown in Figure 3.8 (b): the

contour method cut the specimen in two via a wire EDM cut, and an additional wire EDM cut was performed so that there were two segments of equal width and a third smaller segment. Only Segment A was subjected to thermal shock, which is described in more detail later in this chapter. Table 3.4 identifies which measurements were made in the post-weld heat-treated plate before and after it was subjected to thermal shock.

The contour measurement was carried out by the Open University. More details on the contour measurement are reported in reference [83]. The ICHD measurements were carried out by Veqter Ltd to 1 mm depth (2 mm hole diameter), except ICHD5 which was 2 mm deep (4 mm hole diameter). The DHD measurements were carried out by the author at the University of Bristol. As a result of the finite element analysis presented in Section 3.3, the smallest practical DHD size was employed in order accurately measure the high stress gradients expected near the interface between the cladding and parent materials. The diameter of the reference hole was 1.5 mm, and the diameter of the trepan was 5 mm. The trepan was machined using EDM with a tubular copper electrode. The diameter of the reference hole was measured using an air probe manufactured by Mercer with a nominal diameter of 1.5 mm. Measurements were made at eight angles (i.e. every 22.5°) in 0.1 mm increments of depth. A full measurement of the reference hole therefore involved measurement at n number of positions:

$$n = 8 \times \frac{t}{0.1} \tag{3.3}$$

where t is the total thickness of the measurement in millimetres. The air probe was calibrated before and after each full measurement of the reference hole using a set of nine calibration rings manufactured by A&E Gauges Ltd, ranging from 1.4843 to 1.5251 mm internal diameter. The drilling and trepanning operations were carried out from the surface of the cladding (i.e. in the positive x_2 direction in Figure 3.1).

These residual stress measurement techniques used in this chapter are all mechanical strain relaxation methods which require a value for the Young's modulus. 172.4 GPa was used for the Alloy 82, which is the value given in Table 3.2 measured by tensile testing, and 206 GPa was used for the SA508 Grade 4N steel.

Table 3.3 A summary of the stress components measured by each residual stress measurement technique, and the region over which stress is measured.

Method	Measured Stress Components	Measured Region
DHD	σ_{11}, σ_{33}, σ_{13}	1D line along x_2 – through-thickness.
ICHD	σ_{11}, σ_{33}, σ_{13}	1D line along x_2 – near-surface.
Contour	σ_{33}	2D area map in the x_1-x_2 plane.

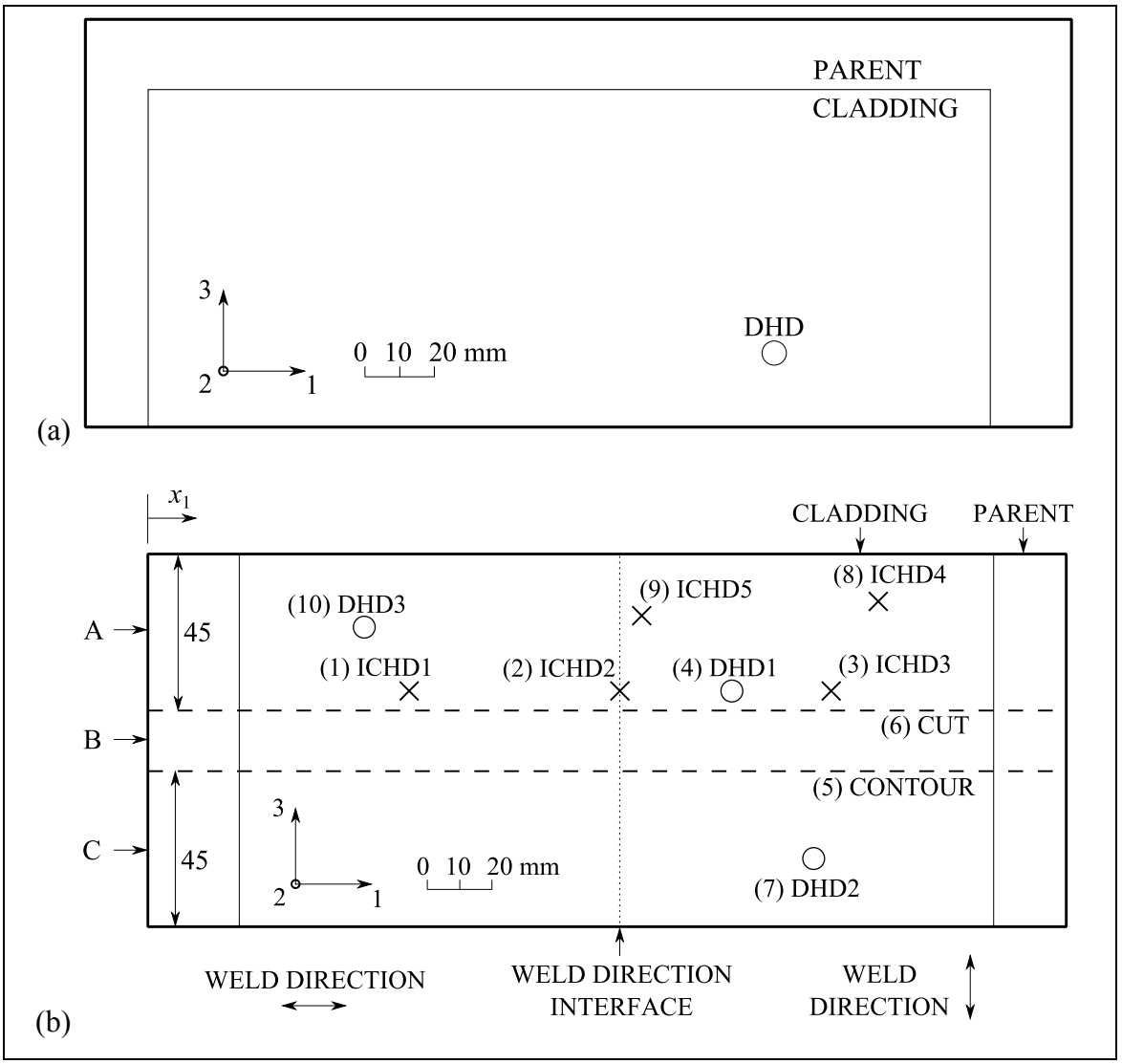

Figure 3.8 Position of residual stress measurements on the as-welded (a) and post-weld heat-treated (b) plates, drawn as if looking down onto the cladding surface from above. Dimensions are in mm.

Table 3.4 A summary of residual stress measurements carried out on the post-weld heat-treated block before and after experiencing thermal shock.

Before Thermal Shock	After Thermal Shock
ICHD1	
ICHD2	ICHD4
ICHD3	ICHD5
DHD1	DHD3
DHD2	
Contour	

3.4.3 Thermal shock test

The post-weld heat-treated plate was chosen for thermal shock tests since it best represents the state of the material in an RPV. Segment A in Figure 3.8 (b) was subjected to thermal shock using the arrangement illustrated in Figure 3.9. Water at a temperature of 20°C is supplied to a spray nozzle via a submersible pump. The spray nozzle is an aluminium box with 21 holes drilled on one face. The holes have a diameter of 2 mm and are arranged in two rows so that water is sprayed evenly over the specimen surface. The procedure used to subject the specimen to thermal shock was as follows. The specimen was first heated up to 480°C in a furnace. The specimen was then removed from the furnace and positioned over the spray nozzle. Finally, the nozzle pump was switched on, spraying the surface of the cladding with cold water at a rate of 13.8 l/min. The temperature throughout the specimen was monitored during heating and quenching by K-type thermocouples at three different depths which are shown in Figure 3.9: two were welded directly to the surface of the cladding (T1); two were secured in drilled holes at the mid-thickness (T2); and two were welded directly onto the unclad surface (T3). The method by which the surface thermocouples were attached to the specimen is described in more detail in Section 4.2.3. A picture of the thermal shock apparatus is shown in Figure 3.10 as the specimen was being subjected to thermal shock.

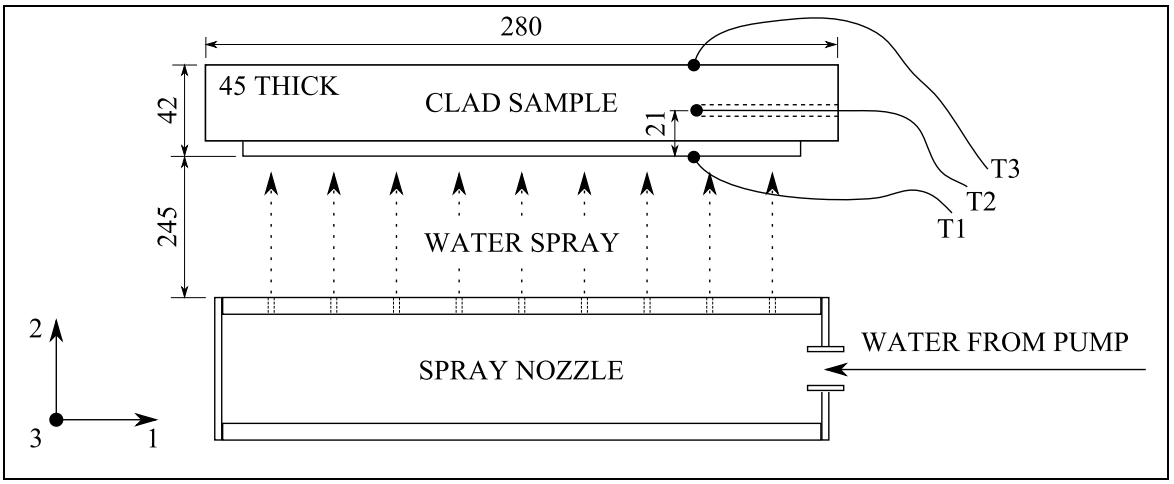

Figure 3.9 **The arrangement used to subject the post-weld heat-treated plate to thermal shock. The thermocouples are attached at positions T1, T2, and T3. Dimensions are in mm.**

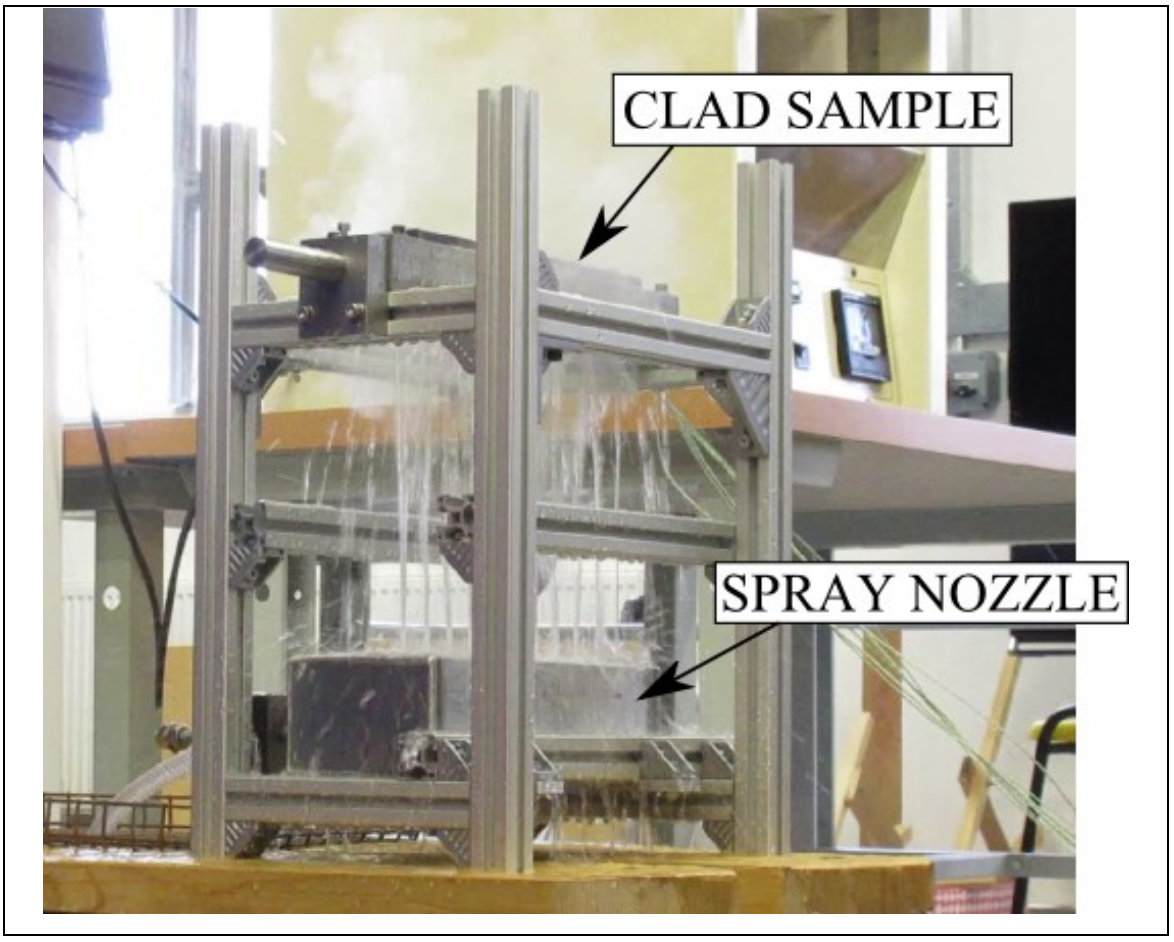

Figure 3.10 **A picture of the clad sample being subjected to thermal shock.**

3.5 Finite element method

A finite element model was made to investigate the physical causes of residual stress redistribution occurring during thermal shock. The model was analysed using the finite element code, Abaqus 6.14 [75]. The model consists of a heat transfer analysis followed by a stress analysis. The heat transfer analysis calculates the temperatures throughout the geometry at discrete increments of time during thermal shock. The results are then prescribed to the stress analysis, which calculates the stress due to thermal strain. The stress analysis also includes cladding residual stress. A schematic of the model geometry is shown in Figure 3.11. This is a quarter-model representation of Segment A of the heat-treated block, shown in Figure 3.8 (b). Symmetry boundary conditions were applied to two faces (at $x_1 = 0$ and $x_3 = 0$) for the stress analysis. The geometry was constructed using 26,320 eight node linear brick elements of type DC3D8 for the heat transfer analysis and of type C3D8R for the stress analysis. The same geometry was used for both the heat transfer and stress analyses.

For the heat transfer analysis, the mesh was initially at a uniform temperature of 480°C, which is the temperature that the clad sample was heated to before it was subjected to thermal shock. The surface of the cladding was then instantaneously adjusted to 20°C, representing perfect heat transfer, and the transient temperature throughout the mesh was calculated at progressively larger increments of time starting with 0.1 seconds. All other surfaces were assumed adiabatic. Simulating thermal shock in this manner circumvents prescribing a film heat transfer coefficient, which is difficult to calculate reliably and in practice varies with time during thermal shock [64]. This approach is akin to prescribing an infinite film heat transfer coefficient, and so the model can be considered an upper bound or severe simulation of thermal shock. This method is satisfactory given the purpose of the model is to better-understand a physical effect rather than exactly simulate the thermal shock. Note that heat flux is non-zero in only one direction (x_2 in Figure 3.11), and so in theory a one-dimensional mesh could be used. A three-dimensional mesh was used instead to simplify the process of transferring the results to the stress analysis.

For the stress analysis, the mesh was initially stress-free at a temperature of 580°C, which represents the post-weld heat-treatment temperature. The whole model was then cooled to 20°C. The effect is to generate cladding residual stress due to the difference in thermal expansion between the cladding and parent materials. No yielding occurred during this

elastic cooldown since the resulting residual stress was well below the yield strength of both materials. Finally, the transient stress during thermal shock was calculated by prescribing the time-dependant temperatures calculated in the heat transfer analysis.

Material properties used in the model are shown in Table 3.5 for the parent and Table 3.6 for the cladding. Thermal conductivity, specific heat, thermal expansion coefficient, and density were obtained from data published in the open literature [84-87]. Where data for the SA508 Grade 4N and Alloy 82 were unavailable, values for alloys with similar compositions were used instead. The thermal expansion coefficient is defined in this work as the mean linear coefficient from 20°C to the indicated temperature, so that free linear thermal expansion is calculated by:

$$\varepsilon_{th} = \alpha(T - 20) \tag{3.4}$$

where ε_{th} is the thermal strain (in m/m), α is the thermal expansion coefficient (in m/m°C), and T is the current temperature (in °C). Poisson's ratio and density were assumed temperature-independent. The room temperature Young's moduli of both materials were the same as those used for residual stress measurements. The parent was assumed to be elastic perfectly plastic with a room temperature yield strength equal to the 0.2% proof of the bulk material calculated from tensile testing (Section 3.4.1). In reality the yield strength is higher in the heat affected zone directly beneath the cladding than in the bulk material, but in this model the bulk value was used throughout the parent for simplicity. The Young's moduli of both materials and the yield strength of the parent were reduced at elevated temperatures using factors calculated from data published in the literature for comparable alloys [86, 88, 89]. For the elastic-plastic behaviour of the cladding, the stress-strain curve of the transverse specimen shown in Figure 3.7 (a) was converted to true stress and strain, discretised, and then input into Abaqus as an incremental plasticity material with isotropic hardening. True strain, ε_t, was calculated using:

$$\varepsilon_t = ln\left(\frac{l}{l_0}\right) \tag{3.5}$$

where l is the extended length and l_0 is the undeformed length. True stress, σ_t, was calculated by assuming that the specimen volume was conserved during the test:

$$\sigma_t = \frac{Fl}{A_0 l_0} \tag{3.6}$$

where F is the load and A_0 is the undeformed area. Equation (3.6) is strictly only true if the elastic strain (in which volume is not conserved) is much smaller than the plastic strain. At large total strains this holds true, and at small total strains the error is negligible because the change in cross sectional area is insignificant. The yield stress shown in Table 3.6 is the 0.2% proof stress. The elastic-plastic behaviour of the cladding was assumed temperature-independent. Limited data in the literature from tensile testing Alloy 82 weld metal suggests the yield strength of the cladding would in practice reduce with increasing temperature [78] which could promote more residual stress redistribution than calculated by the model, although it is expected that the effect would be small because the cladding rapidly cools during thermal shock.

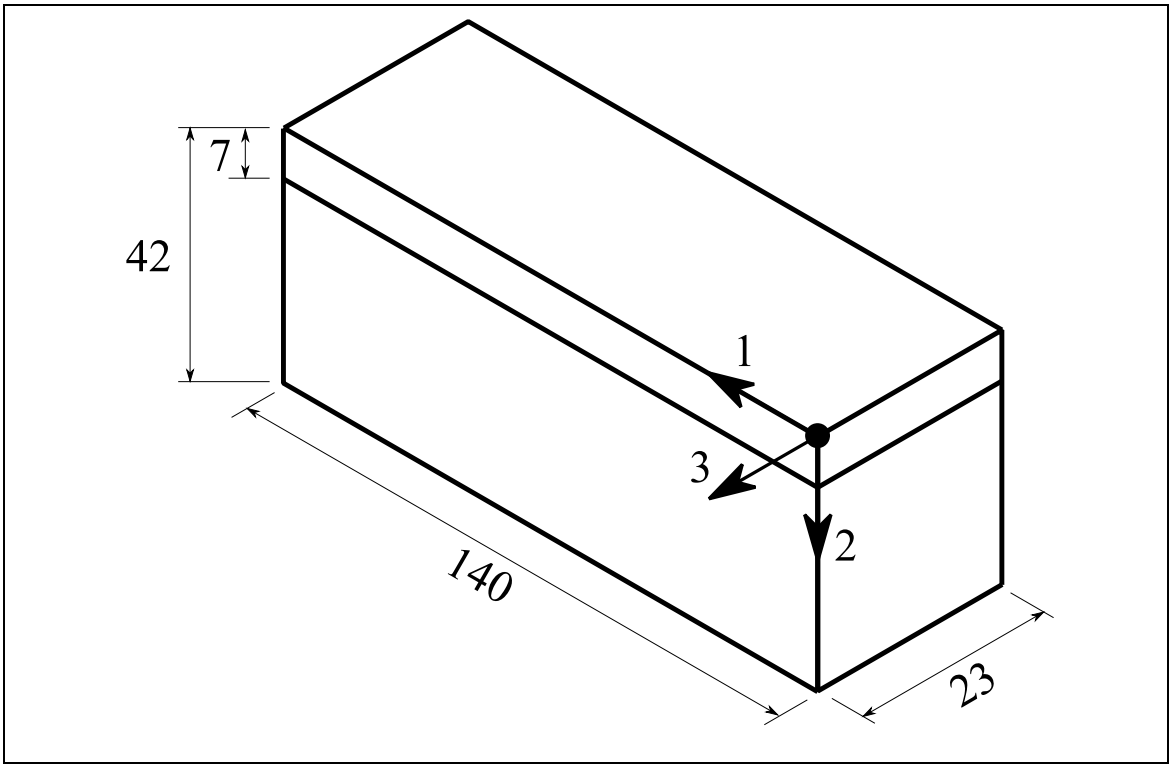

Figure 3.11 Geometry of the finite element model of thermal shock in Segment A of the post-weld heat-treated plate. Symmetry boundary conditions were prescribed to the $x_1 = 0$ and $x_3 = 0$ faces. Dimensions are in millimetres.

Table 3.5 Material properties used for the parent in the finite element analysis.

Temperature (°C)	Thermal conductivity, κ (W m^{-1} K^{-1})	Specific heat, c_p (J kg^{-1} K^{-1})	Thermal expansion coefficient, α (μm m^{-1} K^{-1})	Young's modulus, E (GPa)	Poisson's ratio, v	Yield stress, σ_y (MPa)	Density, ρ (kg m^{-3})
20	41.6	466	11.80	206	0.3	703	7790
100	41.3	495	12.14	204	0.3	664	7790
200	40.5	532	12.29	197	0.3	637	7790
300	39.3	570	12.51	192	0.3	620	7790
400	37.2	623	13.01	183	0.3	595	7790
500	34.7	695	13.59	173	0.3	537	7790
600	31.6	795	14.04	164	0.3	417	7790

Table 3.6 Material properties used for the cladding in the finite element analysis.

Temperature (°C)	Thermal conductivity, κ (W m^{-1} K^{-1})	Specific heat, c_p (J kg^{-1} K^{-1})	Thermal expansion coefficient, α (μm m^{-1} K^{-1})	Young's modulus, E (GPa)	Poisson's ratio, v	Yield stress, σ_y (MPa)	Density, ρ (kg m^{-3})
20	14.9	444	11.03	172	0.3	310	8470
100	15.9	465	11.33	169	0.3	310	8470
200	17.3	486	11.35	165	0.3	310	8470
300	19.0	502	11.35	160	0.3	310	8470
400	20.5	519	12.45	155	0.3	310	8470
500	22.1	536	14.03	151	0.3	310	8470
600	23.9	578	16.22	145	0.3	310	8470

3.6 Results

In figures in this section, the position of the interface between the cladding and parent materials is indicated with a vertical line that is labelled ‘interface’. The coordinate system is defined in Figure 3.1. The depth, x_2, is measured from the surface of the cladding.

3.6.1 Residual stress measurements in the as-welded plate

The through-thickness stress in the as-welded plate measured by DHD is shown in Figure 3.12. The stress is approximately symmetric, which is as expected since the as-welded block is clad on both sides. The maximum tensile stress is 650 MPa, which occurs in the parent material approximately 3 mm beneath the cladding.

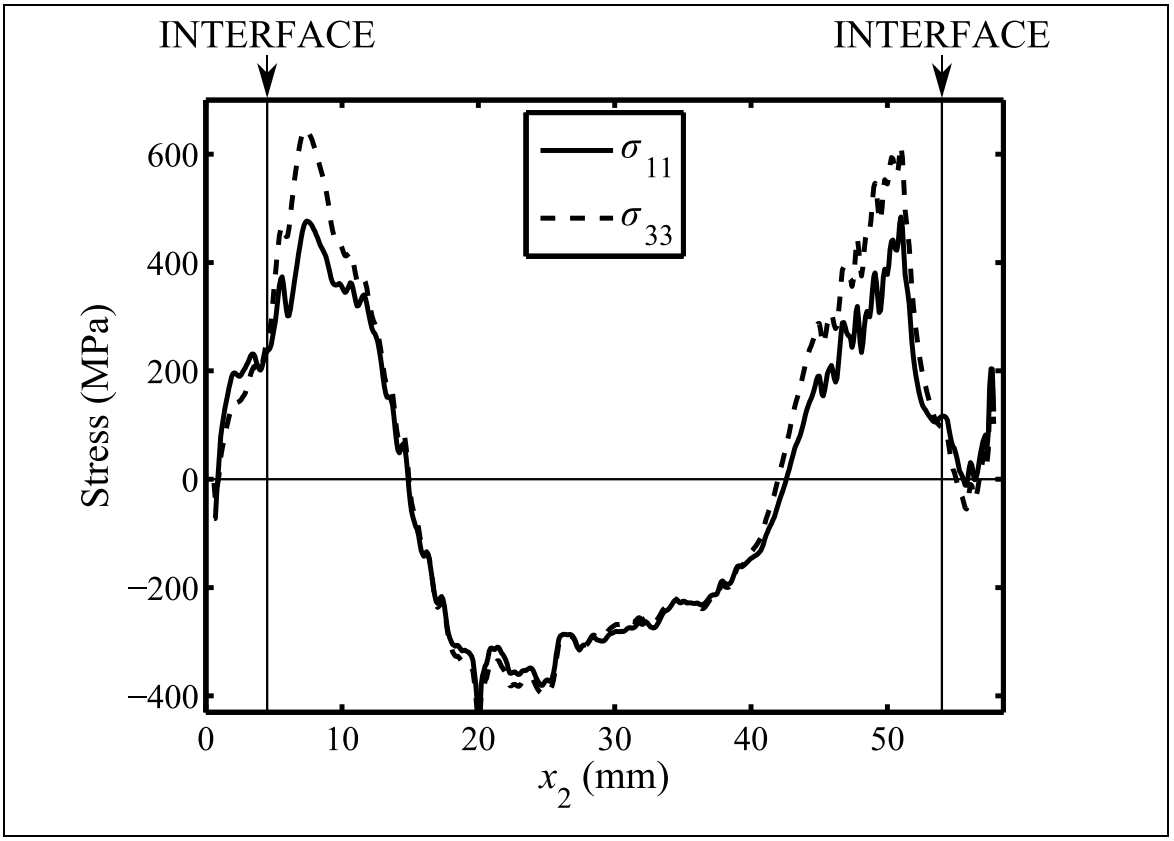

Figure 3.12 Residual stress in the as-welded plate measured by DHD.

3.6.2 Residual stress measurements in the post-weld heat-treated plate

The through-thickness residual stress of the post-weld heat-treated plate measured by DHD and a representative line of the contour measurement is shown in Figure 3.13 (a) (σ_{11} component) and Figure 3.13 (b) (σ_{33} component). Results from the contour measurement plotted in Figure 3.13 (b) were extracted at the position $x_1 = 220$ mm, where x_1 is defined in Figure 3.8 (b). Both the σ_{11} and σ_{33} components are tensile in the cladding and become compressive near the interface with the parent material. All measured magnitudes of stress are well below the yield strengths of the cladding (310 MPa) and the parent (703 MPa). DHD2, which was carried out after the plate was cut into three segments, shows good agreement with DHD1 and the contour measurement. Therefore, it can be assumed that cutting the plate caused negligible residual stress relaxation.

To investigate the variation in residual stress across the length of the plate, results from the contour measurement were extracted at six positions: at x_1 = 50, 80, 110, 220, 225, and 230 mm, where x_1 is defined in Figure 3.8 (b). The stress at each x_2 position was averaged over the six x_1 positions, and the results are plotted in Figure 3.14. The error bars represent the range of values measured at the different x_1 positions. The variation of residual stress with the x_1 position is greatest at 3.5 mm beneath the cladding in the parent material, where the range of measurements is up to 86 MPa. There is less variability in the cladding (around 50 MPa) and at the back face of the specimen (around 10 MPa). The variability exists because the measurement encompasses regions with different weld directions, as shown in Figure 3.8 (b), and because there is some variability of residual stress with the position relative to the weld bead. The latter cause of variability has been demonstrated in previous measurements on stainless steel cladding [46].

The ICHD measurements shown in Figure 3.15 (a) (σ_{11} component) and Figure 3.15 (b) (σ_{33} component) provide a more detailed characterisation of the residual stress within 1 mm of the cladding surface. Both components of stress are compressive at the surface. The magnitude and shape of the stress is strongly dependant on direction: the σ_{11} component of stress changes sign between 0.5 and 0.8 mm deep, and the σ_{33} component changes sign between 0.1 and 0.2 mm.

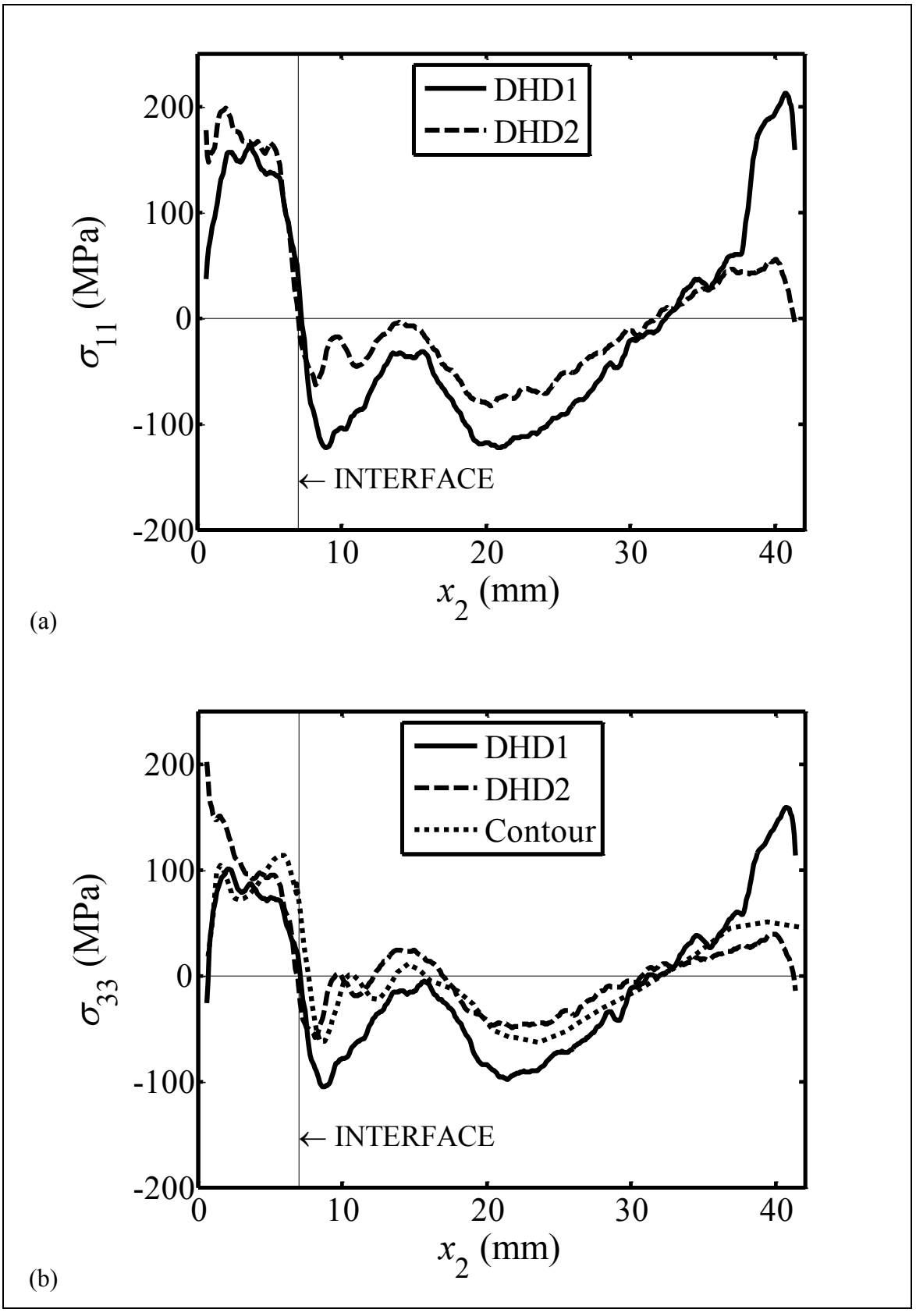

Figure 3.13 Through thickness residual stress in the post-weld heat-treated plate measured using DHD and contour methods. The σ_{11} component is shown in (a), and the σ_{33} component in (b). The contour data was provided by F. Hosseinzadeh at the Open University.

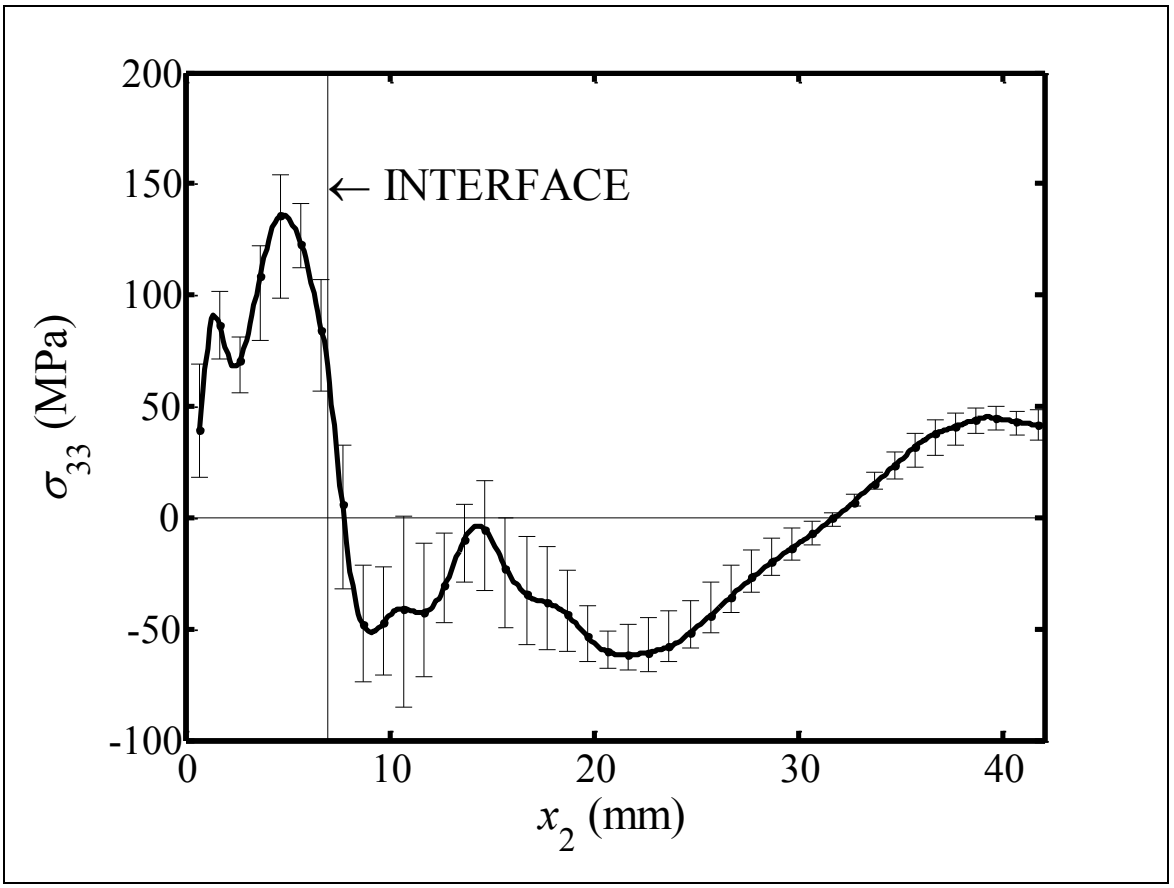

Figure 3.14 The range of through-thickness residual stresses measured by the contour method at different positions across the post-weld heat-treated plate [83]. Data provided by F. Hosseinzadeh at the Open University.

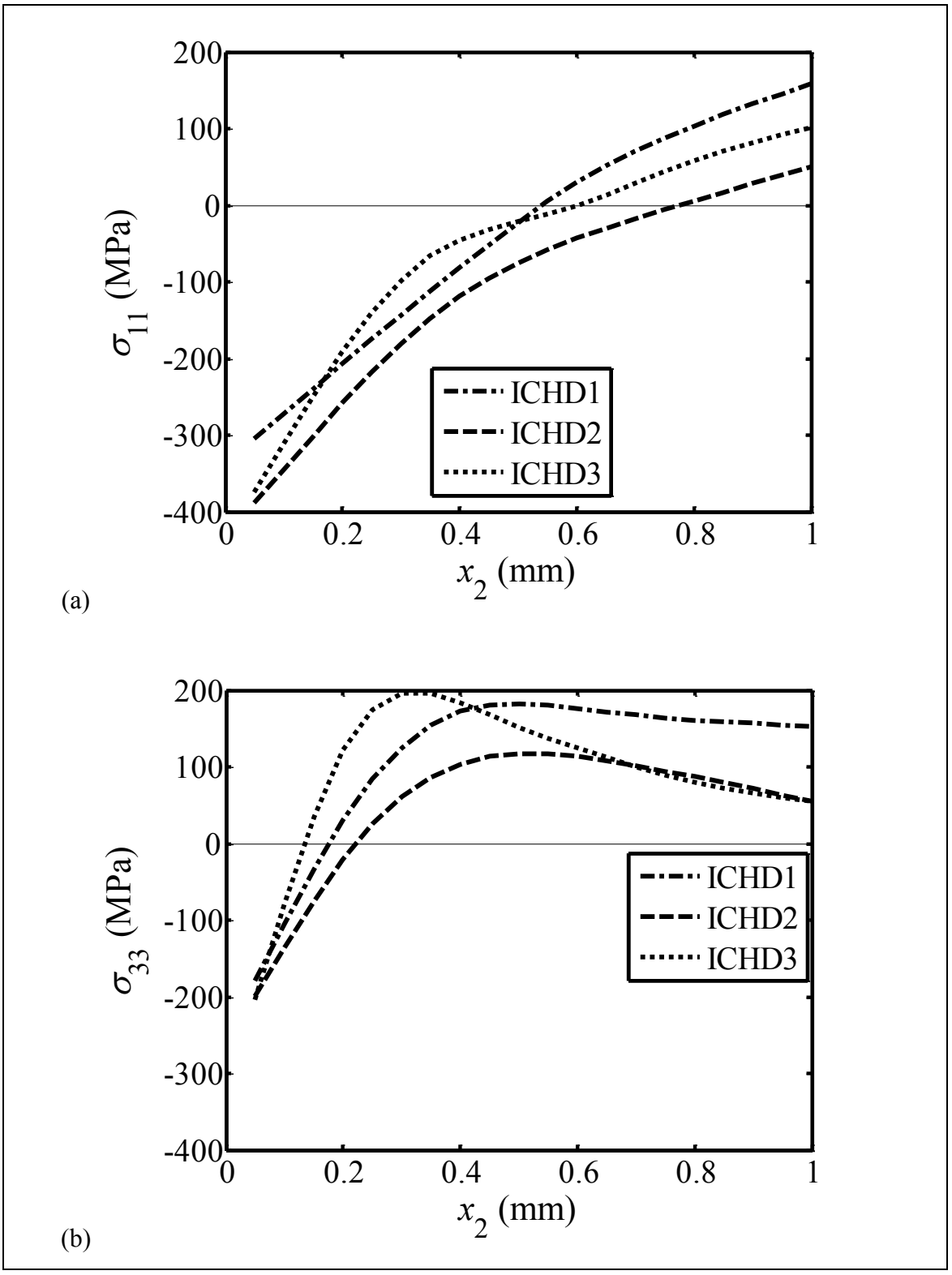

Figure 3.15 Near-surface residual stress in the post-weld heat-treated plate measured by ICHD: the σ_{11} component (a) and the σ_{33} component (b).

3.6.3 Rate of cooling during thermal shock

The temperatures measured in the post-weld heat-treated plate during thermal shock are shown in Figure 3.16. The surface of the cladding cooled by 370°C within the first second of thermal shock. The maximum temperature anywhere in the material was 50°C after four minutes. The thermocouple positions are more precisely illustrated in Figure 3.9. The results in Figure 3.16 use the average value from the two thermocouples at each position.

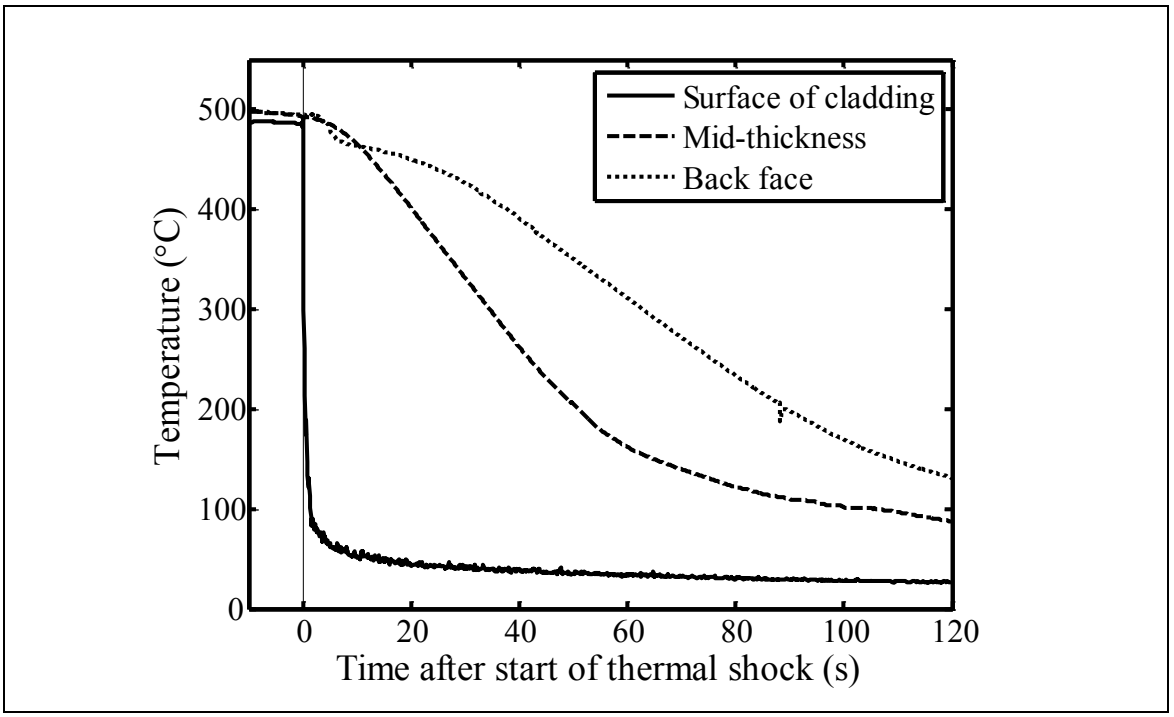

Figure 3.16 Temperatures measured in the post-weld heat-treated plate during thermal shock.

3.6.4 Residual stress measurements after thermal shock

Figure 3.17 compares DHD measurements made on the post-weld heat-treated plate before and after it was subjected to thermal shock. The σ_{11} component of stress is shown in Figure 3.17 (a) and the σ_{33} component in Figure 3.17 (b). Whereas before thermal shock the residual stress is tensile throughout the cladding, after thermal shock both components of stress are compressive to a depth of 2.6 mm. Residual stress redistribution occurred to a depth of approximately 10 mm.

The near-surface residual stresses measured by ICHD on the post-weld heat-treated plate before and after thermal shock are shown in Figure 3.18. The σ_{11} component of stress is shown in Figure 3.18 (a) and the σ_{33} component in Figure 3.18 (b). Whereas before

thermal shock the near-surface residual stress is strongly direction-dependant, after thermal shock the stress is approximately equi-biaxial. The residual stress after thermal shock is also entirely compressive throughout the measurement depth, which shows good agreement with the DHD measurements shown in Figure 3.17.

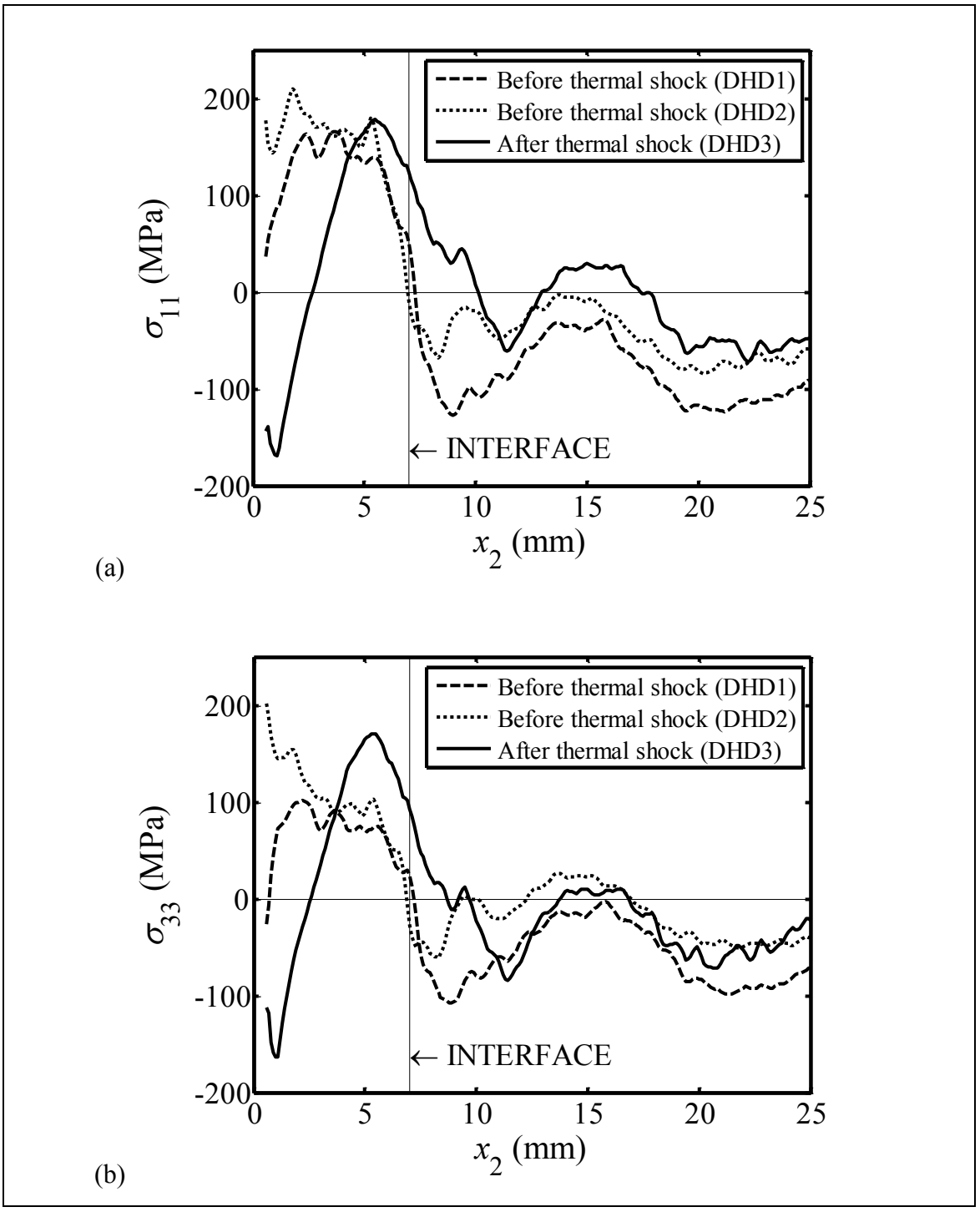

Figure 3.17 Comparison of DHD measurements on the post-weld heat-treated plate before and after thermal shock in the σ_{11} component (a) and σ_{33} component (b).

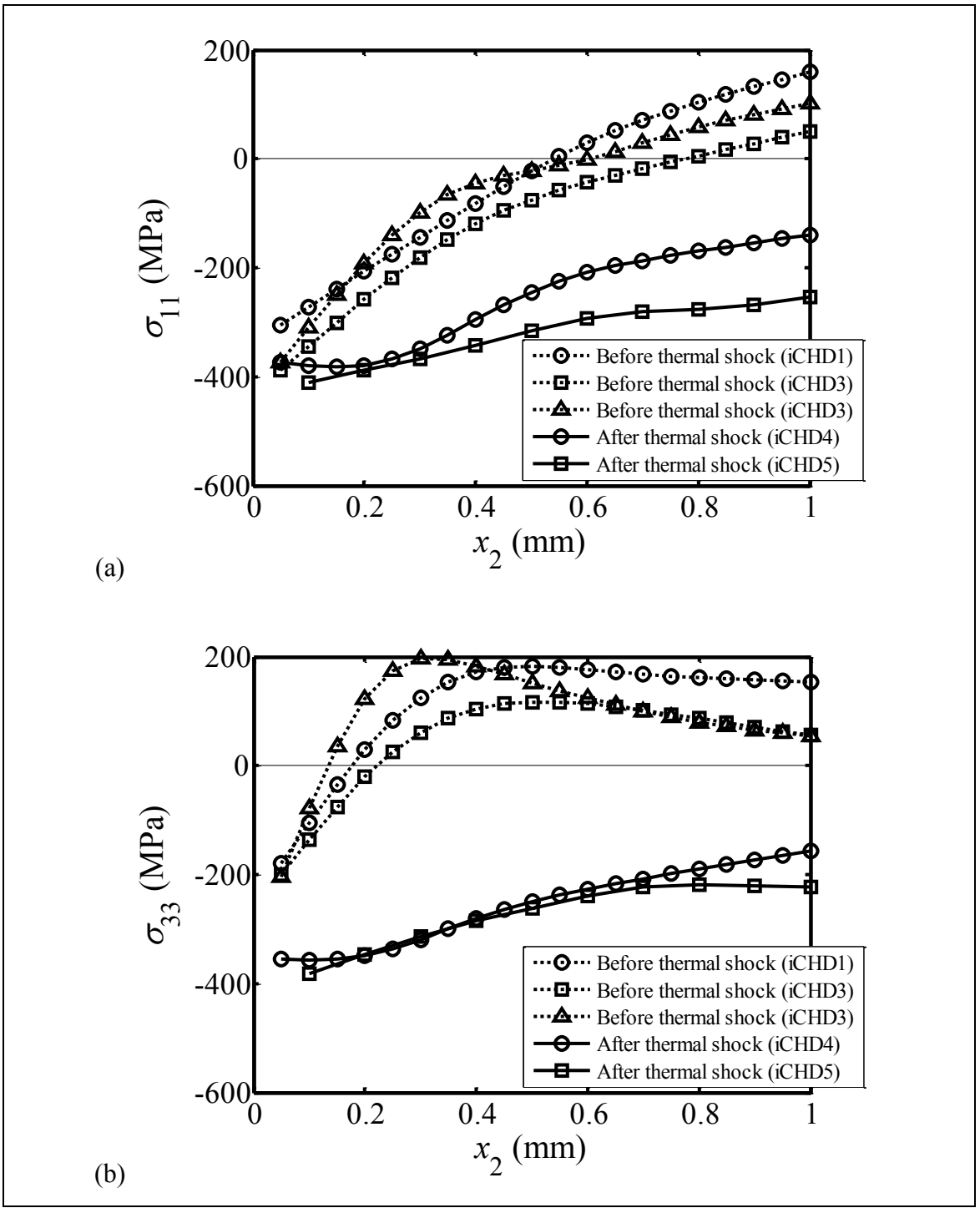

Figure 3.18 Near-surface residual stress before and after thermal shock measured by ICHD in the σ_{11} component (a) and σ_{33} component (b).

3.6.5 Finite element analysis

Figure 3.19 shows the residual stress at 20°C calculated by the finite element model before and after thermal shock. Before thermal shock the residual stress arises due to the difference in thermal expansion between the cladding and parent materials on cooling from zero stress at 580°C. The stress in each material is a combination of uniaxial stress

and bending. This basic method of generating cladding residual stress achieves similar magnitudes as those measured in the cladding (see Figure 3.13 (a)), but it is unable to accurately account for phase transformation effects occurring during welding in the heat affected zone in the parent [48]. After thermal shock the finite element model predicts yield-magnitude compressive stress at the surface of the cladding and smaller tensile stress towards the interface. The bending component of stress in the parent has changed direction and the stress directly beneath the interface is now tensile. The material in the parent does not yield during the simulation, and so the redistribution in the parent is entirely due to yielding in the cladding.

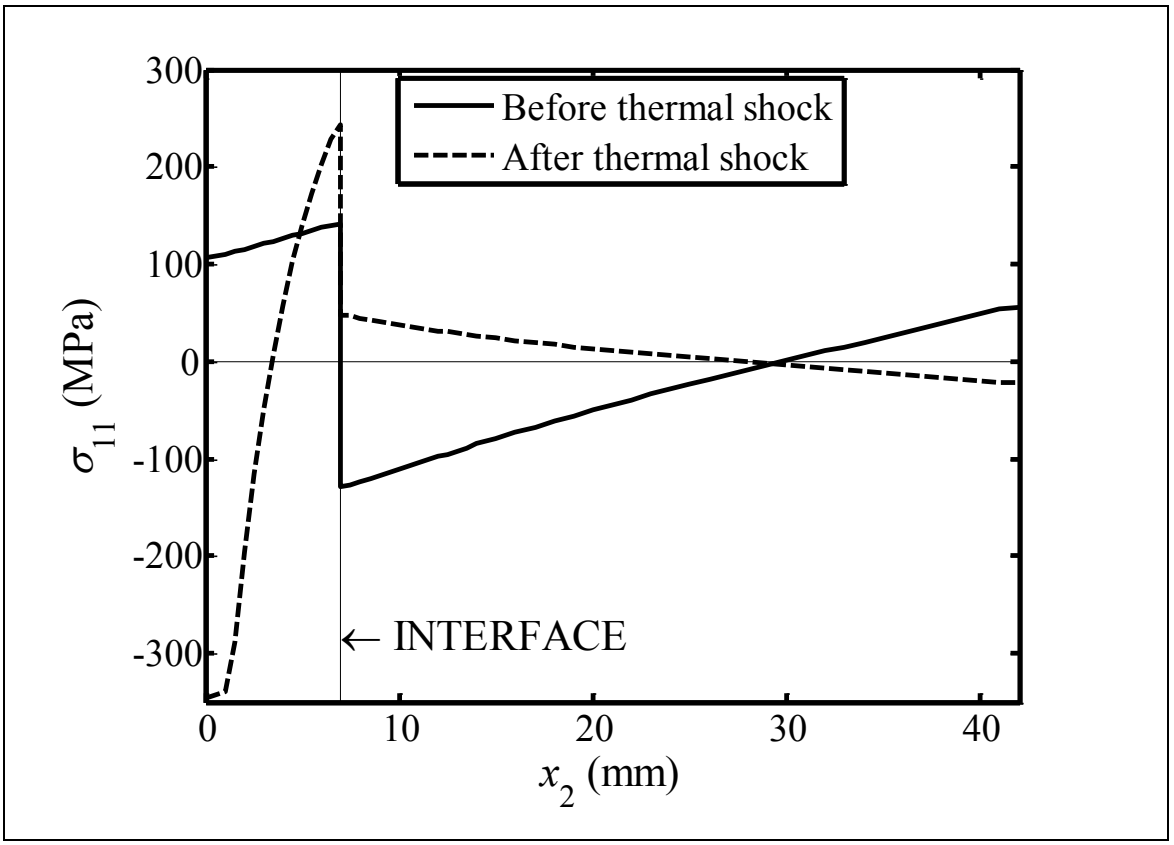

Figure 3.19 Residual stress calculated before and after thermal shock using finite element analysis.

3.7 Discussion

3.7.1 Residual stress in as-welded and post-weld heat-treated material

Figure 3.20 compares the residual stresses measured in the as-welded and post-weld heat-treated plates. The depth from the cladding surface, x_2, has been normalised by the thickness of the cladding because the cladding thickness is different in each plate. The as-welded result is from the single DHD measurement carried out on the as-welded plate. The plotted stress component is transverse to the weld direction in both plates. Residual stress is plotted down to a depth of only three times the cladding thickness, because deeper into the material the residual stress could be different just due to the different plate geometries rather than different heat treatments. The stress in the cladding is mostly tensile and of similar magnitude in both as-welded and heat-treated conditions. Beneath the cladding, the heat-treated block contains low-magnitude compressive stress whereas the as-welded block contains high-magnitude tensile stress with a peak of around 480 MPa. Similar findings have been reported in previous work on stainless steel cladding, where the main benefit of performing post-weld heat-treatment has been to reduce tensile stresses in the parent without causing significant redistribution in the cladding [47, 48, 52, 55]. The benefits to structural integrity of carrying out post-weld heat-treatment are quantified using stress intensity factor calculations in Section 3.7.3.

The through-thickness residual stress measured in the post-weld heat-treated material, for example shown in Figure 3.13 and Figure 3.14, is similar both in terms of magnitude and shape to measurements reported by Jones et al [49] on similar-sized post-weld heat-treated plates (38 mm total thickness) clad with 6 mm of Alloy 600 nickel-base alloy. The compressive surface stresses shown in Figure 3.15 are not commonly reported in the existing literature on cladding residual stress, in which measurements have been typically made on cladding which has not been machined flat after overlay welding. However, one study measured similar compressive surface stresses in milled and polished 309/316 stainless steel cladding using ICHD and X-ray diffraction [90].

One of the objectives of this work was to provide data on the residual stress in nickel-alloy cladding, whereas most existing work focuses on stainless steel cladding. The residual stress in these two types of cladding material might be expected to be different, for example if the thermal expansion coefficients are different. Measurements on the

nickel-alloy cladding from this work are compared with measurements on stainless steel cladding from other work in Figure 3.21. All measurements in Figure 3.21 are on post-weld heat-treated material, and the residual stresses are the in-plane components (i.e. σ_{11} or σ_{33} in Figure 2.2). The results for the nickel-base cladding are broadly similar to results for stainless steel cladding. It is difficult to make firm conclusions about the level of cladding residual stress obtained from two different cladding materials because there are many other factors which affect the residual stress, including: specimen geometry, the method used to deposit the cladding, and the post-weld heat-treatment conditions. This explains the large amount of scatter in the stainless steel results which were all obtained from different studies.

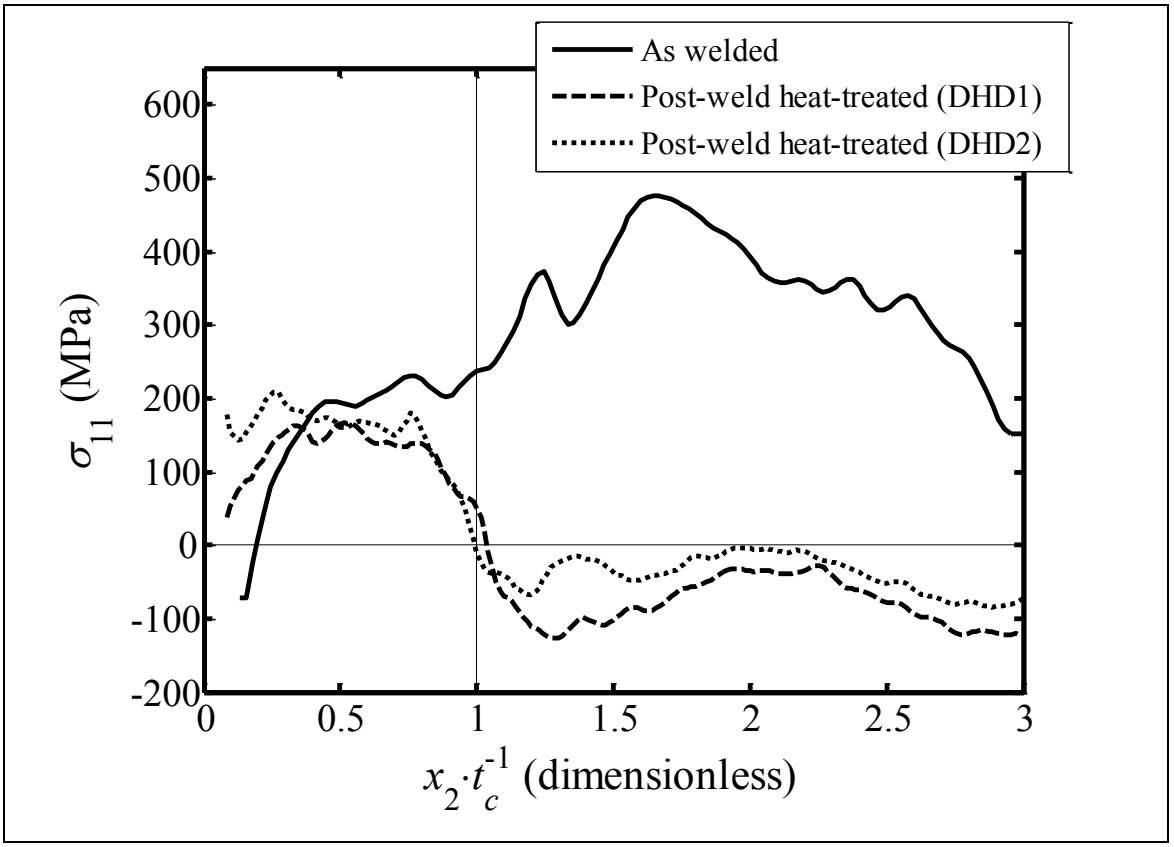

Figure 3.20 A comparison of through-thickness residual stresses in the as-welded and post-weld heat-treated plates.

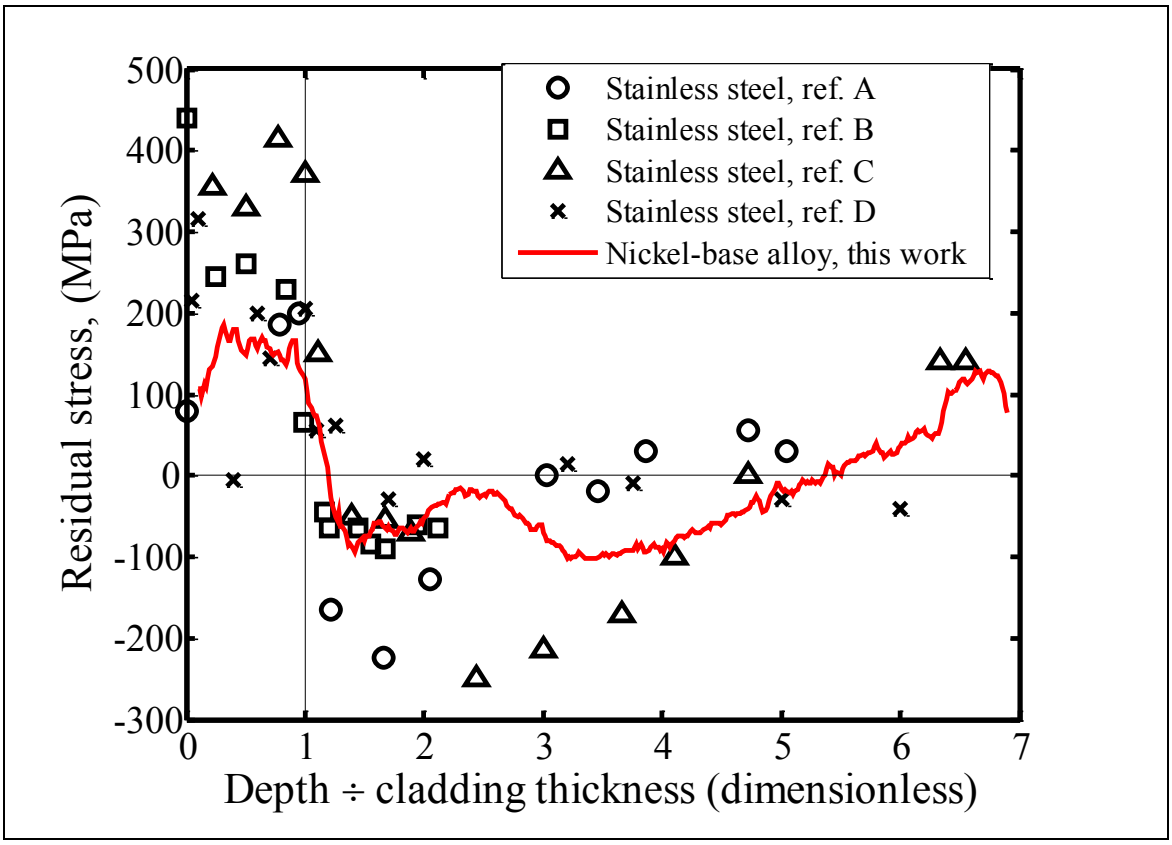

Figure 3.21 A comparison of in-plane residual stresses measured in stainless steel and nickel-base cladding. All measurements are in post-weld heat-treated material. The nickel-base measurements are the average of DHD1 and DHD2 in this work (σ_{11}). The stainless steel measurements are from various sources: ref. A [7], 6.35 mm type 308/304 cladding on A533-B, 32 mm total thickness; ref. B [47], 9 mm 24/21% Chromium stainless steel cladding on A508, 96 mm total thickness; ref. C [55], 9 mm type 309/308 cladding on A508, 59 mm total thickness; ref. D [50], 10 mm type 304 cladding on A533B, 135 mm total thickness.

3.7.2 The effect of thickness on cladding residual stress

Residual stress measurements presented in this chapter were carried out on 42 mm (post-weld heat-treated) and 58 mm (as-welded) thick plates. The cladding thickness in a typical RPV is similar at 5 – 7 mm [61], but the total wall thickness is much larger at 180 – 200 mm. Measurements in previous work by James et al [53] showed that the residual stress in a clad plate was significantly affected by reducing the thickness of the plate from 80 mm to 30 mm. Rybicki et al [7] extracted 32 mm thick samples from a larger clad plate, and found that reducing the thickness of the cladding by half from 8.9 to 4.4 mm significantly increased the magnitude of residual stress in the cladding. The results from this latter study suggested that the relative thickness of the cladding and parent materials had a significant effect on the residual stress in post-weld heat-treated material. Therefore, a finite element investigation is presented here to estimate the effect of plate thickness on the magnitude of cladding residual stress, so that the measurements made in this work

could be scaled up to a full-size RPV. The model geometry is shown in Figure 3.22. This is a plane stress model constructed and analysed using 8-node quadrilateral elements of type CPS8R in Abaqus 6.14 [75]. The model was initially stress-free, and then the temperature was uniformly reduced by ΔT, which is the same method of generating cladding residual stress used by the thermal shock model described in Section 3.5. The thickness of the parent was then reduced in steps by deleting elements, and the retained residual stress was calculated at each step. The cladding and parent materials were both linearly elastic with a Poisson's ratio of 0.3, and a Young's modulus of 206 GPa in the parent and 172.4 GPa in the cladding.

Figure 3.23 shows how the residual stress in the cladding varies with the thickness of the parent. On the y-axis, the residual stress averaged over the cladding thickness, σ_{av}, is normalised by the Young's modulus of the cladding, E_c, the difference in thermal expansion coefficient between the two materials, $\Delta\alpha$, and the change in temperature used to generate residual stress, ΔT. On the x-axis, the thickness of the parent, t_p, is normalised by the thickness of the cladding, t_c. The magnitude of residual stress increases as the thickness of the parent relative to the cladding increases. This is because changing the value of t_p/t_c changes the relative stiffness of the parent and cladding, as previously noted by Rybicki et al [7]. The cladding residual stress in this simple model is generated entirely by the difference in thermal expansion coefficient between the parent and cladding. If the materials were separate and unconstrained, they would contract by different amounts on cooling from the stress-free post-weld heat-treatment temperature. In practice the two materials are restrained from contracting freely because they are joined by welding. The degree of restraint depends on the relative stiffness of the two materials. For example, when the thickness of the parent tends towards zero ($t_p/t_c = 0$ in Figure 3.23) the residual stress tends towards zero because the stiffness of the parent is small compared to the cladding and provides negligible restraint. When the parent is thick ($t_p/t_c \rightarrow \infty$ in Figure 3.23) the stiffness of the parent is high compared to the cladding and the normalised residual stress tends towards one.

The geometries of the post-weld heat-treated plate used in this work and a typical RPV are located on the x-axis in Figure 3.23. The typical RPV was assumed to have a cladding thickness of 6 mm and a parent thickness of 180 mm. The magnitude of cladding residual stress in the typical RPV is 1.5 times greater than the post-weld heat-treated block tested in this work. Therefore, the residual stress in a full-thickness RPV could be estimated by

multiplying the residual stresses measured on the post-weld heat-treated plate in this work (before it was subjected to thermal shock) by a factor of 1.5. Referring to Figure 3.13 (a), this would increase the magnitude of residual stress in the cladding from 150-200 MPa to 225-300 MPa which is close to the yield strength of the Alloy 82 (310 MPa).

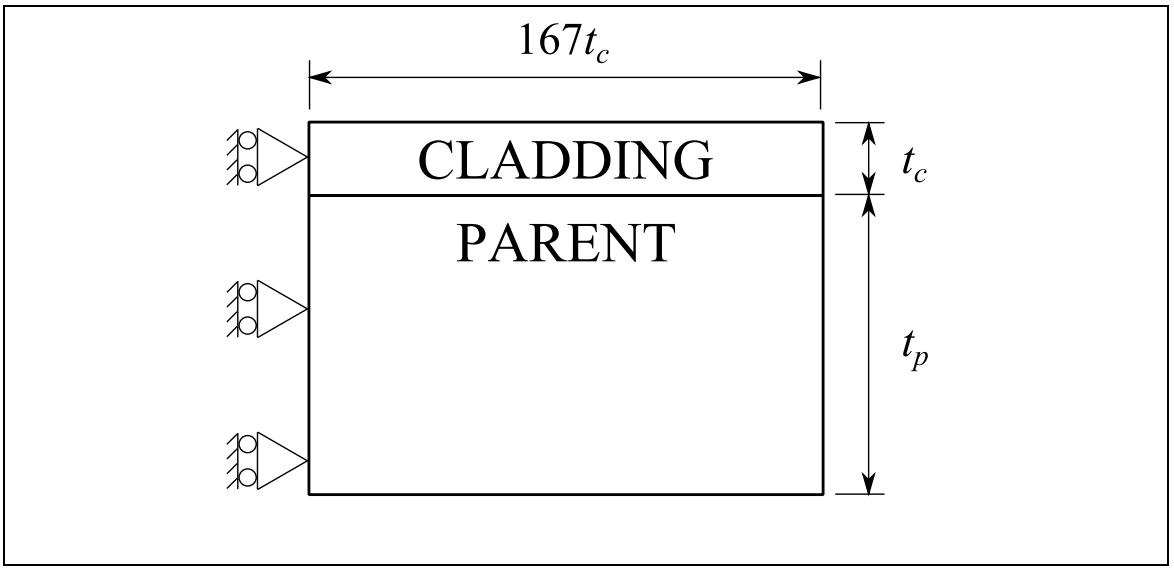

Figure 3.22 Geometry of the FE model used to investigate the effect of plate thickness on the magnitude of cladding residual stress.

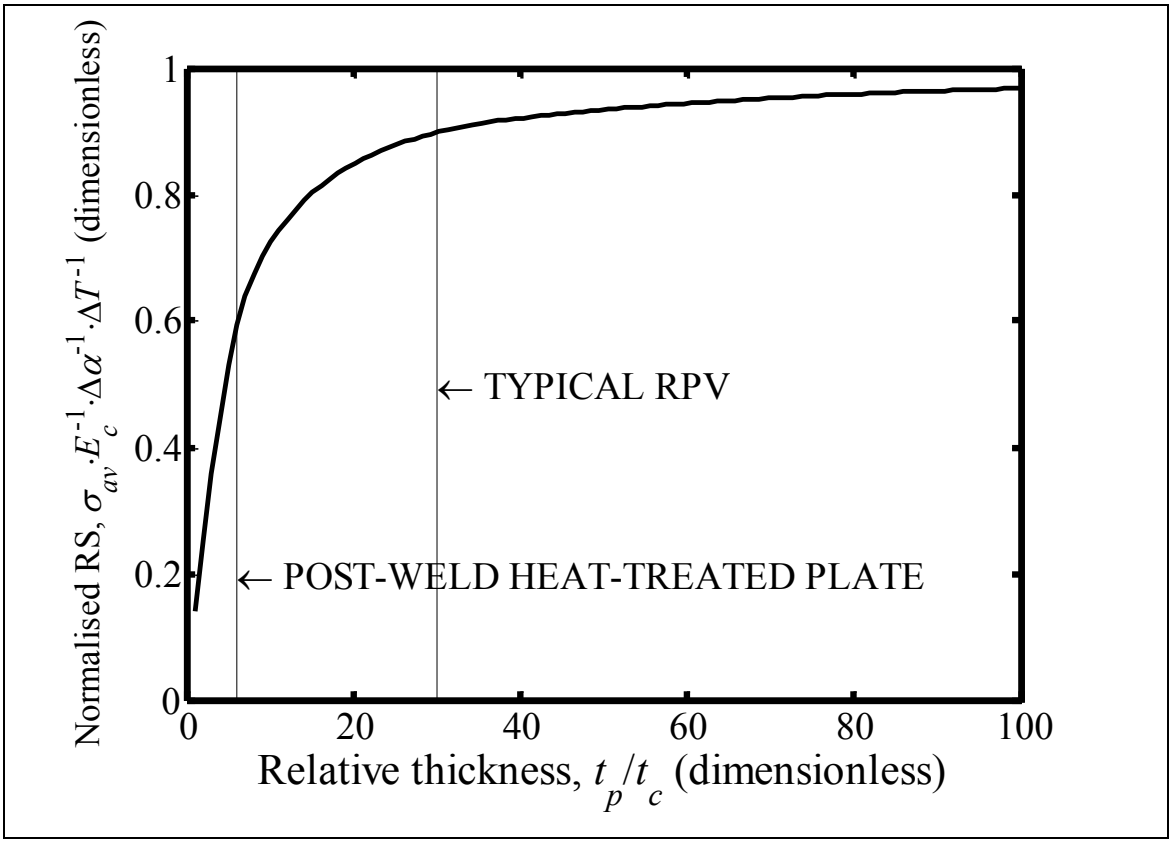

Figure 3.23 The average residual stress (RS) in the cladding, σ_{av}, for different ratios of parent to cladding thickness (t_p = parent, t_c = cladding).

3.7.3 Stress intensity factors calculated from residual stress

One motivation behind characterising residual stress in RPVs is so that the contribution of residual stress to failure by fracture can be accounted for. Therefore, a basic cracked-body analysis has been carried out using the weight function method to calculate the stress intensity factor resulting solely from residual stress loading, K_{RS}. The geometry of the model is shown in Figure 3.24. This is a two-dimensional model with a one dimensional through crack of length a extending from the edge. Such a configuration may exist in practice when stress corrosion cracking forms a defect which extends from the surface of the cladding. The following calculation for an edge crack in a semi-infinite plane presented by Wu and Carlsson [15] was used:

$$K_{RS} = \sqrt{a} \int_0^1 \sigma_{11}(X_2) \cdot m(X_2) \cdot dX_2 \tag{3.7}$$

$$m(X_2) = \frac{1}{\sqrt{2\pi}} \cdot \sum_{i=1}^{5} \beta_i (1 - X_2)^{i-\frac{3}{2}} \tag{3.8}$$

In Equation (3.7), σ_{11} is the stress normal to the crack, X_2 is x_2/a, and m is the weight function. In Equation (3.8), β_i is a set of coefficients given in reference [15]. Equation (3.7) was evaluated using trapezoidal numerical integration. The inputs σ_{11} and X_2 were refined near the crack tip using linear interpolation so that the integral could be accurately evaluated near the singularity of the weight function at $X_2 = 1$.

Figure 3.25 compares the stress intensity factors calculated using the residual stresses measured in the post-weld heat-treated and as-welded plates. Results for the heat-treated plate are presented both before thermal shock (BTS) and after thermal shock (ATS). The crack length, a, has been normalised by the thickness of the cladding, t_c, because the cladding thickness is different in each plate. For the as-welded material, the input stress in Equation (3.7), σ_{11}, was set to the results of the single DHD measurement carried out on the plate. For the post-weld heat-treated plate before thermal shock, σ_{11} was the average of ICHD1, 2, and 3 up to 1 mm deep, and the average of DHD1 and DHD2

thereafter. For the calculation after thermal shock, σ_{11} was set to the average of ICHD4 and ICHD5 up to 1 mm deep, and DHD3 thereafter.

The benefit of subjecting the material to a post-weld heat-treatment can be demonstrated by comparing the as-welded curve with the post-weld heat-treated BTS curve. The stress intensity factor is much higher in the as-welded plate than in the heat-treated plate, except for cracks shorter than the cladding thickness for which the magnitudes are similar in both as-welded and heat-treated conditions. The maximum value of K_{RS} is 3.4 times greater in the as-welded condition than in the post-weld heat-treated condition.

Now comparing results for the post-weld heat-treated plate before and after thermal shock, K_{RS} was significantly reduced after thermal shock for surface cracks shorter than the cladding thickness. The difference in K_{RS} is small for deeper defects. This is an important result since it allows allow better judgement of the structural integrity of an RPV that is expected to re-enter service after experiencing thermal shock due to a fault.

Note that the plate thickness effect discussed in the previous section would also mean that K_{RS} could be significantly different in a full-thickness RPV than in the relatively thin plates measured in this work. For example, K_{RS} for a crack smaller than the cladding thickness in the post-weld heat-treated plate before thermal shock would in practice be enhanced by the same factor as stress making it 1.5 times greater than shown in Figure 3.25. The maximum K_{RS} for a surface crack would then be 28 MPa $m^{1/2}$, at 6 mm deep ($a/t_c = 0.86$).

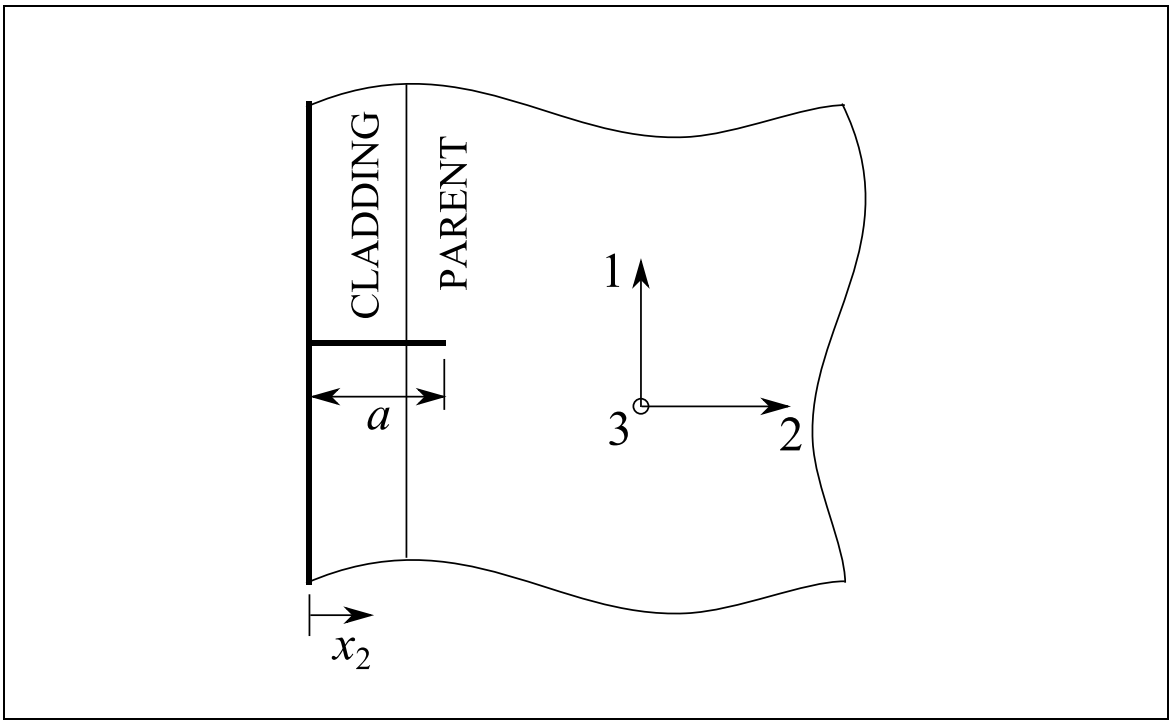

Figure 3.24 The geometry used for calculation of stress intensity factors induced by the measured residual stress distributions.

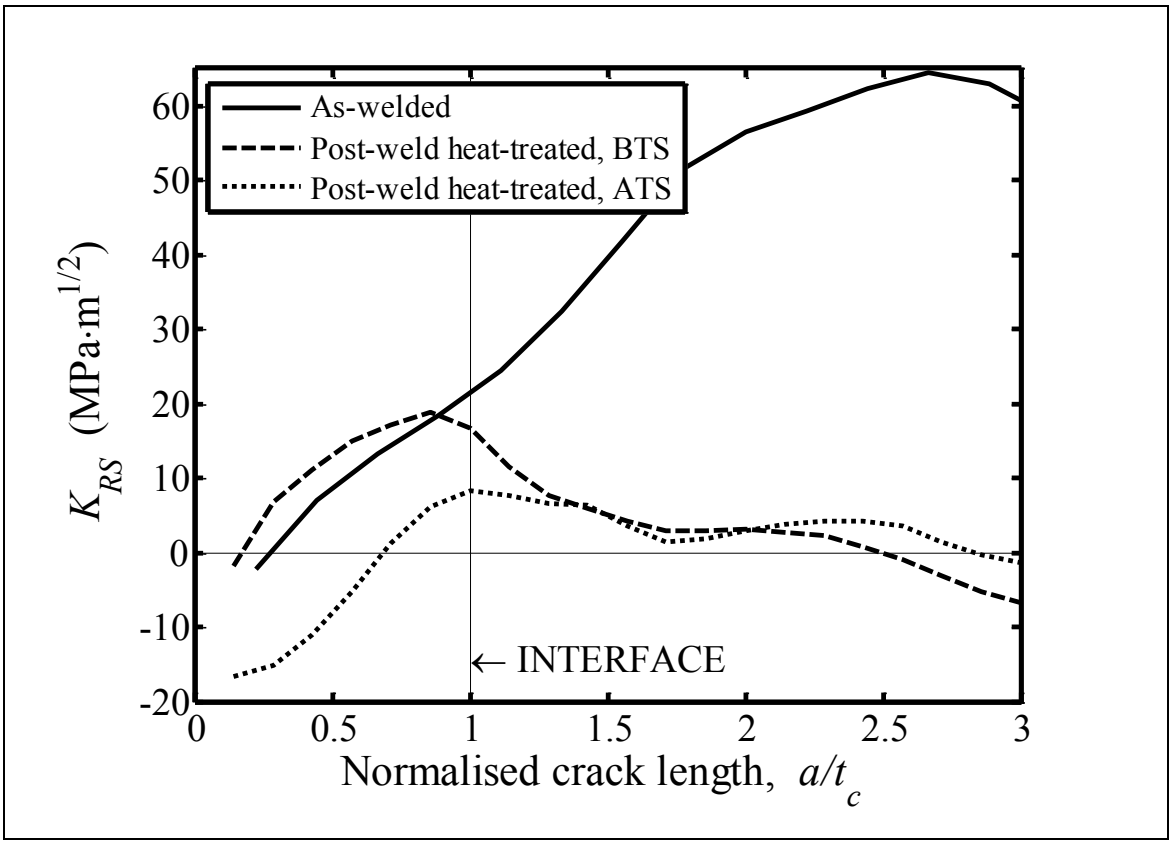

Figure 3.25 Stress intensity factors due to residual stress in the as-welded plate, and in the post-weld heat-treated plate before thermal shock (BTS) and after thermal shock (ATS).

3.7.4 General discussion

It was shown in Figure 3.17 that subjecting the post-weld heat-treated plate to thermal shock caused significant residual stress redistribution to a depth of at least 10 mm beneath the surface of the cladding. The residual stress after thermal shock simulated using FEA and measured using DHD3 and ICHD5 is shown in Figure 3.26. The measurements in the cladding broadly match the finite element prediction: the stress is compressive near the surface and tensile near the interface. This is similar to the shape of near-surface stresses measured in previous work on quenched bars [91], and in quenched cylinders and spheres [92]. The finite element model predicted significant residual stress redistribution throughout the parent (see Figure 3.19), which was caused by yielding and redistribution in the cladding since no yielding occurred in the parent. Given that the thermal shock simulated by the finite element model was impractically severe, it is reasonable to suggest that the measured redistribution in the parent material, although shallower and less significant than in the model, occurred by the same mechanism.

It has been demonstrated in previous work that residual stress relaxation can occur when combined with mechanical load [18, 19] whereas this thermal shock experiment has demonstrated redistribution solely due to thermal load. In doing so, it has been demonstrated that thermal and residual stresses interacted inelastically during thermal shock, because residual stress redistribution could only have been caused by yielding. The significance of this result can be demonstrated by comparison with the R6 structural integrity assessment procedure [20] which is widely used by the nuclear industry in the UK. In this thermal shock experiment, all sources of stress were secondary (i.e. thermal and residual). In the absence of primary stress (e.g. internal pressure or mechanical load), the interaction parameter, ξ, in Equation (2.4) equals one and so Equation (2.3) reduces to:

$$K = K_{J,S} \tag{3.9}$$

The calculation of $K_{J,S}$ is provided in R6 Section II.6.8 for the special case when the combined thermal and residual stresses exceed yield:

$$K_{J,S} = K_{J,th} + K_{RS} \tag{3.10}$$

where $K_{J,th}$ is the stress intensity factor due to thermal stress calculated using elastic-plastic analysis, and K_{RS} is the linearly-elastic stress intensity factor due to residual stress. Combining Equations (3.9) and (3.10):

$$K = K_{J,th} + K_{RS} \tag{3.11}$$

In the absence of primary stress, failure occurs when K is equal to the fracture toughness of the material. Equation (3.11) assumes that the thermal shock stresses and the residual stresses combine elastically, whereas the thermal shock experiment presented in this chapter has shown that this could be a conservative assumption for some defects. For example, Figure 3.25 shows that K_{RS} for a 4 mm crack was 16 MPa $m^{1/2}$ before thermal shock and -4 MPa $m^{1/2}$ after thermal shock, a reduction of 20 MPa $m^{1/2}$.

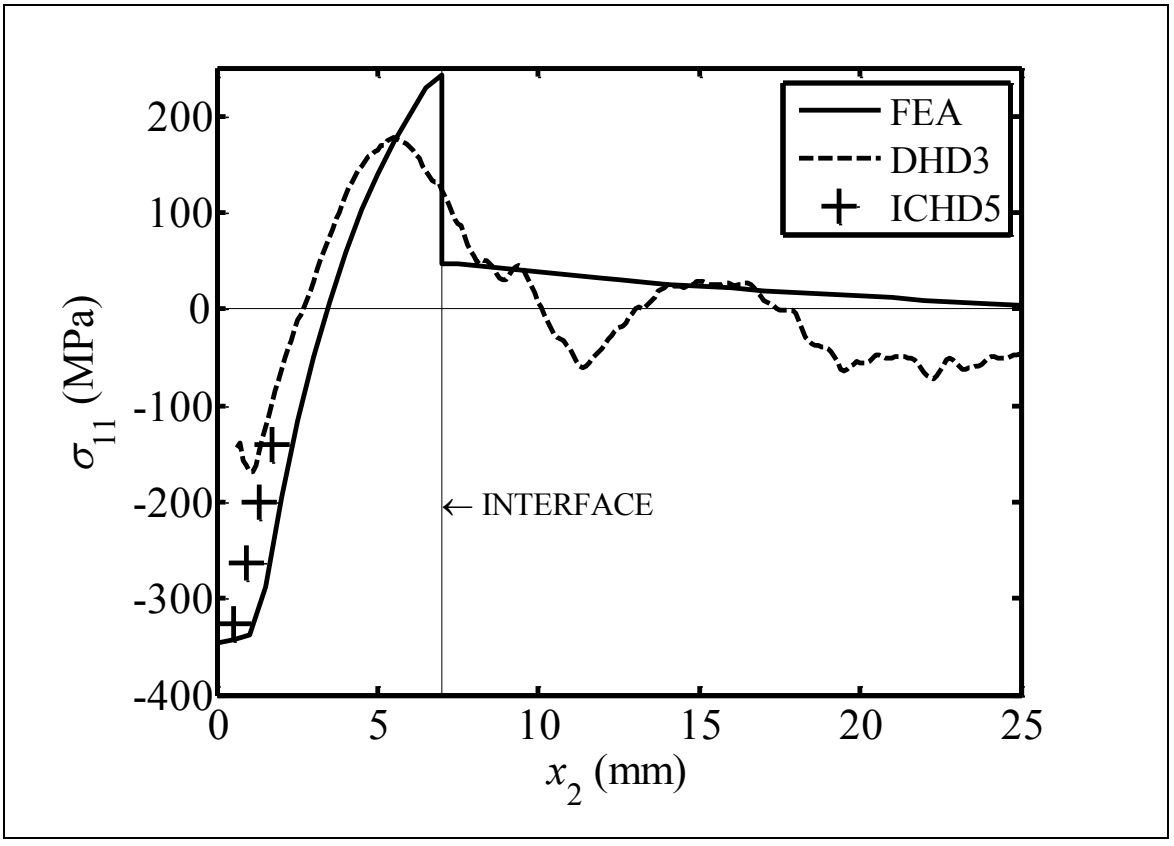

Figure 3.26 Residual stress in the post-weld heat-treated block after being subjected to thermal shock, simulated using FEA and measured using DHD3 and ICHD5.

3.8 Chapter summary

This chapter presented modelling and experiments concerning the residual stresses in two plates of SA508 Grade 4N nuclear pressure vessel steel, clad with Alloy 82 nickel-base alloy. Measurements of residual stress were made in both plates, one as-welded, the other post-weld heat-treated. The post-weld heat-treated plate was subjected to thermal shock, and the residual stress was measured again afterwards to see whether any redistribution occurred.

A finite element simulation of deep hole drilling found the method to be inaccurate near a step change of stress intended to represent high stress gradients expected at the interface between the parent and cladding. Reducing the diameters of the reference hole and trepan improved the accuracy, and so the smallest practical DHD size, which uses a 1.5 mm diameter reference hole and 5 mm trepan, was used for measuring residual stresses in the clad plates.

Tensile tests were carried out using specimens extracted from the cladding and parent regions of the clad plates. The 0.2% proof stress was 310 MPa in the cladding, and 703 MPa in the bulk of the parent. The 0.2% proof stress in the parent directly beneath the cladding in the heat affected zone was 34% greater than the bulk value.

Residual stress measurements showed that the residual stress was mostly tensile in the cladding in both the as-welded and post-weld heat-treated material, except within 0.5 mm of the surface of the cladding where the stress was compressive. Post-weld heat-treatment caused significant residual stress relaxation in the parent, but only moderate residual stress redistribution in the cladding.

It was demonstrated using a finite element model that the relative thickness of the cladding and parent materials significantly affects the magnitude of cladding residual stress. Hence, the magnitude of residual stress would be greater in a full-thickness RPV than in smaller mock-ups such as those measured in this work. From the measurements made in this work, it was estimated that the residual stress in the cladding of a full-thickness post-weld heat-treated RPV clad with nickel-base alloy would be 225-310 MPa. The peak stress intensity factor due to residual stress would be 28 MPa $m^{1/2}$ for a surface defect.

Subjecting the post-weld heat-treated material to thermal shock caused significant residual stress redistribution to a depth of at least 10 mm from the surface of the cladding. This demonstrates that the thermal and residual stresses interacted in an inelastic manner, and that combining them elastically, as suggested in the R6 structural integrity assessment procedure, is therefore conservative. The stress intensity factor for a 4 mm surface crack calculated from the residual stress reduced from 16 MPa $m^{1/2}$ before thermal shock to -4 MPa $m^{1/2}$ after thermal shock.

4 Measurements of Stress During Thermal Shock Using In-Situ Time-Resolved Synchrotron X-ray Diffraction

4.1 Introduction

The aim of the work presented in this chapter was to measure stress in clad RPV material during thermal shock. This was achieved by developing a novel experimental technique whereby thin specimens were extracted from the post-weld heat-treated clad plate described in Section 3.2, and were subjected to thermal shock using a bespoke self-contained thermal shock rig which enabled simultaneous measurements of stress by synchrotron X-ray diffraction.

In this chapter, the experimental method is first described in Section 4.2. A test rig was designed to subject specimens to thermal shock, whilst simultaneously enabling measurements of stress using synchrotron X-ray diffraction (XRD). Seven specimens were extracted from the post-weld heat-treated clad plate which was described in Section 3.2, and surface cracks (through-cladding) were machined in four of them. The specimens were subjected to thermal shock on Beamline I12 [13] at Diamond Light Source, the UK's national synchrotron facility. Time-resolved stress was measured during thermal shock at a single point close to the crack tip at a sample rate of 30 Hz. In addition, the stress around the crack tip was mapped under steady-state conditions before thermal shock at 20°C and 360°C, and after thermal shock at 20°C. Section 4.3 presents a finite element model which represents a typical thermal shock analysis method for comparison with the experimental

results. The validated modelling approach could then be used as a benchmark to be modified for thermal shock analyses on different materials and geometries. The model calculates the elastic-plastic strains and stresses during thermal shock in a three-dimensional representation of the thin specimens used in the experiment. The results from the experiment and model are shown in Section 4.4, followed by a discussion in Section 4.5. It is shown that peak tensile stresses measured near the tip of the surface cracks occur within the first second of thermal shock and are up to 966 MPa. The finite element model predicts that peak stresses occur at similar times, but their magnitude is higher. Agreement between the model and the experiment diverges beyond the point of peak stress, and some sources of experimental error which could cause this difference are discussed.

Dr Chris Simpson of the University of Bristol analysed the raw X-ray diffraction data to provide the experimental stresses and strains used in this chapter. The procedure is briefly described in Section 4.2.5. Andrew James of the University of Bristol carried out the grain size measurements reported in Table 4.1. All other work reported in this chapter was undertaken by the author.

4.2 Experimental method

4.2.1 Specimens

For this work, specimens were extracted from the post-weld heat-treated plate described in detail in Section 3.2. The geometry of the specimens is shown in Figure 4.1. The specimens are relatively thin at only 2 mm thick to enable sufficient X-ray transmission for a high diffraction sample rate (30 Hz), so that the transient stresses during thermal shock could be accurately captured. Some specimens contain a through-crack of length, a, at their mid length, which represents a through-cladding surface defect. The cracks were machined from the surface of the cladding (i.e. the bottom of the specimen as shown in Figure 4.1) using wire EDM with a 0.1 mm diameter wire. A total of seven specimens were extracted from the post-weld heat-treated plate. Two specimens were crack-free. Two specimens contained 7.4 mm long cracks, terminating in the parent just beyond the

interface with the cladding. Two specimens contained 10 mm long cracks, terminating well beyond the interface in the parent. One final specimen was manufactured with a comb feature to relieve stresses in the material for measurement of stress-free lattice constants. The comb feature is illustrated in Figure 4.2.

Specimens were extracted from the post-weld heat-treated plate following the program of residual stress measurements and thermal shock experiments described in Chapter 3. Therefore, the plate was in three segments which are shown in Figure 4.3 (a). Segment A had been subjected to thermal shock, whereas Segments B and C had not. The positions from which specimens were extracted for this work are also shown in Figure 4.3. Four specimens were extracted from Segment B and three specimens were extracted from Segment C. The specimens were extracted using wire EDM. The orientation of the specimens is illustrated in Figure 4.3 (b) in the context of the clad plate in its original, as-received condition. The co-ordinate system used in this chapter is consistent with that of the post-weld heat-treated clad plate shown in Figure 3.1. The depth of the cladding in the specimens shown in Figure 4.1 is 7 mm, but in practice the cladding depth varied between 6.6 and 7.4 mm because of melting and redistribution of material occurring during overlay-welding.

Measurements of grain size in the parent (SA508 Grade 4N ferritic steel) were made to inform the slit size and acquisition time chosen for the set-up of the X-ray diffraction equipment. The slit size is the size of the X-ray beam projected onto the specimen surface, and it was chosen to ensure a sufficient number of grains were sampled to represent the bulk material and acquire high-quality diffraction data. Measurements were carried out by Andrew James at the University of Bristol using polishing and etching techniques. The results are summarised in Table 4.1. Measurements were not made in the cladding because it was already known from preliminary trials at Diamond Light Source that the grain size in the Alloy 82 was large enough (of the order of millimetres [43]) to make X-ray diffraction impractical in this region.

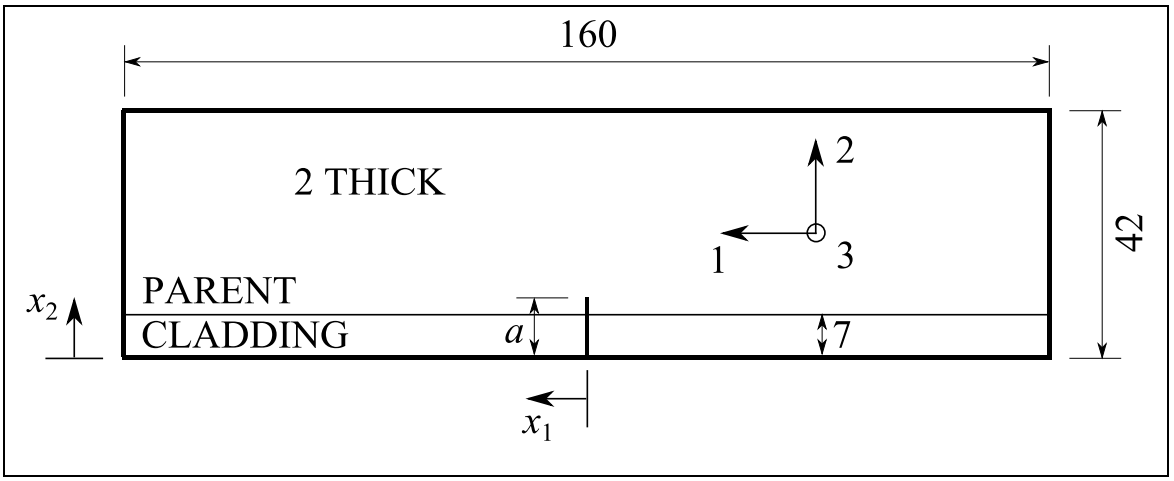

Figure 4.1 **Geometry of the specimens in which stress was measured during thermal shock using in-situ X-ray diffraction. Dimensions are in millimetres.**

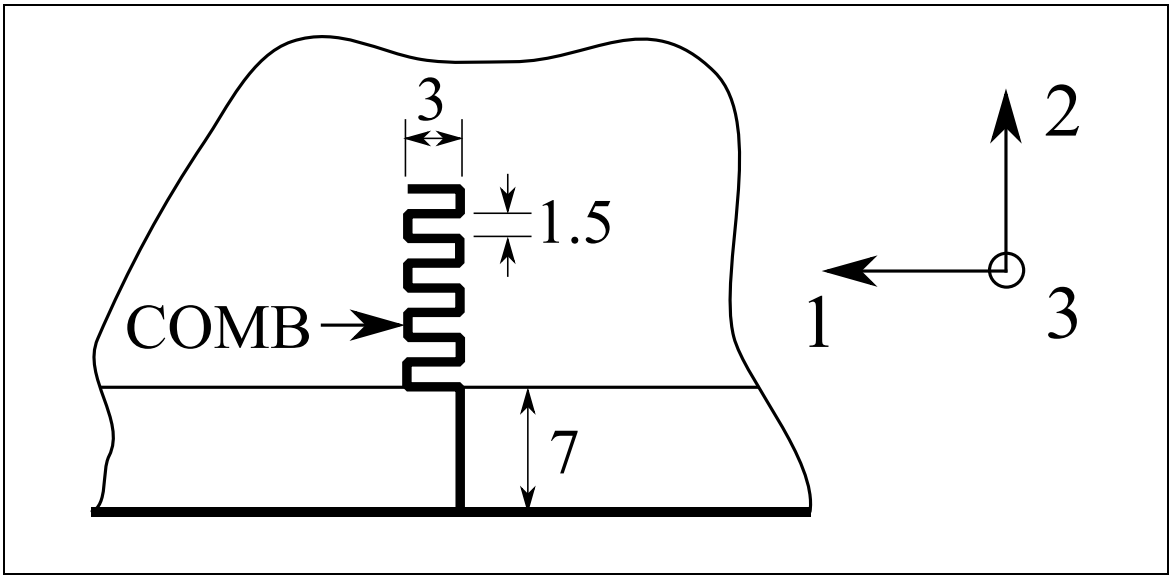

Figure 4.2 **Diagram of the comb feature machined in the middle of the single specimen used for measuring stress-free lattice constants. Dimensions are in millimetres.**

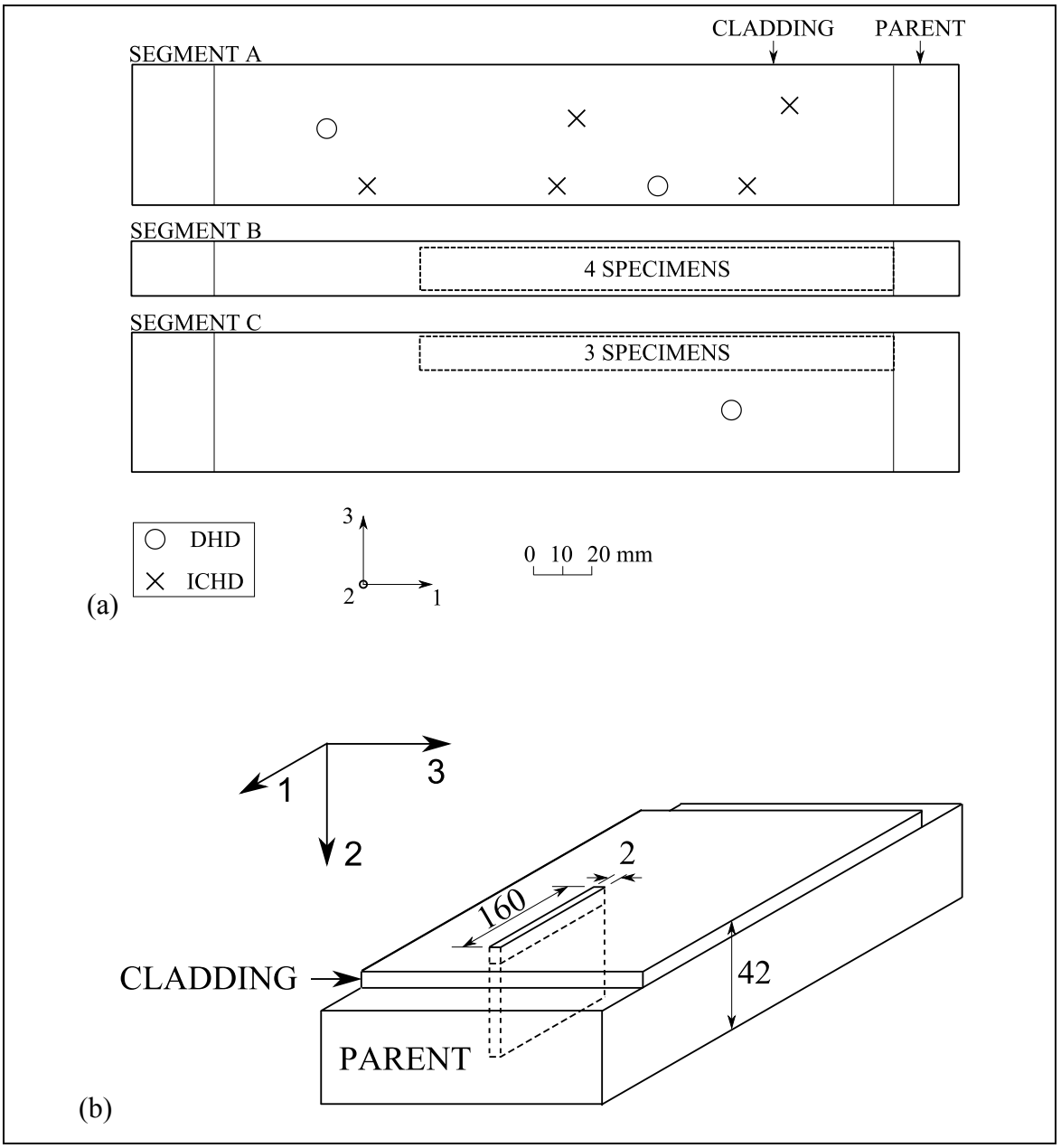

Figure 4.3 Drawing of the position in the post-weld heat-treated plate from which specimens were extracted (a) and illustration of the orientation of a single specimen in the context of the original clad plate (b). Dimensions are in millimetres.

Table 4.1 Grain sizes in the SA508 Grade 4N parent material in the post-weld heat-treated clad plate.

Region	Depth beneath cladding-parent interface (mm)	Grain size (μm)
Fine-grained HAZ	0 → 2.5	4
Coarse-grained HAZ	2.5 → 6	10
Bulk	6 → rest	46

4.2.2 The thermal shock rig

A self-contained thermal shock rig was designed to be operated on beamline I12 at Diamond Light Source. The test rig needed to subject the specimens to thermal shock whilst simultaneously allowing measurements of stress by X-ray diffraction. A schematic of the thermal shock rig is shown in Figure 4.4. The specimen is suspended clad-side-down over a bath of water called the quench bath. The initial water level, W_i, is 15 mm below the bottom of the specimen. An adjacent tank contains more water and a submerged pump feeding into the quench bath. The tank contains just enough water to increase the water level in the quench bath by 20 mm to the final water level, W_f. The specimen is sandwiched between two 110 V electric strip heaters. The X-ray diffraction measurement point is immediately ahead of the crack tip. The rig operates as follows. The specimen is first heated to approximately 350°C. The heaters are then switched off and the pump is switched on simultaneously. The water level increases until the bottom 5 mm of the specimen is submerged, thereby subjecting it to thermal shock. It takes two seconds for the water level to rise. The whole assembly was encased in a clear polycarbonate box which was made watertight using silicon sealant.

The thermal shock rig was powered and controlled via a bespoke control box. More information on the design of the control box including a circuit diagram is given in Appendix A. Briefly, the control box contains: power supplies for the pump and heaters; a proportional-integral-derivative (PID) temperature controller to control the temperature of the specimen; and a safety interlock circuit. The control box was designed so that the heaters and pump could be controlled from an external switch-box situated outside the experimental hutch in the beamline control room.

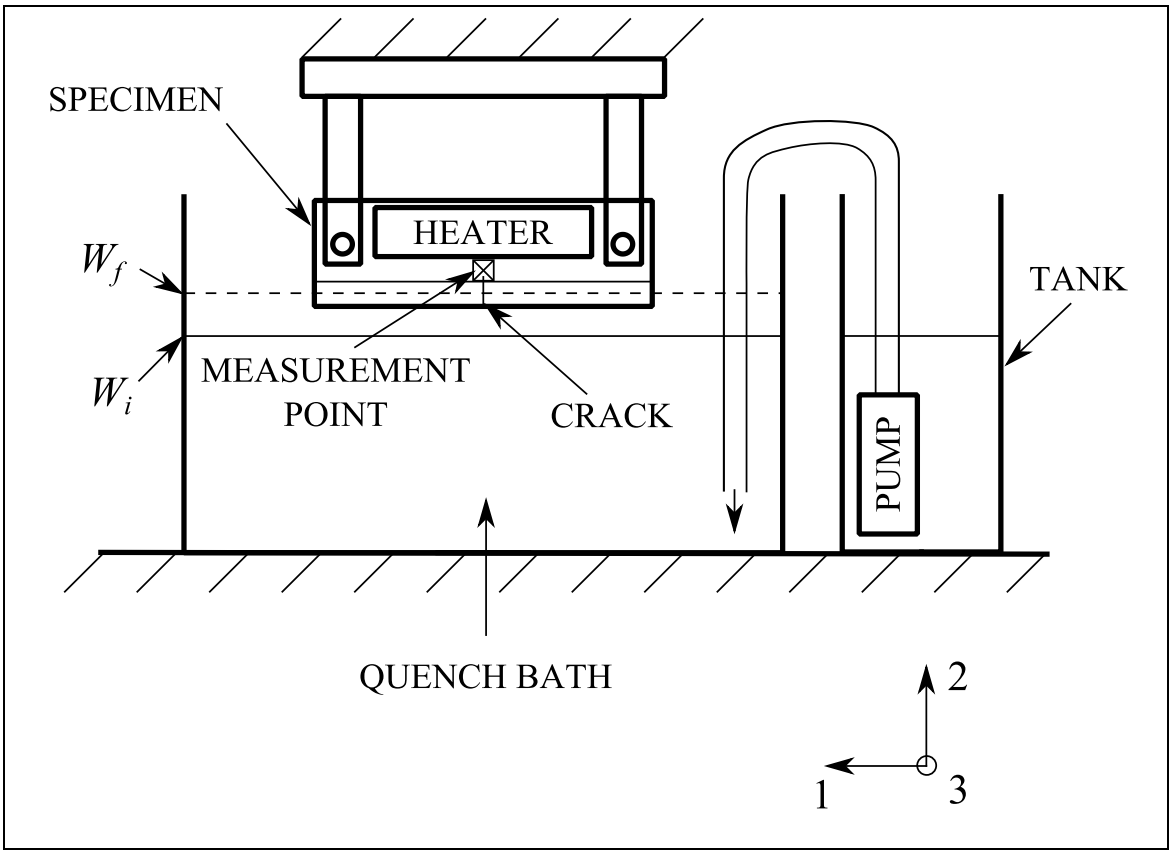

Figure 4.4 Schematic of the thermal shock rig.

4.2.3 Temperature measurement

It was important that the temperatures in the specimens were known during diffraction because the stress-free lattice spacing used to calculate macroscopic stresses and strains varies with temperature. Temperature measurements were made by attaching thermocouples to all specimens. The thermocouple measurement positions are indicated in Figure 4.5 and Table 4.2. The thermocouples were constructed out of *K*-type thermocouple wire insulated with glass fibre. Each thermocouple comprises two wires of diameter 0.5 mm, insulated individually. Each wire of the thermocouple was individually spot-welded to the measurement surface. The junctions between each of the two wires and the specimen surface were separated by 3 mm. The measured temperature is therefore a weighted mean of the temperature at each junction [93]. The two junctions of a single thermocouple were oriented so that each wire was attached at the same x_2 position but a different x_1 position. Severe temperature gradients were only expected with respect to x_2

(i.e. large dT/dx_2), therefore the error from averaging across thermocouple junctions was expected to be small.

The temperatures measured by thermocouples T1 – T5 were recorded during thermal shock by a System 8000 data logger manufactured by Micro-Measurements. The sample rate was 1000 Hz. Thermocouple T6 was used as the control input for the PID controller.

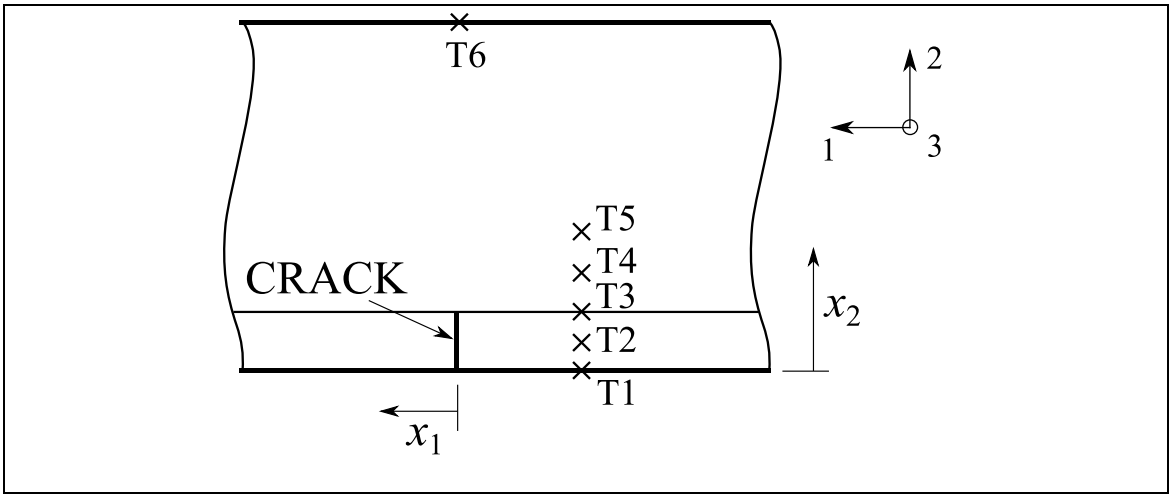

Figure 4.5 Schematic of the positions of temperature measurement by thermocouples (T1 – T6). The co-ordinates of each position are given in Table 4.2.

Table 4.2 Co-ordinates of the temperature measurement points, referring to the diagram in Figure 4.5. The x_1 co-ordinate is the average position of the two junctions of each thermocouple. Therefore, the co-ordinates listed here represent the approximate effective measurement point.

Thermocouple ID	x_1 (mm)	x_2 (mm)
T1	-12	0
T2	-12	3.5
T3	-12	7
T4	-12	12
T5	-12	17
T6	0	42

4.2.4 X-ray diffraction measurements

The principles of using synchrotron X-ray diffraction techniques for measuring strain have been well described elsewhere [94]. Briefly, material is exposed to X-rays and the

resulting scatter angle is measured. The scatter angle is related to the distance between lattice planes via Bragg's law:

$$2d^{hkl} \sin \theta^{hkl} = \lambda \tag{4.1}$$

where: d^{hkl} is the spacing between the *hkl* lattice planes, θ^{hkl} is the diffraction angle, and λ is the X-ray beam wavelength. The lattice spacing, d^{hkl}, can then be used to calculate macroscopic elastic strain and stress. Diffraction by Bragg's law only occurs when the *hkl* plane lies within a very small range of orientations relative to the incident X-ray beam. Therefore, diffraction only occurs in a small proportion of preferentially-oriented grains.

X-ray diffraction was carried out in Experimental Hutch 1 on Beamline I12 [13] at Diamond Light Source. A monochromatic X-ray beam was used with an energy of 80.4 keV. Two different kinds of X-ray diffraction measurements were made: steady-state, when the specimen temperature was maintained either at room temperature or at high temperature; and transient, when the specimen was rapidly cooled by subjecting it to thermal shock.

The steady-state measurement positions are shown in Figure 4.6 for cracked (a) and crack-free (b) specimens. In the cracked specimens, measurements were made at approximately 900 points over a square region around the crack tip with a 10 mm side length. The square region was split into three square sub-regions with higher resolution near the crack tip, identified as coarse, intermediate, and fine in Figure 4.6 (a). In the crack-free specimens, measurements were made along four lines normal to the interface between the cladding and parent. The spatial resolution was increased in a fine region near the interface. The measurement parameters for each region are given in Table 4.3 for specimens with and without cracks. The slit size is the size of the X-ray beam projected onto the specimen surface. The projected area is a square with side length equal to the slit size. The slit sizes were different to allow accurate measurement in regions with different grain sizes (see Table 4.1) and to allow greater spatial resolution in the fine measurement regions.

The transient measurement was made during thermal shock at a single point close to the crack tip. The geometry of the measurement point is shown in Figure 4.7. The slit size was 200 μm and the centre of the measurement point was located 150 μm from the crack

tip. A transient measurement was also made in a crack-free specimen, in which case the measurement was made in the same position as for a specimen containing a 10 mm crack.

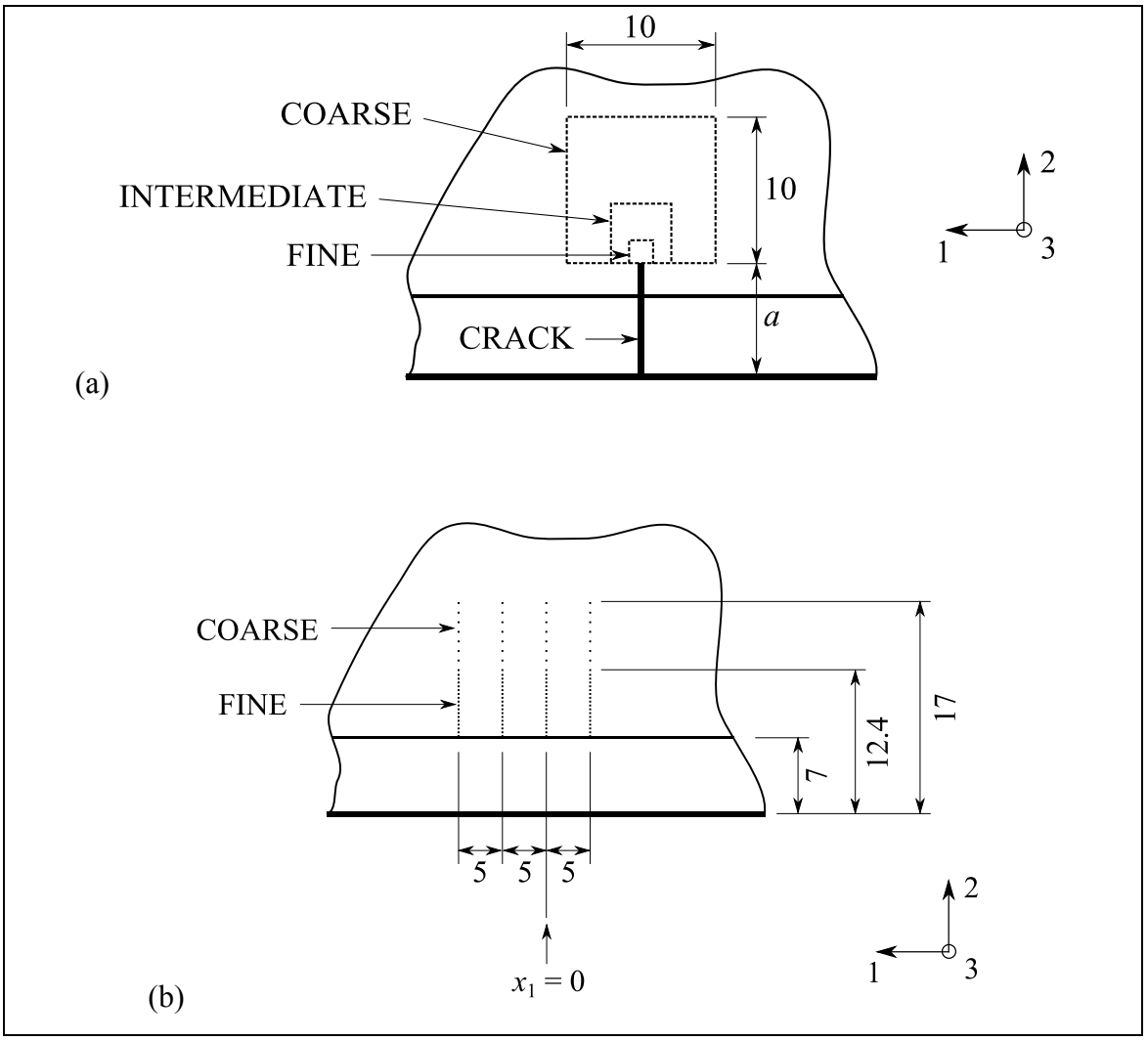

Figure 4.6 Regions of the specimen measured under steady-state conditions: (a) specimens containing cracks of length, *a*, in which measurements were made over a 10 x 10 mm square region with refined regions near the crack tip; and (b) crack-free specimens in which measurements were made along four measurement lines with increased resolution near the cladding-parent interface. Dimensions are in mm.

Table 4.3 Geometries of the steady-state X-ray diffraction measurements.

Specimen type	Region	Length of region (mm)	Slit size (μm)	Resolution (μm)
Cracked	Coarse	10	500	500
Cracked	Intermediate	3	200	150
Cracked	Fine	1.2	100	100
Crack-free	Coarse	4.6	500	500
Crack-free	Fine	5.4	200	200

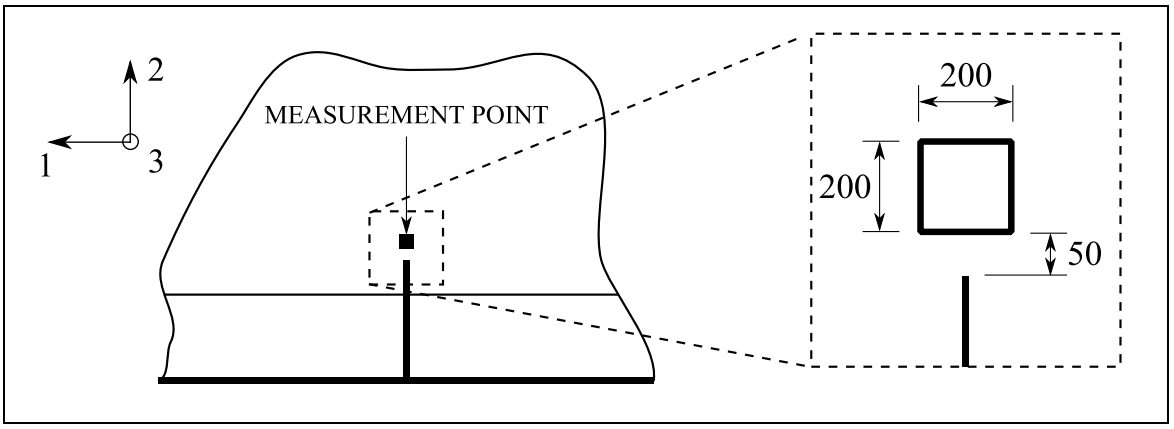

Figure 4.7 Geometry of the single point used for transient measurements during thermal shock. Dimensions are in µm.

4.2.5 Analysis of raw X-ray diffraction data

This section describes the conversion of the raw X-ray diffraction data to macroscopic stress and elastic strain. The analysis was carried out by Chris Simpson at the University of Bristol and has been described in detail in previous work by the author and others [95], but is briefly included here for completeness.

The raw diffraction data from a single measurement is an image recorded by the X-ray detector containing a series of concentric rings corresponding to diffraction spectra from different *hkl* lattice planes. In this work, only a single ring corresponding to the {110} plane was used for analysis. For example, a single diffracted ring is shown in Figure 4.8. The ring is not perfectly circular: its radius varies with the azimuthal angle, φ. The ring was split into 36 slices, and the diffraction spectrum was integrated across each slice (i.e. across $\Delta\varphi = 10°$). The position of peak X-ray intensity in each slice, Q_φ^{hkl}, was calculated by fitting to a Gaussian function using the pyXe Python package [96]. The peak position is related to the lattice spacing, d_φ^{hkl}, using Equation (4.2):

$$Q_\varphi^{hkl} = \frac{2\pi}{d_\varphi^{hkl}} \tag{4.2}$$

where d_φ^{hkl} is the lattice spacing, which is related to the diffraction angle via Bragg's law in Equation (4.1). The lattice strain, $\varepsilon_\varphi^{hkl}$, can therefore be calculated using Equation (4.3):

$$\varepsilon_\varphi^{hkl} = \frac{d_\varphi^{hkl} - d_0^{hkl}}{d_0^{hkl}} = \frac{Q_0^{hkl}}{Q_\varphi^{hkl}} - 1 \tag{4.3}$$

where d_0^{hkl} is the stress-free lattice spacing and Q_0^{hkl} is the corresponding stress-free peak position. Q_0^{hkl} was measured in the specimen which was manufactured with a stress-free reference comb, as shown in Figure 4.2. Measurements were made at different angles (φ), different positions (x_2), and different temperatures between 20°C and 450°C. The temperature of the reference specimen was adjusted using the same heating arrangement as the thermal shock rig, which was discussed in Section 4.2.2. In theory the stress-free peak position, Q_0^{hkl}, should be independent of φ. However, in practice some variation is usually observed because of misalignment and other calibration errors. These errors are accounted for by using the measured angle-dependent values for Q_0^{hkl} in Equation (4.3).

The method for calculating stress and strain tensors from the measured strain, $\varepsilon_{\varphi}^{hkl}$, is described in detail elsewhere [94, 95]. Briefly, it was assumed for the analysis that the specimen was in a state of plane stress ($\sigma_{33} = 0$). The lattice plane specific components of strain, ε_{11}^{hkl}, ε_{22}^{hkl}, and ε_{12}^{hkl}, were calculated from the measured strains, $\varepsilon_{\varphi}^{hkl}$, using co-ordinate system transformations. The stress tensor was then calculated using Hooke's law for plane stress with bulk elastic constants replaced with lattice plane specific values. For example:

$$\sigma_{11} = \frac{E^{hkl}}{(1-(\nu^{hkl})^2)}(\varepsilon^{hkl}{}_{11} + \nu^{hkl}\varepsilon^{hkl}{}_{22}) \tag{4.4}$$

where E^{hkl} and ν^{hkl} are the lattice plane specific modulus and Poisson's ratio. In this case, only a single lattice plane was used for analysis, corresponding to {hkl} = {110}. Values for E^{110} and ν^{110} were estimated from bulk values, E and ν, using factors given in reference [42] for ferritic steel. The bulk values used at 20°C were $E = 206$ GPa and $\nu = 0.3$, and the corresponding lattice plane specific values were $E^{110} = 218$ GPa and $\nu = 0.28$. Poisson's ratio was assumed temperature independent whereas the modulus was reduced by 15% from 20°C to 450°C.

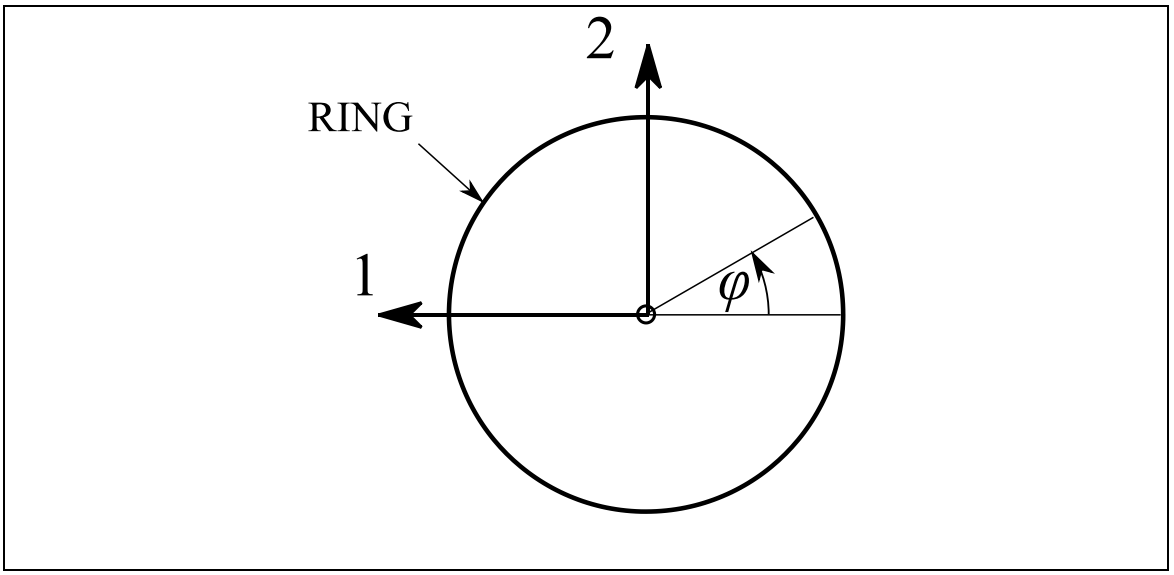

Figure 4.8 Example of raw diffraction data.

4.2.6 Overview of experimental set-up

Figure 4.9 shows a diagram of the experimental setup. The experiment was carried out in Experimental Hutch 1 on Beamline I12 at Diamond Light Source. The control box was connected to a switch located outside the experimental hutch in the control room. The switch initiated thermal shock by simultaneously turning the heaters off and turning the pump on. The X-ray diffraction data and the temperatures in the specimen were recorded by different systems: the diffraction data was recorded by the beamline data acquisition system, and the temperatures were recorded by the data logger. It was important to accurately synchronise the temperature and diffraction data because the temperature of the diffraction measurement point, and therefore the stress-free lattice spacing, was expected to change rapidly during thermal shock. Synchronisation was achieved by supplying a 5 Vdc signal into the beamline data acquisition system via a relay in the data logger which was activated when the temperature of the bottom of the specimen dropped below 300°C. The 5 V signal was also routed back into the data logger so that any delay in activating the relay could be accounted for.

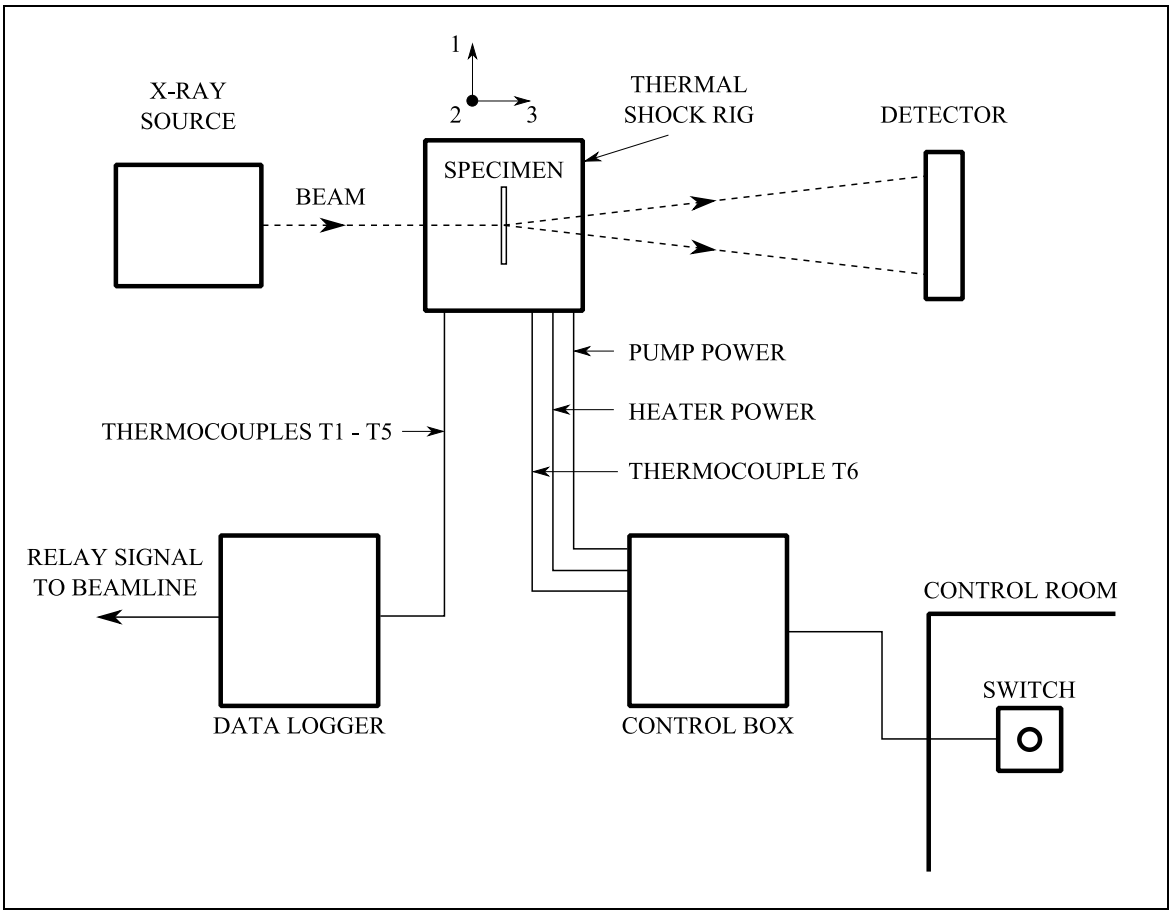

Figure 4.9 **Diagram of the experimental set-up.**

4.2.7 Summary of tests

The completed tests and successful X-ray diffraction measurements are summarised in Table 4.4. Steady-state measurements were carried out at room temperature (RT) and high temperature (HT). Room temperature was 20°C. For high temperature measurements, the temperature at the surface of the cladding (thermocouple T1 in Figure 4.5) was 327°C.

Table 4.4 Summary of X-ray diffraction measurements for each specimen.

Specimen ID	Crack length, *a* (mm)	Steady-state before thermal shock: RT (20°C)	Steady-state before thermal shock: HT (327°C)	Transient during thermal shock	Steady-state after thermal shock: RT (20°C)
A	Stress-free reference comb	N/A	N/A	N/A	N/A
B	7.4	✓	✓	✓	✓
C	7.4			✓	
D	0	✓	✓	✓	✓
E	0				✓
F	10	✓	✓	✓	✓
G	10			✓	

4.3 Finite element analysis

A finite element model was made to calculate the near-tip stresses during thermal shock for comparison with the experimental X-ray diffraction measurements. The model was constructed and analysed using the Abaqus 6.14 [75] finite element code. The basic model procedure was similar to that described in Section 3.5, involving a heat transfer analysis followed by a stress analysis. The heat transfer analysis calculates the temperatures in the model at discrete intervals of time during thermal shock. The calculated temperatures were then prescribed to the stress analysis, which calculates the stress from thermal strain. Schematics of the models used for heat transfer and stress analyses are shown in Figure 4.10 (a) and (b). The models were three-dimensional. The geometry used for both analyses is a quarter model representation of the thin clad specimen shown in Figure 4.1. The finite element meshes used for the heat transfer and stress analyses are shown in Figure 4.11 (a) and (b). Twenty-node quadratic brick elements of type DC3D20 were used for the heat transfer analysis, and eight-node linear brick elements of type C3D8R were used for the stress analysis. The mesh used for the stress analysis contains a refined region around the crack tip where the elements are of uniform size of $20 \times 20 \times 125$ μm. In both models, the mesh density is uniform in the x_3 direction: there are five elements along x_3 in the heat transfer model (i.e. mesh side length 0.2 mm), and there are eight elements along x_3 in the stress model (i.e. mesh side length 0.125 mm). A total of five models were run to account for different specimen geometries and cooling scenarios, which are summarised in Table 4.5. Two different cooling scenarios were studied. In the first scenario, cooling from thermal shock was assumed to occur over Region A in Figure 4.10 (a), which simulates the water level rising to 5 mm above the bottom of the specimen during the experiment. In the second scenario, cooling was also specified in an extra region which included the crack face and the region around the crack tip. Specifically, cooling was prescribed to both Region A and Region B in Figure 4.10 (a). This second cooling scenario was modelled because water marks were observed on the specimens in the experiment after thermal shock which suggested that water may have been drawn up the crack faces and provided extra cooling. This effect is discussed further in Section 4.5.1. A description of the modelling procedure now follows.

For the heat transfer analysis, the mesh was set to a uniform initial temperature of 360°C, which represents an average of the experimental temperatures measured in the specimens

under steady-state conditions before thermal shock. Thermal shock was then simulated by instantaneously adjusting the surface temperature to 20°C at either Region A or both Region A and B in Figure 4.10 (a). Region A corresponds to Scenario 1 in Table 4.5, and Regions A and B correspond to Scenario 2. Instantly cooling the surfaces in this manner represents perfect heat transfer. This approach has been discussed in more detail in Section 3.5. The transient temperatures were calculated at progressively larger increments of time after applying surface cooling, starting with 0.02 seconds.

For the stress analysis, the model was initially crack-free by applying symmetry boundary conditions along the crack face. The mesh was set to an initial stress-free temperature of 580°C and was then uniformly cooled down to 20°C. This method of generating cladding residual stress is discussed in more detail in Sections 3.5 and 3.6.5. The crack was then introduced by removing the symmetry boundary condition along the crack face. Finally, the transient stress during thermal shock was calculated by prescribing the temperatures calculated by the heat transfer model. Stresses were extracted from a cuboid ahead of the crack tip equivalent to the X-ray diffraction measurement volume shown in Figure 4.7 (i.e. $0.2 \times 0.2 \times 2$ mm with the centre located 0.15 mm from the crack tip). The stresses were averaged over the volume.

Material properties were required for three different regions which are illustrated in Figure 4.11: the parent, the HAZ and the cladding. Temperature-dependant values used are listed in Table 4.6 for the HAZ and parent, and Table 4.7 for the cladding. The thermal conductivity, specific heat, density, and Poisson's ratio were the same as those listed in Table 3.5 and Table 3.6 and were derived from values published in the open literature, as discussed in Section 3.5. Values for Young's modulus at 20°C were calculated from tensile tests described in Section 3.4.1, and were reduced with increasing temperature by factors derived from data published for similar alloys [86, 88]. A series of temperature-dependant elastic-plastic stress-strain curves were derived for each material, which were prescribed to the model as incremental plasticity materials with isotropic hardening. The stress-strain curves are shown in Figure 4.12 for the parent (a), the HAZ (b), and the cladding (c). In Figure 4.12 (a-c), the solid curves are tensile test results and the markers are the discrete data points used to define the material in the model. The tensile test curves are from room temperature tensile tests described in Section 3.4.1, and were converted to true stress and true strain using Equations (3.6) and (3.5). Specimen P1 from the SA508 4N (see Figure 3.6) was used for the parent, and specimen P3 was used for the HAZ. The

tensile test curves were then discretised and stresses were reduced with increasing temperature by factors derived from temperature dependant yield strengths given in the literature for similar materials [78, 89]. It was assumed that no further strain hardening occurred beyond the maximum strains given in Figure 4.12.

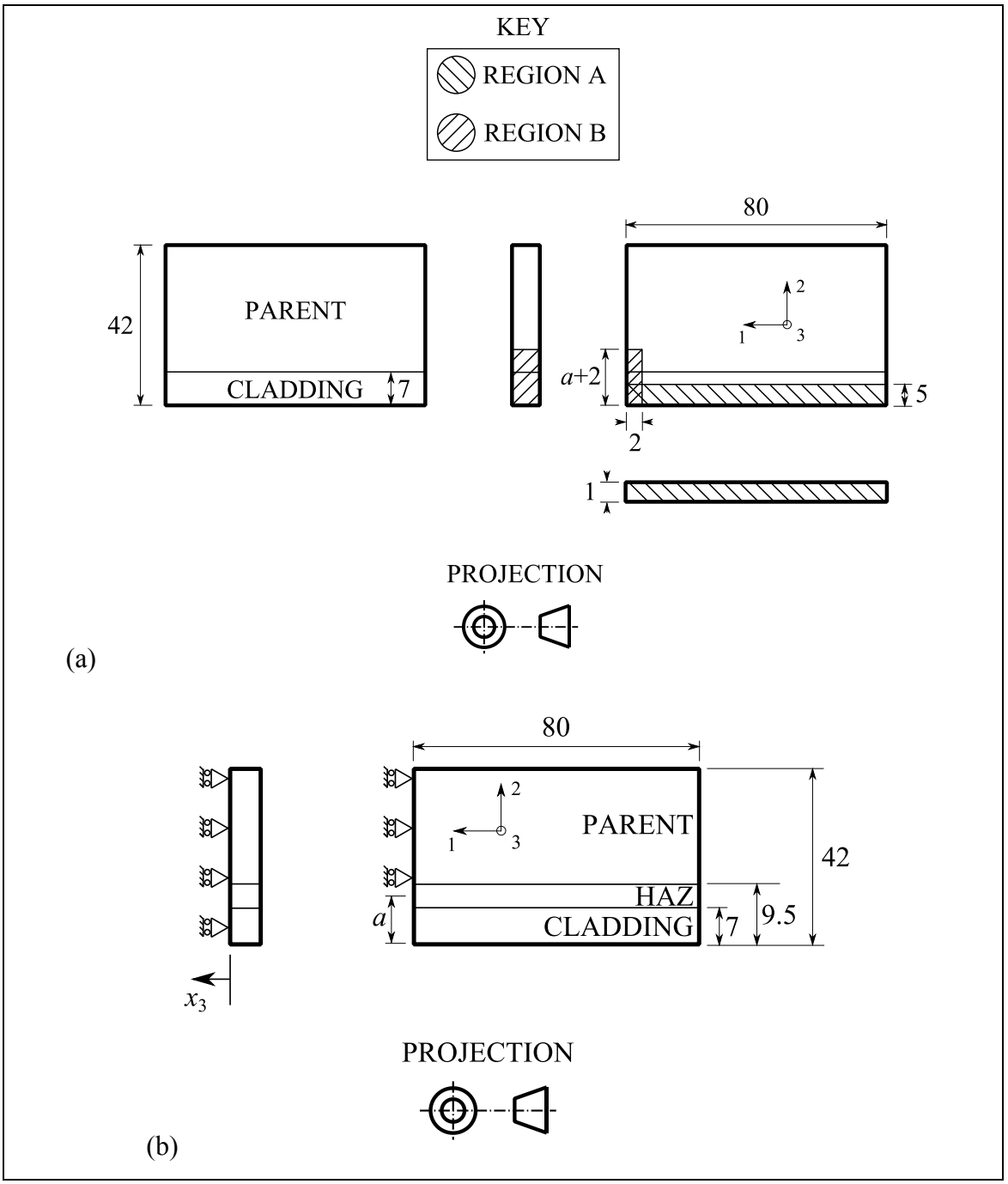

Figure 4.10 Schematic of the (a) heat transfer and (b) stress finite element models. Dimensions are in millimetres.

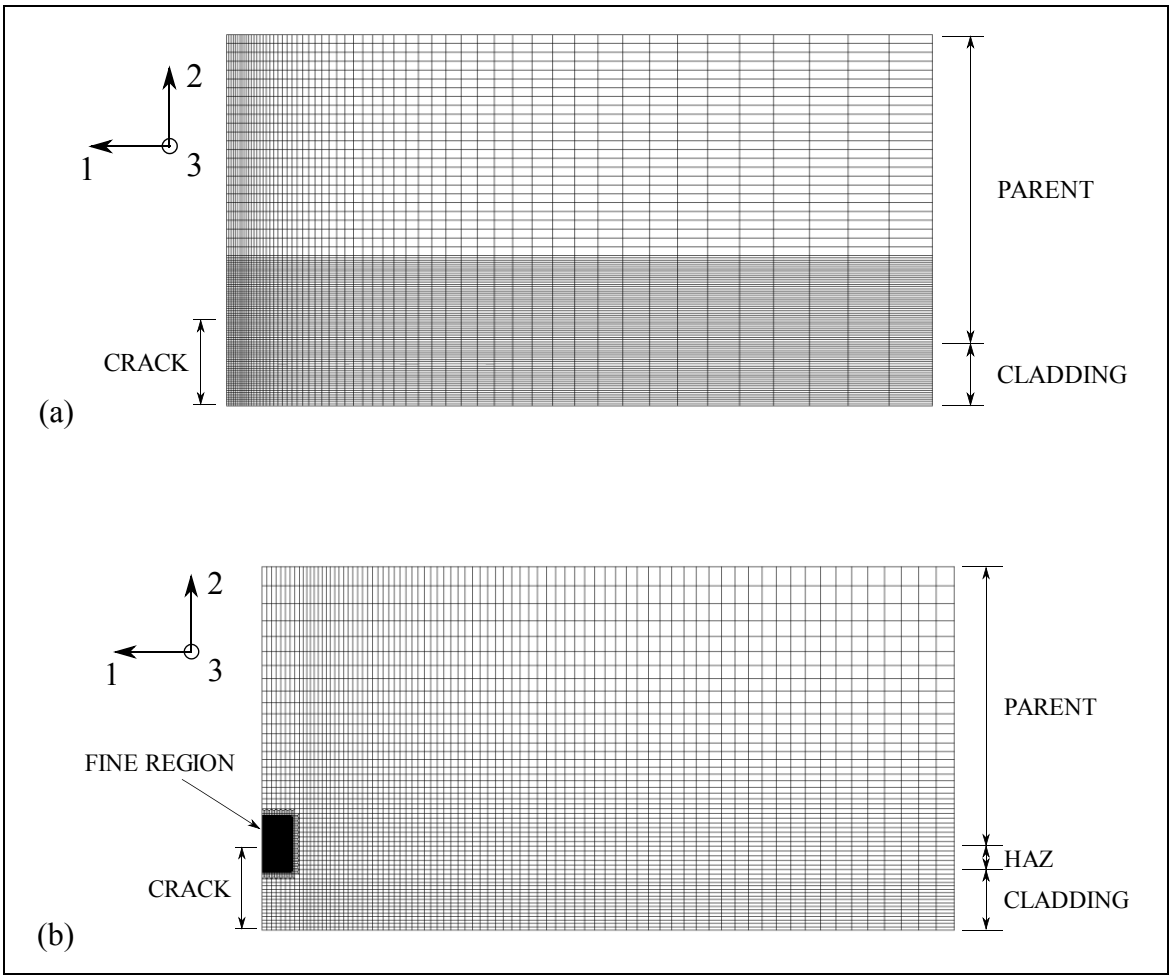

Figure 4.11 Finite element meshes used for the (a) heat transfer and (b) stress analyses.

Table 4.5 Summary of the different specimen geometries and cooling scenarios modelled using finite element analysis.

Crack length (mm)	Scenario 1: without cooling around the crack	Scenario 2: with cooling around the crack
0	✓	N/A
7.4	✓	✓
10	✓	✓

Table 4.6 Material properties used for the HAZ and parent materials in the finite element model.

Temperature (°C)	Thermal conductivity, κ (W m^{-1} K^{-1})	Specific heat, c_p (J kg^{-1} K^{-1})	Thermal expansion coefficient, α (μm m^{-1} K^{-1})	Young's modulus, E (GPa)	Poisson's ratio, ν	Density, ρ (kg m^{-3})
20	41.6	466	11.80	203	0.3	7790
100	41.3	495	12.14	201	0.3	7790
200	40.5	532	12.29	194	0.3	7790
300	39.3	570	12.51	189	0.3	7790
400	37.2	623	13.01	181	0.3	7790
500	34.7	695	13.59	170	0.3	7790
600	31.6	795	14.04	162	0.3	7790

Table 4.7 Material properties used for the cladding in the finite element model.

Temperature (°C)	Thermal conductivity, κ (W m^{-1} K^{-1})	Specific heat, c_p (J kg^{-1} K^{-1})	Thermal expansion coefficient, α (μm m^{-1} K^{-1})	Young's modulus, E (GPa)	Poisson's ratio, ν	Density, ρ (kg m^{-3})
20	14.9	444	11.03	172	0.3	8470
100	15.9	465	11.33	169	0.3	8470
200	17.3	486	11.35	165	0.3	8470
300	19.0	502	11.35	160	0.3	8470
400	20.5	519	12.45	155	0.3	8470
500	22.1	536	14.03	151	0.3	8470
600	23.9	578	16.22	145	0.3	8470

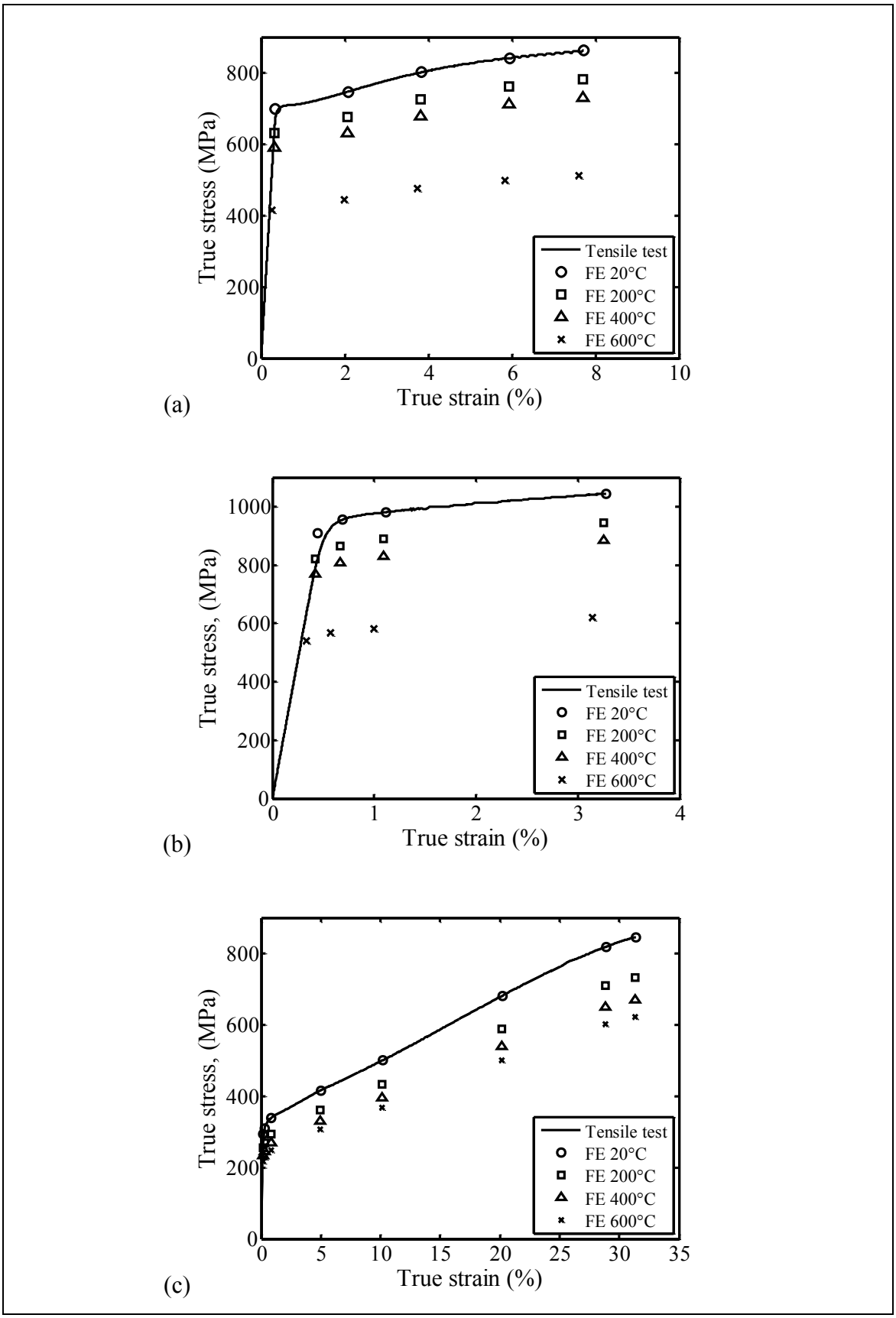

Figure 4.12 Elastic-plastic stress-strain curves used in the finite element model for: (a) the parent, (b) the HAZ, and (c) the cladding.

4.4 Results

4.4.1 Steady-state measurements before and after thermal shock

Figure 4.13 shows the temperatures measured in the specimens during steady-state X-ray diffraction measurements at high temperature. The temperatures at each thermocouple position (T1-T5, referring to Figure 4.5) have been averaged over the duration of the X-ray diffraction measurement (one hour). The temperatures fluctuated by <1°C during the measurement. There is a temperature gradient because the strip heaters did not cover all of the specimen and they did not provide perfectly uniform heating. Temperatures were uniform at room temperature conditions (20°C) before and after thermal shock.

Figure 4.14 shows contour maps of room-temperature steady-state stress in Specimen B before (a) and after (b) thermal shock, and the corresponding maps for Specimen F are shown in Figure 4.15. Specimen B contained a 7.4 mm crack, and Specimen F contained a 10 mm crack. The stress shown in both figures is the component normal to the crack (σ_{11}). Before thermal shock, the stress is the cladding residual stress which has been redistributed by inserting a crack. In both specimens, the stress around the crack tip is tensile before thermal shock, whereas after thermal shock a smaller region of compressive stress has formed around of the crack tip.

The steady-state stresses were extracted from the contour maps along the crack line (at $x_1 = 0$) and are plotted in Figure 4.16. Results for Specimen B (7.4 mm crack) are shown in Figure 4.16 (a) and results for Specimen F (10 mm crack) are shown in Figure 4.16 (b). Stresses are plotted under three different steady-state conditions: before thermal shock at room temperature (RT); before thermal shock at high temperature (HT); and after thermal shock at room temperature. In both specimens, high tensile stresses exist near to the crack tip before thermal shock at room temperature. The magnitude of the near-tip stresses is reduced at high temperature. After thermal shock, the near-tip stresses are high-magnitude and compressive. The stresses under different steady-state conditions are consistent to within 50 MPa at distances greater than 1.5 mm from the crack tip.

Steady-state measurements of stress in Specimen D, which was crack-free, are shown in Figure 4.17 at different positions relative to the crack: x_1 = -5 (a), 0 (b), and 5 mm (c), where $x_1 = 0$ is the middle of the specimen (i.e. in the same position as the cracks in the

cracked specimens). At each x_1 position, stresses are plotted as before for the three different steady-state conditions: before thermal shock at room temperature and high temperature, and after thermal shock. At each position, the overall shape of the stress versus distance curve is the same for the three different steady-state conditions, although the precise value of stress changes by a small amount. Relative to the virgin state of the specimen (before thermal shock at room temperature), stresses were less than 40 MPa higher at high temperature, and were less than 60 MPa higher after thermal shock.

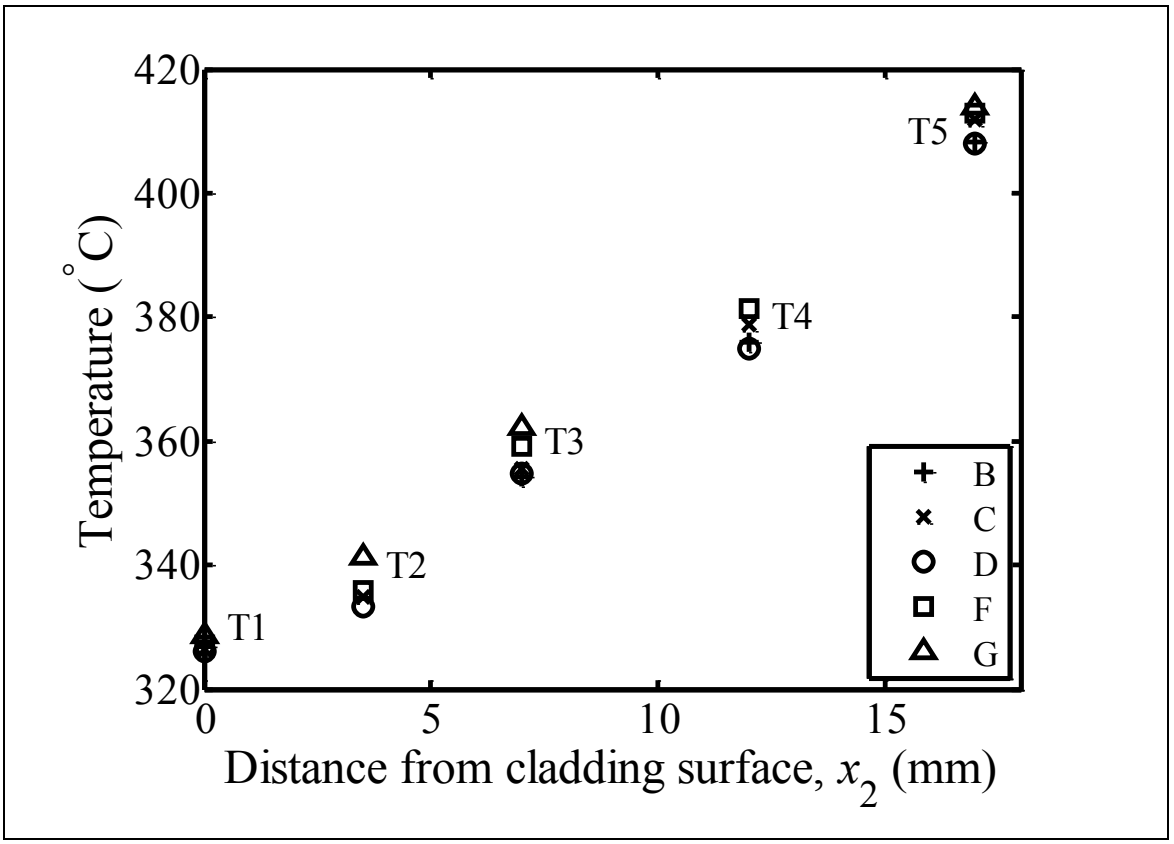

Figure 4.13 Temperatures measured with thermocouples T1-T5 in Specimens B, C, D, F, and G during the steady-state X-ray diffraction measurement at high temperatures.

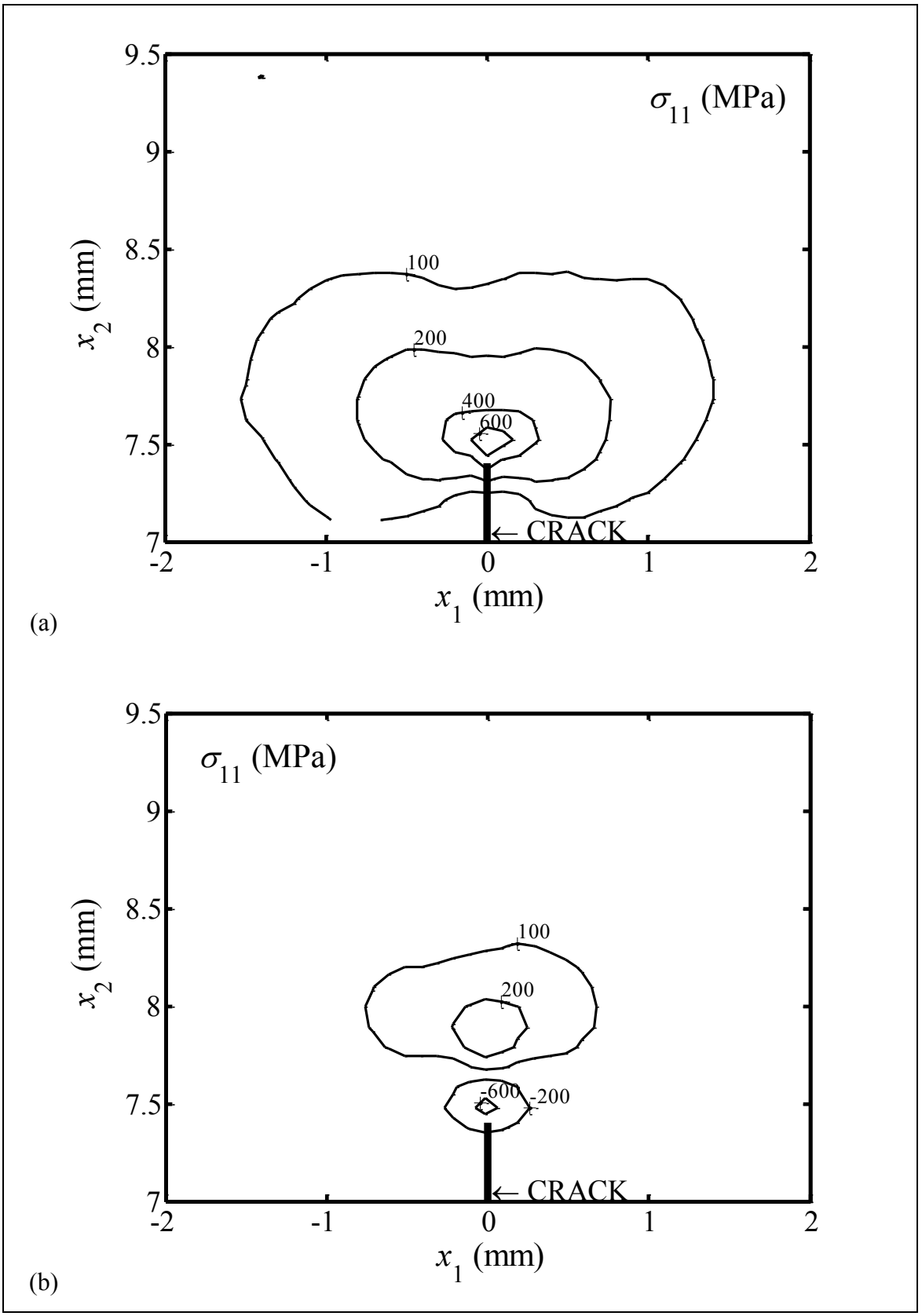

Figure 4.14 Contour plot of stress normal to the crack (σ_{11}) measured by XRD in Specimen B (7.4 mm crack) before (a) and after (b) thermal shock.

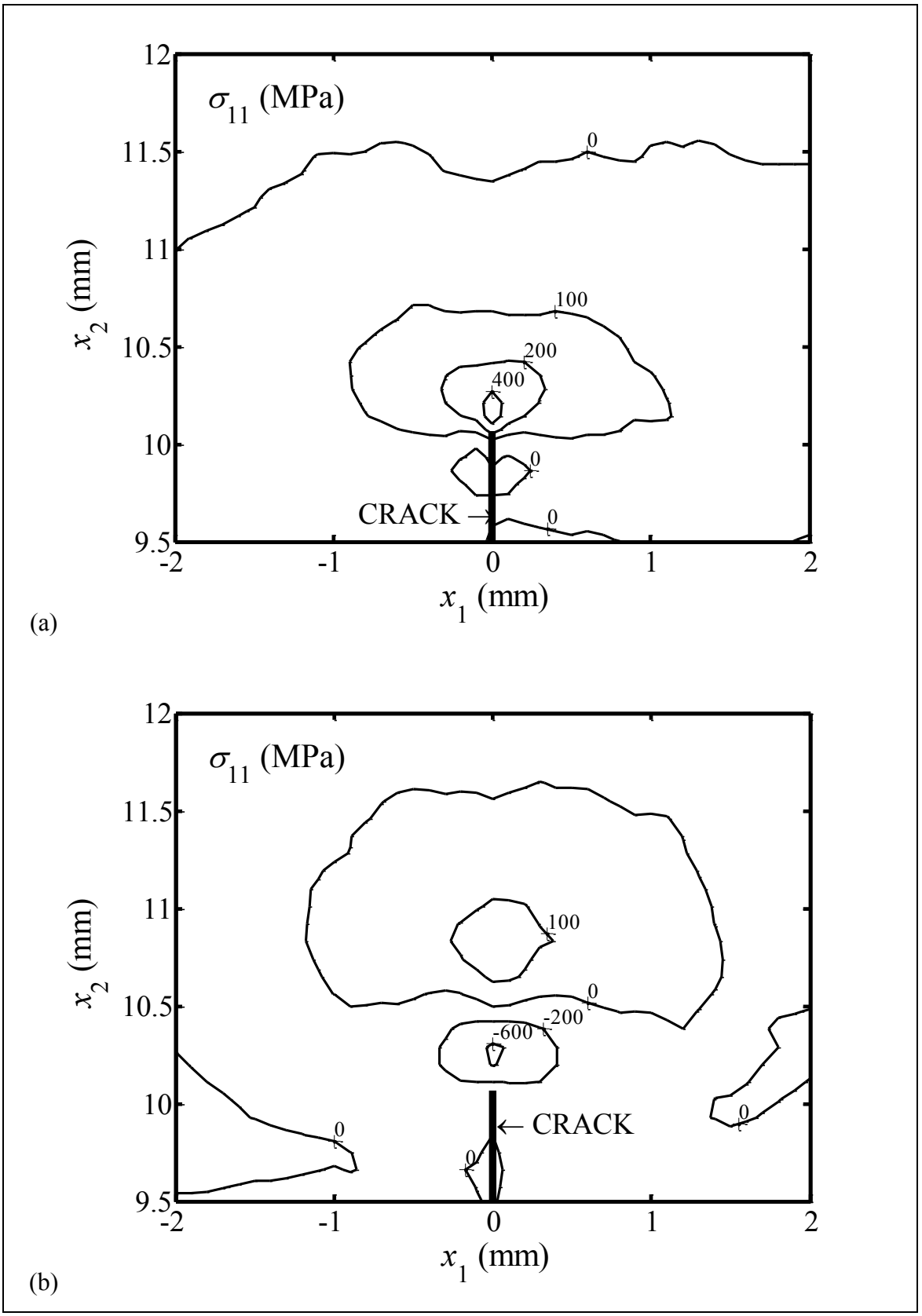

Figure 4.15 Contour plot of stress normal to the crack (σ_{11}) measured by XRD in Specimen F (10 mm crack) before (a) and after (b) thermal shock.

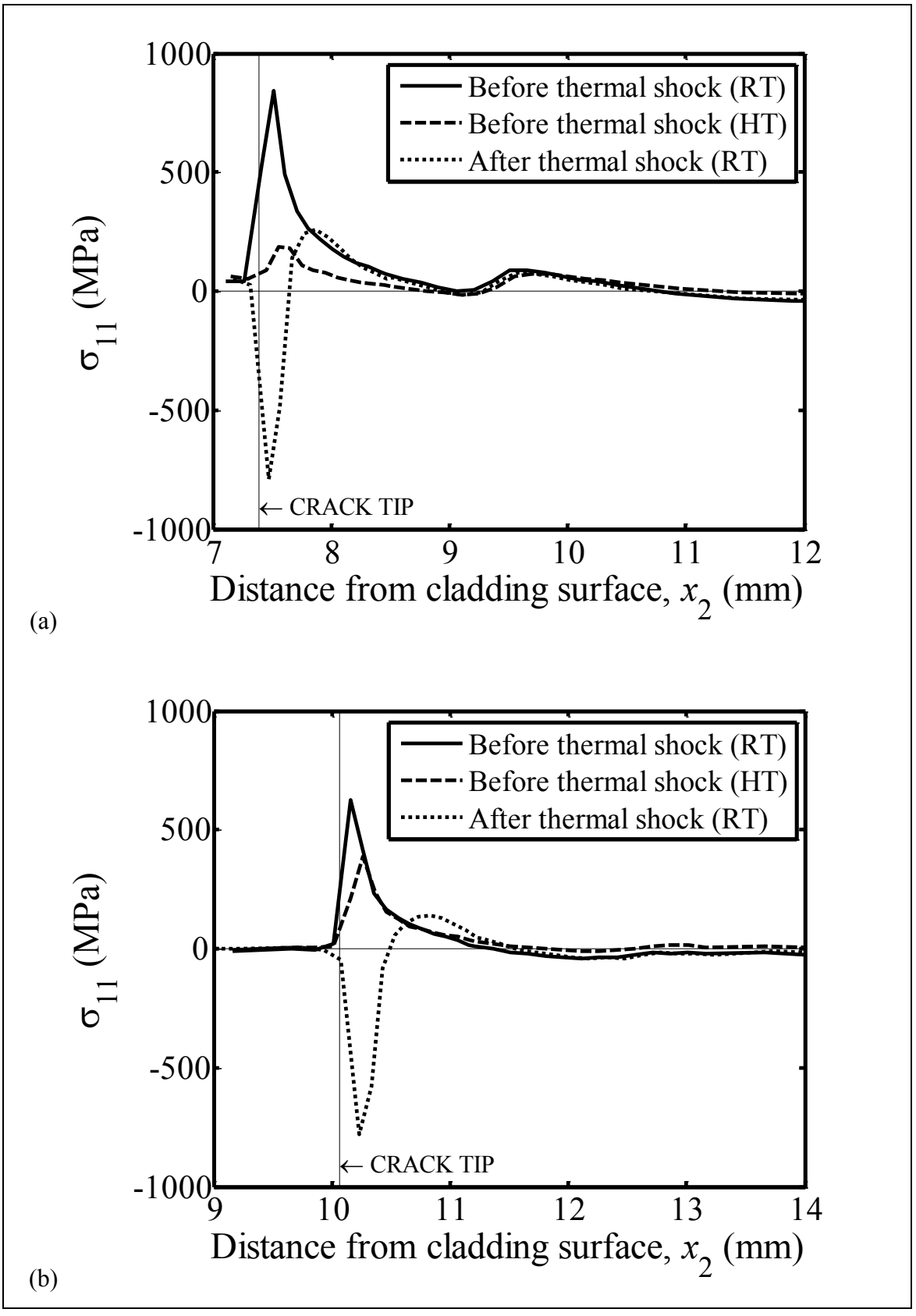

Figure 4.16 Stress normal to the crack (σ_{11}) measured under steady state conditions in (a) Specimen B (7.4 mm crack) and (b) Specimen F (10 mm crack). Stresses are plotted along the crack line (at $x_1 = 0$ in Figure 4.1). RT = room temperature (20°C), HT = high temperature (see Figure 4.13).

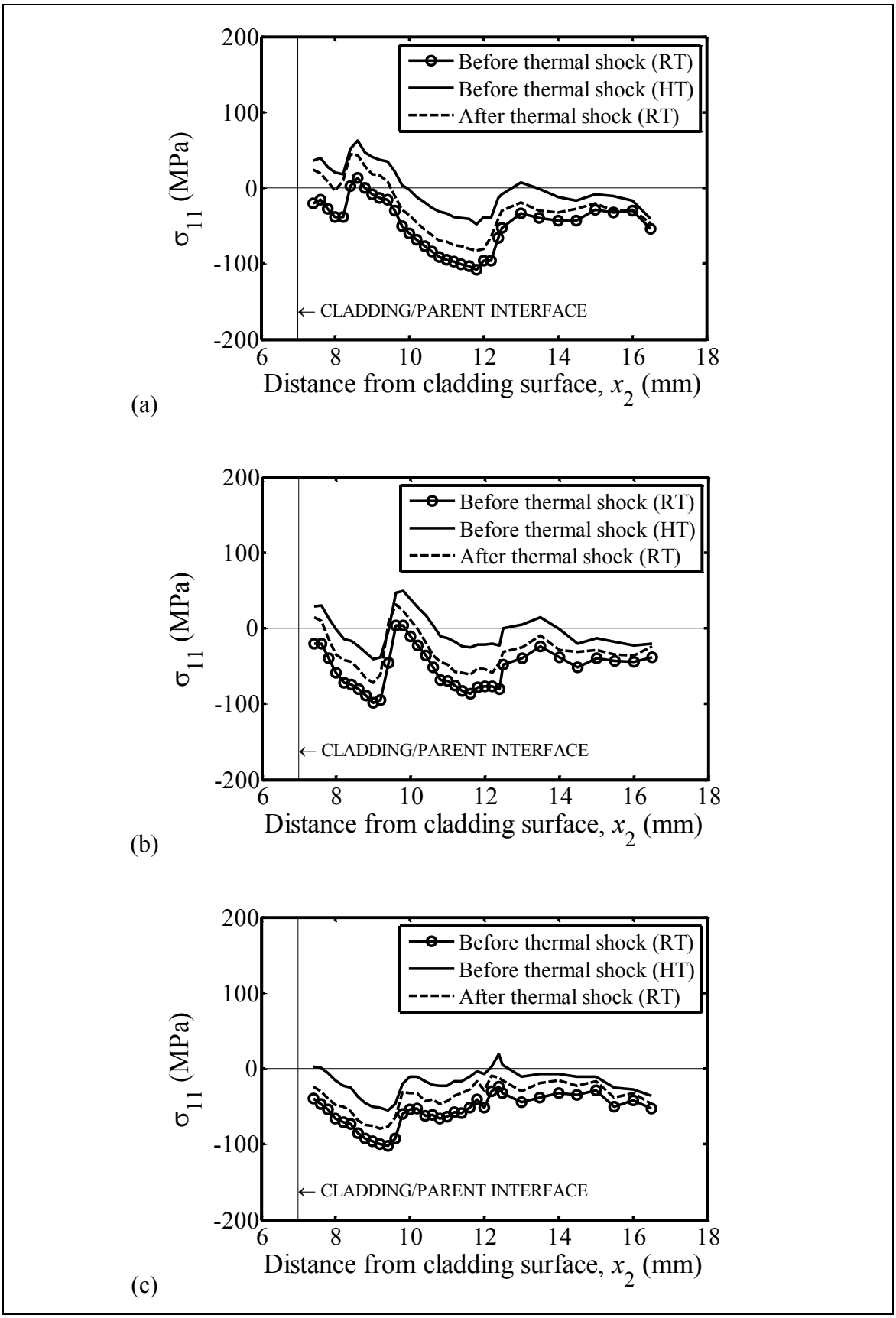

Figure 4.17 Stress component parallel to the interface (σ_{11}) measured under steady state conditions in Specimen D (crack-free) at: (a) x_1 = -5 mm, (b) x_1 = 0, and (c) x_1 = 5 mm, where x_1 is defined in Figure 4.1. RT = room temperature (20°C), HT = high temperature (see Figure 4.13).

4.4.2 ***Residual stress measurements in a virgin, crack-free specimen and comparison with deep hole drilling***

This section presents XRD measurements of stress just on Specimen D (crack-free) in the virgin state (i.e. before heating or thermal shock). These are the residual stresses which are retained by the specimen after extraction from the post-weld heat-treated clad plate described in Chapter 3. Therefore, these residual stresses as measured by X-ray diffraction are compared with measurements made on the larger clad plate. X-ray diffraction enabled measurement of the out of plane stress component (σ_{22} in Figure 3.1) which was not obtained using the mechanical strain relaxation techniques described in Chapter 3. The fine resolution offered by diffraction also enabled investigation of the variation of residual stress beneath different parts of the weld bead of the cladding.

Figure 4.18 compares the residual stresses measured by X-ray diffraction (XRD) and DHD. The XRD measurement is the average of measurements made on one of the crack-free thin specimens, Specimen D, at different x_1 positions. The error bars on the XRD measurement indicate the range of values obtained at the different positions. The DHD result is the average of the DHD1 and DHD2 measurements made on the clad plate, which are described in Chapter 3. The single error bar on the DHD measurement represents the typical uncertainty of approximately 35 MPa obtained from measurements on reference bushes in previous work on a repair weld [72]. There is good agreement between the DHD and XRD measurements.

Figure 4.19 shows the σ_{11} and σ_{22} stress components measured by XRD in Specimen D. As above, the results are the average obtained at different x_1 positions, and the error bars indicate the range of values obtained at the different positions. The stress component, σ_{22} (see Figure 4.1), is the out-of-plane component on the full clad plate (see Figure 3.1) which was not measured using the DHD, contour, or ICHD methods described in Chapter 3. The σ_{22} component is small compared to σ_{11}. The maximum measured magnitude of σ_{22} is 40 MPa. Measurements of this component of stress, which is normal to the cladding surface, are not commonly reported in the literature but they are important because they provide the driving forces for defects parallel to the cladding surface which can form at the interface between the cladding and parent materials.

Figure 4.20 shows XRD measurements of stress made in Specimen D (crack-free) at different x_1 positions, where x_1 is zero at the mid-length of the specimen (see Figure 4.1).

For reference, the measurement positions are shown in Figure 4.6 (b). The x_1 position of the measurement causes up to 100 MPa variation in residual stress, which occurs near the interface between the cladding and parent. The variation is small (< 20 MPa) beyond 6 mm beneath the interface. The variation occurs because the x_1 position represents the position relative to the bead width of the weld-overlay, approximately 18 mm. The variation is significant even though the plate has been post-weld heat-treated. Variability of residual stress with position relative to the weld bead has been demonstrated in previous measurements on pressure vessel plate clad with stainless steel [46].

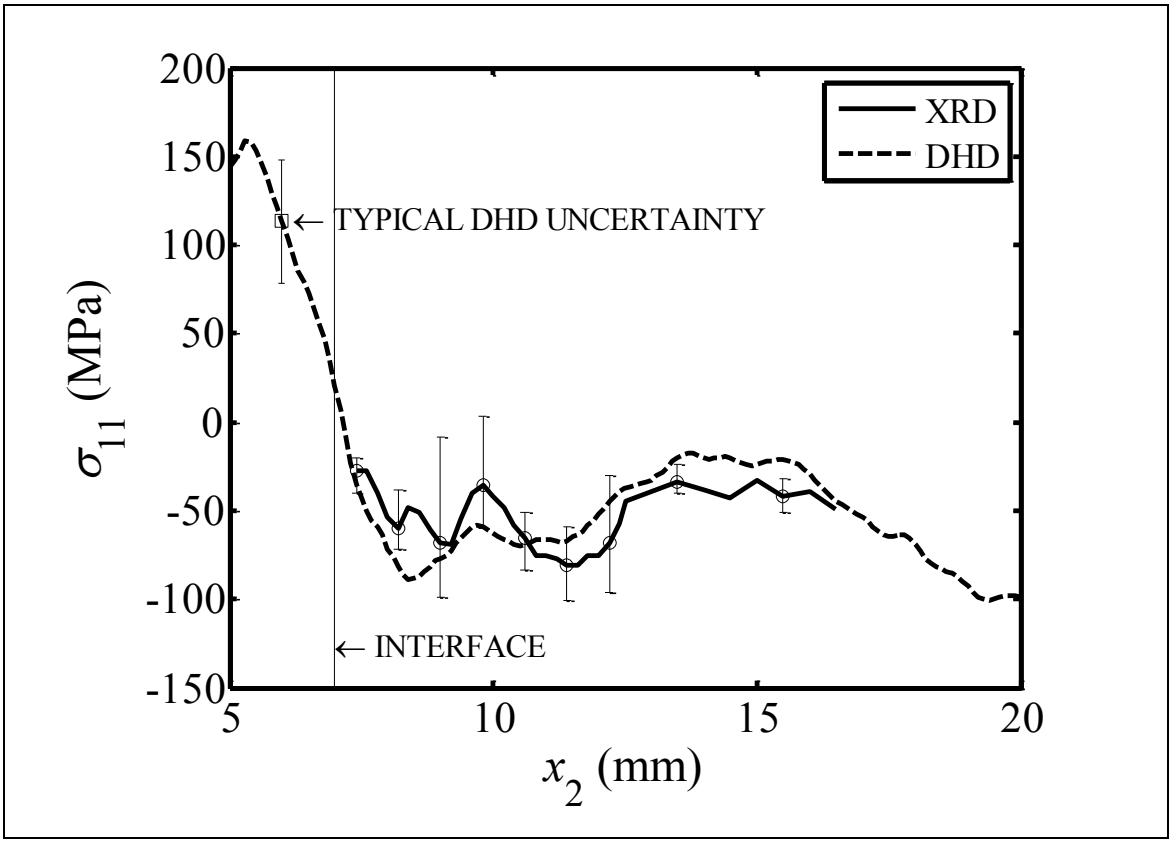

Figure 4.18 Comparison of residual stress measurements made in the post-weld heat-treated plate by DHD, and by XRD on a thin specimen (Specimen D).

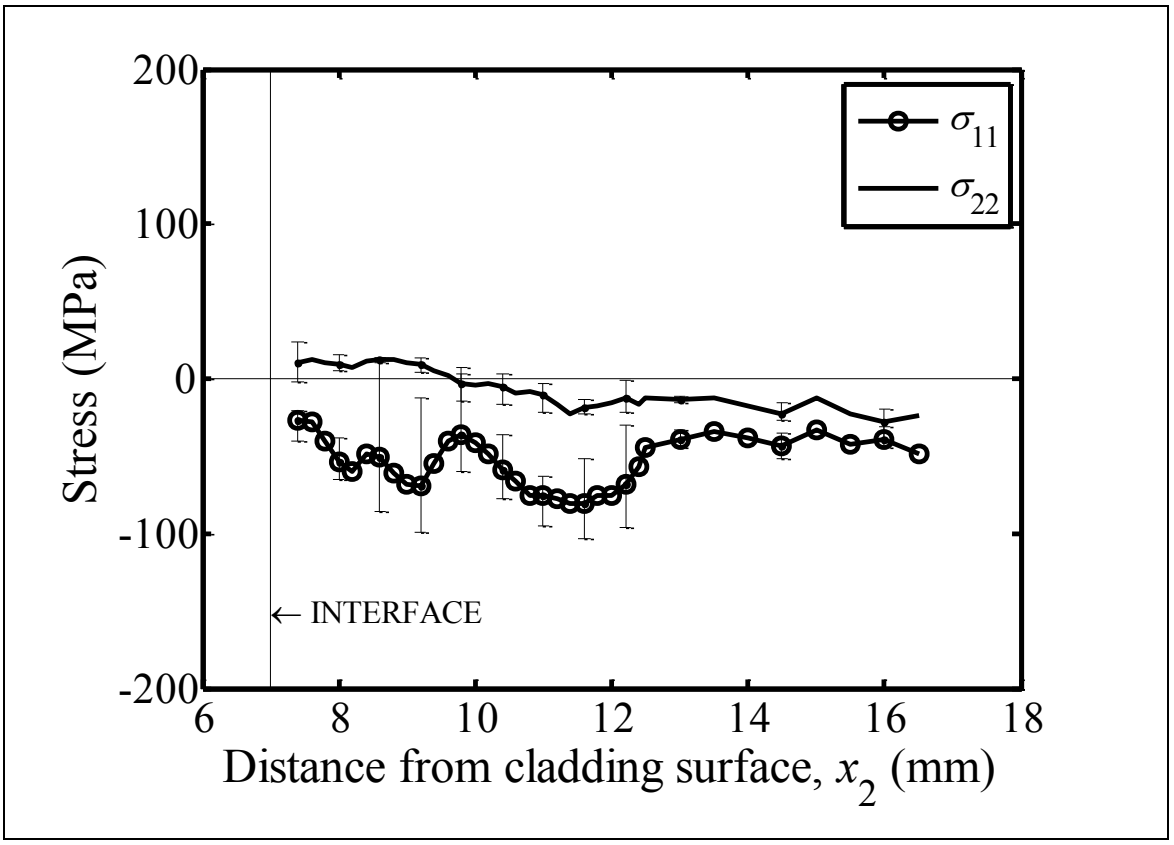

Figure 4.19 **Residual stresses measured by XRD in a thin crack-free specimen (Specimen D).**

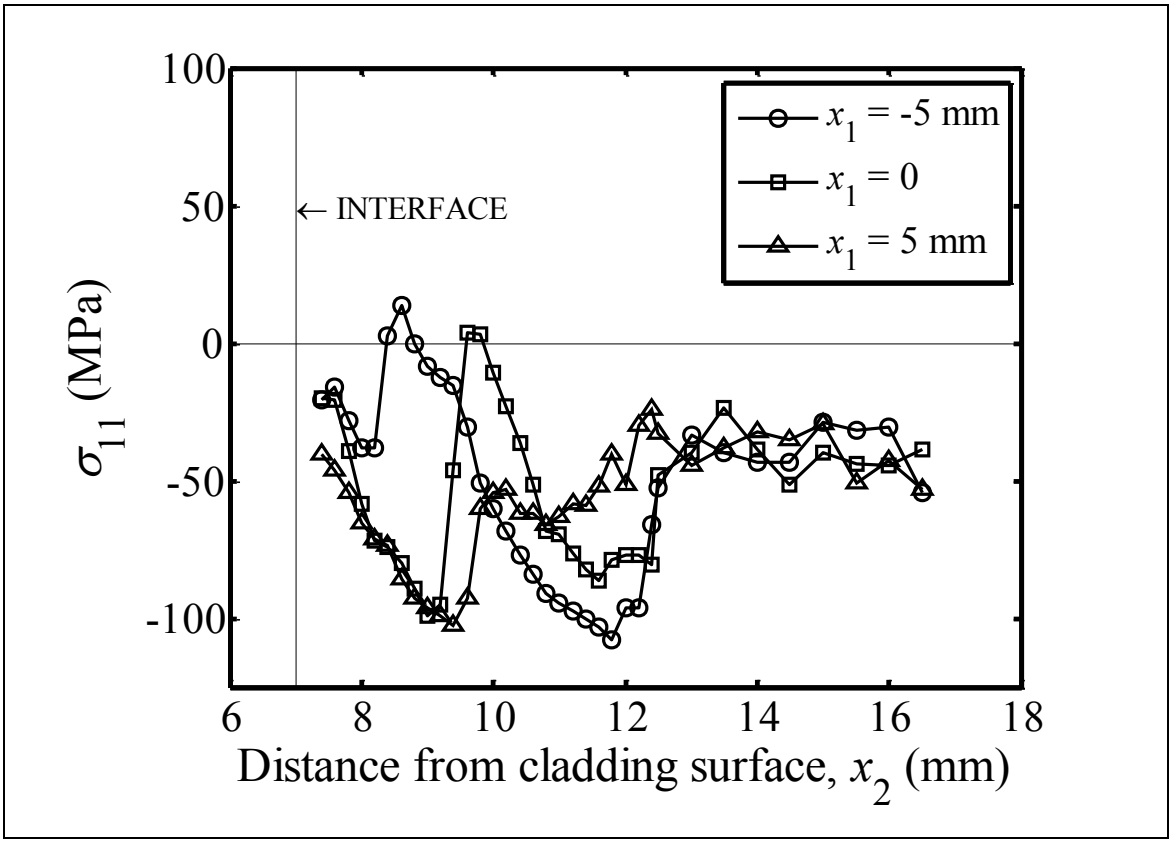

Figure 4.20 **Residual stresses measured by XRD in a thin specimen (Specimen D) at different x_1 positions.**

4.4.3 Transient measurements during thermal shock

Figure 4.21 shows the temperatures measured in Specimen B during thermal shock plotted over (a) 30 seconds and (b) 10 minutes. Temperatures were measured by thermocouples T1, T3, and T5 at positions shown in Figure 4.5 and Table 4.2. Results have been shown for only a single specimen for clarity, although these results are reasonably representative of the temperatures experienced by all the specimens during thermal shock. The cooling rate measured at the start of thermal shock (at zero seconds) was -235°C s^{-1}.

The stresses measured during thermal shock are shown in Figure 4.22 for specimens with (a) 7.4 mm long cracks, (b) 10 mm long cracks, and (c) no crack. In the specimens containing cracks, the stresses were measured 150 μm ahead of the crack tip (see Figure 4.7). In the crack-free specimen, the stress was measured 10.15 mm from the bottom of the specimen, at x_2 = 10.15 mm (i.e. at the same point as the specimens with 10 mm long cracks). Repeat measurements were made (i.e. two specimens) on specimens containing cracks, whereas only one measurement was made on a single crack-free specimen. Zero seconds is defined as the time at which the temperature at the bottom of the specimen measured by thermocouple T1 dropped below 300°C, and therefore represents the start of thermal shock. In the cracked specimens, the stress rises rapidly after the start of thermal shock and reaches a maximum tensile value within one second and then rapidly reduces towards compression within six seconds. The peak tensile stress was 966 MPa in the specimens with 10 mm cracks (Specimen G) and 902 MPa in the specimens with 7.4 mm cracks (Specimen C). The stress in the crack-free specimen (Figure 4.22 c) dropped rapidly after the start of thermal shock, reaching a peak compressive value of -141 MPa within 0.8 seconds.

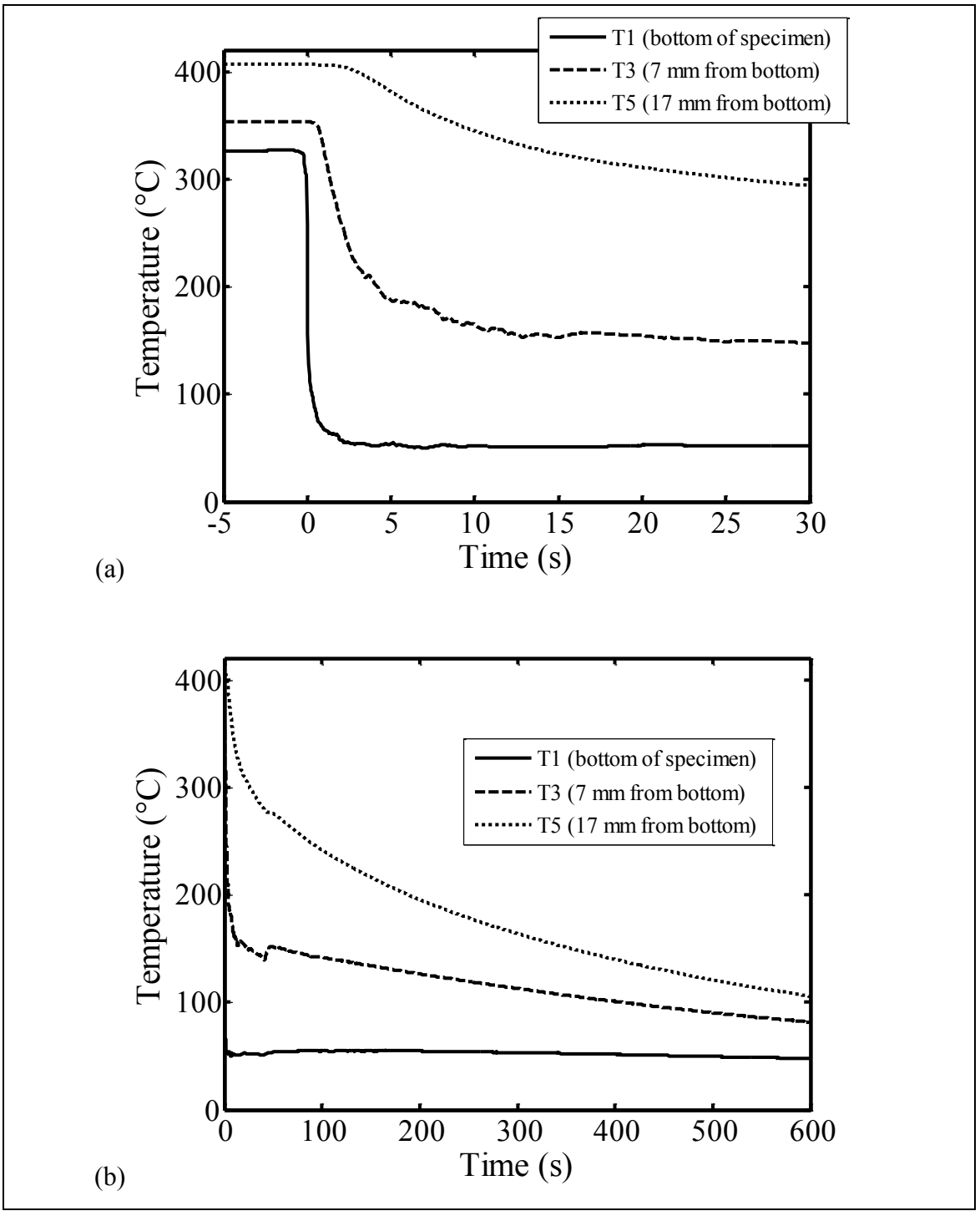

Figure 4.21 Temperatures measured in Specimen B (7.4 mm crack) during thermal shock by thermocouples T1, T3, and T5. The same results are plotted over 30 seconds (a) and 10 minutes (b).

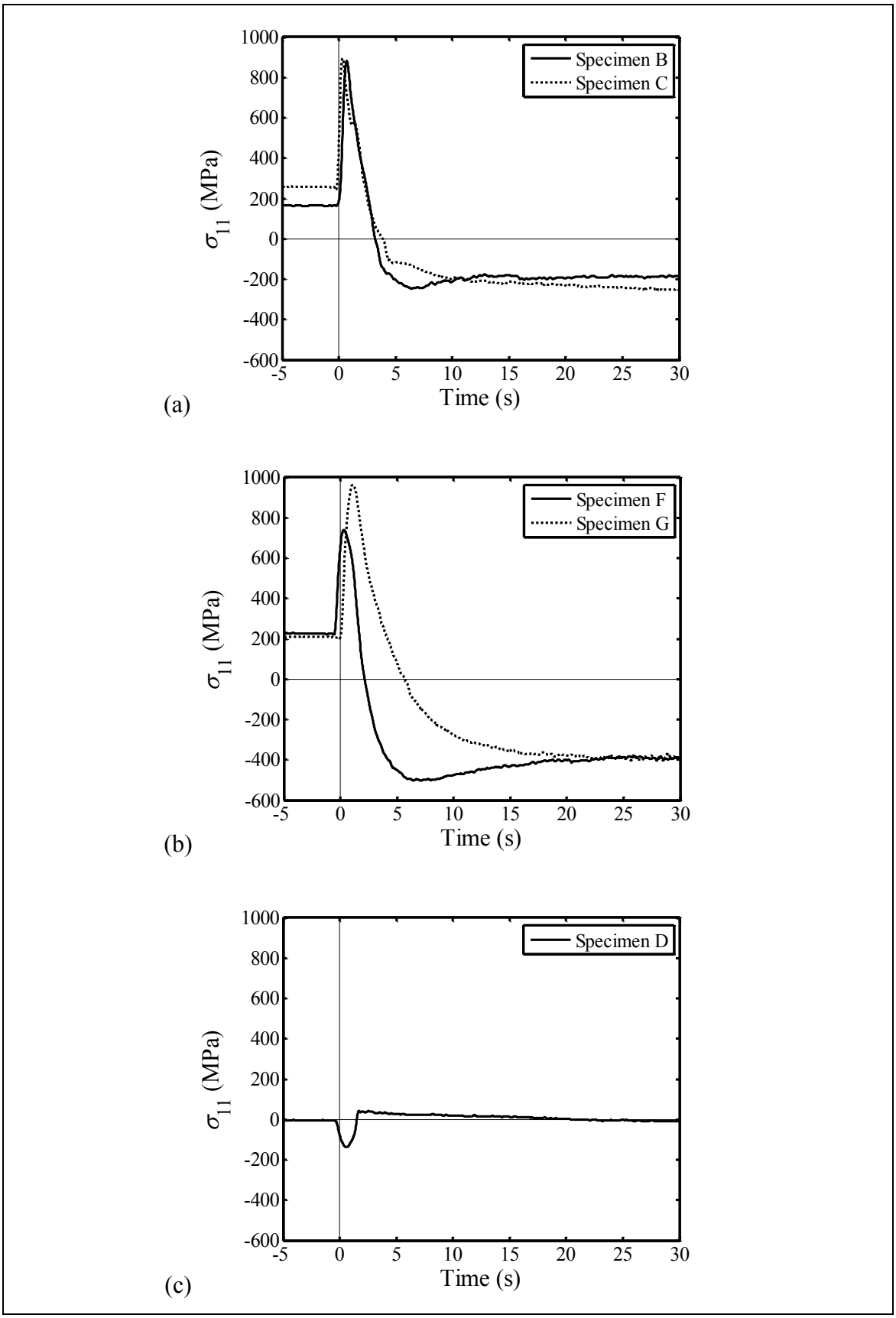

Figure 4.22 Stresses measured 150 µm ahead of the crack tip during thermal shock by XRD in: (a) Specimens B and C with 7.4 mm long cracks; (b) Specimens F and G with 10 mm long cracks; and (c) Specimen D with no crack (stress measured at the same point as Specimens F and G). The stress component, σ_{11}, is normal to the crack and parallel to the interface, as shown in Figure 4.1.

4.4.4 Finite element analysis

The temperatures during thermal shock calculated by finite element analysis (FEA) are shown in Figure 4.23 and are compared with experimental results from Specimen G (10 mm crack) at different positions, T1 and T4, which refer to the thermocouple positions given in Figure 4.5 and Table 4.2. T1 is on the bottom surface of the specimen which is in contact with the cold water, and T4 is 12 mm from the bottom. Finite element results are given with and without cooling around the crack (see Section 4.3). The finite element model initially assumes that the specimen is at a uniform temperature of 360°C, whereas in the experiment there was a temperature gradient caused by non-uniform heating. The cooling rate during thermal shock is faster in the finite element model than the experiment because the boundary conditions applied to simulate thermal shock (i.e. instantaneously adjusting the surface temperature to 20°C) are equivalent to applying an infinite film heat transfer coefficient. Accounting for cooling around the crack increases the cooling rate.

The stresses calculated using finite element analysis are shown in Figure 4.24 for models containing cracks of length: (a) 7.4 mm, (b) 10 mm, and (c) zero (crack-free). The results for each crack length are compared with the experimental measurements. Finite element results are given for both cooling scenarios: with and without cooling around the crack. Generally, the finite element model predicts larger magnitude peak stresses during thermal shock. The time during thermal shock at which peak stresses were calculated shows good agreement with the experimental measurements. Agreement diverged beyond the point of peak stress, with experimental measurements in the cracked specimens becoming compressive much faster than in the model. The model which accounted for cooling around the crack generally showed improved agreement with the experiment.

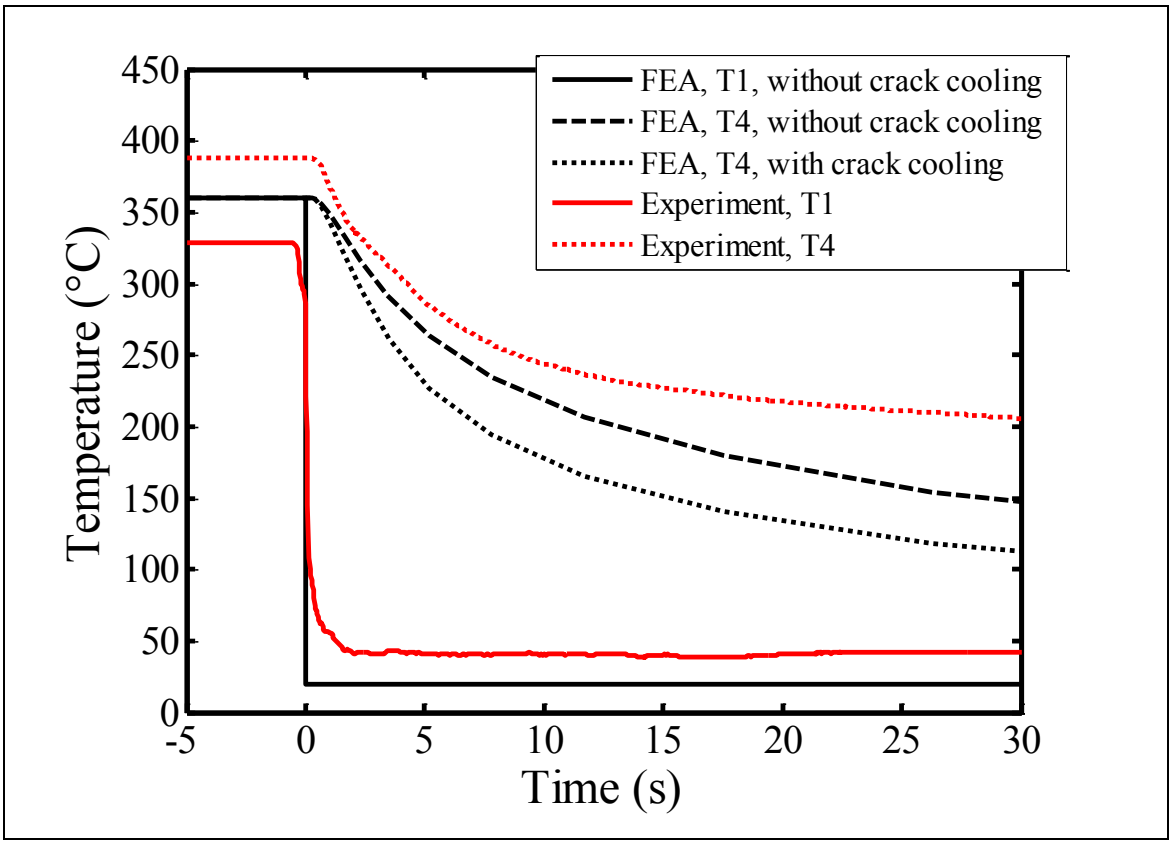

Figure 4.23 Temperatures during thermal shock at different distances from the bottom of the specimen, x_2, calculated by FEA and compared with experimental results from Specimen G (10 mm crack).

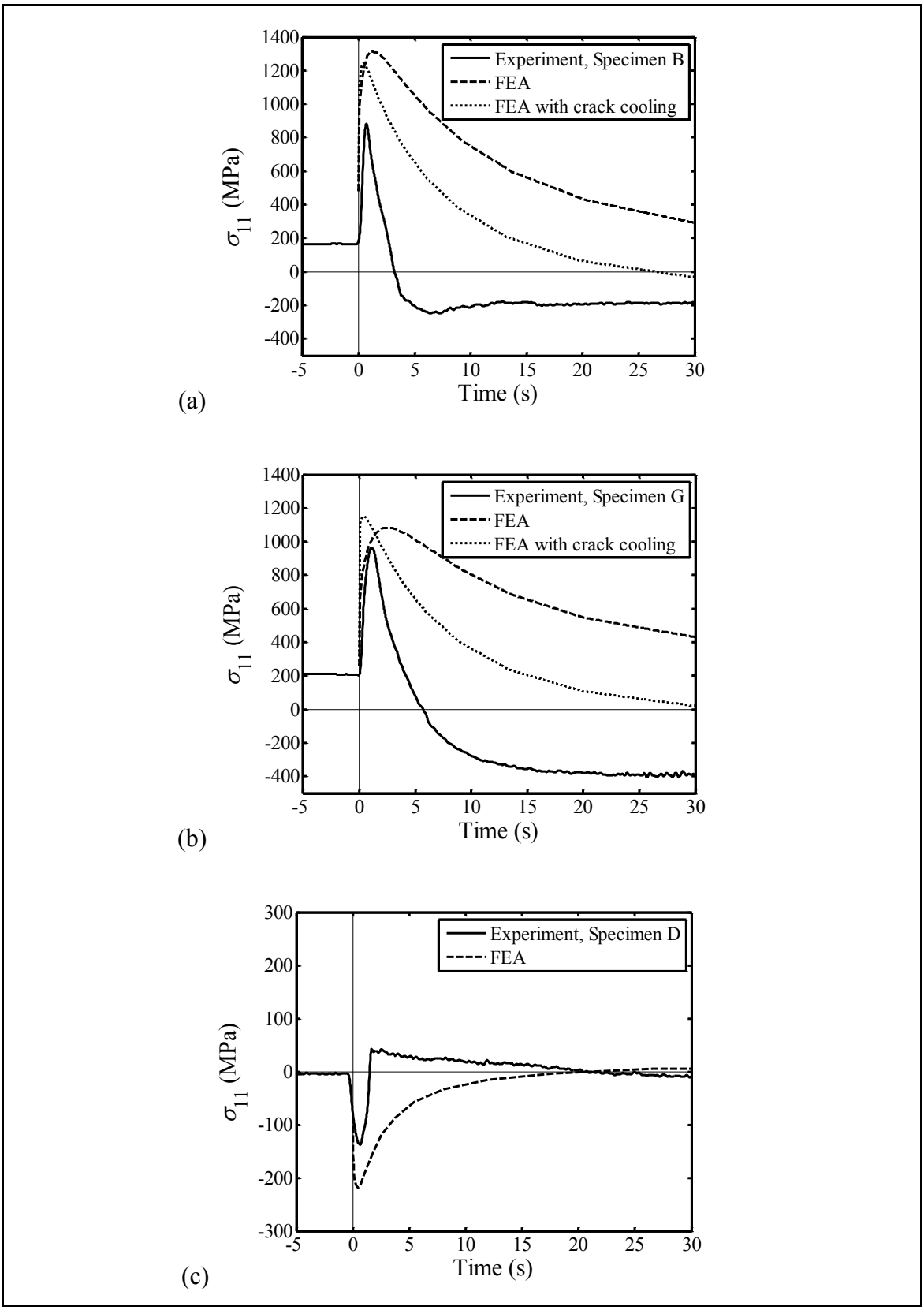

Figure 4.24 Stress 150 μm ahead of the crack tip during thermal shock calculated using FEA and compared with the experimental results for specimens containing: (a) a 7.4 mm crack, (b) a 10 mm crack, and (c) no crack (stress at the same point as the specimen with a 10 mm crack). FEA results for the cracked specimens in (a) and (b) are given both with and without cooling around the crack (as discussed in Section 4.3). The stress component, σ_{11}, is normal to the crack and parallel to the interface, as shown in Figure 4.1.

4.5 Discussion

4.5.1 Sources of experimental error

This section investigates some possible sources of error in the measurements of stress. The specimen and its coordinate system are illustrated in Figure 4.25. Under plane stress conditions ($\sigma_{33} = 0$) and in the absence of significant strain hardening, according to the Tresca yield criterion both the σ_{11} and σ_{22} stress components should be limited by the measured uniaxial yield strength of the material as long as the principal components of stress have the same sign. To check this, the stresses measured in the cracked specimens during thermal shock were normalised by the yield strength of the measurement point, σ_y. The results are plotted in Figure 4.26. The yield stress is the 0.2% proof stress calculated from tensile tests described in Section 3.4.1. The position of the measurement point relative to the HAZ was accounted for: 945 MPa was used for specimens with 7.4 mm cracks (B and C) and 783 MPa was used for specimens with 10 mm cracks (F and G). The yield stress has been adjusted to account for the changing temperature of the XRD measurement point (reduced by 14% at 360°C vs 20°C) using factors derived from temperature-dependant tensile data reported in the literature for pressure vessel steel [89]. Specimens B, C, and F all have similar normalised peak stress values of 1.1 to 1.15, whereas the peak stress in Specimen G was larger at 1.4 times the yield strength.

One explanation for the peak stresses in Figure 4.26 exceeding the yield stress is that the stress state near to the crack tip was triaxial ($\sigma_{33} \neq 0$) rather than plane stress ($\sigma_{33} = 0$), which would allow individual components to exceed the uniaxial yield stress without causing the material to yield. Only the in-plane components of strain (ε_{11}, ε_{22}, ε_{12}) were measured by X-ray diffraction, and so either a plane strain or plane stress assumption was required for calculation of the stress tensor. Plane stress was assumed ($\sigma_{33} = \sigma_{13} = \sigma_{23} = 0$) because the specimens were thin. For example, the component of stress acting normal to the crack, σ_{11}, was calculated using Equation (4.5):

$$\sigma_{11} = \frac{E}{1-\nu^2}(\varepsilon_{11} + \nu\varepsilon_{22}) \tag{4.5}$$

This is a two-dimensional formulation of Hooke's law which does not account for the non-zero σ_{33}, σ_{13}, and σ_{23} components. This is a reasonable assumption for measurements

which were made far from the crack tip and at the surfaces at $x_3 = 0$ and $x_3 = 2$ mm in Figure 4.25. However, close to the crack tip σ_{33} is always non-zero within the specimen thickness [97]. The general, three-dimensional formulation of Hooke's law is given in Equation (4.6):

$$\sigma_{11} = \frac{E}{1+\nu}\varepsilon_{11} + \frac{\nu E}{(1+\nu)(1-2\nu)}(\varepsilon_{11} + \varepsilon_{22} + \varepsilon_{33}) \tag{4.6}$$

An estimate was made of the error caused by the plane stress assumption used to calculate stresses from the measured elastic strains. This was achieved by simulating an XRD measurement using elastic strains calculated by the finite element model during thermal shock. Two simulated measurements of stress were made: the first method used Equation (4.5), which is the plane stress method used in the experiment; the second method used Equation (4.6), which represents a perfect measurement that makes no prior assumption about the stress state. It was found that the peak magnitude of σ_{11} during thermal shock was up to 17% larger using the perfect measurement compared with the plane stress assumption. Therefore, the peak tensile stress measured in the experiment, for example shown in Figure 4.22, could be up to 17% smaller than reality.

Another source of error in the experimental measurements of stress could exist because of the difference in the temperature measured by the thermocouples and the actual temperature at the measurement point. The calculation of stress requires reliable knowledge of the temperature at the measurement point so that the correct value of stress free lattice spacing, d_0^{hkl}, is used in Equation (4.3). In this experiment, the temperature of the measurement point was assumed the same as that measured by thermocouples located 12 mm away, as shown in Figure 4.5 and Table 4.2. This is a reasonable assumption in the crack-free specimen, because the temperature is only expected to significantly vary in the x_2 direction which is normal to the water surface. This may not be a fair assumption in the specimens with cracks because water marks observed in the specimens after thermal shock suggested that water was drawn up the crack, providing additional cooling on the crack faces and around the tip. The problem is illustrated in Figure 4.27, which shows a trace of the water mark left on Specimen B (7.4 mm crack) after thermal shock. The water mark is a white deposit which formed as water evaporated from the surface during thermal shock (tap water was used which could have contained various impurities). The thermocouples are located above the water mark, whereas the XRD measurement point

is below. Therefore, the actual temperature at the measurement point could have been significantly lower than the value measured by the thermocouples, causing the assumed value of stress-free lattice spacing to be unrealistically high. This in turn would make the measured strains and stresses too low.

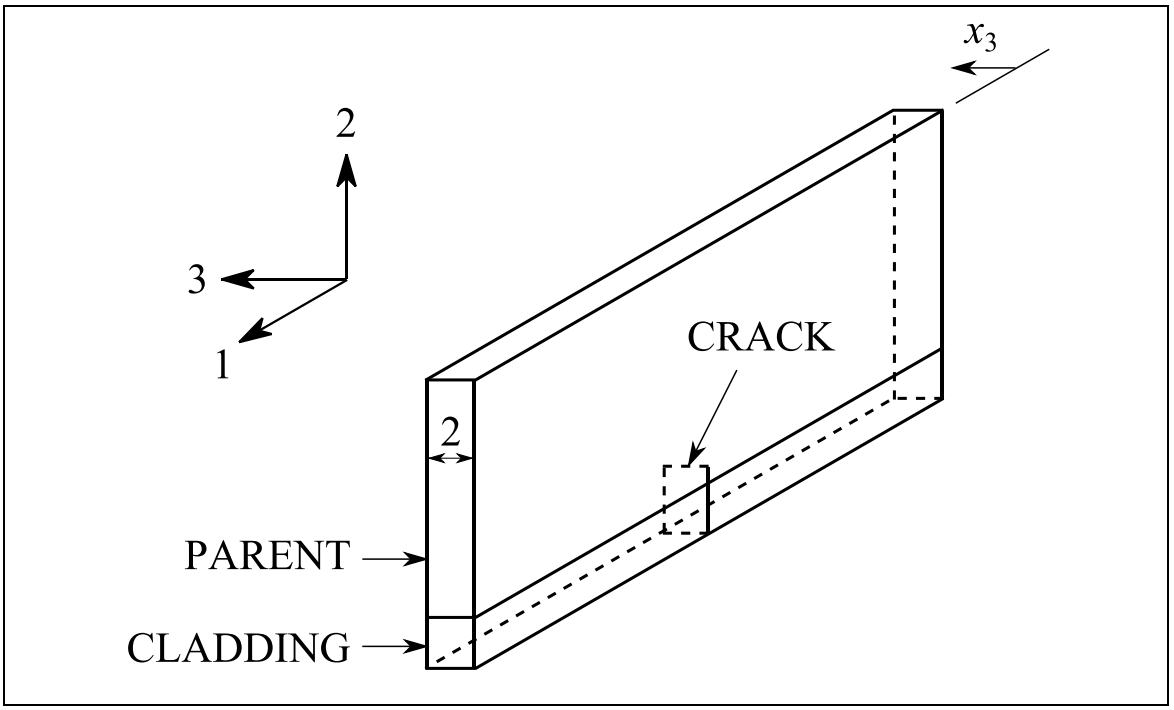

Figure 4.25 Schematic of one of the specimens containing a crack. Dimensions are in mm.

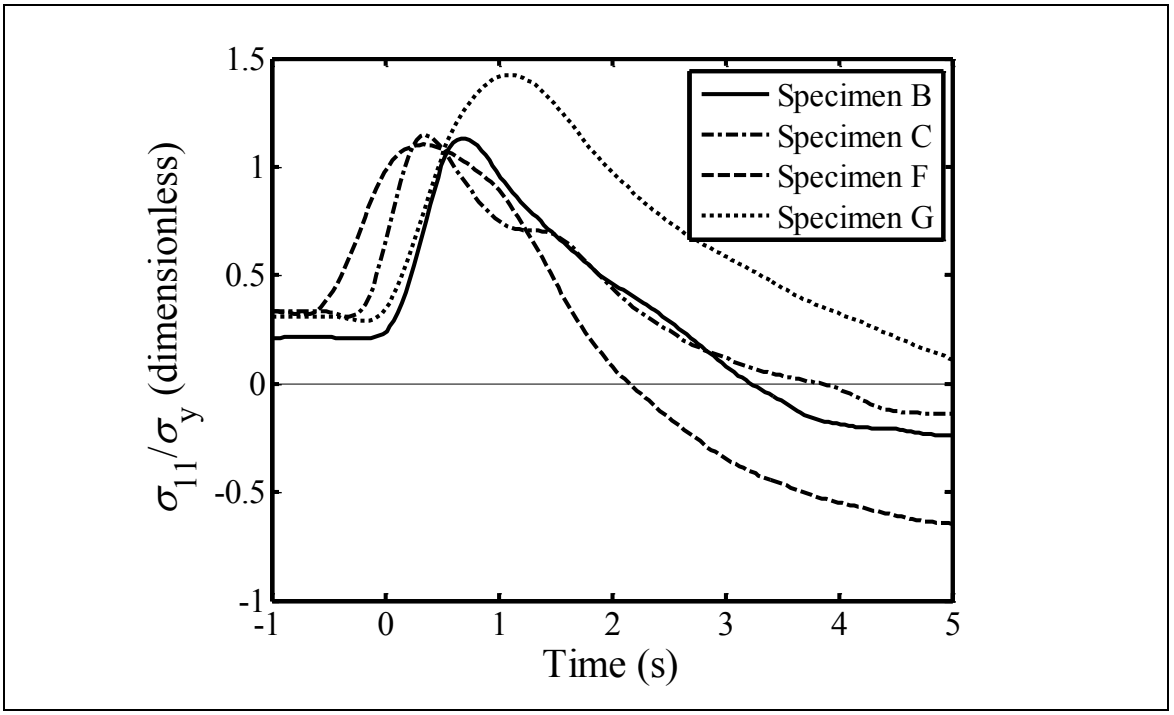

Figure 4.26 Stress normal to the crack (σ_{11}) calculated by XRD during thermal shock and normalised by the temperature-dependant (and therefore time-dependant) yield stress of the measurement point.

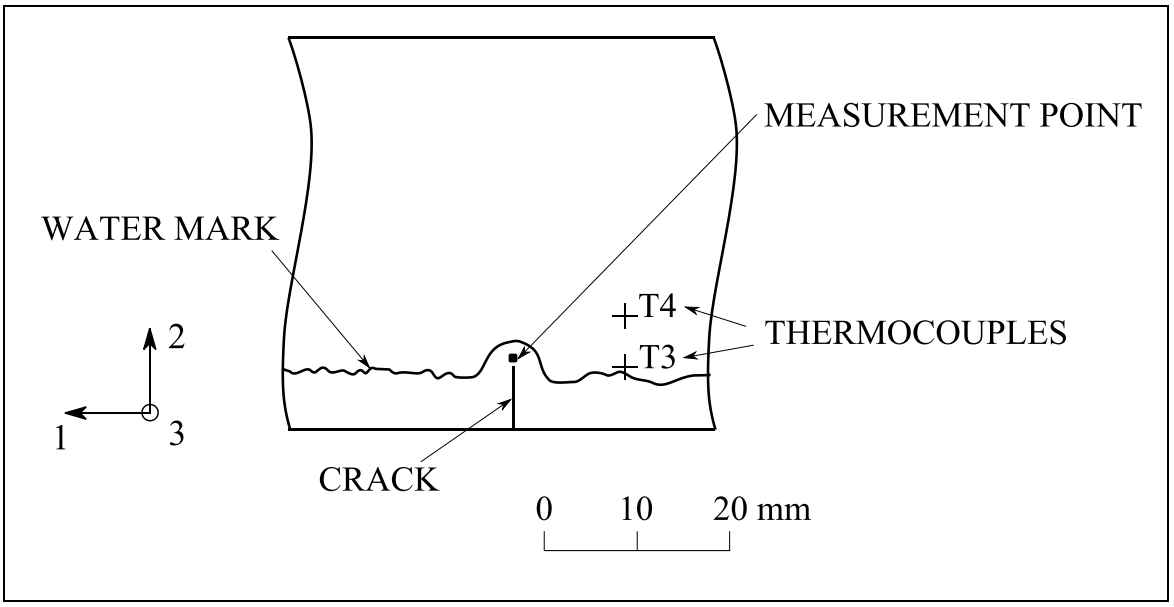

Figure 4.27 A trace of the water mark observed on Specimen B after thermal shock, and the relative positions of two of the thermocouples.

4.5.2 Stress intensity factors

Stress intensity factors have been estimated from the measurements of stress made during thermal shock in specimens containing cracks. The stress intensity factors were calculated using the solution for the stress fields near to the tip of a crack in a linearly elastic material [98]:

$$\sigma_{11} = \frac{K}{\sqrt{2\pi r}} cos\left(\frac{\theta}{2}\right)\left[1 + sin\left(\frac{\theta}{2}\right) sin\left(\frac{3\theta}{2}\right)\right] \tag{4.7}$$

where: σ_{11} is the stress normal to the crack, K is the stress intensity factor, and θ and r are polar coordinates defined in Figure 4.28. First, an averaging step was carried out to simulate the averaging effect of the measurement, which was carried out over a projected square area (shown in Figure 4.28) rather than at an infinitesimal point. The average stress over the area of measurement point, $\sigma_{11,a}$, was calculated by numerically integrating Equation (4.7) over the area with K assigned an arbitrary value of K_a. The stress intensity factor was then calculated from the measured stresses using Equation (4.8):

$$\frac{K_m}{K_a} = \frac{\sigma_{11,m}}{\sigma_{11,a}} \tag{4.8}$$

where K_m is the stress intensity factor calculated from the measured stress, $\sigma_{11,m}$. Equation (4.7) is strictly valid for sharp cracks, whereas the cracks in the specimens were machined

using EDM and so had a finite tip radius. However, it is reasonable to use Equation (4.7) in this case because the tip radius is small (54 – 64 μm, measured using a shadow graph). For example, the value of K_m only reduced by 2% when the finite tip radius was accounted for using published solutions for the elastic stresses near the tip of a blunt crack [99].

The stress intensity factors during thermal shock calculated from the measured stresses are plotted in Figure 4.29 for specimens containing (a) 7.4 mm cracks and (b) 10 mm cracks. Equation (4.7) assumes that the material is linearly elastic, and so the calculation of stress intensity factors is only strictly valid if the region of material encompassed by the measurement point has not yielded (i.e. yielding is limited to a region very close to the crack tip). Equation (4.7) was therefore used to calculate a threshold value of K_m required for half of the area of the measurement point to contain stresses above the uniaxial yield stress. In the specimens with 7.4 mm cracks, the threshold value of K_m is 28 MPa $m^{1/2}$, and in specimens with 10 mm cracks, the threshold is 21 MPa $m^{1/2}$. The threshold is different for the different crack lengths because the measurement points are in regions with different yield strengths: 945 MPa for the 7.4 mm cracks, and 783 MPa for the 10 mm cracks, as measured by tensile tests described in Section 3.4.1. These threshold values are indicated in Figure 4.29. If plane stress conditions are assumed ($\sigma_{33} = 0$), then the threshold is the point at which half of the material in the measurement point has yielded, and so values of K_m which exceed the threshold are clearly invalid. This threshold may be pessimistic because in practice the stresses are triaxial which inhibits yielding, as discussed in the previous section.

Table 4.8 shows stress intensity factors calculated from measurements of stress made before, during, and after thermal shock. Stress intensity factors before and after thermal shock are room temperature values (20°C) calculated using the weight function method from ICHD and DHD residual stress measurements on the post-weld heat treated clad plate. The measurements were described in Chapter 3 and the stress intensity factor calculation was presented in Section 3.7.3. The stress intensity factors during thermal shock are the peak values shown in Figure 4.29 (a) and (b). The results in Table 4.8 show that for 7.4 mm and 10 mm surface cracks, the maximum stress intensity factor from thermal and residual stresses occurs during thermal shock, rather than before or after.

The maximum stress intensity factor experienced during thermal shock by the specimens with 7.4 mm cracks was 24.6 MPa $m^{1/2}$. In previous analysis by Udagawa et al [60] a peak

stress intensity factor of 95 MPa $m^{1/2}$ was calculated for a 10 mm surface crack in an RPV during thermal shock caused by a loss of coolant accident. The stress intensity factor calculated from the measurements made in this work is much lower because the geometry of the specimen (Figure 4.1) was different to that of a full-size RPV. The total thickness of the clad plate from which the specimens were extracted was 42 mm, whereas RPVs typically have a wall thickness of 180 - 200 mm. This has two effects. The first effect is that the cladding residual stress is higher in the RPV, which was demonstrated in Section 3.7.2. The second effect is that the RPV can sustain tensile thermal stresses to a greater depth from the inner (cooled) wall. For example, in the analysis of an RPV by Udagawa et al [60], when the stress intensity factor during thermal shock was highest the stress normal to the crack (σ_{11}) was tensile all the way from the inner wall to a depth of 65 mm. Clearly it is impossible for the specimen used in this work (Figure 4.1) to sustain a similar stress state because it was extracted from a plate which is only 42 mm thick. Furthermore, the residual and thermal stresses must be self-balancing (i.e. sum to zero when integrated over the specimen section), and so the specimen used in this work can only sustain tensile stress down to a much smaller depth. Finally, the specimens used in this experiment were thin (2 mm) and so the thermal stresses were approximately uniaxial, acting normal to the crack (σ_{11}). In an RPV, the thermal stresses are approximately biaxial ($\sigma_{11} = \sigma_{33}$, referring to the coordinate system used for the clad plate in Figure 3.1), in which case it can be shown using Hooke's law that their magnitude is increased by a factor of $(1-\nu)^{-1}$ compared with uniaxial thermal stresses [61].

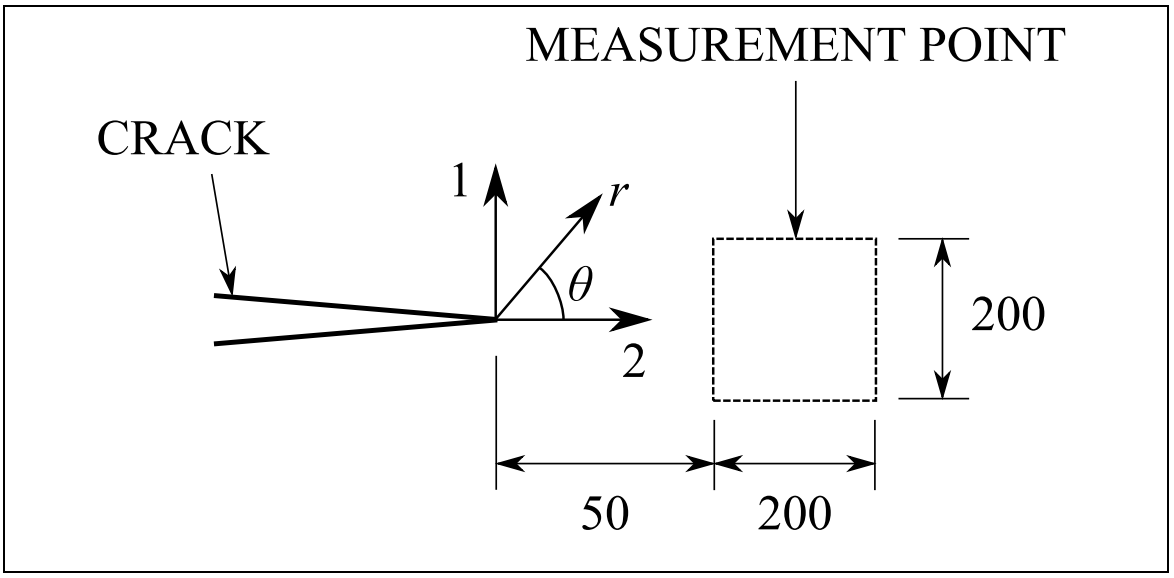

Figure 4.28 Schematic showing the polar coordinate system at the crack tip and the XRD measurement point. Dimensions are in µm.

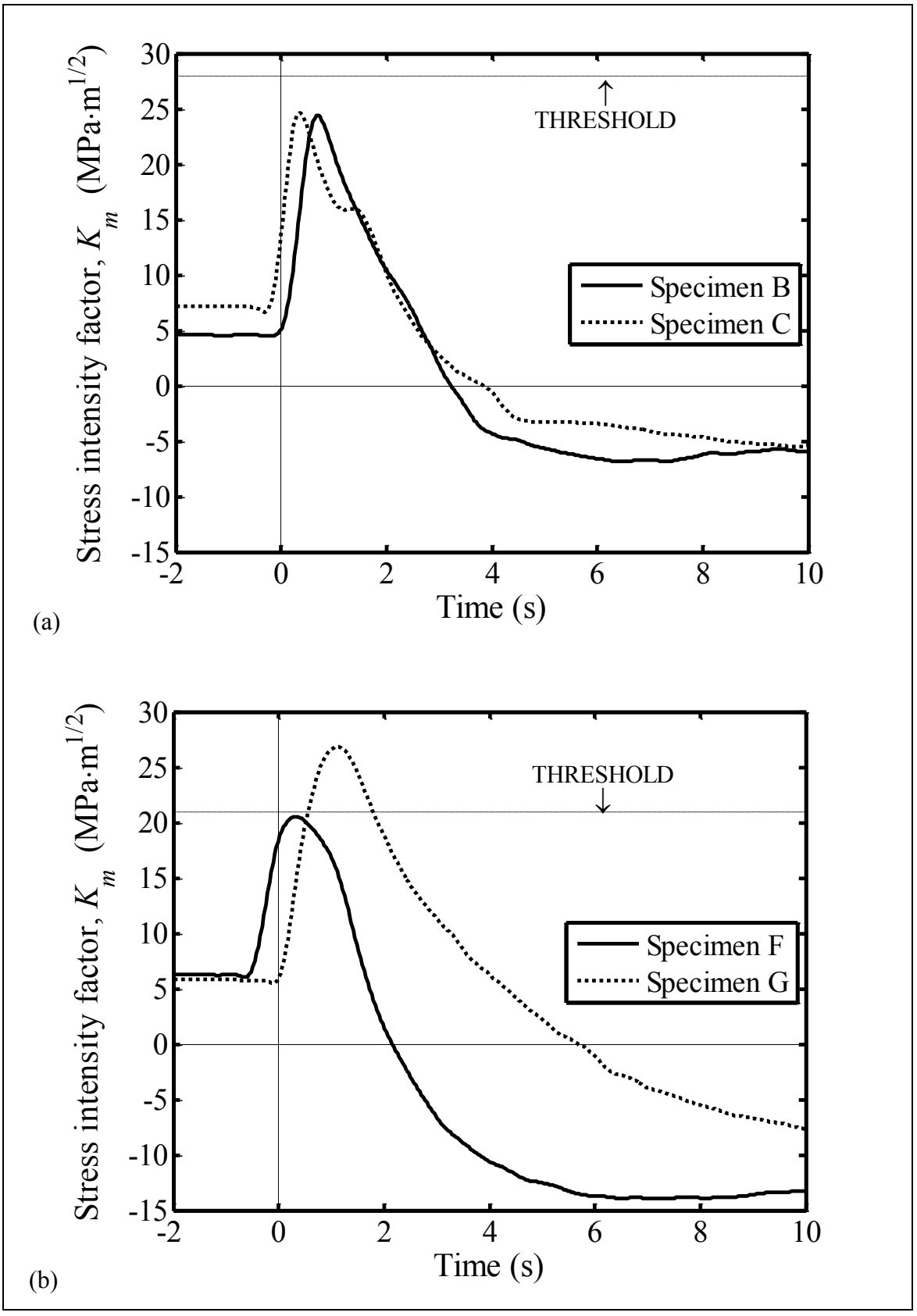

Figure 4.29 Stress intensity factors calculated from the near-tip stress measured in specimens containing: (a) a 7.4 mm crack, and (b) a 10 mm crack. The threshold line is the value of K_m at which the stresses in half the area of the measurement point exceed the uniaxial yield stress.

Table 4.8 Stress intensity factors calculated from measured stresses before (at 20°C), during, and after (at 20°C) thermal shock. 'Before' and 'after' values were calculated from residual stress measurements on the post-weld heat treated clad plate (see Section 3.7.3). 'During' values were calculated from transient measurements on the thin specimens during thermal shock using the method described in this section.

Crack length (mm)	Stress intensity factor before thermal shock, K_{RS} (MPa $m^{1/2}$)	Peak stress intensity factor during thermal shock, K_m (MPa $m^{1/2}$)	Stress intensity factor after thermal shock, K_{RS} (MPa $m^{1/2}$)
7.4	14.6	24.3 – 24.6	8.0
10	6.0	20.6 – 26.8	6.3

4.5.3 General discussion

An experiment in which stress was measured during thermal shock has been presented in this chapter. A significant amount of work has been previously carried out to calculate stresses and fracture parameters during thermal shock using analytic methods [5, 60, 66, 100, 101]. To the best knowledge of the author, this is the first time that stresses near to the tip of a crack have been measured during thermal shock. The significance of near-tip stresses is that their magnitude characterises the onset of crack propagation. For example, in mild steel unstable crack propagation occurs when the stresses exceed a critical value over a distance of two grain sizes ahead of the crack [102]. The finite element method is one of the methods often used in calculations of stresses during thermal shock [52, 103]. The method is typically used to calculate fracture parameters such as K or J which provide a convenient single-parameter measure of the intensity of the near-tip stresses. In this work, the near-tip stresses were calculated directly from the model, rather than using fracture parameters, for comparison with the experimental results. The validated modelling approach could then be used as a benchmark to be modified for thermal shock analyses on different materials and geometries.

The agreement between the model and the experiment, shown in Figure 4.24 (a-c), was mediocre. Agreement was improved in the cracked specimens using the model which accounted for cooling around the crack. The time during thermal shock at which peak stresses occurred was well-predicted by the model which accounted for cooling around the crack. The models containing cracks, for which results are shown in Figure 4.24 (a–b), predicted higher peak stresses than measured in the experiment. The plane stress assumption made in the experimental measurements, which was discussed in Section

4.5.1, could account for some of the difference. Additionally, the rate of cooling in the model was faster than in the experiment, as shown in Figure 4.23, and so may have induced unrealistically high stresses. Agreement between the finite element model and the experiment diverged beyond the point of peak stress. This could be explained by the measured stresses being too high because of the error in the assumed temperature of the XRD measurement point, as discussed in the previous section. The fact that agreement was better in the crack-free specimen, as shown in Figure 4.24 (c), supports this argument. With no crack to draw water up to the measurement point, this specimen would not have suffered from the same magnitude of temperature measurement errors experienced in the specimens containing cracks.

During thermal shock, the XRD measurement was carried out at the same (x_1, x_2) position in the specimens containing 10 mm cracks (Specimen F and Specimen G) and the crack-free specimen (Specimen D). However, the results in the two types of specimens are very different. At the onset of thermal shock, the stress in the crack-free specimen became low-magnitude compressive (Figure 4.22 (c)) whereas the stress in the cracked specimens became high-magnitude tensile (Figure 4.22 (b)). This is because the stresses in the cracked specimens are the near-tip stresses, typically described by fracture parameters like the stress intensity factor [98], which depend on the stresses acting over the entire length of the crack, whereas the stress in the crack-free specimen is just a point measurement which is not affected by the presence of a crack. In this case the stress acting over the crack faces is mostly tensile because the cladding residual stresses and thermal shock stresses are both tensile in the cladding, whereas in the absence of a crack the stress at the measurement point is compressive. This behaviour is also demonstrated by the finite element model, as shown in Figure 4.24 (b) and (c).

Results from the steady-state measurements of stress provide extra insight into how the stresses in the material change during thermal shock. The experiments presented in Chapter 3 showed that residual stress redistribution occurred in the crack-free clad plate during thermal shock, whereas in this experiment the stresses before and after thermal shock were measured around cracks. These are the residual stresses which have been redistributed, first by introducing a crack, and subsequently by thermal shock. The near-tip stresses shown in Figure 4.16 change from high-magnitude tensile before thermal shock to high-magnitude compressive after thermal shock. The compressive stresses are caused by reverse plasticity occurring by unloading. The unloading occurs beyond the

point of peak stress measured during thermal shock, for example shown in Figure 4.22 (a) and (b). This behaviour is consistent with predictions by warm pre-stress models that the stress immediately adjacent to the crack tip become compressive as soon as any unloading occurs [104]. The change in near-tip stresses before and after thermal shock supports one of the findings of Chapter 3 that the stress intensity factor due to residual stress, K_{RS}, is different before and after thermal shock and therefore the thermal shock stresses and the residual stresses must have combined inelastically during thermal shock.

The measurements made on one of the crack-free specimens, shown in Figure 4.17, show only a small difference in stress before and after thermal shock. This is reasonable since it was shown in experiments on the post-weld heat-treated clad plate described in Chapter 3 that most of the residual stress redistribution by thermal shock occurs in the cladding. In the same experiments, some redistribution was measured in the parent (see Figure 3.17) up to around 3 mm beneath the cladding. However, the thermal shock experienced by the clad plate was more severe than in the experiment on thin specimens described in this chapter, because the initial temperature was higher (480°C vs 360°C). Furthermore, the stress state in the thin specimens was likely to have been close to plane stress ($\sigma_{33} = 0$), whereas in the clad plate the thermal shock stresses may have been approximately equi-biaxial ($\sigma_{33} = \sigma_{11}$). It can be shown using Hooke's law that the magnitude of thermal shock stresses are enhanced by a factor of $(1-\nu)^{-1}$ if they are assumed biaxial [61], which would have promoted more yielding and residual stress redistribution in the clad plate than in the thin specimens.

4.6 Chapter summary

This chapter presented a novel experiment to measure stresses in RPV material under transient conditions during thermal shock. The experiment required the development of a new technique in which thin specimens were extracted from the post-weld heat-treated clad plate described in Section 3.2, and were subjected to thermal shock by a bespoke self-contained thermal shock rig which enabled simultaneous measurements of stress by synchrotron X-ray diffraction. Using this technique, the time-resolved stresses were measured during thermal shock at a single point in the parent in crack-free specimens, and at the crack tip in specimens with through-cladding surface cracks. Stresses were also measured under steady-state conditions before and after thermal shock. Stresses were only measured in the parent material (SA508 4N) because the grain size in the cladding (Alloy 82) was too large for reliable X-ray diffraction measurements.

Steady state measurements in the specimens containing cracks found high tensile stresses near the crack tip before thermal shock, which changed to high-magnitude compressive stresses after thermal shock. These results support one of the findings from the thermal shock experiment described in Chapter 3 that the thermal and residual stresses combine inelastically during thermal shock.

Residual stresses in the crack-free specimens were only different by a small amount (< 60 MPa) before and after thermal shock. The measurements made on the virgin specimens (before thermal shock) agreed well with the measurements on the clad plate made by mechanical strain relaxation methods described in Chapter 3. The residual stress in the parent directly beneath the cladding varies with position relative to the bead of the weld-overlay by up to 100 MPa. The variation is small at depths greater than 6 mm beneath the cladding. The component of stress normal to the cladding surface (σ_{22}) was measured in the parent up to 10 mm beneath the cladding and it was found to be relatively small with a maximum magnitude of 40 MPa.

Transient measurements of stress during thermal shock made at the crack tip in specimens with cracks showed that peak tensile stresses of up to 966 MPa occurred within a second of the start of cooling. The stresses become compressive and remain so for the duration of thermal shock from 2 – 5 seconds after the start of cooling. Stress intensity factors were estimated from the stresses measured during thermal shock. It was found that the

maximum stress intensity factor from thermal and residual stresses occurs during thermal shock, rather than before or after. The peak stress intensity factor was 24.6 MPa $m^{1/2}$ in the specimens with 7.4 mm surface cracks.

A finite element model was made as a benchmark thermal shock analysis method which could be validated using the experimental results. The near-tip stresses were calculated at a position equivalent to the X-ray diffraction measurement point. The time of peak stress calculated by the model showed good agreement with the experiment. The peak stresses were generally higher in the model than in the experiment. Agreement between the model and experiment was generally improved when cooling on the crack faces and around the crack tip was accounted for in the model. Some sources of experimental error were identified which account for some of the differences between the experimental and analytic results.

5 Studying the Role of Residual Stress in Failure Using Fixed-Displacement Four-Point Bending

5.1 Introduction

The aim of the work presented in this chapter was to experimentally investigate the interaction between residual and applied stresses in different materials. This was achieved by developing a new experimental technique which represents residual stress in a specimen by subjecting it to fixed-displacement four-point bending. The specimen can then be loaded simultaneously under tension, representing applied load. This new technique was used to study the interaction of residual stress with applied load and the effect of residual stress on fracture in two materials: one with a high ratio of toughness to yield strength (P355 steel) and one with a relatively low ratio of toughness to yield strength (7075 T7351 aluminium alloy).

In this chapter, the new technique for imparting residual stress on test specimens is first introduced in Section 5.2. The technique addresses some of the common limitations suffered by existing methods for imparting residual stress on test specimens, which were discussed in Section 2.3. In summary, with existing methods the level of residual stress is uncertain and requires measurement, and the level of residual stress is difficult to vary. Using the new technique, the residual stress is simple to calculate and can be easily adjusted. The experimental method is described in Section 5.4. A fixed-displacement four-point bending fixture was designed and manufactured. The fixture was used to

impart residual stress on steel and aluminium specimens. The specimens were then subjected to simultaneous tension using a servo-hydraulic test machine, and the redistribution of residual stress was monitored using a load cell integrated in the bending fixture. Some specimens contained cracks and were loaded to fracture. The results are presented in Section 5.5, followed by a discussion in Section 5.6. It is shown that if the applied load is normalised by the net section collapse load, which accounts for the reduction in ligament width caused by the crack, then the amount of residual stress relaxation depends on the crack length. No effect of residual stress on fracture was measured in the steel specimens, whereas a significant effect was measured in the aluminium specimens.

5.2 The new technique for imparting residual stress on test specimens

A new method was devised for subjecting test specimens to residual stress. The technique is illustrated in Figure 5.1. The test specimen is a rectangular bar of width, b, and thickness, t. There is a crack of length, a, in the middle of the specimen on one edge. The specimen is bent up to the desired magnitude of initial bend load, $F_{b,i}$, and the fixture displacement, δ_b, is locked in place. The specimen is then loaded simultaneously under tension, F_t. The bend load represents residual stress and the tensile load represents applied stress. Therefore, F_b is the residual load causing residual stress, σ_{RS}, and F_t is the applied load causing applied stress, σ_{app}. Each roller provides a force equal to $F_b/2$ to the specimen. The inner and outer rollers are separated by s_i and s_o.

Fixed-displacement four-point bending has previously been used to subject rectangular beams to a known residual stress field, thereby validating simultaneous measurement by deep hole drilling [72, 105]. The new technique extends this concept by introducing simultaneous applied load to study the effects of residual stress on failure. Other previous studies have subjected specimens to combined bending and tension by applying load offset from (but parallel to) the neutral axis of the specimen [106, 107], or by applying

load at an angle to the neutral axis (i.e. not parallel) [108]. However, in those experiments the bending and tension stresses could not be independently adjusted because both were applied concurrently by a single off-axis load. Another study used combined tension and four-point bending to study the effect of load history on collapse loads in single-edge notched bars made out of stainless steel [109]. The tension and bending were applied by two hydraulic actuators arranged so that their loading axes were perpendicular. To the best knowledge of the author, a combined tension and fixed-displacement four-point bending experiment has not been reported in the open literature for any purpose.

The new technique shown in Figure 5.1 has various advantages over previous methods for applying residual stress to specimens. The level of residual stress can be monitored in real-time during subsequent application of tension load using a load cell positioned between the fixed-displacement condition and the bend fixture, as shown in Figure 5.1. When a fracture test is conducted on a cracked specimen using this system, the magnitudes of both the applied load and the redistributed residual load will be known at failure. Previously, residual stress redistribution during applied load has only been monitored in-situ using synchrotron X-ray diffraction [18], a complex, high-cost technique which requires use of one of a limited number of facilities in existence worldwide.

Another advantage of this method is that the magnitude and shape of the initial residual stress field is well known and easy to calculate. Figure 5.2 shows the residual stress induced in a linearly-elastic, crack-free specimen, which can be calculated using Euler-Bernoulli bending theory:

$$\sigma_{RS}(x_2) = \frac{M \cdot \left(x_2 - \frac{b}{2}\right)}{I} = -\frac{3F_b \cdot (s_o - s_i) \cdot \left(x_2 - \frac{b}{2}\right)}{tb^3} \tag{5.1}$$

where x_2 is the position defined in Figure 5.2, I is the second moment of area, and t is the thickness of the specimen. The maximum (outer-fibre) bending stress, σ_b, can therefore be calculated using:

$$\sigma_b = \frac{3F_b(s_o - s_i)}{2tb^2} \tag{5.2}$$

Equations (5.2) and (5.1) are only valid for a linearly-elastic material. Therefore, this calculation of residual stress only applies if the bending force is smaller than that required

to cause yielding. Below yield the bending stress is proportional to F_b, and so its magnitude can be adjusted by changing the displacement of the bend fixture, δ_b. Therefore, it is straightforward to test specimens containing many different levels of residual stress whereas it was shown in the literature review that existing methods for imparting residual stress on test specimens typically only allow the investigation of two levels of residual stress.

The applied stress, σ_{app}, is simply:

$$\sigma_{app} = \frac{F_t}{tb} \tag{5.3}$$

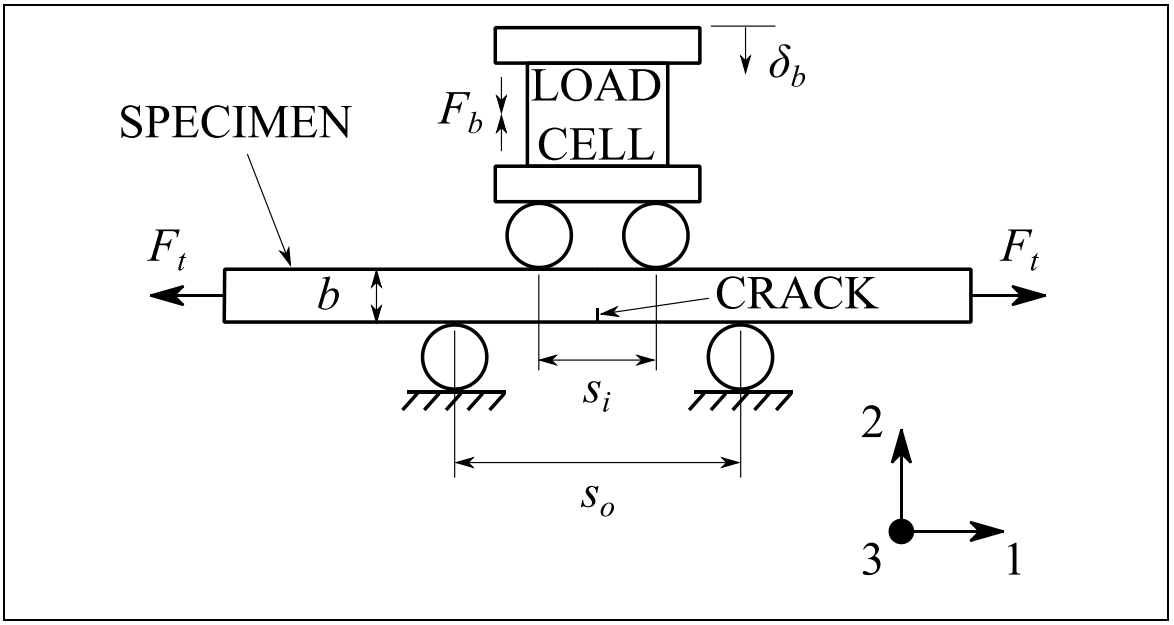

Figure 5.1 Schematic of the fixed-displacement four-point bend concept for representing residual stress and applied load.

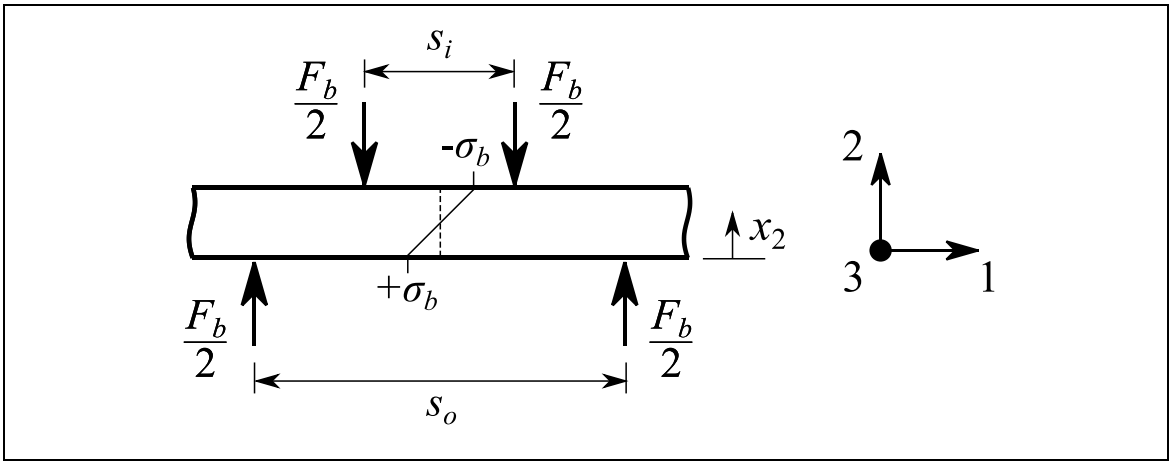

Figure 5.2 The shape of the residual stress field in a linearly-elastic, crack-free specimen.

5.3 Finite element analysis of concept

5.3.1 Introduction

A finite element study was conducted to investigate whether the fixed-displacement bending technique shown in Figure 5.1 was truly representative of combined residual stress and applied load. Two fundamental analyses were used for this. First, if the specimen is linearly-elastic, the residual stress and applied load should perfectly superimpose. Second, if the specimen is elastic-plastic, the residual stress should relax as the magnitude of the applied load increases beyond the point where the elastically-combined stresses exceed yield. This section shows that these conditions are broadly satisfied, although there are some interaction effects which are unique to the geometry and design of the fixed-displacement bending technique and do not necessarily represent the general behaviour of materials under combined residual and applied stress. The model is used to fully understand these effects so that they can be accounted for in the interpretation of experimental results.

5.3.2 Description of model

The model was constructed and analysed using the finite element code, Abaqus v6.14 [75]. A schematic of the model is shown in Figure 5.3. This is a half-model representation of the arrangement illustrated in Figure 5.1. The specimen has a half-length of 300 mm, which consists of a deformable solid part connected to a rigid part. The deformable solid part has a half-length of 200 mm, and is constructed using CPS8R quadrilateral plane stress elements. The rigid part is 100 mm long and is intended to efficiently model the part of the specimen which is clamped in the test machine without using finite elements. The four-point bending is applied via two rollers of 50 mm diameter, which are constructed using the same elements as the finite element part of the specimen. The rollers were assigned linearly-elastic material properties representative of steel, with a Young's modulus of 210 GPa and a Poisson's ratio of 0.3. Frictionless contact was defined between the rollers and the specimen. The crack was introduced by removing the symmetry boundary condition along the crack face. Crack face contact [110] was not modelled because the stresses acting over the crack face due to bending and applied load were tensile for all crack lengths studied in this work.

The loading was applied to the model in two steps. In the first step, the initial bend load, $F_{b,i}$, was introduced by subjecting the inner roller to a point load of magnitude, $F_{b,i}/2$. In the second step, the current position of the inner roller in the x_2 direction was held fixed and the tensile load, F_t, was applied as a point force in the middle of the rigid part of the specimen. Rotation around the x_3 axis was unconstrained, representing pin-loaded grip conditions. The bending force, F_b, was monitored as the magnitude of F_t was increased by extracting the vertical reaction force at the inner roller, which was equal to $F_b/2$. Abaqus can carry out analyses using either small displacement or large displacement formulations. In a small displacement analysis, the elements are formulated using the original (undeformed) configuration, whereas in a large displacement analysis, they are formulated using the current (deformed) configuration [111]. The type of analysis is specified by turning the NLGEOM switch on (large displacement analysis) or off (small displacement analysis). Models were run using both formulations in order to study non-linear geometry effects.

Numerous studies were carried out using this basic modelling procedure for specimens with different crack configurations and material properties. These studies are described in the following sections. The different crack configurations are shown in Figure 5.4. The co-ordinate system is consistent with Figure 5.3 so that the crack is always opposite the inner rollers.

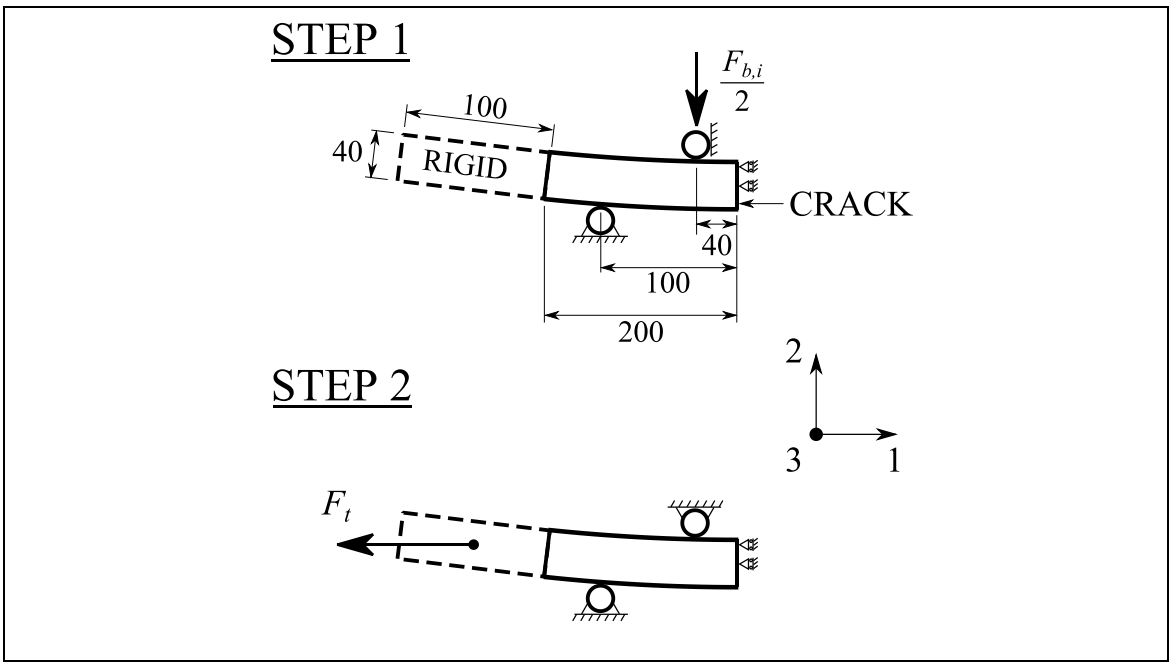

Figure 5.3 Diagram of the finite element model of the fixed-displacement four-point bending technique for representing residual stress. Dimensions are in mm.

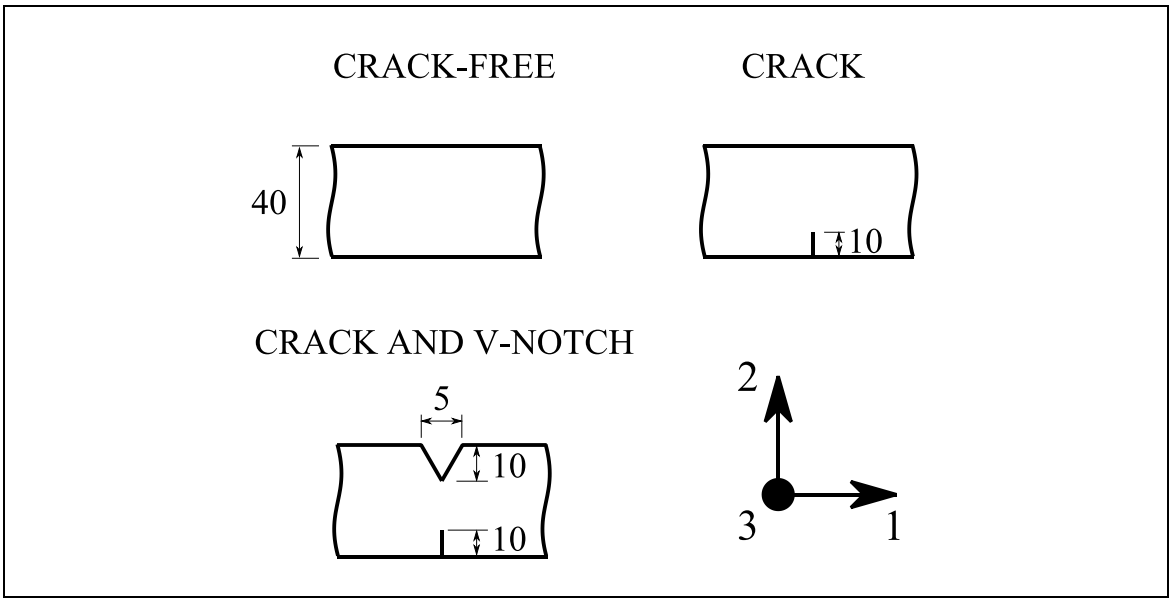

Figure 5.4 Different specimen configurations modelled using FEA. Dimensions are in millimetres.

5.3.3 Elastic interaction between residual and applied stresses

In order to show that the combined bending and tension concept truly represents residual stress and applied load, it must be demonstrated that the residual and applied stresses interact elastically in a linearly-elastic specimen. That is, the residual stress should remain constant as the magnitude of applied stress increases so that the total stress state can be calculated by superimposing the two sources of stress. To check this, various models were run using a linearly-elastic specimen with different crack configurations and geometries. All models in this section used small displacement assumptions (i.e. NLGEOM switched off). Except where indicated, 210 GPa and 0.3 were chosen for the Young's modulus and Poisson's ratio of the specimen, values typical of low-alloy steel.

Figure 5.5 shows the variation of residual load (F_b) with applied load (F_t) for specimens with different geometries. On the *y*-axis, the residual load is normalised by the initial residual load, $F_{b,i}$, so that when this quantity is one the residual stress is unchanged. On the *x*-axis, the applied load is normalised by the initial residual load. When the quantity on the *x*-axis is 4.5, the initial maximum (outer fibre) bending stress is equal to the applied tensile stress (i.e. $\sigma_{app} = \sigma_b$). The different geometries are identified in the figure legend, and are fully defined in Figure 5.4. The residual load in the crack-free specimen relaxes by a small amount because the specimen contracts away from bend fixture under applied load by an amount proportional to the Poisson's ratio. This explanation is confirmed by setting Poisson's ratio to zero ('crack-free, $\nu = 0$' in the legend). In this case the residual

load does not relax with applied load because the beam section width, b, remains constant. Introducing a crack in the specimen ('crack' in the legend) causes significantly more residual load relaxation than experienced by the crack-free specimen. This effect is caused by the crack changing the position of the neutral axis, which is illustrated in Figure 5.6. The applied load introduces a bending moment, M_{os}, which acts to bend the specimen away from the rollers and reduce the bending force they provide. The effective neutral axis offset, d_{os}, is smaller than half the crack length because the stress profile across the net (cracked) section is non-linear (i.e. the magnitude of the stress is considerably greater near the crack tip than at the back face). This neutral axis offset effect could be compensated by introducing a feature opposite the crack which offsets the neutral axis back in the other direction by the same value of d_{os}. In theory, such a feature would be another crack of equal length to the original, thereby creating a double-edge cracked specimen. This would then introduce undesirable crack closure effects because the compensating crack would bear load under compressive stress ($F_b >> F_t$) but not tensile stress ($F_b << F_t$). A compromise, developed using trial and error, is to machine a V-shaped notch opposite the crack, as shown in Figure 5.4. The result from this compensating geometry is also plotted in Figure 5.5 ('crack and V-notch' in the legend). The residual load relaxes by a similar amount as the crack-free specimen.

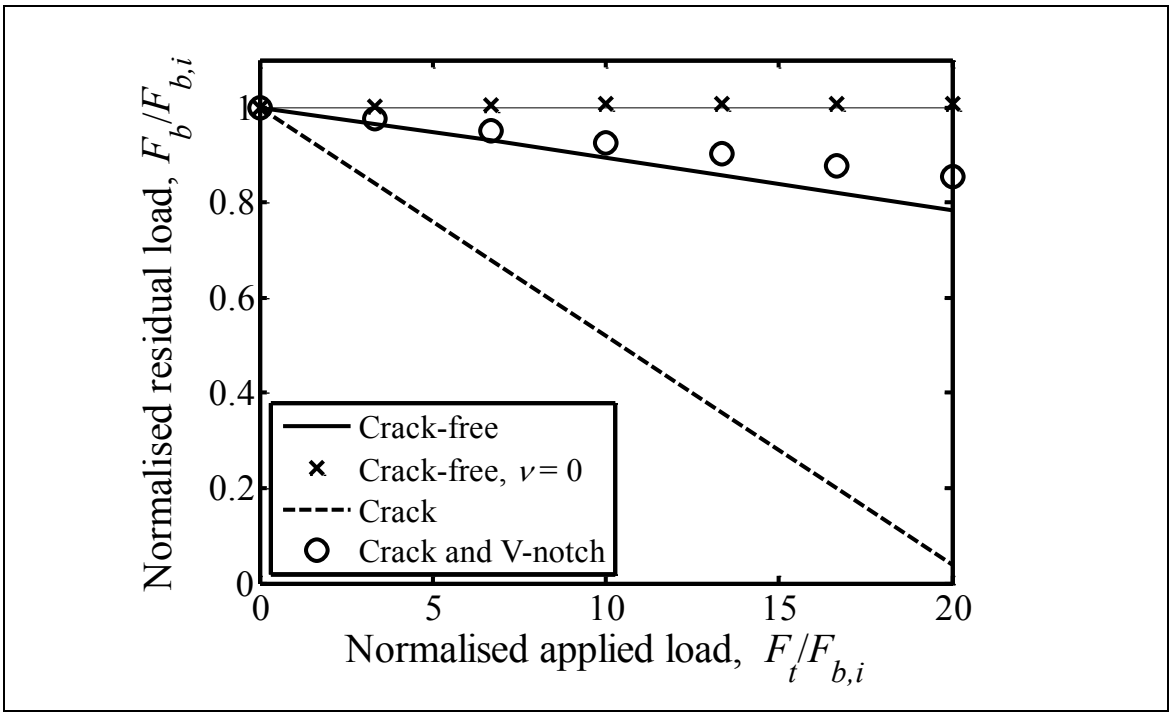

Figure 5.5 Interaction between residual and applied loads in a linearly-elastic specimen. Poisson's ratio, ν, is 0.3 except where indicated.

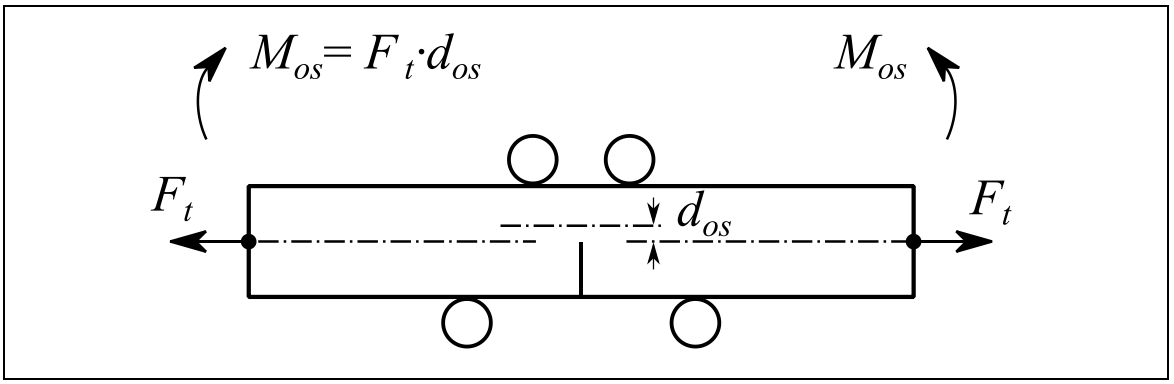

Figure 5.6 The neutral axis offset effect caused by introducing a crack in the specimen.

5.3.4 Elastic plastic interaction between residual and applied stresses

In order to show that the combined bending and tension concept truly represents residual stress and applied load, it must also be demonstrated that the residual and applied stresses interact inelastically in an elastic perfectly plastic specimen. That is, the residual stress relaxes by yielding with increasing applied stress, eventually fully relaxing when the applied load reaches the collapse load.

In this section, the specimen was assigned material properties representing low alloy steel. The material was either linearly-elastic, with $E = 210$ GPa and $v = 0.3$, or elastic perfectly plastic with the same values for E and v and a yield stress $\sigma_y = 500$ MPa. The specimen was crack-free (geometry A in Figure 5.4). Models were run with different magnitudes of initial residual load, $F_{b,i}$, relative to the bending collapse load, $F_{b,c}$, defined as:

$$F_{b,c} = \frac{\sigma_y b^2 t}{s_o - s_i} \tag{5.4}$$

which is 1.5 times the force required to cause first yielding at the edge of the elastic-plastic specimen. The results are plotted in Figure 5.7. On the y-axis, the residual load, F_b, is normalised by the initial residual load, $F_{b,i}$, so that when this quantity is one the residual stress is unchanged. On the x-axis, the applied load, F_t, is normalised by the tension collapse load, $F_{t,c}$, defined as:

$$F_{t,c} = \sigma_y b t \tag{5.5}$$

There are four sets of results in Figure 5.7. Two curves are results for elastic-plastic specimens with different normalised initial residual loads (‘0.225’ and ‘0.45’ in the figure legend), and two are for linearly-elastic specimens subjected to the same initial residual

loads. There is a small amount of bend load relaxation in the elastic-plastic specimens at low magnitudes of applied load. When the elastically-combined magnitude of bending and tension stresses is less than yield, the gradient of the curve is equal to that calculated for a crack-free specimen in the previous section (Figure 5.5). When the elastically-combined stresses exceed yield, the residual load relaxes by yielding and the elastic-plastic curves deviate from the elastic curves until the residual load relaxes to zero at the collapse load.

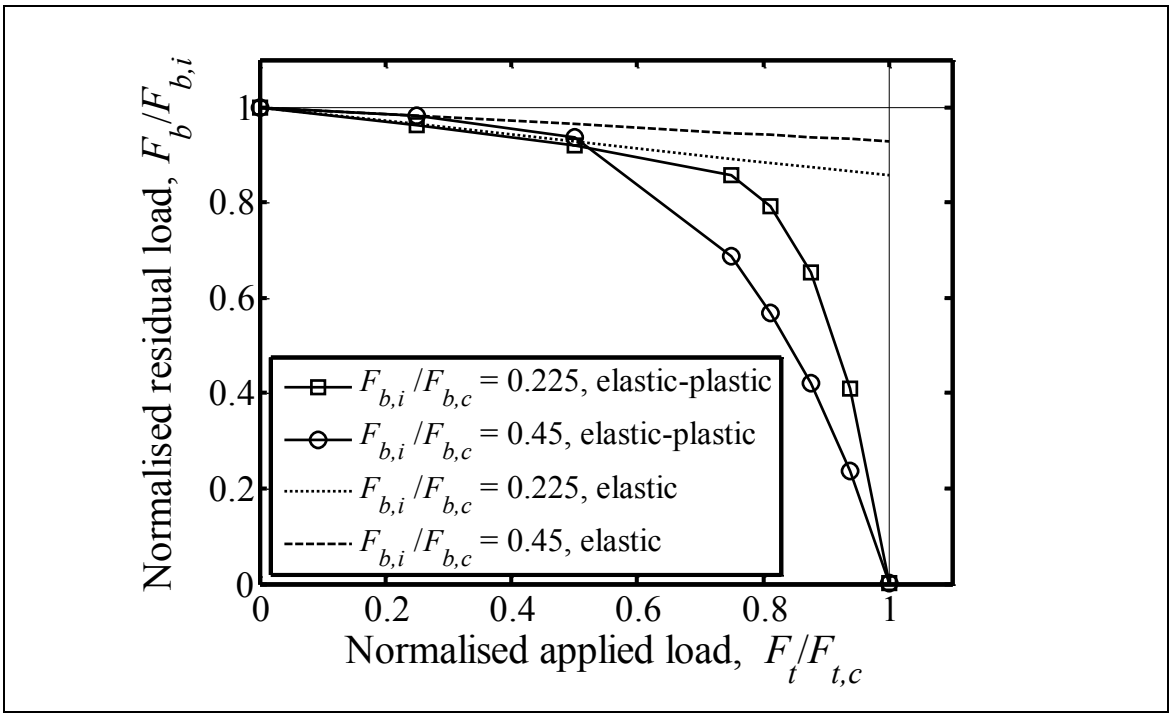

Figure 5.7 Residual load redistribution with applied load in elastic perfectly plastic specimens containing different amounts of initial residual load.

5.3.5 Large-displacement bending effect

Large displacement analysis (i.e. with NLGEOM switched on in Abaqus) was carried out to check for non-linear effects on the interaction between applied and residual loads. The specimen was assigned linearly-elastic material properties representative of low alloy steel, with E = 210 GPa and ν = 0.3. The geometry was crack-free. Two models were run, one with NLGEOM switched on, and one with NLGEOM switched off. The results are shown in Figure 5.8. The axes are the same as Figure 5.5, so that a value of one on the y-axis indicates zero residual load relaxation. When the quantity on the x-axis is 4.5, the initial maximum (outer fibre) bending stress is equal to the applied tensile stress. The initial residual load, $F_{b,i}$, was 20 kN for the model with NLGEOM switched on, which gives a maximum (outer fibre) bending stress of 112.5 MPa. When NLGEOM is switched

off, the result is the same as for the crack-free specimen in Figure 5.5 and is independent of $F_{b,i}$. A small amount of residual load relaxation occurs because of the Poisson effect, which is discussed in Section 5.3.3. The relaxation varies linearly with increasing applied load. With NLGEOM switched on (i.e. large displacement analysis), the residual load redistributes non-linearly with applied load. The physical cause of this non-linearity is illustrated in Figure 5.9. When the specimen is subjected to bending, $F_{b,i}$, it deflects, which creates an offset, d_{os}, between the point of application of the subsequent applied load, F_t, and the neutral axis at the mid-length of the specimen. This offset means that the applied load introduces a bending moment, M_{os}. The bending moment acts in opposite direction to the four-point bending, and so the magnitude of load borne by the four-point bend fixture, which is the residual load (F_b), increases. The magnitude of M_{os} increases with the initial residual load, $F_{b,i}$, and decreases with applied load, F_t, as M_{os} bends the beam back towards its original undeflected configuration.

This non-linear geometry effect is exacerbated by anything which increases the initial bending deflection, such as: using an aluminium specimen, which has a Young's modulus approximately 1/3 that of steel; subjecting the specimen to a higher initial residual load, $F_{b,i}$; or introducing a crack in the specimen, which reduces the bending stiffness.

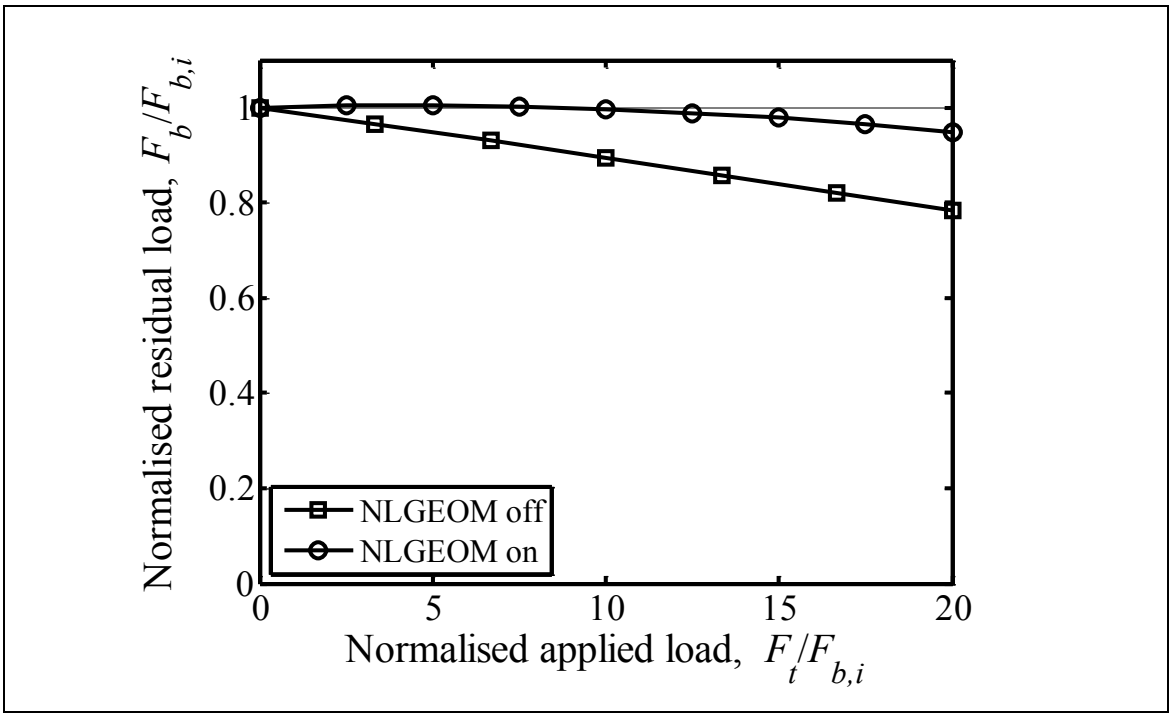

Figure 5.8 Residual load redistribution with applied load in linearly-elastic specimens calculated using small (NLGEOM off) and large (NLGEOM on) analyses.

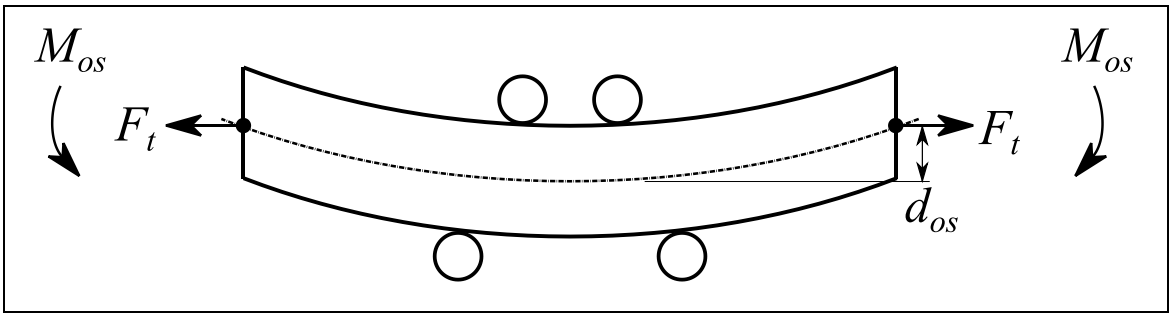

Figure 5.9 The neutral axis offset effect caused by large bending displacements.

5.3.6 Summary

The purpose of this finite element study was to investigate whether the concept shown in Figure 5.1 was truly representative of combined residual stress and applied load. Two fundamental tests were used for this. First, if the specimen is linearly-elastic, the residual and applied loads should perfectly superimpose. Second, if the specimen is elastic-plastic, the residual load should relax as the magnitude of the applied load increases beyond the point where the elastically-combined stresses exceed yield. The latter was shown to be true in Figure 5.7. Some caveats to the former were identified as follows:

POISSON EFFECT - A small amount of residual stress relaxation occurs in a linearly-elastic specimen because the beam contracts away from the bend fixture under applied load. This effect is discussed in Section 5.3.3.

ASYMMETRY EFFECT - Introducing a crack on a single edge of the specimen means that the applied load, F_t, also induces a bending moment which causes linear residual load relaxation with increasing applied load. This can be compensated by machining a V-notch the same length of the crack in the opposite side of the specimen. This effect is discussed in Section 5.3.3.

NON-LINEAR BENDING EFFECT – This effect, discussed in Section 5.3.5, causes the residual load to increase under small amounts of applied load. The effect is larger if the initial bending deflection of the beam is made larger, for example by increasing the initial residual load, or increasing the compliance of the specimen.

These effects demonstrate some limitations of the proposed method for subjecting specimens to combined residual and applied stresses. The concept has been demonstrated to work reasonably well for crack-free specimens. The asymmetry effect is significant for the 10 mm cracks assumed in this study, but will be less significant for shorter cracks.

There are significant benefits to the concept, as discussed in the introduction of this chapter. Therefore, a test rig was designed to subject specimens to combined fixed-displacement bending and applied tension, and the concept was tested experimentally. The experiment is described in the remaining sections of this chapter. The finite element study provided an understanding of the limitations of the concept, which enables them to be accounted for in the interpretation of experimental results.

5.4 Experimental method

5.4.1 Design and manufacture of the fixed-displacement four-point bending fixture

A fixed-displacement four-point bend fixture was designed to enable specimens to be subjected to combined tension load and fixed-displacement bending, as illustrated in Figure 5.1. The bend fixture subjects specimens to fixed-displacement bending so that they can then be loaded in tension simultaneously using a servo-hydraulic test machine. Full details of the design and manufacture of the fixture are given in Appendix B. The fixture is briefly described here.

The bending fixture was designed to accommodate a rectangular specimen with: section height, b, of 40 mm; thickness, t, of 20 mm; and length greater than 600 mm. Referring to Figure 5.1, the inner support span, s_i, is 80 mm and the outer support span, s_o, is 200 mm. Figure 5.10 shows an engineering assembly drawing of the bending fixture. The specimen is locked under fixed-displacement bending by displacing the load pin by δ_b and then tightening the lock nut. Various measures were taken to ensure that the test rig was very stiff so that the initial bending displacement was as close to being truly fixed as possible. The main load-bearing part of the fixture was constructed out of two 40 mm thick steel plates (labelled ‘outer support plate’ in Figure 5.10). The rollers were made stiff by making them large (50 mm diameter) and axially short. The distance between the lock nut and the inner rollers was made as short as possible by using a special low-profile load cell manufactured by Novatech (part number F313 with 160 kN capacity and a

quoted stiffness of 8×10^9 N/m). The load pin was made thick (60 mm diameter) both to increase its stiffness and to reduce the compliance in the threaded interface with the locknut. The inner rollers are mounted in the inner support plate, and the outer rollers are mounted in the outer support plates. The rollers are supported by bearings (not shown in Figure 5.10) so that friction effects caused by the specimen stretching under load are negligible. Full-compliment, drawn-cup needle roller bearings were used, which were chosen because they were the radially-stiffest bearings available and had the largest radial load capacities. The bearing design requires that the shaft functions as the inner race. Therefore, the rollers were manufactured to special tolerances defined by the bearing manufacturer and were surface-hardened. More details are given in Appendix B.

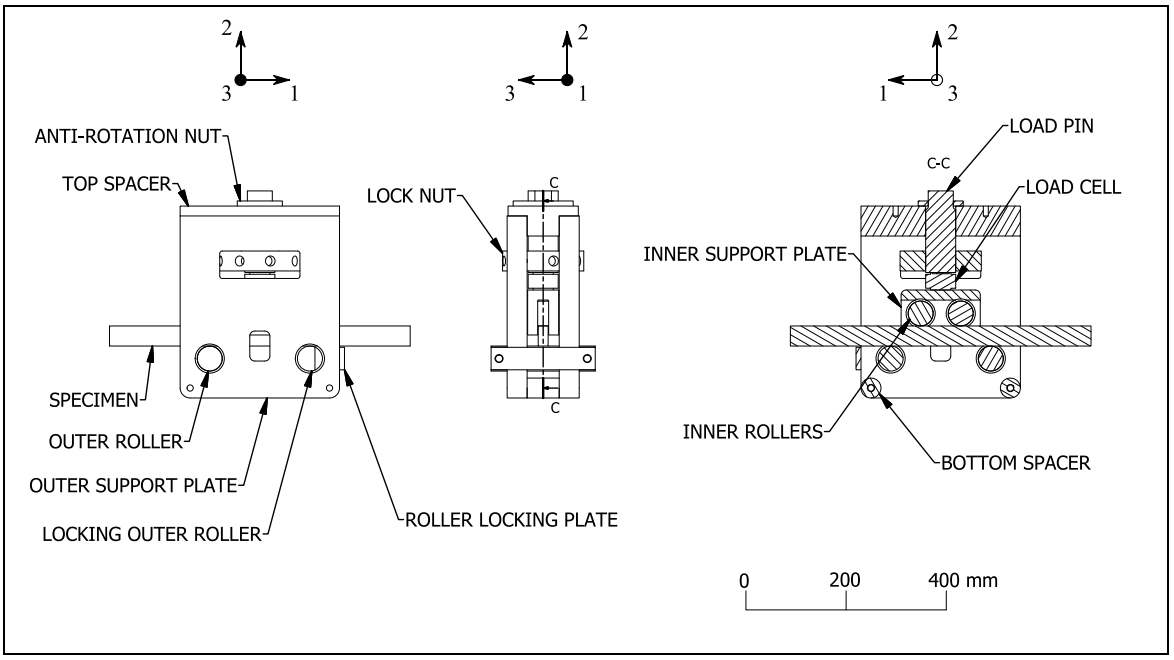

Figure 5.10 Assembly drawing of the fixed-displacement four-point bending fixture.

5.4.2 Materials

In the literature review it was shown that the effect of residual stress on fracture depends on the amount of yielding which occurs before failure. If failure occurs near the collapse load, the effect of residual stress is small, whereas if failure occurs at relatively low loads, the effect of residual stress is significant. Two materials were chosen for manufacturing specimens to ensure tests could be carried out in both regimes. The first material was a pressure vessel steel with designation BS EN 10028:3 P355 NL1/NL2, which has a relatively high toughness to yield strength ratio so that residual stress has a small effect

on fracture. The second material was 7075 T7351 aluminium alloy, which has a relatively low toughness to yield strength ratio so that residual stress has a significant effect on fracture.

Tensile tests were carried out on both materials to determine the Young's modulus and full stress-strain curves for use in finite element modelling, and to determine the yield stress which was required to calculate collapse loads. Two tensile specimens were extracted from each material. The tensile specimens were aligned longitudinally with the beam specimens described in Section 5.4.3. The geometries were rectangular, sheet-type specimens defined in ASTM E8/E8M [76]. Specimens were tested using an Instron 100 kN servo-hydraulic test machine under displacement control. Specimen extension was monitored using an extensometer with a 50 mm gauge length. Prior to loading to failure, one specimen of each material was subjected to several load-unload cycles, between 0.01 % and 0.07% strain in the steel specimen and between 0.01% and 0.2% strain in the aluminium specimen. The Young's modulus was calculated as the average gradient of these initial load-unload cycles.

The resulting stress-strain curves are plotted in Figure 5.11. Only the results for one specimen of each material are plotted for clarity because the curves were practically identical between specimens of the same material. There is a discontinuity in the stress-strain curve of the steel in the form of an extended yield point. Similar behaviour has been observed in ferritic steels in other work [112, 113] and has been attributed to Lüders bands [114]. Table 5.1 shows some commonly reported material properties, all of which were calculated using engineering rather than true stress-strain data.

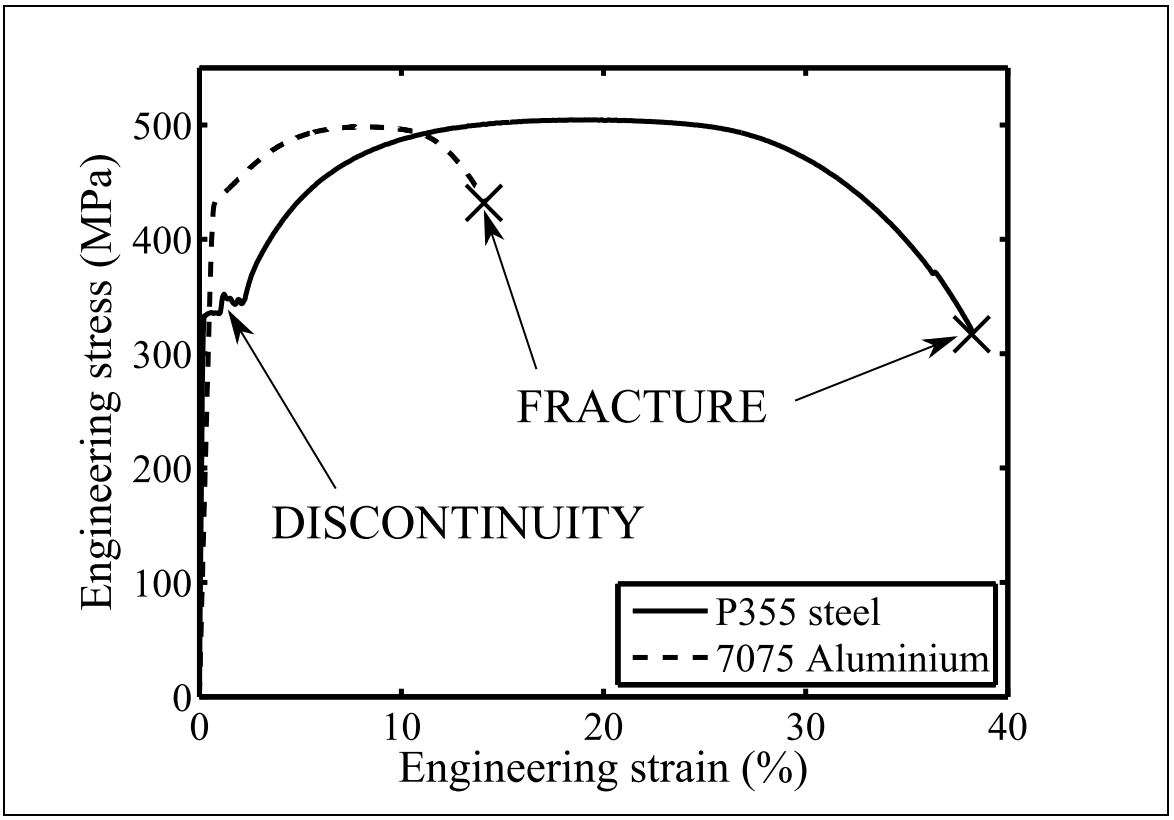

Figure 5.11 **Tensile test results of P355 steel and 7075 T7351 aluminium alloy.**

Table 5.1 **Material properties of the 7075 aluminium and P355 steel determined by tensile testing.**

Material	Young's modulus, E (GPa)	0.2% proof stress, $\sigma_{0.2\%}$ (MPa)	Ultimate tensile strength, σ_{UTS} (MPa)
7075 T7351 aluminium	71.1	435	499
P355 steel	193	327	500

5.4.3 ***Specimen design***

The overall geometry of the specimens is shown in Figure 5.12. The specimens are rectangular beams with a 20 x 40 mm section. The length is 610 mm for the steel specimens, and 700 mm for the aluminium specimens. The specimens are long so that the jaws of the test machine, which grip either end of the specimen directly, could be spaced

apart far enough to allow clearance for the bending fixture in between. The steel specimens, which were manufactured first, were only just long enough to be clamped by two thirds of the height of the jaws, and so the aluminium specimens were manufactured longer as a precaution against the specimens slipping in the jaws.

Whilst all specimens shared the same overall geometry, various features were machined in the middle of some of the specimens. The geometries of these features are shown in Figure 5.13. There are five different types of specimen, which have the following designations: NN-0 (No side grooves, No v-notch, no crack); NN-6 (No side grooves, No v-notch, 6 mm crack); NN-15 (No side grooves, No v-notch, 15 mm crack); SN-6 (Side grooves, No v-notch, 6 mm crack); SV-10 (Side grooves, V-notch, 10 mm crack). All features were aligned so that the crack was located exactly at the mid-length of the specimen. The coordinate system is consistent with Figure 5.1, so that the crack is always opposite the inner rollers and therefore in a region of tensile residual stress. The SV-10 geometry is a practical realisation of the 'crack and V-notch' geometry in Figure 5.4 which was shown to compensate for the asymmetry effect caused by introducing a crack, as discussed in Section 5.3.3.

The steel specimens were extracted from a single parent plate of steel, and the aluminium specimens were extracted from a single parent plate of aluminium. All specimens of each material were extracted in the same orientation. The parent plates were both 20 mm thick, so that the thickness of the specimen, t, is the unmachined thickness of the plate. Specimens were first roughly extracted using a plate saw, and then machined to their final overall dimensions (shown in Figure 5.12) by milling. The cracks, side grooves, and notches shown in Figure 5.13 were machined using wire EDM.

Fatigue pre-cracking is typically mandatory in fracture toughness testing standards [38] because testing specimens with as-machined notches can cause the apparent toughness to be unrealistically high [115, 116]. However, the objective of these tests was to compare results from nominally identical specimens containing different amounts of residual stress, rather than to determine the toughness properties of the material. For this purpose, machining the cracks to final length using EDM was considered superior because the consistency in crack length between specimens is limited only by machining tolerances, whereas fatigue pre-cracking was considered inferior because it is more difficult to consistently control the final length and shape of the crack. The cracks were therefore

machined to final length using wire EDM with a 0.1 mm wire, which was the smallest diameter available. Previous work by Mostafavi [117] found no measurable difference in apparent fracture toughness in 2024 Aluminium specimens with either fatigue pre-cracks or with EDM cracks manufactured using 0.1 mm wire. The average crack tip radius, measured using a shadowgraph, was 73 μm in the steel specimens and 75 μm in the aluminium specimens.

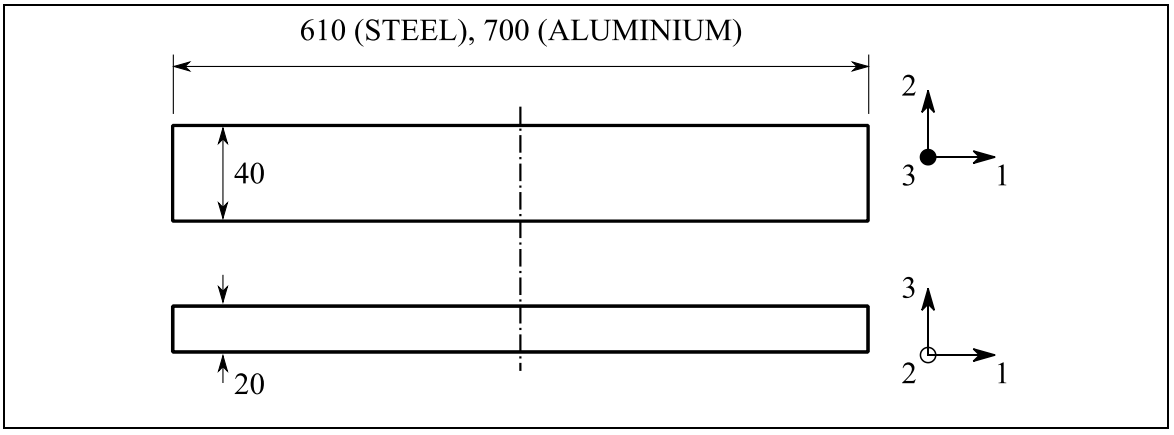

Figure 5.12 Overall geometry of the beam specimens. Dimensions are in millimetres.

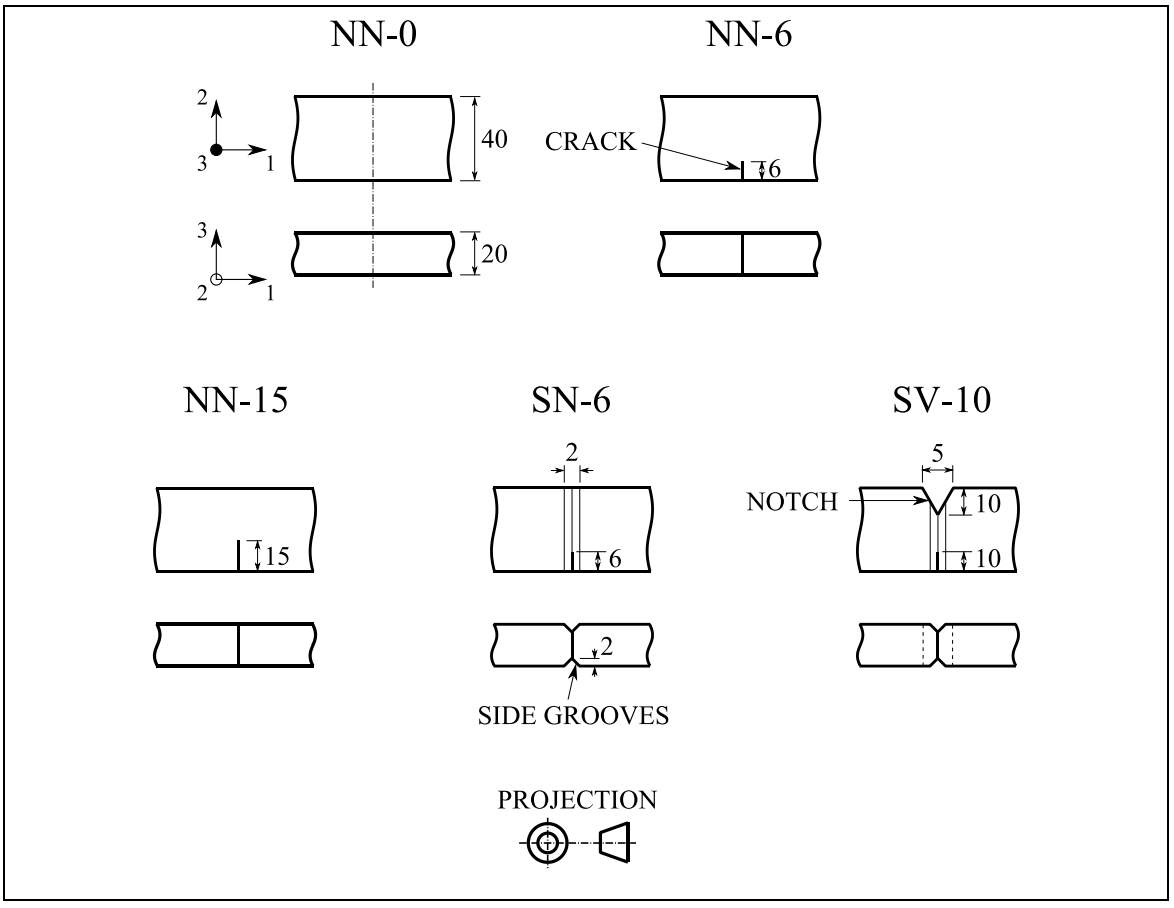

Figure 5.13 Features machined at the centre region of the beam specimens. Dimensions are in millimetres.

5.4.4 Calculation of nominal collapse loads

This section presents collapse load calculations for beam specimens subjected to bending or tension, including all cracked configurations shown in Figure 5.13. The calculations presented in this section are nominal collapse loads which assume that collapse occurs when the stress over the entire section of the specimen is equal to the yield stress, σ_y. The 0.2% proof stress calculated from tensile tests described in Section 5.4.2 was used for the value of the yield stress. The true collapse loads would be larger because strain hardening would allow the specimens to sustain higher loads. A distinction is made between net section and gross section collapse loads. Net section collapse calculations account for localised reductions in cross sectional area caused by notches, cracks, and side grooves. Gross section collapse loads assume the specimen is flawless (i.e. the geometry is NN-0 in Figure 5.13). Therefore, the net section collapse loads are unique to each specimen configuration shown in Figure 5.13, whereas the gross section collapse load is the same for all geometries. Note that the gross and net section collapse loads used in this thesis are different to the commonly reported global and local collapse loads, which have a different definition that is only relevant to two-dimensional cracks (i.e. not through-cracks) [118].

With the exception of the modifications to account for side grooves and the calculations for geometry SV-10 in Figure 5.13, all of the following solutions are published in the R6 structural integrity assessment procedure [20]. The solutions all assume plane stress conditions and use the Tresca yield criterion. The collapse bending forces presented in this section have been converted from the collapse bending moments reported in R6, using:

$$F_b = \frac{4M}{s_o - s_i} \tag{5.6}$$

where F_b is the bending force defined in Figure 5.2, M is the bending moment, s_o is the distance between the outer rollers (200 mm), and s_i is the distance between the inner rollers (80 mm). Equation (5.6) is a general conversion between bending moment and bending force which can be derived from a shear force and bending moment diagram.

In the following solutions, the gross section collapse loads are $F_{t,gc}$ (tension) and $F_{b,gc}$ (bending), and the net section collapse loads are $F_{t,nc}$ (tension) and $F_{b,nc}$ (bending).

GROSS SECTION COLLAPSE / FLAWLESS PLATE (NN-0)

For all of the geometries studied in this work, the gross section collapse load is equal to the net section collapse load in a flawless plate.

$$F_{t,gc} = F_{t,nc} = \sigma_y bt \tag{5.7}$$

$$F_{b,gc} = F_{b,nc} = \frac{\sigma_y b^2 t}{s_o - s_i} \tag{5.8}$$

PLATE WITH SINGLE EDGE CRACK (NN-6 / NN-15)

The calculation of $F_{t,c}$ here assumes a pin-loaded rather than fixed-grip boundary condition at the point at which the load is applied. The distinction is that the pin-loaded plate is free to rotate and so there is an additional bending stress caused by the asymmetry introduced by the single edge crack.

$$F_{t,nc} = bt\sigma_y \left(\sqrt{\left(1 - \frac{a}{b}\right)^2 + \left(\frac{a}{b}\right)^2} - \frac{a}{b} \right) \tag{5.9}$$

$$F_{b,nc} = \frac{\sigma_y b^2 t}{s_o - s_i} \cdot \left(1 - \frac{a}{b}\right)^2 \tag{5.10}$$

PLATE WITH SINGLE EDGE CRACK AND SIDE GROOVES (SN-6)

In this case, the geometry is the same as a plate with a single edge crack except the section thickness has been reduced by the presence of side grooves. Therefore, $F_{t,nc}$ and $F_{b,nc}$ were calculated by multiplying the right hand side of Equations (5.9) and (5.10) by the reduction factor, V_g:

$$V_g = 1 - \frac{2t_s}{t} \tag{5.11}$$

where t_s is the depth of the side grooves. Therefore:

$$F_{t,nc} = bt\sigma_y \left(\sqrt{\left(1 - \frac{a}{b}\right)^2 + \left(\frac{a}{b}\right)^2} - \frac{a}{b} \right) \cdot V_g \tag{5.12}$$

$$F_{b,nc} = \frac{\sigma_y b^2 t}{s_o - s_i} \cdot \left(1 - \frac{a}{b}\right)^2 \cdot V_g \tag{5.13}$$

PLATE WITH EDGE CRACK, OPPOSITE V-NOTCH, AND SIDE GROOVES (SV-10)

In this case, the section is reduced by the combined presence of the crack and notch, both of depth a, and the side grooves.

$$F_{t,nc} = \sigma_y (b - 2a) t \cdot V_g \tag{5.14}$$

$$F_{b,nc} = \frac{\sigma_y (b - 2a)^2 t}{s_o - s_i} \cdot V_g \tag{5.15}$$

If V_g is set to one in Equation (5.14) (i.e. the side groove depth is zero), the solution is the same as for a double edge cracked plate under tension given in R6.

5.4.5 Procedure for loading specimens

A 500 kN servo-hydraulic test machine manufactured by Dartec was used to apply bending and tension loads to the specimens. For specimens containing residual stress, the loads were applied in two steps. The bending displacement (residual stress) was applied first, followed by tension. The procedure is illustrated schematically in Figure 5.14, and photographs of the set-up are shown in Figure 5.15. The bending fixture was first positioned between the grips of the Dartec test machine as shown in Figure 5.14 (a). Flat platens were attached to the grips to enable the test machine to apply compressive load to the bending fixture. Compressive load was applied to the load pin under load control. When the desired magnitude of $F_{b,i}$ was reached, the test machine was switched to position control mode and the lock nut was tightened-up, thereby locking the bending

displacement in place. The upper grip on the test machine was then moved under position control away from the bending fixture so that the test machine was under zero load. The reading of the load cell in the bending fixture typically reduced by a small amount (< 5% of $F_{b,i}$) during this final step.

After the bending displacement was applied, the bending fixture was removed from the Dartec test machine. The platens were removed from the grips to allow access to the jaws. Flat plates were attached to the lower grip. The bending fixture was then rotated on two axes and positioned between the grips of the Dartec test machine as shown in Figure 5.14 (b). The initial distance between the grips was constant across all specimens so that the machine displacement could be used to characterise the overall stretch of the specimen. The specimen was then aligned between the hydraulic jaws of the Dartec test machine and the jaws were closed. At this point, the reading of the load cell in the bending fixture was recorded as the value for the initial residual load, $F_{b,i}$. Finally, the distance between the grips was gradually increased under position control. Before each test, the load cell in the bending fixture was calibrated against the load cell in the Dartec test machine and both load-cells were re-balanced to read zero under zero load.

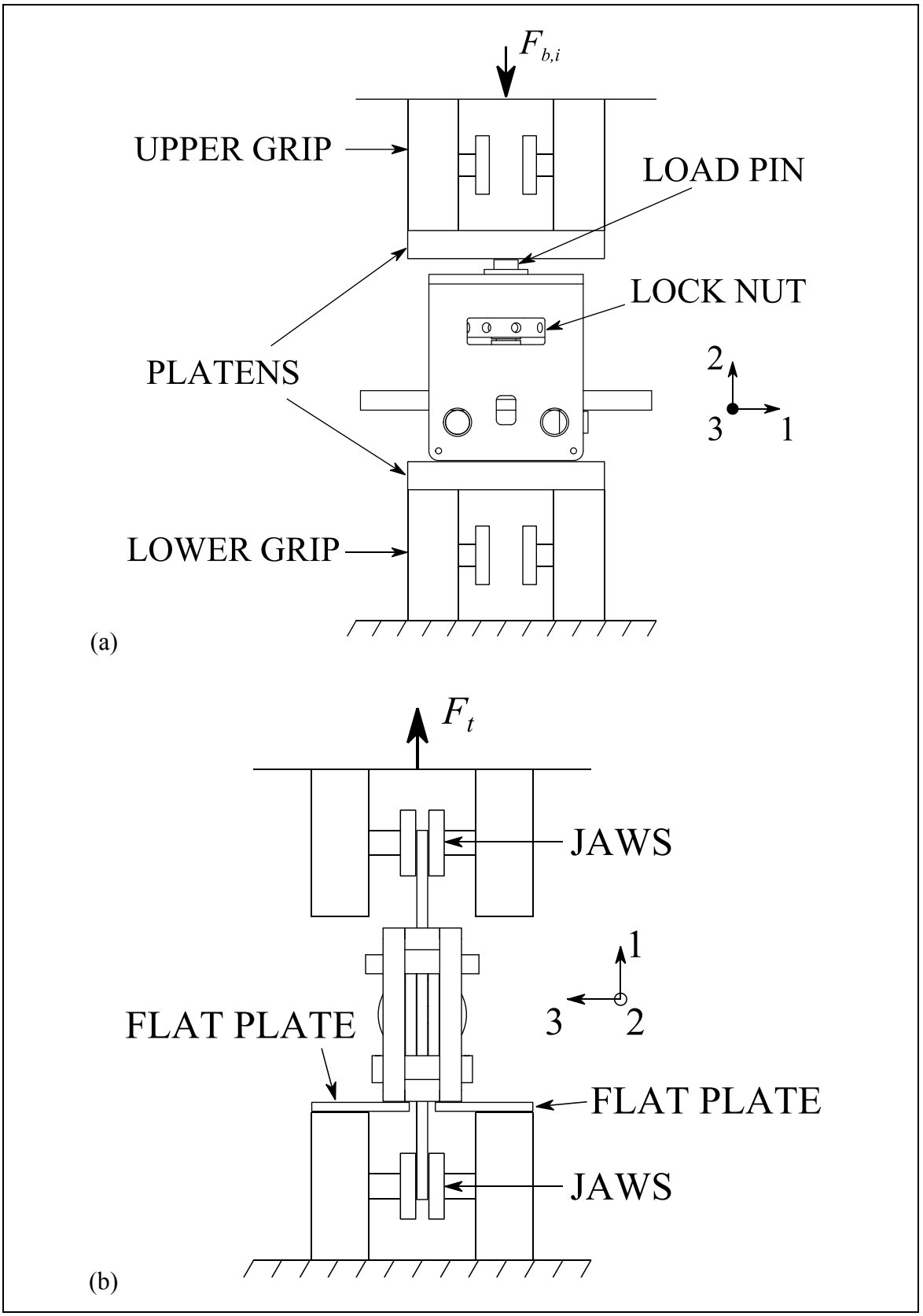

Figure 5.14 **Diagram of arrangement used to apply fixed-displacement bending (a) and subsequent tension (b) to the specimens. The coordinate system indicates the orientation of the bending fixture and specimen.**

(a)

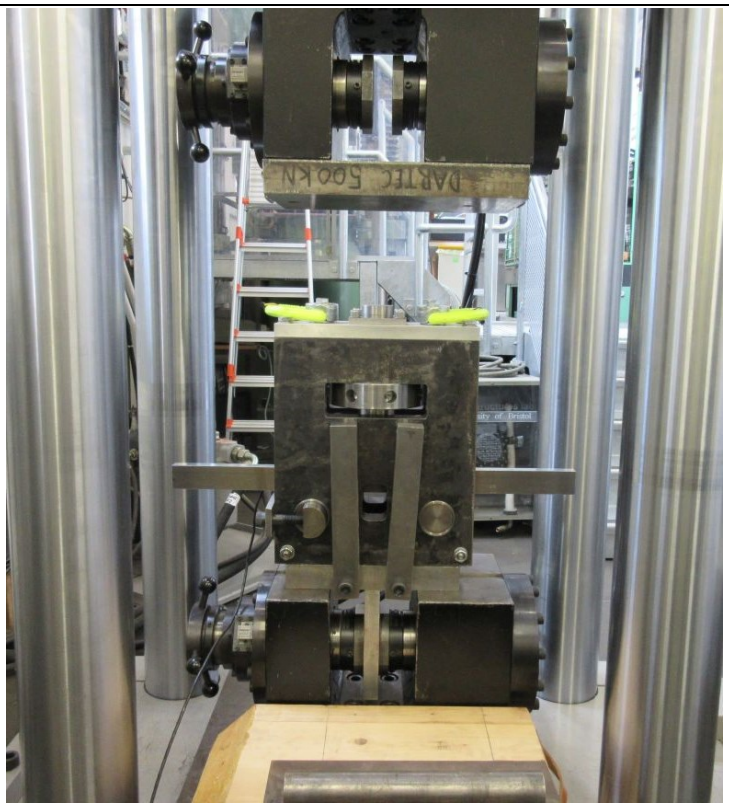

(b)

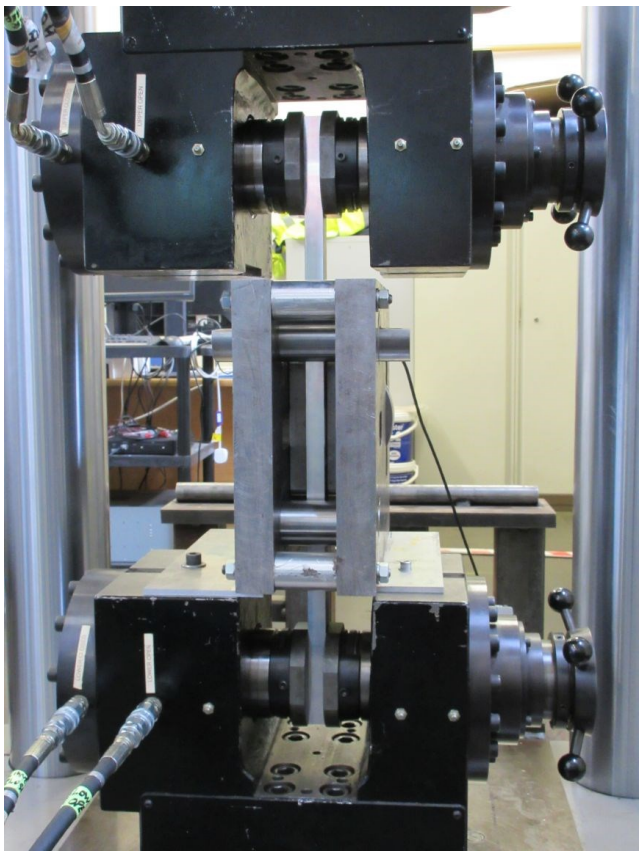

Figure 5.15 Pictures of the fixed-displacement four-point bending fixture mounted in the Dartec test machine in the (a) bending and (b) tension configurations.

5.4.6 Special procedures for fracture tests

Some aluminium and steel specimens containing cracks were loaded in tension (F_t) to fracture, both with and without initial bending (residual load). In all tests, F_t was increased by separating the test machine grips under position control. The aluminium specimens failed by sudden unstable fracture with no observable prior crack extension, and so the fracture event was characterised by the maximum value of applied load, F_t, achieved during the test. The steel specimens failed by stable ductile tearing, and so the fracture behaviour could not be completely characterised by the maximum test load. Therefore, some method was required which would enable measurement of crack extension at different applied loads. One convenient approach used in standard fracture tests is to measure crack mouth opening displacement (CMOD) using a clip gauge, and calculate the elastic compliance from partial unloading at different applied loads. The CMOD compliance can then be converted to crack length using correlations typically developed using elastic finite element analysis. Generating correlations for specimens with cracks on one edge loaded under tension (SENT specimens) is complex because of non-linear rotation and plasticity effects [119-121]. Some specimens also contained initial bending (residual load) imparted by the bending fixture, which adds to the complexity. Some preliminary elastic finite element analysis was carried out by the author using the model described in Section 5.3.2 to investigate the feasibility of calculating crack extension from measurements of CMOD compliance with the specimens containing initial bending. It was found that CMOD compliance was a function of the residual load, F_b, the applied load, F_t, and the crack length. Therefore, it was considered impractical to develop a set of correlations for converting CMOD compliance to crack length for this work.

Instead, a multiple specimen approach was adopted, in which specimens were loaded under tension to different displacements, and the resulting crack extension was measured in each specimen. The procedure for measuring crack length was as follows. First, the specimens were put in a furnace, preheated to 300°C, for one hour. This process, referred to as 'heat tinting' in the ASTM E1820 fracture toughness testing standard [38], marks the crack by oxidation. The specimens were then cooled to cryogenic temperatures by submerging them in a bath of liquid nitrogen, and fractured under three-point bending. The crack extension from fracture testing, now marked by heat-tinting, was accurately measured by observing the fracture surface under a microscope with a computer-controlled sample stage manufactured by Alicona. Accurate measurement of the depth of

the side grooves was made using the same technique. For example, Figure 5.16 shows a picture of one of the fracture surfaces and an accompanying trace. The crack extension, Δa, was measured at the mid-thickness of the specimen. The deepest part of the crack from the fracture test was at the edges by the side grooves. This multiple specimen approach was applied to steel specimens both with residual stress ($F_{b,i} = 0$) and without residual stress ($F_{b,i} \approx F_{b,nc}$).

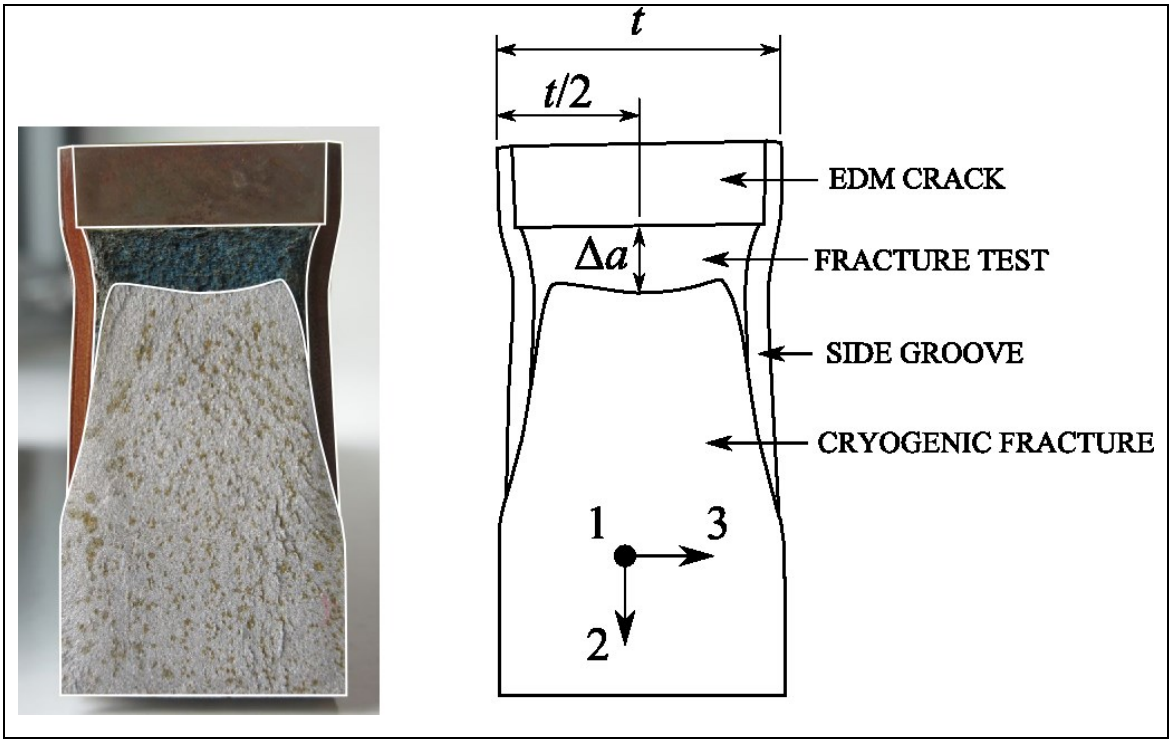

Figure 5.16 Trace (right hand side) of the fracture surface (left hand side) of one of the steel specimens after being broken apart by cryogenic fracture.

5.4.7 Summary of completed tests

A total of twenty-two tests were carried out on steel specimens. Ten of these tests were for measuring the redistribution of residual load with applied load in specimens with various geometries. These tests are listed in Table 5.2. The remaining twelve steel specimens were used for fracture testing, meaning the cracks were measured after testing by following the multiple specimen procedure described in the previous section. These tests are listed in Table 5.3. Six specimens were tested with zero residual stress, and six were tested with approximately the same magnitude of residual stress ($F_{b,i}/F_{b,nc} \approx 1$). The magnitude of residual stress was assumed the same in each set of six specimens, so that

each test provided a single value of crack extension. Some of the steel fracture tests also provided useful measurements of residual stress redistribution.

Seven fracture tests were carried out on cracked aluminium specimens with different magnitudes of residual stress. These tests are listed in Table 5.4. Test A7 was loaded under four-point bending to fracture, representing failure under zero applied load. All tests were carried out at room temperature.

Table 5.2 Residual stress redistribution tests on steel specimens with various geometries.

Test ID	Geometry ID (refer to Figure 5.13)	Normalised residual load, $F_{b,i}/F_{b,gc}$
S1	NN-6	0.26
S2	NN-15	0.53
S3	SV-10	0.18
S4	SV-10	0.37
S5	NN-0	0.25
S6	NN-0	0.45
S7	NN-0	0.54
S8	NN-0	0.96
S9	NN-0	0.34
S10	NN-0	0.98

Table 5.3 Fracture tests on cracked steel specimens.

Test ID	Geometry (refer to Figure 5.13)	Normalised residual load, $F_{b,i}/F_{b,gc}$	Final test machine displacement, d (mm)
S11	SN-6	0	22.1
S12	SN-6	0.59	10.6
S13	SN-6	0.6	5.3
S14	SN-6	0	5.3
S15	SN-6	0	18
S16	SN-6	0	19
S17	SN-6	0	20
S18	SN-6	0.58	21.04
S19	SN-6	0.53	18
S20	SN-6	0.56	19
S21	SN-6	0.56	20
S22	SN-6	0	22

Table 5.4 Fracture tests on cracked aluminium specimens. *Test A7 was loaded under four-point bending to fracture.

Test ID	Geometry (refer to Figure 5.13)	Normalised residual load, $F_{b,i}/F_{b,gc}$
A1	NN-6	0
A2	NN-6	0.40
A3	NN-6	0.18
A4	NN-6	0.28
A5	NN-6	0.09
A6	NN-6	0.46
A7*	NN-6	0.58

5.5 Results

5.5.1 Residual stress redistribution in steel specimens

Figure 5.17 shows the redistribution of residual load with applied load in crack-free steel specimens containing different amounts of residual load. On the y-axis, the current residual load, F_b, is normalised by the initial residual load, $F_{b,i}$. When this ratio equals one, the residual stress is unchanged. On the x-axis, the applied load, F_t, is normalised by the collapse load defined in Equation (5.7). Results are plotted for three different magnitudes of residual load. Each curve is labelled with the value of $F_{b,i}/F_{b,gc}$, where $F_{b,gc}$ is the bending collapse load defined in Equation (5.8). Residual stress redistribution occurs at lower applied loads in specimens with higher initial residual loads. This is because smaller amounts of applied load are required to cause yielding if the magnitude of residual stress is larger. A significant amount of relaxation occurs in all specimens as the applied load reaches the collapse load ($F_t/F_{t,gc} = 1$). A small amount of residual stress is retained above the collapse load by specimens with larger magnitudes of initial residual stress. The residual load in the specimen with $F_{b,i}/F_{b,c} = 0.54$ does not appear to fully relax at high applied load. This is an error caused by drift in the load cell in the bending fixture, which was in-turn caused by the load cell being incorrectly orientated relative to the load pin. The orientation was correct in all other tests.

Figure 5.18 shows the redistribution of residual load with applied load in specimens with different crack lengths, including one without a crack. On the x-axis, applied load, F_t, is normalised by the net section collapse load, $F_{t,nc}$, which is unique to each geometry as defined in Section 5.4.4. The specimens initially contained the same magnitude of residual load ($F_{b,i}/F_{b,gc} = 0.53$). When the applied load reaches the net section collapse load (i.e. $F_t/F_{t,nc} = 1$), the residual load in the crack-free specimen almost completely relaxes whereas the cracked specimens retain significant residual load.

A similar result is observed in Figure 5.19, which shows the redistribution of residual load with applied load measured in four nominally identical specimens during the steel fracture tests listed in Table 5.3. The quantities of applied load and residual load on the x and y-axes have been normalised by the gross section collapse load, which is geometry-independent and is defined in Section 5.4.4. The net section collapse load is also indicated on the x-axis ($F_t = F_{t,nc}$). There is still a significant amount of residual load retained at the

net section collapse load, whereas the residual load almost completely relaxes at the gross section collapse load.

It was demonstrated in Section 5.3.3 that introducing a single edge crack in the specimen induces an asymmetry effect which could cause a significant amount of residual load relaxation even if the specimen is linearly elastic. It was also shown (see Figure 5.5) that machining a V-shaped notch opposite the crack could compensate for this effect. Therefore, two specimens were manufactured and tested with a 10 mm crack and opposite V-notch (geometry SV-10 in Figure 5.13). Figure 5.20 compares the redistribution of residual load with applied load in two specimens: one crack-free, and one with the compensating geometry (crack and V-notch). The specimens contain similar amounts of initial residual load ($F_{b,i}/F_{b,gc} \approx 0.36$). At small applied loads the material is approximately elastic and so the initial gradient of each curve at $F_l/F_{t,nc} \rightarrow 0$ can be compared with the finite element results shown in Figure 5.5. The initial gradient for the compensating geometry was significantly higher than for the crack-free geometry, whereas the finite element results in Figure 5.5 predicted that the gradients would be very similar. This is because the net-section width of the specimen with the crack and V-notch is much smaller than the width of the crack-free specimen (20 vs 40 mm). Therefore, the bending stiffness is smaller and the non-linear bending effect described in Section 5.3.5, which was not accounted for in Figure 5.5, is significant.

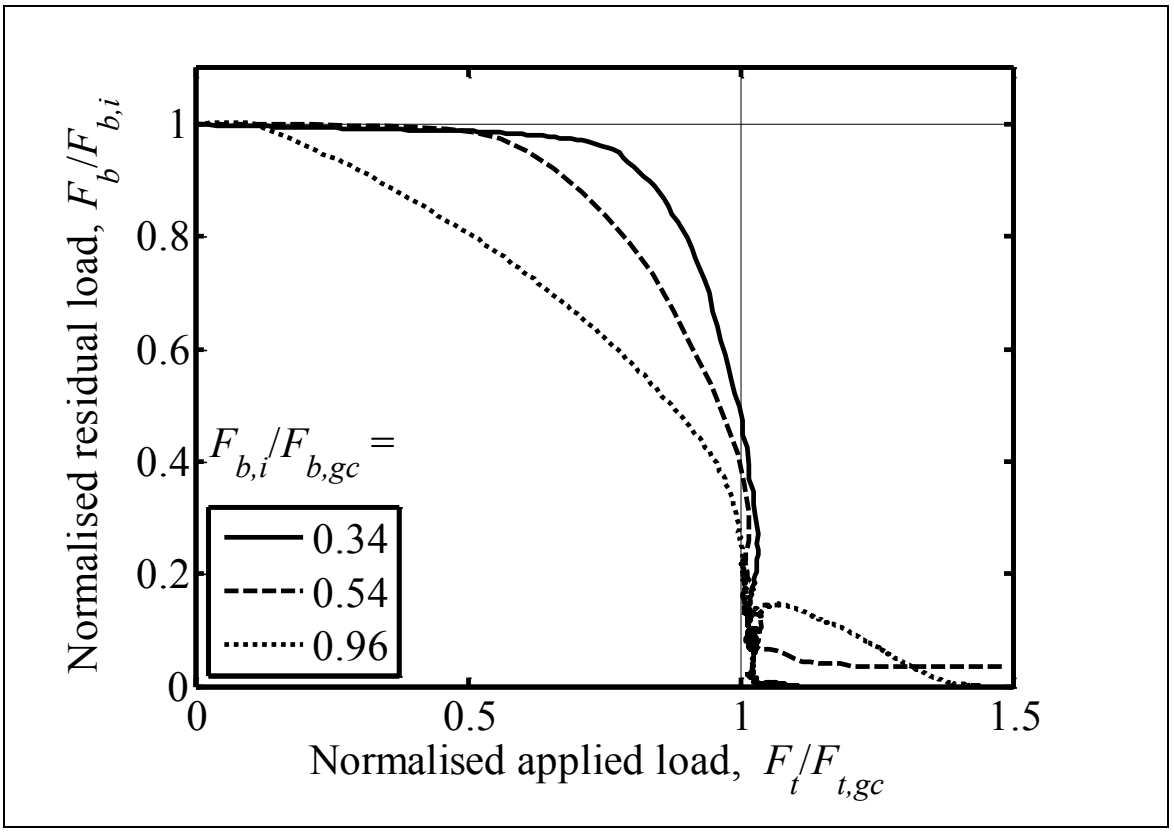

Figure 5.17 Redistribution of residual load with applied load in crack-free steel specimens containing different magnitudes of normalised initial residual stress ($F_{b,i}/F_{b,gc}$ = 0.34, 0.54, and 0.96).

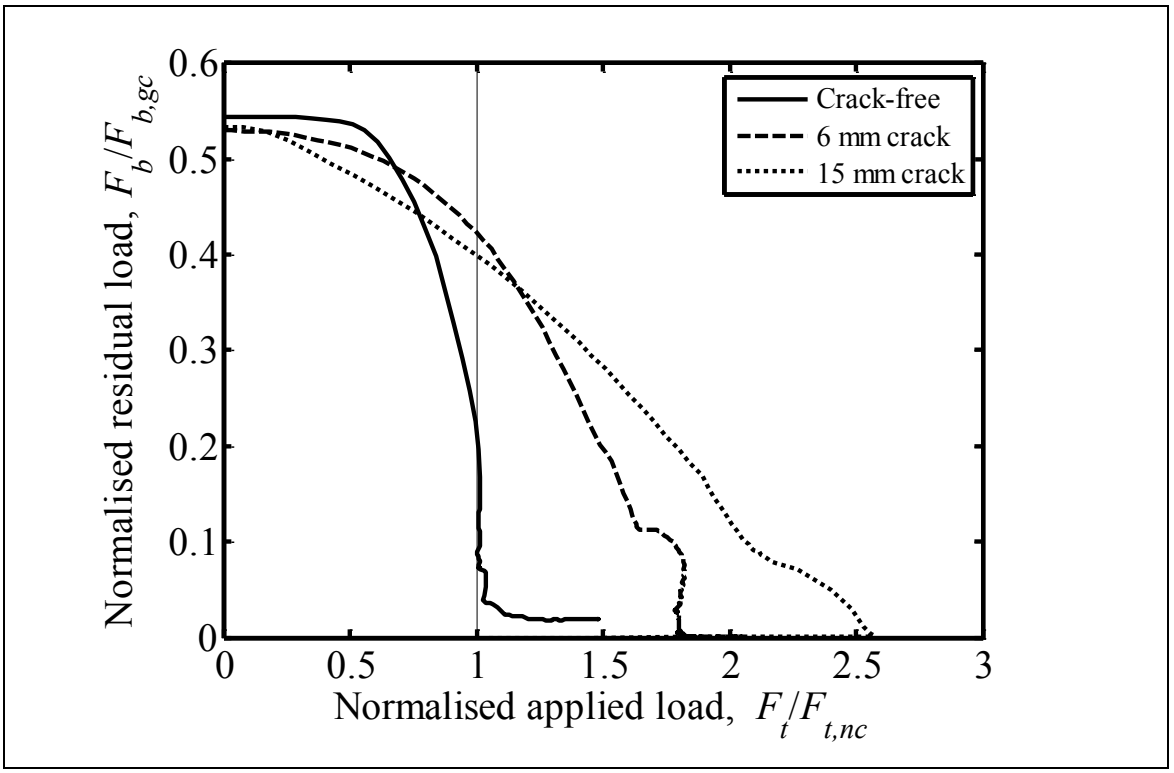

Figure 5.18 Redistribution of residual load with applied load in specimens with the same initial residual load ($F_{b,i}/F_{b,gc} \approx 0.53$) but different crack geometries: crack-free, 6 mm crack, and 15 mm crack (NN-0, SN-6, and NN-15 in Figure 5.13).

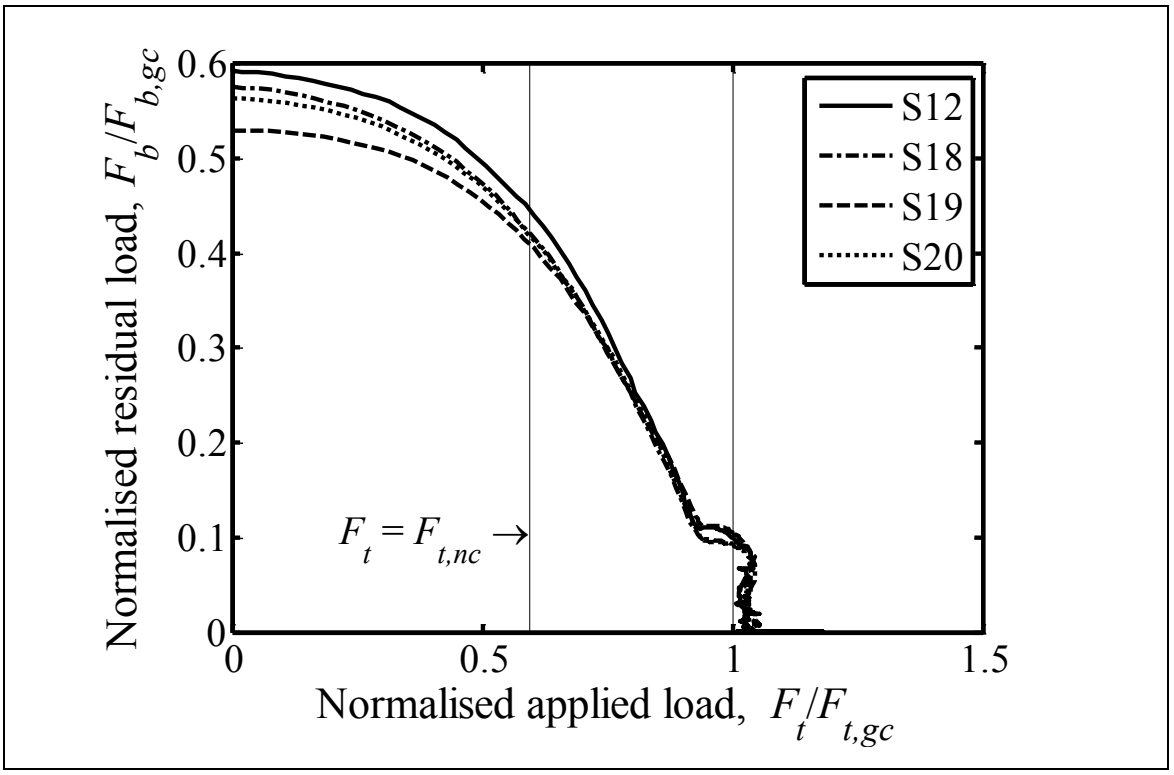

Figure 5.19 Redistribution of residual load with applied load in four of the steel fracture specimens with side grooves and 6 mm cracks (geometry SN-6 in Figure 5.13). Each curve corresponds to a different test number (S12, S18, S19, S20) in Table 5.3.

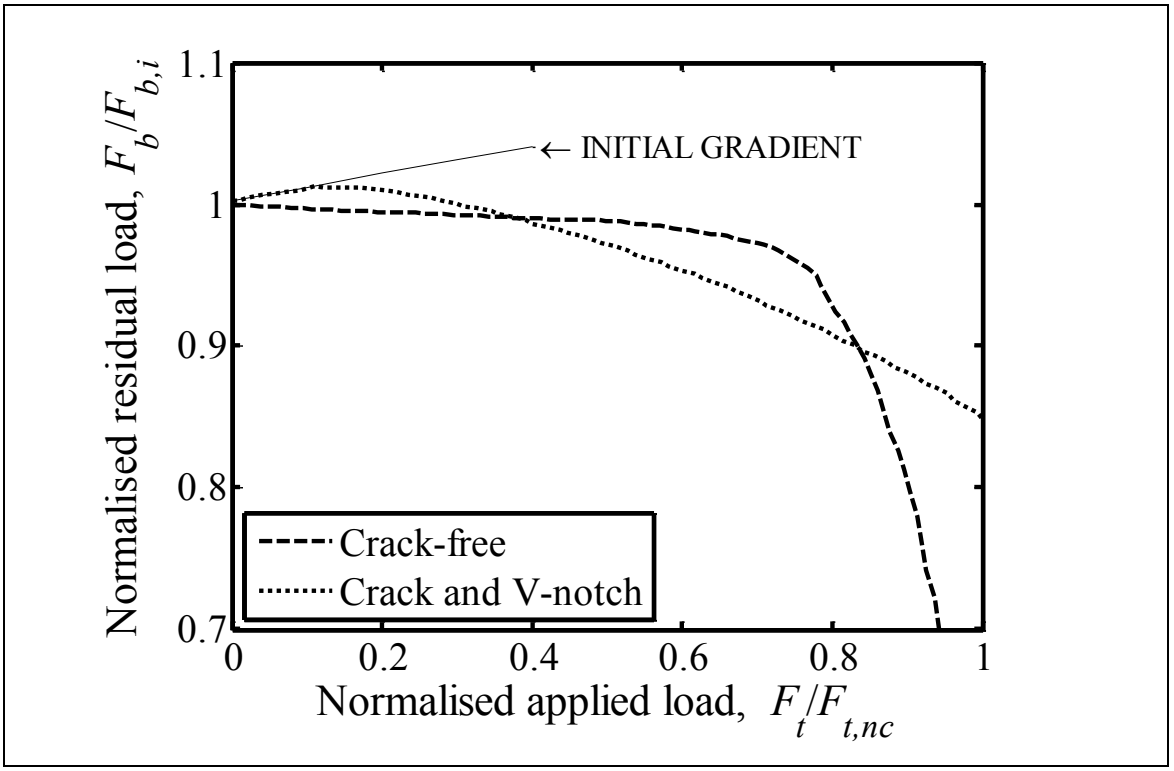

Figure 5.20 Redistribution of residual load at low applied loads in two specimens with similar amounts of initial residual load ($F_{b,i}/F_{b,gc} \approx 0.36$) but different geometries. The results are from tests S4 (crack and V-notch) and S9 (crack-free) in Table 5.2.

5.5.2 Steel fracture tests

This section presents results from the steel fracture tests listed in Table 5.3. The specimens contained 6 mm long cracks and 2 mm deep side grooves (geometry SN-6 in Figure 5.13). Two sets of specimens were tested. One set did not contain any residual stress. The other set contained residual load initially equal to the net section bending collapse load ($F_{b,i} \approx F_{b,nc}$). Each specimen in a set was strained to a different machine displacement and the resulting crack extension was measured by breaking the specimen apart and inspecting the fracture surface. The full procedure is described in Section 5.4.6. Note that the actual initial residual load varied slightly between specimens because it was practically difficult to achieve the target value exactly. This variation can be seen in Figure 5.19 at low applied loads.

Figure 5.21 shows the crack extension, Δa, plotted against the maximum applied load experienced by the specimen, $F_{t,max}$, normalised by the net section collapse load, $F_{t,nc}$. The maximum applied load was different in each test because the specimens were strained by different amounts (see Table 5.3). The applied load is normalised by the net section rather than gross section collapse load to account for the variation of the true depth of the side grooves, equivalent to 3% of the specimen thickness. Results are plotted for specimens with and without residual stress. There is no apparent difference between the two sets of results. The magnitude of current residual load, F_b, was practically zero for all results in Figure 5.21, even in specimens which contained residual load at the start of the test. This is because all of the specimens were strained to beyond their gross section collapse load, $F_{t,gc}$, at which point the residual load completely relaxes as shown in Figure 5.19.

Three specimens were subjected to strains beyond the point of maximum load, $F_{t,max}$, which represents the load-bearing capacity of the specimen. One of these specimens contained residual load, and two did not. The maximum loads obtained from these tests are given in Table 5.5. There was no significant difference in the load-bearing capacity of specimens with and without residual load.

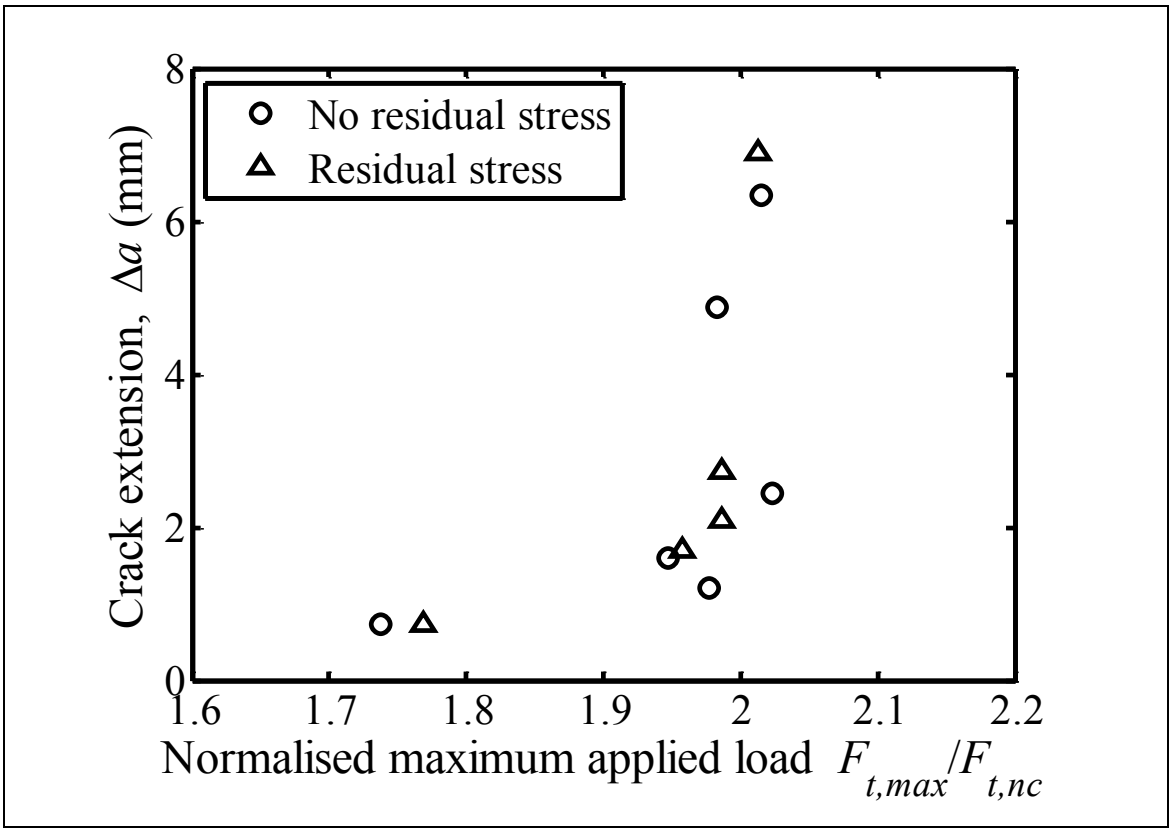

Figure 5.21 Crack extension vs maximum applied load for steel fracture specimens with ($F_{b,i} \approx F_{b,nc}$) and without residual stress.

Table 5.5 Load-bearing capacity of steel specimens with and without residual stress.

Normalised residual load, $F_{b,i}/F_{b,gc}$	Tests	Normalised maximum applied load, $F_{t,max}/F_{t,nc}$
0	S11, S22	1.98, 2.02
0.58	S18	2.01

5.5.3 Aluminium fracture tests

This section presents results from the aluminium fracture tests listed in Table 5.4. The specimens contained 6 mm edge cracks (geometry NN-6 in Figure 5.13). A different magnitude of residual load was imparted on each specimen, and the specimen was then loaded to failure. In all tests, the specimen failed by sudden unstable fracture with no prior

crack extension observed. The final crack length after unstable fracture is plotted against the normalised initial residual load in Figure 5.22. On the *y*-axis, the final crack length, a_f, is normalised by the specimen width, so that when this quantity is one the specimen has broken completely in half. In specimens containing small amounts of residual load, the crack propagated all the way through the specimen, thereby completely breaking it in two. In specimens with higher residual load, the crack arrested before reaching the back face.

Figure 5.23 shows the effect of residual load on the magnitude of applied load required to cause fracture, $F_{t,fail}$. On the *x*-axis, the initial residual load is normalised by the gross section bending collapse load. On the *y*-axis, the fracture load ($F_{t,fail}$) is normalised by the net section collapse load. Fracture loads obtained from the tests are plotted alongside a line of constant combined stress intensity factor, *K*, defined as:

$$K = K_t + K_b \tag{5.16}$$

where K_t is the stress intensity factor calculated from the fracture load, $F_{t,fail}$, and K_b is the stress intensity factor calculated from the initial residual load, $F_{b,i}$. K_t, was calculated using the following result for a pin-loaded specimen [14]:

$$K_t = \sigma_{app} \cdot \sqrt{\pi a} \cdot \sqrt{\frac{2b}{\pi a} tan\left(\frac{\pi a}{2b}\right)} \cdot \frac{0.752 + \frac{2.02a}{b} + 0.37\left[1 - sin\left(\frac{\pi a}{2b}\right)\right]^3}{cos\left(\frac{\pi a}{2b}\right)} \tag{5.17}$$

where *a* is the crack depth (6 mm), *b* is the specimen width, and σ_{app} is the applied stress calculated using Equation (5.3). K_b was calculated using the following result for a beam with a single edge crack under remotely applied bending [14]:

$$K_b = \sigma_b \cdot \sqrt{\pi a} \cdot \sqrt{\frac{2b}{\pi a} tan\left(\frac{\pi a}{2b}\right)} \cdot \frac{0.923 + 0.199\left[1 - sin\left(\frac{\pi a}{2b}\right)\right]^4}{cos\left(\frac{\pi a}{2b}\right)} \tag{5.18}$$

where σ_b is the maximum (outer fibre) bending stress calculated using Equation (5.2). In Figure 5.23, the same set of fracture loads are plotted using two different methods. The first method, marked by a cross (×), plots the fracture load against the initial residual

load, $F_{b,i}$, as shown on the x-axis. The second method, marked by a plus sign (+), plots the fracture load against the residual load at failure, $F_{b,fail}$. The two methods give slightly different results when the fracture load is high because the residual load has partially relaxed with applied load. The first method (×) is reasonably well described by the line of constant total stress intensity factor calculated by elastic superposition. In general, Figure 5.23 shows that specimens with higher residual stresses sustained lower magnitudes of applied load before fracturing. Note that one specimen, A7 in Table 5.4, fractured under zero applied load because the initial bend load was increased until fracture.

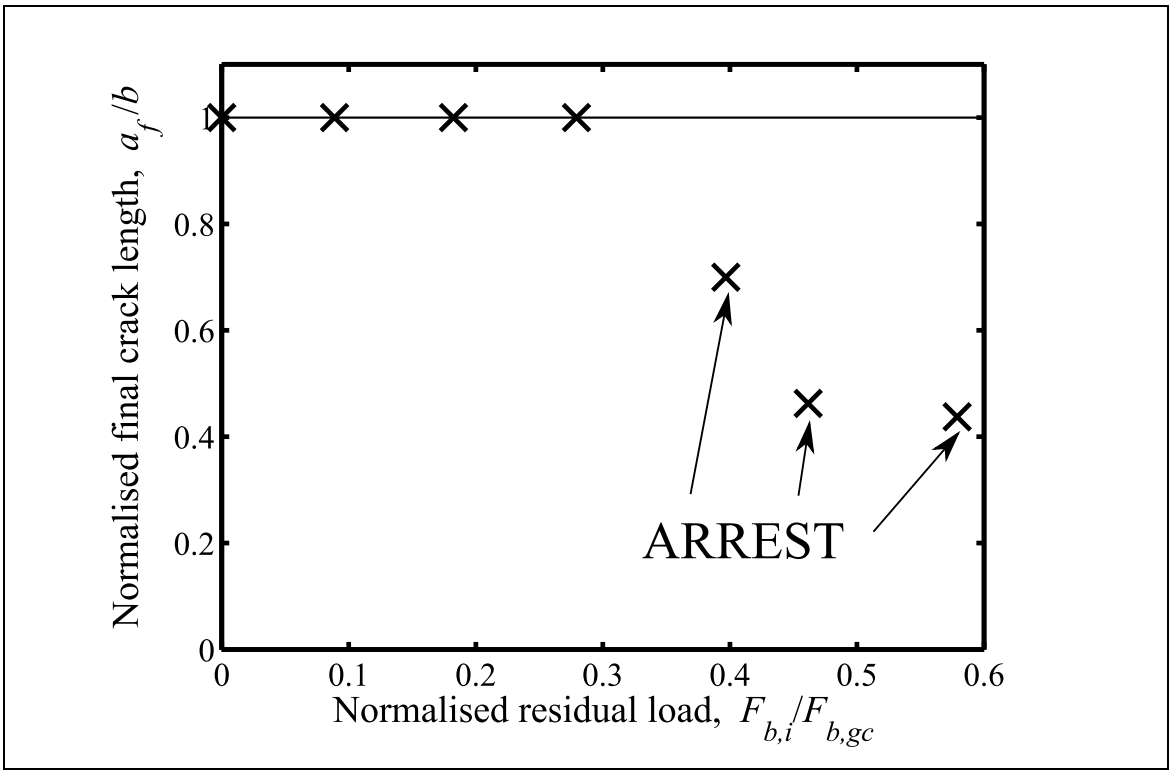

Figure 5.22 Final crack length after sudden unstable fracture in 7075 aluminium alloy specimens with different amounts of initial residual load.

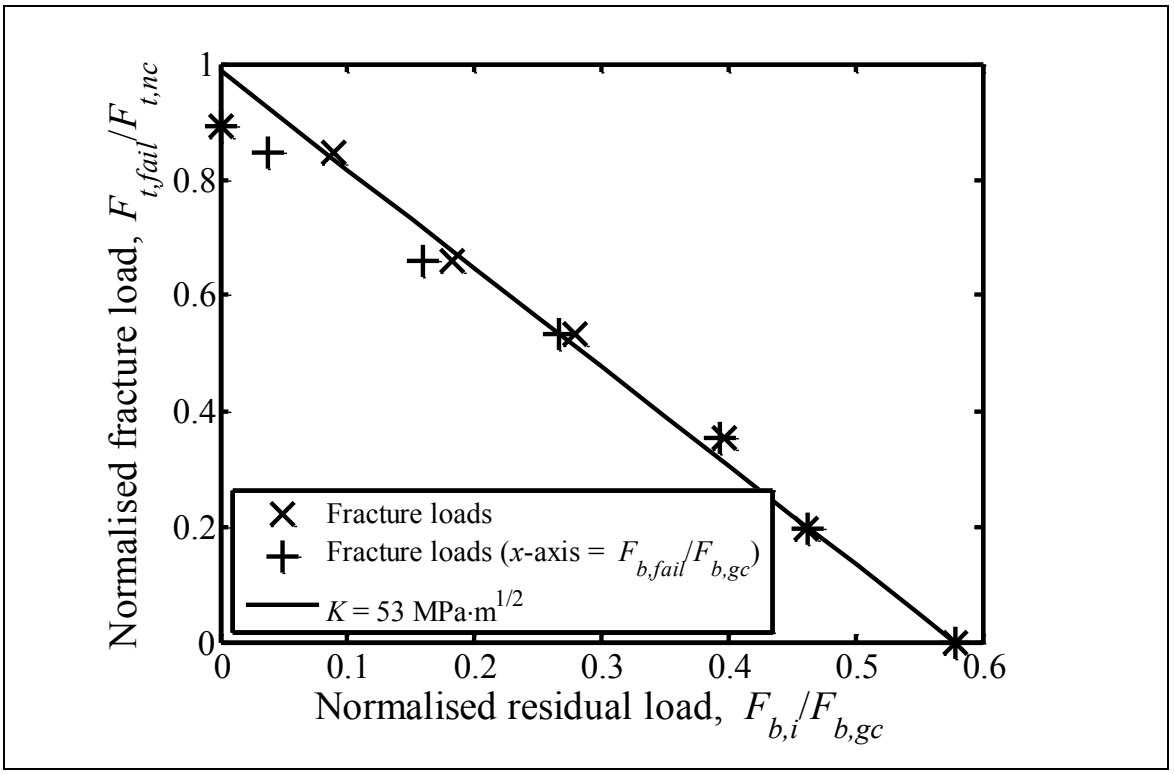

Figure 5.23 Fracture loads in 7075 aluminium alloy specimens with different amounts of initial residual load. The experimental results are marked with a cross (×). The plus sign (+) plots the same results except the final ($F_{b,fail}$) rather than initial ($F_{b,i}$) residual load is plotted on the x-axis. Also shown is a line of constant total stress intensity factor (K = 53 MPa m$^{1/2}$) calculated from the combination of $F_{b,i}$ and $F_{t,fail}$.

5.6 Discussion

5.6.1 Residual stress relaxation in crack-free steel specimens

It was shown in Figure 5.17 that the residual load always relaxes to zero as long as the applied load is large enough (ignoring the result for $F_{b,i}/F_{b,gc} = 0.54$, in which case the residual load does not eventually fall to zero because of an error in the measurement of F_b). This could, in part, be because the cross section of the specimen contracts during yielding and causes the bend load to reduce. This mechanism is similar to the Poisson effect discussed in Section 5.3.3, which causes the cross section to reduce under elastic conditions. The effect could be significant at high applied loads, because strain accumulates faster with respect to applied load after yielding. Finite element analysis was therefore used to estimate the point at which the contraction effect becomes significant. The model was the same as the crack-free model in Section 5.3.3 (linearly elastic), except different values for Young's modulus and Poisson's ratio were used: $E = 193$ GPa, which was calculated in tensile tests reported in Section 5.4.2; and $\nu = 0.5$, to represent constant volume plastic deformation using an elastic material. The model was elastic in order to decouple the contraction effect from residual stress redistribution caused by yielding. The results from the model were then used to calculate a cut-off point, above which strains from the applied load rapidly accumulate and the contraction effect becomes significant.

Figure 5.17 has been re-plotted in Figure 5.24, except now each curve has been cut-off at the point at which it was estimated that the current bend load would fall to half its initial magnitude just from the contraction effect (i.e. ignoring residual stress redistribution caused by yielding). The value of $F_b/F_{b,i}$ at this cut-off point was between 0.09 and 0.14 in all three specimens, and so the majority of residual load redistribution at this point was caused by yielding rather than the Poisson effect. The cut-off point in each specimen occurs when the applied load is approximately equal to the gross-section collapse load, because it is at this point that the whole specimen starts to yield and so plastic strain rapidly accumulates in the direction of applied load.

This work generated a large amount of experimental data on the redistribution of residual stress with applied load, which provides a good opportunity to compare the experimental results with analytic predictions of the interaction of residual and applied stress. One such calculation was derived by Ainsworth [11]. Ainsworth presented an analysis in terms of

reference stresses, which are measures of equivalent stress arising from different sources of load. For example, if the material is assumed elastic-perfectly plastic, then plastic collapse occurs when the reference stress from any source of load reaches or exceeds the yield stress. The different sources of load are primary sources, such as mechanically applied load, and secondary sources, such as thermal or residual stress. The reference stresses corresponding to primary and secondary loads are σ_{ref}^{P} (primary) and σ_{ref}^{S} (secondary). The combined reference stress, σ_{ref}, is a measure of the current total level of stress, including the combined primary stress and the redistributed secondary stress. Ainsworth calculated the combined reference stress as a function of the primary reference stress, the secondary reference stress (before redistribution caused by primary stress), and the yield stress using the following equation [11]:

$$\frac{\sigma_{ref}}{f^2\left(\frac{\sigma_{ref}}{\sigma_y}\right)} = \frac{\sigma_{ref}^{P} + \sigma_{ref}^{R}}{f^2\left(\frac{\sigma_{ref}^{P} + \sigma_{ref}^{R}}{\sigma_y}\right)} + \frac{\sigma_{ref}^{S} + \sigma_{ref}^{R}}{2\sigma_{ref}^{R}} \cdot \left[\frac{\sigma_{ref}^{S}}{f^2\left(\frac{\sigma_{ref}^{S}}{\sigma_y}\right)} - \frac{\sigma_{ref}^{R}}{f^2\left(\frac{\sigma_{ref}^{R}}{\sigma_y}\right)}\right] \tag{5.19}$$

In Equation (5.19), σ_y is the yield stress of the material and σ_{ref}^{R} is a dummy reference stress which is artificially chosen so that σ_{ref} is a minimum. The function, f, is defined as:

$$f(x) = (1 - 0.14x^2)\left(0.3 + 0.7e^{-0.65x^6}\right) \tag{5.20}$$

which is the R6 Revision 3 failure assessment curve, except the variable x is used here in place of the usual parameter, L_r, which describes the proximity to plastic collapse. Equation (5.19) was used to calculate σ_{ref} using the following procedure. First, the equation was normalised by dividing both sides by σ_y. Then σ_{ref}^{R} was iteratively adjusted between zero and one until the right hand side of the equation was a minimum value. Finally, the equation was solved for σ_{ref}/σ_y using the 'vpasolve' function in Matlab 2014a [122]. Alternative calculations of the redistribution of residual stress with applied load have been derived more recently in other work [123-125]. The significance of Equation (5.19) is that it is used by the R6 structural integrity assessment procedure in the derivation of parameters governing the interaction between primary and secondary sources of stress. These parameters are used when assessing the integrity of RPVs under severe loading conditions, such as pressurised thermal shock in which there is primary stress (internal pressure) and high secondary stress (combined thermal and residual

stress). It is therefore important that the analytic principles behind assessment procedures are experimentally validated.

Figure 5.25 (a) compares the redistribution of residual stress calculated using Equation (5.19) with experimental results obtained from a crack-free steel specimen with an initial level of normalised residual load of $F_b/F_{b,gc} = 0.34$. A measure of combined load is plotted on the *y*-axis. The combined reference stress calculated using Equation (5.19) is related to the combined load using:

$$\frac{\sigma_{ref}}{\sigma_y} = \frac{F_t}{F_{t,gc}} + \frac{F_b}{F_{b,gc}} \tag{5.21}$$

The normalised applied load is plotted on the *x*-axis. The relationship between the primary reference stress in Equation (5.19) and applied load is:

$$\frac{\sigma_{ref}^P}{\sigma_y} = \frac{F_t}{F_{t,gc}} \tag{5.22}$$

The equivalent relationship between secondary reference stress and residual load is:

$$\frac{\sigma_{ref}^S}{\sigma_y} = \frac{F_{b,i}}{F_{b,gc}} \tag{5.23}$$

Three curves are plotted in Figure 5.25 (a). One curve is an experimental result from a crack-free specimen with a normalised initial residual load, $F_{b,i}/F_{b,gc}$, of 0.34. The other two curves, labelled 'analytic' in the figure, are results calculated using Equation (5.19) for zero initial residual stress ($\sigma_{ref}^S/\sigma_y = 0$) and for a residual stress equivalent to the experiment ($\sigma_{ref}^S/\sigma_y = 0.34$). Figure 5.25 (b) and (c) show similar comparisons between the analytic and experimental results for two other magnitudes of initial normalised residual load, $F_{b,i}/F_{b,gc} = 0.54$ (b) and $F_{b,i}/F_{b,gc} = 0.96$ (c). A gradient equal to one represents the residual and applied stresses superimposing elastically.

In Figure 5.25 (a-c), at low applied loads ($F_t/F_{t,gc} < 1$) more residual load relaxation was predicted by Equation (5.19) than was experimentally measured. One explanation is that the bend fixture is not truly stiff compared to the specimen, despite best efforts to make it so. This would mean that the bending displacement, δ_b in Figure 5.1, is not truly fixed, thereby introducing elastic follow-up into the system [18, 33]. The residual load would

then not behave perfectly like a secondary stress, which is assumed in the analytic solutions plotted in Figure 5.25. Another explanation is that the non-linear bending effect discussed in Section 5.3 enhances the residual load. It is likely that both explanations contribute to the disparity between the analytic prediction and experimental results at low loads. The initial gradient ($F_t/F_{t,gc} \rightarrow 0$) of the experimental results in Figure 5.25 (a) & (b) is correctly equal to one, because the combined magnitude of the residual and applied stress is below yield and so the two sources of stress superimpose.

In Figure 5.25 (a-c) at high applied loads ($F_t/F_{t,gc} > 1$) less residual load relaxation was predicted than measured. The difference is largest for large amounts of residual load, for example in Figure 5.25 (c). A similar result was demonstrated in previous work by Horne [18], who carried out an experiment in which the relaxation of weld residual stress with applied load was monitored using synchrotron X-ray diffraction. The results were compared with Equation (5.19) and it was found that the measured residual stresses relaxed more than predicted at high applied loads in a similar fashion to Figure 5.25. However, in Figure 5.25 in the regions of high applied loads greater than the collapse load ($F_t/F_{t,gc} > 1$) it is not clear whether the residual load relaxes because of residual stress redistribution by yielding or because of the contraction effect discussed at the beginning of this section. For example, the curves in Figure 5.24 were terminated at the point at which the contraction effect was estimated to be significant, which was around the gross section collapse load. Therefore, beyond $F_t/F_{t,gc} \approx 1$ it is difficult to make firm conclusions about the difference between the analytic and experimental results.

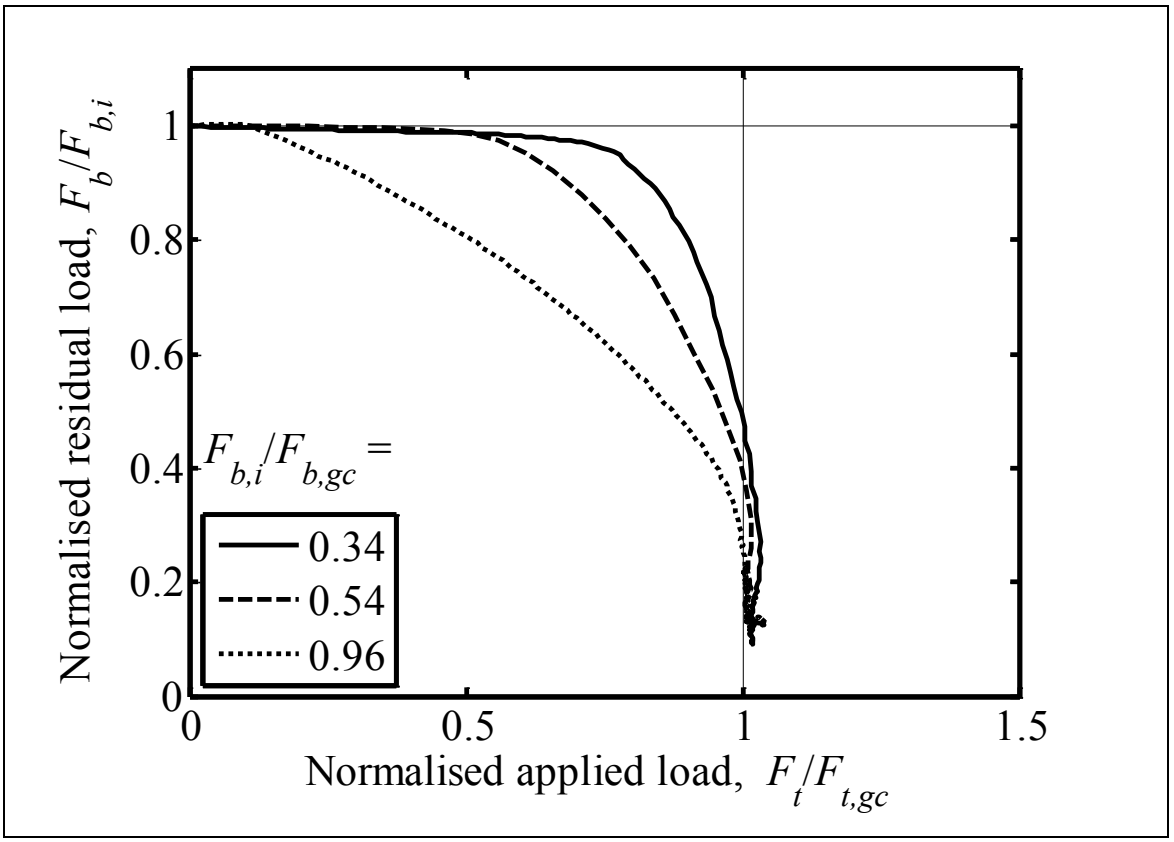

Figure 5.24 Redistribution of residual load with applied load in crack-free steel specimens containing different magnitudes of normalised initial residual stress ($F_{b,i}/F_{b,gc}$ = 0.34, 0.54, and 0.96). This figure has been replotted from Figure 5.17, except the curves have been cut-off at the point at which the Poisson effect becomes large.

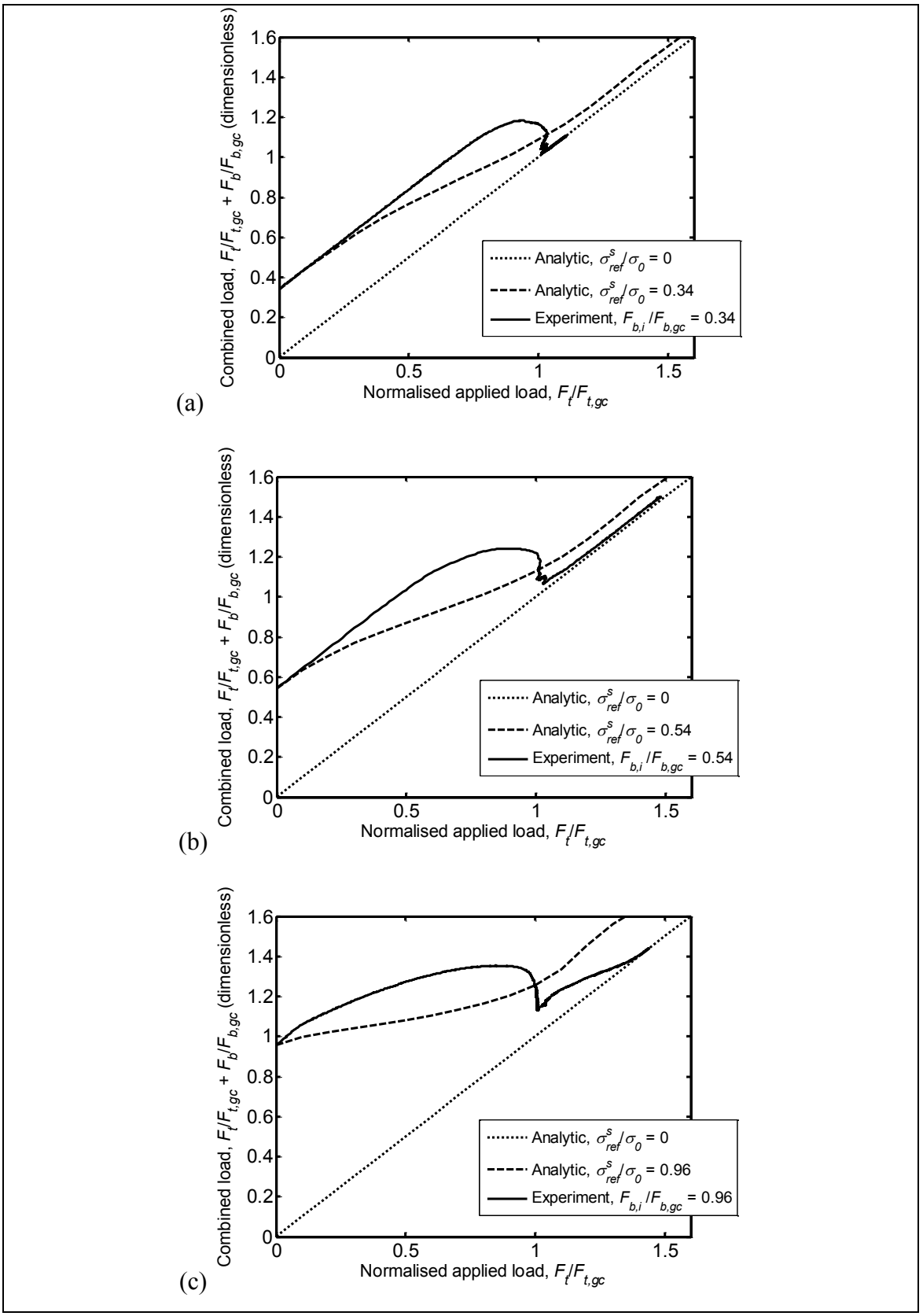

Figure 5.25 A comparison between experimental measurements and analytic predictions of the evolution of combined load (residual and applied) with applied load. Each graph shows results for a different level of normalised residual load, $F_{b,i}/F_{b,gc}$ = 0.34 (a), 0.54 (b), and 0.96 (c). Experimental results are from tests S9 (a), S7 (b), and S8 (c) listed in Table 5.2. Analytic results were calculated using Equation (5.19).

5.6.2 *Residual stress relaxation in cracked specimens*

The relaxation of residual load with applied load for specimens with similar amounts of initial residual load but different crack geometries was shown in Figure 5.18. In the crack-free specimen, the residual load relaxes considerably as the applied load approaches the net section collapse load, whereas in the cracked specimens significant relaxation only occurred well above the net section collapse load. In Figure 5.19, the residual load in the steel fracture specimens was plotted against the applied load normalised by the gross rather than net section collapse load. The shape of the graph was similar to the crack-free results in Figure 5.17, which appears to suggest residual load relaxation is best described by proximity to the gross section collapse load, even in specimens containing cracks. However, this may be a premature conclusion for various reasons now discussed.

First, the solution chosen for the net section collapse load, $F_{t,nc}$, may not have been appropriate. The collapse load for a specimen with a single edge crack under tension depends on the yield criterion assumed (Tresca or von Mises) and whether or not the ends of the specimen are free to rotate. If the ends are free to rotate (pin-loaded) then the tension load induces an additional bending moment because of the asymmetry introduced by the crack. If the ends are not free to rotate (fixed grip) then there is no such bending moment and the collapse load is larger. Figure 5.26 plots the net section collapse load calculated using different methods against the ratio of crack length to specimen width. The different calculation methods are identified in the figure legend. Method A has been used in all previous calculations in this chapter, which uses the Tresca yield criterion and assumes pin-loaded ends. The pin-loading condition was used because the jaws of the Dartec test machine, illustrated in Figure 5.14, are free to rotate when they are open. When the jaws are closed under hydraulic pressure, there may be considerable friction, thereby invalidating the pin-loaded assumption. Choosing Method C (fixed-grip) over Method A (pin-loaded) increases the calculated collapse load by 19% for the 6 mm crack and 77% for the 15 mm crack. This is not sufficient to account for all of the difference between the crack-free and cracked results in Figure 5.18. Besides, jaw rotation was observed in some of the tests and so the true end condition is probably somewhere between fixed grip and pin loaded. Choosing Method B (von Mises yield criterion) over Method A (Tresca) increases the calculated collapse load by only 15% for 6 mm and 15 mm cracks. In summary, the choice of collapse load could account for some, but not all, of the difference between the results for specimens with and without cracks.

The difference in behaviour between the cracked and crack-free specimens in Figure 5.18 could also be partly explained by the non-linear bending effect discussed in Section 5.3. This effect, which acts to increase the residual load, is larger in specimens containing longer cracks because the bending stiffness of the specimen decreases and so the neutral axis offset (d_{os} in Figure 5.9) increases.

In order to investigate the result in Figure 5.18 further, the finite element model described in Section 5.3.2 was run using the material properties measured by tensile testing. The stress-strain curve for the P355 steel, shown in Figure 5.11, was converted to true stress and strain using the method described in Section 3.5. The true stress-strain curve was then discretised and input into Abaqus as an incremental plasticity material model with isotropic hardening. Figure 5.27 shows the results of three different models: one model with a crack-free specimen and with NLGEOM switched on (i.e. including non-linear bending effects); one model with a 10 mm crack and NLGEOM switched on; and one model with a 10 mm crack and NLGEOM switched off (i.e. ignoring non-linear bending effects). First, disregarding the final curve (10 mm crack, NLGEOM switched off), the results are very similar to the experimental results shown in Figure 5.18. When the applied load is equal to the net section collapse load, the residual load is almost zero in the crack-free specimen but is still significant in the cracked specimen. The final curve (10 mm crack, NLGEOM switched off) demonstrates that the non-linear bending effect accounts for some, but not all of this difference. The specimen still retains 35% of its initial residual load even when the non-linear bending effect is ignored.

Therefore, the experimental results in Figure 5.18 and the finite element results in Figure 5.27 show that the redistribution of residual load with applied load can depend significantly on the length of the crack. If the ratio of applied load to the net section collapse load is used to characterise the redistribution of residual stress, as is the case in the R6 assessment procedure and Equation (5.19), then the results suggest that account must also be taken of the length of the crack. Alternatively, it may be more appropriate to use the gross section rather than net section collapse load to characterise the residual stress redistribution. This point is illustrated in Figure 5.28, which plots the same results shown in Figure 5.18 except the applied load on the x-axis is now normalised by the gross section rather than net section collapse load, and the residual load on the y-axis is now normalised by the initial residual load rather than the gross section collapse load.

Regardless of geometry, the residual load in all of the specimens relaxes to approximately zero when the applied load reaches the gross section collapse load.

The collapse loads calculated in this work are nominal collapse loads which assume that the material is elastic perfectly plastic with a yield strength equal to the 0.2% proof strength. The true collapse loads (i.e. the maximum load which can be sustained by the specimen) are higher because of strain hardening. For example, it was demonstrated in Figure 5.18 that a steel specimen containing a 15 mm crack was able to sustain applied load equal to 2.5 times the nominal net section collapse load. If the material was elastic perfectly plastic, then the specimen would not be able to exceed the net section collapse load. One of the findings of this work (see Figure 5.18) is that if two specimens with the same initial level of residual stress, one crack-free and one with a crack, are loaded to the same amount of applied load relative to their nominal net section collapse load, then the residual stress remaining after redistribution could be much larger in the specimen with a crack than the crack-free specimen. If the material was elastic perfectly plastic, then the residual stress must relax to zero at the net section collapse load, regardless of whether a crack is present. Therefore, the difference in residual stress redistribution in specimens with and without cracks must be affected by strain hardening.

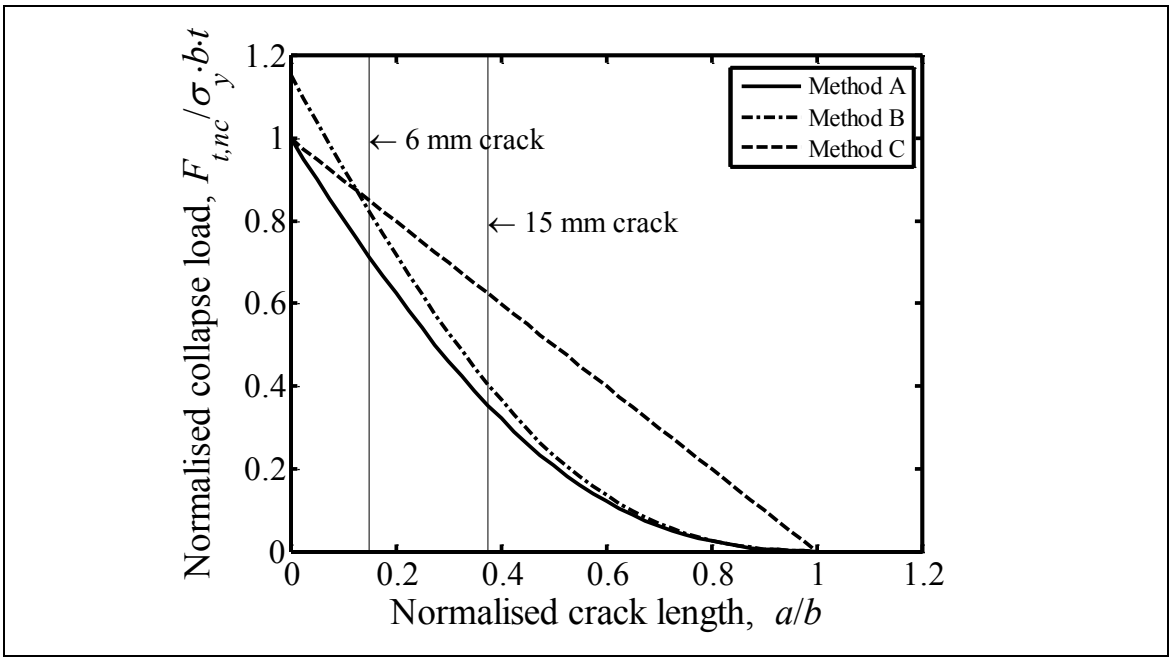

Figure 5.26 Net section collapse loads calculated using different assumptions: Method A (pin-loaded, plane stress, Tresca yield criterion), Method B (pin-loaded, plane stress, von Mises yield criterion), and Method C (fixed-grip, plane stress, Tresca yield criterion).

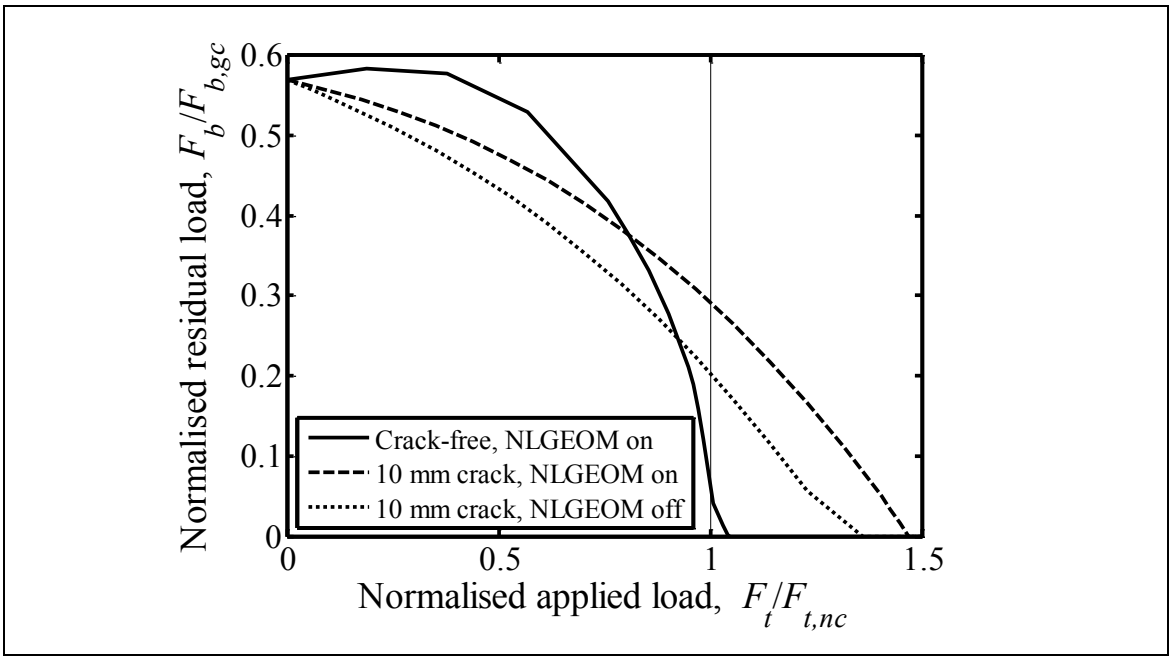

Figure 5.27 Residual load redistribution with applied load in P355 steel, calculated using FEA for various geometries with NLGEOM switched on and off (large and small displacement formulations).

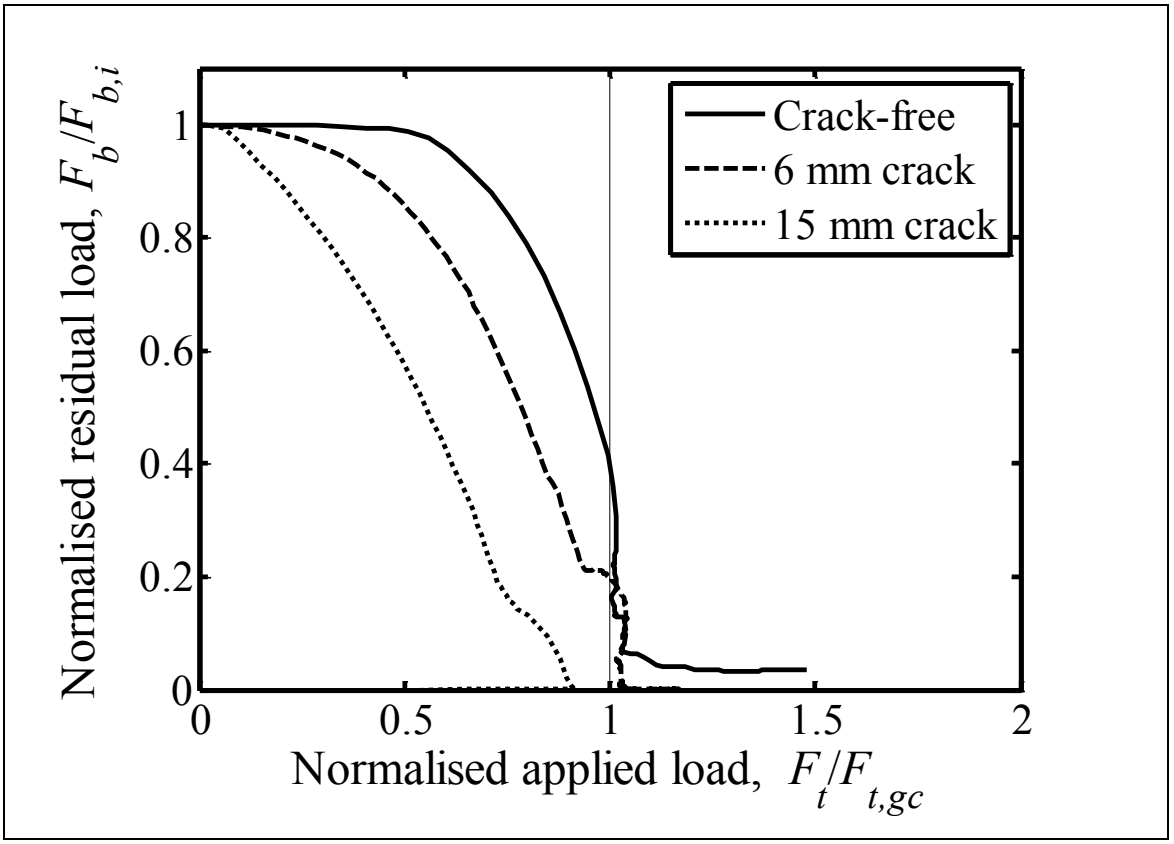

Figure 5.28 Residual load redistribution with applied load in specimens with similar amounts of initial residual load but different crack geometries (including crack-free). The results are the same as in Figure 5.18 except F_t has been normalised by the gross rather than net section collapse load ($F_{t,gc}$ instead of $F_{t,nc}$), and F_b has been normalised by the initial bend load ($F_{b,i}$) rather than the gross section collapse load.

5.6.3 The compensating V-notch geometry

It was demonstrated in Section 5.3.3 that introducing a single edge crack in the specimen induces an asymmetry effect which could cause a significant amount of residual load relaxation even in a linearly elastic specimen. It was also shown (see Figure 5.5) that machining a V-shaped notch opposite the crack could compensate for this effect. Only two specimens were manufactured and tested with a 10 mm crack and opposite V-notch (geometry SV-10 in Figure 5.13), whereas the majority of specimens containing cracks were machined without the compensating V-notch. This was done for two reasons. First, it was difficult to accurately align all of the different features in the centre of the specimens during manufacture. As shown in Figure 5.13, the SV-10 geometry contained a V-notch, side grooves, and a crack. All three features were machined using wire EDM, and the specimen needed to be re-oriented in the machine for each individual feature. The second reason is that the V-notch reduced the net-section area by twice as much as a specimen containing only a crack and no V-notch, which reduced the bending stiffness and therefore increased the non-linear geometry effect discussed in Section 5.3.5. It was shown in Figure 5.20 that this non-linear geometry effect was significant compared to a crack-free specimen. Therefore, whilst the compensating V-notch geometry in theory offered a promising method of reducing one of the interaction effects discussed in Section 5.3, in practice it increased one of the other interaction effects and proved difficult to manufacture.

5.6.4 Fracture tests

There was no measured effect of residual stress on the results of the fracture tests on steel specimens, either in terms of maximum load-bearing capacity (Table 5.5) or load vs crack extension (Figure 5.21). All values of crack extension shown in Figure 5.21 were measured in specimens which had been subjected to applied loads greater than the gross section collapse load. It was shown in Figure 5.19 that the residual load almost completely relaxed at the gross section collapse load, and so the maximum residual load retained for any of the results plotted in Figure 5.21 was less than 0.5% of its original value, $F_{b,i}$. As discussed in Section 5.6.1, it is unclear whether the relaxation of residual load at applied loads greater than the gross section collapse load is caused primarily by residual stress redistribution or by the Poisson effect. However, the results are consistent with previous experimental studies which found that residual stress had a small or negligible influence

on fracture at large levels of applied load relative to the collapse load [26, 28, 32]. In comparison, residual stress had a significant effect on the fracture load in the aluminium fracture specimens, as shown in Figure 5.23, and the fracture load was reasonably well predicted by elastic superposition of the stress intensity factors calculated separately from the initial residual stress and from the applied load at failure.

5.6.5 Residual stress classification

In order to aid the development of structural integrity assessment methods, the residual and applied stresses in this work can also be categorised using terminology encountered in structural integrity assessments. The residual stresses arising from fixed-displacement bending are consistent with the R6 [20] definition of secondary stress, because they do not affect the plastic collapse load. This was demonstrated experimentally. For example, the level of initial bend load, $F_{b,i}$, did not affect the load-bearing capacity in the steel fracture specimens (Table 5.5), which failed well above their nominal gross and net section collapse loads. In these tests, there was zero residual bend load at the maximum applied load, since it was demonstrated in Figure 5.19 that the bend load completely relaxes above the nominal gross section collapse load.

Structural integrity assessment procedures tend to also classify the length scale (or range) over which the residual stresses equilibriate. In Section II.7.4.1 of R6, short-range residual stresses are defined as those which self-equilibriate through the thickness. In terms of forces, the fixed-displacement bending stresses shown in Figure 5.2 equilibriate through the thickness, i.e.:

$$\int_0^b \sigma_{RS}(x_2) \cdot t \cdot dx_2 = 0 \tag{5.24}$$

where: t is the specimen thickness, b is the specimen width, σ_{RS} is the residual stress, and x_2 is defined in Figure 5.2. However, moment equilibrium is not satisfied in the specimen alone, i.e.:

$$\int_0^b \sigma_{RS}(x_2) \cdot t \cdot \left(x_2 - \frac{b}{2}\right) \cdot dx_2 \neq 0 \tag{5.25}$$

However, moment equilibrium is satisfied by the whole structure because the bend fixture imparts a balancing bending moment on the specimen. Therefore, the residual stress is not short-range, but must be either medium-range or long-range.

5.7 Chapter summary

A new technique was proposed as an improved method for studying the effect of residual stress on fracture and the redistribution of residual stress with applied load. Residual stress is represented by imparting fixed-displacement four-point bending on a rectangular beam specimen, and applied load is represented by simultaneous tension loading. Preliminary finite element analysis of the concept in Section 5.3 identified some interaction effects which are unique to the new technique and may not necessarily represent the general behaviour of materials under combined residual and applied stress. However, it was shown that the fixed-displacement bending concept is broadly representative of residual stress.

A novel four-point bending fixture was designed and manufactured to enable specimens to be tested under combined tension and fixed-displacement bending. The fixture was used to investigate the role of residual stress on failure in specimens made from either high-toughness P355 pressure vessel steel or high-strength 7075 T7351 aluminium alloy. Some of the specimens contained cracks and were loaded to fracture. Nominal collapse loads were calculated from the 0.2% proof stress measured by tensile testing. A distinction was made between the net section collapse load, which accounts for the presence of the crack, and the gross section collapse load, which assumes the specimen is crack-free. The residual load in steel specimens almost completely relaxed at magnitudes of applied load equal to the gross section collapse load. Steel specimens containing cracks retained significant residual load at applied loads equal to the net section collapse load. Therefore, the net section collapse load does not accurately characterise the level of applied load at which significant residual stress relaxation occurs equally well for different crack lengths. The amount of residual stress relaxation which occurs in specimens with cracks may be different in materials which experience different amounts of strain hardening.

The redistribution of residual load measured in crack-free steel specimens was compared with an important analytic calculation from which parameters governing the interaction between primary and secondary stresses are derived for use in structural integrity assessment procedures. It was found that combined residual and applied loads were higher than predicted at applied loads smaller than the collapse load. This was attributed

to a combination of interaction effects and the fact that the bending fixture may not have been truly fixed-displacement.

In specimens which were loaded to fracture, no effect of residual stress on fracture was measured in the steel specimens, whereas a significant effect was measured in the aluminium specimens. The aluminium specimens failed by sudden unstable crack propagation. In specimens with low residual loads, the crack propagated all the way through the width of the specimen, thereby breaking it in two. In specimens with high residual loads, the crack arrested before traversing the entire width.

6 Conclusions

6.1 Summary

This thesis presented an investigation into the residual stress in clad nuclear pressure vessel material and the interaction of residual stress with thermal and mechanical loads. The investigation comprised three broadly experimental programmes, which are summarised in the following paragraphs.

The first experimental programme, presented in Chapter 3, characterised the residual stresses in nickel-clad nuclear pressure vessel steel, and measured the redistribution of residual stress after subjecting the material to thermal shock. First, a finite element simulation was carried out to investigate the accuracy of the deep hole drilling method when measuring high stress gradients, which were expected at the interface between the parent and cladding. It was found that the deep hole drilling method was inaccurate near a step change in stress, but that the accuracy could be improved by reducing the size of the reference hole and trepan. A compendium of mechanical strain relaxation methods was used to measure the residual stresses in two plates of SA508 Grade 4N nuclear pressure vessel steel, clad with Alloy 82 nickel-base alloy. One plate was as-welded, the other post-weld heat-treated. The residual stresses were mostly tensile in the cladding in both the as-welded and post-weld heat-treated material, except within 0.5 mm of the surface of the cladding where the stress was compressive. Post-weld heat-treatment caused significant residual stress relaxation in the parent, but only moderate residual stress redistribution in the cladding. It was demonstrated with a finite element model that the relative thickness of the cladding and parent materials significantly affects the magnitude of cladding residual stress. Hence, the magnitude of residual stress would be greater in a full-thickness RPV than in smaller mock-ups such as those measured in this work. The post-weld heat-treated plate was subjected to thermal shock by heating it up and spraying the clad surface with cold water, and the residual stress was measured again

afterwards. The residual stresses redistributed to a depth of at least 10 mm from the surface of the cladding. This demonstrates that the thermal and residual stresses interacted in an in-elastic manner, and that combining them elastically, as suggested in the R6 structural integrity assessment procedure, is therefore conservative. Whereas previous work has measured the redistribution of residual stress with applied mechanical load, this experiment demonstrated the redistribution of residual stress just by thermal load. The experiment also provided valuable data on the residual stress in nickel-clad pressure vessel material on which there are currently only a small number of measurements reported in the literature.

The second experimental programme, presented in Chapter 4, measured the combined thermal and residual stresses in-situ during thermal shock. This was achieved by developing a novel experimental technique, in which thin slices of clad pressure vessel material were subjected to thermal shock whilst simultaneously enabling time-resolved measurements of stress at high temporal resolution using synchrotron X-ray diffraction. A significant amount of thermal shock analysis has been carried out in previous work, whereas in this work the stresses during thermal shock were measured experimentally for the first time. Thin specimens were extracted from the post-weld heat-treated clad plate used in Chapter 3, and were subjected to thermal shock by a bespoke self-contained thermal shock rig on Beamline I12 at Diamond Light Source, the UK's national synchrotron facility. Using this technique, the time-resolved stresses were measured during thermal shock at a single point beneath the cladding in crack-free specimens, and at the crack tip in specimens with through-cladding surface cracks. In the cracked specimens, the near-tip stresses rapidly became high-magnitude and tensile during thermal shock, reaching a peak of up to 966 MPa within a second of the start of cooling. The maximum stress intensity factor calculated from measurements of thermal and residual stresses occurred during, rather than before or after thermal shock. A finite element model of the experiment was made as a benchmark thermal shock analysis method which could be validated using the experimental results. In specimens containing surface cracks, the experimentally measured near-tip stresses showed mediocre agreement with those calculated by a finite element model. The experiment was highly complex and introduced some sources of error which could account for some of the difference. Agreement between the experiment and the model was better in the crack-free specimen. As well as measurements of the transient stress during thermal shock, maps of

stress were generated by measuring at multiple positions in the parent material under steady-state conditions before and after thermal shock. In the cracked specimens, the near-tip stresses changed from high-magnitude tensile before thermal shock to high-magnitude compressive after thermal shock. In the crack-free specimen, the residual stress beneath the cladding before thermal shock varied with position relative to the bead of the weld-overlay by up to 100 MPa. The component of stress normal to the cladding surface (σ_{22}) was measured in the parent up to 10 mm beneath the cladding and it was found to be relatively small with a maximum magnitude of 40 MPa.

The third experimental programme, presented in Chapter 5, investigated the interaction of residual stress with applied load and the effect of residual stress on fracture in high-toughness steel and high-strength aluminium. This was achieved by developing a novel method for imparting residual stress on test specimens. The method represents residual stress in a rectangular beam specimen by subjecting it to fixed-displacement four-point bending. The specimen can then be loaded simultaneously under tension, representing applied load. This new technique was developed to address some of the limitations suffered by existing methods for imparting residual stress on test specimens. Key advantages include the ability to easily tune the magnitude of residual stress, and the ability to monitor the redistribution of residual stress under simultaneous applied load in-situ using a load cell. At the beginning of Chapter 5, a finite element study was presented which demonstrated that the fixed-displacement bending is broadly representative of residual stress, whilst also identifying some interaction effects which are unique to the technique and may not necessarily represent the general behaviour of materials under combined residual and applied stress. The concept was made reality by manufacturing a fixed-displacement four-point bending fixture, and carrying out tests on steel and aluminium specimens under combined residual and applied load. Some of the specimens contained cracks and were loaded to fracture. Nominal collapse loads were calculated from the 0.2% proof stress measured by tensile testing. A distinction was made between the net section collapse load, which accounts for the presence of the crack, and the gross section collapse load, which assumes the specimen is crack-free. The residual load in steel specimens almost completely relaxed when the applied load equalled the gross section collapse load, whereas at the net section collapse load the cracked specimens retained significant residual load. The redistribution of residual load measured in crack-free steel specimens was compared with an important analytic calculation (Section 5.6.1) from

which parameters governing the interaction between primary and secondary stresses are derived for use in structural integrity assessment procedures. It was found that combined residual and applied loads were higher than predicted at applied loads smaller than the collapse load. This was attributed to a combination of interaction effects and the fact that the bending fixture may not have been truly fixed-displacement. In specimens which were loaded to fracture, no effect of residual stress on fracture was measured in the steel specimens, which had a high ratio of fracture toughness to yield strength, whereas a significant effect was measured in the aluminium specimens, which had a lower ratio of toughness to yield strength. The results are consistent with previous experiments reported in the literature which show that the degree to which residual stress influences the fracture load depends on the amount of yielding which occurs before failure.

6.2 Key conclusions

In summary, the key conclusions of this thesis are as follows:

The deep hole drilling method for measuring residual stress can be inaccurate when measuring high out-of-plane stress gradients (i.e. when the in-plane stresses vary abruptly along the axis of the reference hole). The error is smaller for smaller reference hole and trepan diameters. Therefore, when performing a DHD measurement on components which are expected to contain high stress gradients, such as the clad plates studied in this work, the smallest practical DHD size should be used.

The cladding residual stresses and thermal stresses interact inelastically during thermal shock. Therefore, combining the two sources of stress elastically, as suggested in the R6 structural integrity assessment procedure, is conservative.

It has been demonstrated that it is possible to measure the transient stress in clad specimens during thermal shock using in-situ time-resolved synchrotron X-ray diffraction.

Measurements of thermal and residual stresses in a 42 mm thick clad plate were used to calculate stress intensity factors. It was found that the maximum stress intensity factor for 7.4 mm and 10 mm surface cracks occurred during thermal shock, rather than before or after.

A new method has been developed for testing specimens under combined residual and applied load. Residual stress is represented by imparting fixed-displacement four-point bending on a rectangular beam specimen, enabling simultaneous applied load by tension. The advantages of the method are that it is easy to adjust the magnitude of residual stress and it is easy to monitor redistribution with applied load using a load cell.

The initial level of residual stress did not affect the failure load in fracture specimens made out of P355 pressure vessel steel, whereas residual stress significantly affected the failure load in fracture specimens made out of 7075 T7351 aluminium alloy.

The experimental results suggest that comparing the applied load with the net section collapse load (calculated from the 0.2% proof stress) does not accurately characterise the amount of residual stress redistribution equally well for specimens containing different crack lengths.

6.3 Recommended future work

The following could be investigated in future to extend the work described in this thesis and provide further support for the conclusions:

1. In the X-ray diffraction measurements of stress during thermal shock, an error was induced by the temperature of the measurement point being derived from the known temperature at a remote location. It was suggested that this error could be significant in the specimens containing cracks, because water was drawn up the crack faces and may have provided extra cooling. An attempt could be made to quantify the error by carrying out some more tests using the same apparatus to measure the temperature at the crack tip (without carrying out X-ray diffraction). This would improve confidence in the experimental validation of the benchmark finite element analysis.

2. Whereas in this work in-situ synchrotron X-ray diffraction was used to measure the stresses during thermal shock at a single point, the same technique could be used to measure the through-thickness stresses during thermal shock at multiple positions. This could be achieved by measuring a different position in each specimen during thermal shock (i.e. seven specimens could be used to measure the stresses at seven positions). If the specimens were all crack-free, then it would be simple to compare the results with a benchmark finite element analysis. The crack-free specimens would also not suffer to the same degree as this work the error caused by inaccurate knowledge of the temperature of the measurement point at the crack tip.

3. By representing residual stress using fixed-displacement four-point bending, it was shown that the net section collapse load (calculated from the 0.2% proof stress) does not accurately characterise the level of applied load at which significant residual stress relaxation occurs equally well for different crack lengths. It was proposed that this result was affected by strain hardening. Therefore, the effect of strain hardening on the redistribution of residual stress with applied load could be investigated further experimentally and numerically.

Numerically, finite element modelling could be used to calculate residual stress redistribution with applied load in specimens with different crack lengths and using materials with different strain hardening parameters. Experimentally, more tests could be carried out using the fixed-displacement bending fixture to represent residual stress in specimens containing cracks and made out of materials with different amounts of strain hardening. In this work, redistribution tests were only carried out on a single material P355 steel, which has significant capacity for strain hardening. Additional tests could be carried out on a material which experiences only limited strain hardening and behaves more like an elastic perfectly plastic material, such as 1050A aluminium alloy (for example, used in ref. [126]).

4. Crack arrest was observed in some aluminium fracture specimens with high initial residual stresses. Therefore, the fixed-displacement four-point bending technique could be used for an in-depth experimental study of the stability of cracks in residual stress fields.

References

[1] "Nuclear power reactors in the world," IAEA-RDS-2/38, International Atomic Energy Agency, Vienna, 2018.

[2] "ASTM A508/A508M-14 Standard Specification for Quenched and Tempered Vacuum-Treated Carbon and Alloy Steel Forgings for Pressure Vessels," ASTM International, West Conshohocken, PA, 2014.

[3] W. Marshall, "An assessment of the integrity of PWR pressure vessels: summary report," Second Report by a Study Group under the Charimanship of Dr. W. Marshall, United Kingdom Atomic Energy Authority, London, 1982.

[4] J. R. Barber, *Intermediate mechanics of materials*. Boston: McGraw-Hill, 2001.

[5] A. M. Clayton, "Thermal shock in nuclear reactors," *Progress in Nuclear Engineering,* vol. 12, no. 1, pp. 57-83, 1983.

[6] I. Sattari-Far, "The significance of cladding material on the integrity of nuclear pressure vessels with cracks," SA R&D Report No. 89/03, Statens Anläggningsprovning (SA), Stockholm, 1989.

[7] E. F. Rybicki, J. R. Shadley, A. S. Sandhu, and R. B. Stonesifer, "Experimental and computational residual stress evaluation of a weld clad plate and machined test specimens," *Journal of Engineering Materials and Technology,* vol. 110, no. 4, pp. 297-304, 1988.

[8] G. L. Wire, W. J. Beggs, and T. R. Leax, "Evaluation of irradiation embrittlement of A508 Gr 4N and comparison to other low-alloy steels," in *Effects of radiation on materials: 21st International Symposium, ASTM STP1447*, M. Grossbeck, T. Allen, R. Lott, and A. Kumar, Eds. West Conshohocken: ASTM International, 2004.

[9] C. A. English and J. M. Hyde, "Radiation embrittlement of reactor pressure vessel steels," in *Comprehensive structural integrity*, vol. 6, J. Petit and P. M. Scott, Eds., 2003.

[10] W. R. Corwin, R. G. Berggren, R. K. Nanstad, and R. J. Gray, "Fracture behaviour of a neutron-irradiated stainless steel submerged arc weld cladding overlay," *Nuclear Engineering and Design,* vol. 89, no. 1, pp. 199-221, 1985.

[11] R. A. Ainsworth, "The treatment of thermal and residual stresses in fracture assessments," *Engineering Fracture Mechanics,* vol. 24, no. 1, pp. 65-76, 1986.

[12] R. A. Ainsworth, "Consideration of elastic follow-up in the treatment of combined primary and secondary stresses in fracture assessments," *Engineering Fracture Mechanics,* vol. 96, pp. 558-569, 2012.

[13] M. Drakopoulos *et al.*, "I12: the Joint Engineering, Environment and Processing (JEEP) beamline at Diamond Light Source," *J Synchrotron Radiat,* vol. 22, no. 3, pp. 828-38, May 2015.
[14] H. Tada, P. C. Paris, and G. R. Irwin, *The Stress Analysis Of Cracks Handbook*, 3 ed. New York: ASME Press, 2000.
[15] X. R. Wu and A. J. Carlsson, *Weight functions and stress intensity factor solutions*, 1 ed. Oxford: Pergamon Press, 1991.
[16] Y. Lei, N. P. O'Dowd, and G. A. Webster, "Fracture mechanics analysis of a crack in a residual stress field," *International Journal of Fracture,* vol. 106, no. 3, pp. 195-216, Dec 2000.
[17] V. Lacarac, D. J. Smith, and M. J. Pavier, "Residual Stress Creep Relaxation Around Cold Expanded Holes in an Aluminium Alloy," *AIAA Journal,* vol. 42, no. 7, pp. 1444-1449, 2004.
[18] G. C. M. Horne, "Elastic follow-up and the interaction between applied and residual stresses," PhD thesis, Department of Mechanical Engineering, University of Bristol, 2013.
[19] A. Turnbull, J. J. Pitts, and J. D. Lord, "Residual stress relaxation in shot peened high strength low alloy steel," *Materials Science and Technology,* vol. 24, no. 3, pp. 327-334, 2013.
[20] "R6 Revision 4 - Assessment of the integrity of structures containing defects," British Energy, Barnwood, 2001.
[21] Y. Lei, "J calculation for a crack in a welding residual stress field following a FE welding simulation," *Transactions, Structural Mechanics in Reactor Technology (SMiRT) 23, 2015,* Paper ID 213
[22] J. W. Hutchinson, "Plastic Stress and Strain Fields at a Crack Tip," *Journal of the Mechanics and Physics of Solids,* vol. 16, no. 5, pp. 337-347, 1968.
[23] J. W. Hutchinson, "Singular Behaviour at End of a Tensile Crack in a Hardening Material," *Journal of the Mechanics and Physics of Solids,* vol. 16, no. 1, pp. 13-31, 1968.
[24] J. R. Rice and G. F. Rosengren, "Plane Strain Deformation near a Crack Tip in a Power-Law Hardening Material," *Journal of the Mechanics and Physics of Solids,* vol. 16, no. 1, pp. 1-12, 1968.
[25] S. Oliver, M. Pavier, and M. Mostafavi, "Applying Fracture Mechanics to Cracked Components Subjected to Unloading," *Proceedings of the ASME Pressure Vessels and Piping Conference, 2016,* PVP2016-63575.
[26] C. L. Formby and J. R. Griffiths, "The role of residual stress in the fracture of steel," in *Residual stresses in welded construction and their effects, an international conference, London, 15-17 November 1977, Volume 1: Papers,* Cambridge: The Welding Institute, 1978, pp. 359-374.

[27] X. R. Wu, "The effect of welding residual stress on brittle fracture of plates with surface cracks," *Engineering Fracture Mechanics,* vol. 19, no. 3, pp. 427-439, 1984.
[28] R. A. Ainsworth, J. K. Sharples, and S. D. Smith, "Effects of residual stresses on fracture behaviour-experimental results and assessment methods," *Journal of Strain Analysis for Engineering Design,* vol. 35, no. 4, pp. 307-316, Jul 2000.
[29] R. G. Hurlston, J. K. Sharples, and A. H. Sherry, "Understanding and accounting for the effects of residual stresses on cleavage fracture toughness measurements in the transition temperature regime," *International Journal of Pressure Vessels and Piping,* vol. 128, pp. 69-83, 2015.
[30] A. H. Mahmoudi, C. E. Truman, and D. J. Smith, "Using local out-of-plane compression (LOPC) to study the effects of residual stress on apparent fracture toughness," *Engineering Fracture Mechanics,* vol. 75, no. 6, pp. 1516-1534, 2008.
[31] H. E. Coules, D. J. Smith, P. J. Orrock, K. Abburi Venkata, and T. Pirling, "A Combined Experimental and Modelling Approach to Elastic–Plastic Crack Driving Force Calculation in the Presence of Residual Stresses," *Experimental Mechanics,* 2016.
[32] T. Bolinder and J. Faleskog, "Evaluation of the Influence of Residual Stresses on Ductile Fracture," *Journal of Pressure Vessel Technology,* vol. 137, no. 6, p. 061408, 2015.
[33] D. J. Smith, J. McFadden, S. Hadidimoud, A. J. Smith, A. J. Stormonth-Darling, and A. A. Aziz, "Elastic follow-up and relaxation of residual stresses," *Proceedings of the Institution of Mechanical Engineers, Part C: Journal of Mechanical Engineering Science,* vol. 224, no. 4, pp. 777-787, 2010.
[34] S. Nishimura and K. Tokimasa, "Study on the residual stresses in railroad solid wheels and their effect on wheel fracture," *Bulletin of the Japan Society of Mechanical Engineers,* vol. 19, no. 131, pp. 459-468, 1976.
[35] A. Mirzaee-Sisan, C. E. Truman, D. J. Smith, and M. C. Smith, "Interaction of residual stress with mechanical loading in a ferritic steel," *Engineering Fracture Mechanics,* vol. 74, no. 17, pp. 2864-2880, 2007.
[36] P. M. James, P. Hutchinson, C. J. Madew, and A. H. Sherry, "Predictions of elastic-plastic crack driving force and redistribution under combined primary and secondary stresses – Part 2: Experimental application," *International Journal of Pressure Vessels and Piping,* vol. 101, pp. 91-100, 2013.

[37] H. E. Coules, G. C. M. Horne, K. Abburi Venkata, and T. Pirling, "The effects of residual stress on elastic-plastic fracture propagation and stability," *Materials & Design,* vol. 143, pp. 131-140, 2018.
[38] "ASTM E1820-13, Standard Test Method for Measurement of Fracture Toughness," ASTM International, West Conshohocken, PA, 2013.
[39] R. W. Nichols, Ed. *Residual stresses in welded construction and their effects, an international conference, London, 15-17 November 1977, Volume 1: Papers*. Cambridge: The Welding Institute, 1978.
[40] A. Mirzaee-Sisan, C. E. Truman, D. J. Smith, and M. C. Smith, "Interaction of residual stress with mechanical loading in an austenitic stainless steel," *Fatigue & Fracture of Engineering Materials and Structures,* vol. 31, no. 3-4, pp. 223-233, 2008.
[41] R. H. Leggatt, D. J. Smith, S. D. Smith, and F. Faure, "Development and experimental validation of the deep hole method for residual stress measurement," *Journal of Strain Analysis for Engineering Design,* vol. 31, no. 3, pp. 177-186, May 1996.
[42] M. T. Hutchings, P. J. Withers, T. M. Holden, and T. Lorentzen, *Introduction to the characterization of residual stress by neutron diffraction*, 1 ed. Boca Raton: CRC Press, 2005.
[43] W. J. Brayshaw and A. H. Sherry, "Characterisation of microstructure and properties of a transition weld," *Proceedings of the Asme Pressure Vessels and Piping Conference, 2016,* PVP2016-63045 2016.
[44] A. Moitra, P. Parameswaran, P. R. Sreenivasan, and S. L. Mannan, "A toughness study of the weld heat-affected zone of a 9Cr-1Mo steel," *Material Characterization,* vol. 48, pp. 55-61, 2002.
[45] A. H. Mahmoudi, C. Aird, C. E. Truman, A. Mirzaee-Sisan, and D. J. Smith, "Generating well defined residual stresses in laboratory specimens," *Proceedings of the Asme Pressure Vessels and Piping Conference, 2006,* PVP2006-ICPVT-11-93620.
[46] R. Kume, H. Okabayashi, and T. Naiki, "Internal stresses in thick plates weld-overlaid with austenitic stainless steel (Report 1)," *Transactions of the Japan Welding Society,* vol. 5, no. 1, pp. 32-38, 1974.
[47] H. A. Schimmoeller and J. L. Ruge, "Estimation of residual stresses in reactor pressure vessel steel specimens clad by stainless steel strip electrodes," in *Residual stresses in welded construction and their effects, an international conference, London, 15-17 November 1977, Volume 1: Papers,* Cambridge: The Welding Institute, 1978, pp. 251-258.
[48] P. Dupas and D. Moinereau, "Evaluation of Cladding Residual Stresses in Clad Blocks by Measurements and Numerical

Simulations," *Journal de Physique IV,* vol. 06, no. C1, pp. C1-187-C1-196, 1996.
[49] D. P. Jones, W. R. Mabe, J. R. Shadley, and E. F. Rybicki, "Residual stresses in weld-deposited clad pressure vessels and nozzles," (in English), *Journal of Pressure Vessel Technology-Transactions of the Asme,* vol. 121, no. 4, pp. 423-429, Nov 1999.
[50] E. Kingston, M. Udagawa, J. Katsuyama, K. Onizawa, and D. J. Smith, "Measurement of residual stresses in stainles steel cladded specimens," *Proceedings of the Asme Pressure Vessels and Piping Conference, 2010,* PVP2010-25315.
[51] N. Naveed, F. Hosseinzadeh, and J. Kowal, "Residual stress measurement in a stainless steel clad ferritic plate using the contour method," *Proceedings of the Asme Pressure Vessels and Piping Conference, 2013,* PVP2013-97101.
[52] J. Katsuyama, H. Nishikawa, M. Udagawa, M. Nakamura, and K. Onizawa, "Assessment of Residual Stress Due to Overlay-Welded Cladding and Structural Integrity of a Reactor Pressure Vessel," *Journal of Pressure Vessel Technology,* vol. 135, no. 5, p. 051402, 2013.
[53] M. N. James, M. Newby, P. Doubell, D. G. Hattingh, K. Serasli, and D. J. Smith, "Weld residual stresses near the bimetallic interface in clad RPV steel: A comparison between deep-hole drilling and neutron diffraction data," *Nuclear Engineering and Design,* vol. 274, pp. 56-65, 2014.
[54] K. Serasli, H. Coules, and D. J. Smith, "Residual stresses in clad nuclear reactor pressure vessel steels; prediction, measurement and reconstruction.," *Proceedings of the ASME Pressure Vessels and Piping Conference, 2015,* PVP2015-45224.
[55] K. Serasli, "Measurement and mapping of residual stresses in welded nuclear components," PhD thesis, Department of Mechanical Engineering, University of Bristol, 2014.
[56] M. Brand, J. Hohe, and D. Siegele, "Numerical investigations on the residual stress field in a cladded plate due to the cladding process," *Welding in the world,* vol. 56, pp. 107-113, 2012.
[57] M. F. Ashby and D. R. H. Jones, *Engineering Materials 1*. Oxford: Elsevier, 2005.
[58] M. Sireesha, S. K. Albbert, V. Shankar, and S. Sundaresan, "A comparative evaluation of welding cosumables for dissimilar welds between 316LN austenitic stainless steel and Alloy 800," *Journal of Nuclear Materials,* vol. 279, pp. 65-76, 2000.
[59] Y. Mikami, K. Sogabe, T. Hashimoto, S. Nishikawa, and M. Mochizuki, "Evaluation of residual stress distribution in Ni base alloy clad welds by numerical simulation and X-ray stress measurement,"

Science and Technology of Welding and Joining, vol. 18, no. 2, pp. 114-119, 2013.

[60] M. Udagawa, J. Katsuyama, and K. Onizawa, "Effects of residual stress by weld overlay cladding and PWHT on the structural integrity of RPV during PTS," *Proceedings of the Asme Pressure Vessels and Piping Conference, 2007,* PVP2007-26556.

[61] J. F. Knott, "Structural integrity of nuclear reactor pressure vessels," *Philosophical Magazine,* vol. 93, no. 28-30, pp. 3835-3862, 2013.

[62] "NESC-1 Project Overview," Final report EUR 19051 EN, European Commission, 2001.

[63] G. Rogers and Y. Mayhew, *Engineering Thermodynamics: Work and Heat Transfer*, 4 ed. Pearson, 1992.

[64] R. F. Price and A. J. Fletcher, "Determination of surface heat-transfer coefficients during quenching of steel plates," *Metals Technology,* vol. 7, pp. 203-211, 1980.

[65] H. S. Hasan, M. J. Peet, J. M. Jalil, and H. K. D. H. Bhadeshia, "Heat transfer coefficients during quenching of steels," *Heat and Mass Transfer,* vol. 47, no. 3, pp. 315-321, 2010.

[66] V. F. González-Albuixech, G. Qian, M. Sharabi, M. Niffenegger, B. Niceno, and N. Lafferty, "Integrity analysis of a reactor pressure vessel subjected to a realistic pressurized thermal shock considering the cooling plume and constraint effects," *Engineering Fracture Mechanics,* vol. 162, pp. 201-217, 2016.

[67] R. D. Cheverton, J. W. Bryson, D. J. Alexander, and T. Slot, "Thermal-shock experiments with flawed clad cylinders," *Nuclear Engineering and Design,* vol. 124, pp. 109-119, 1990.

[68] I. Sattari-Far and M. Lorentzon, "Overview and evaluation of the NESC projects for fracture assessments of nuclear components," Report number 2011:05, Swedish Radiation Safety Authority (SSM), 2011, Stockholm.

[69] M. W. Biddulph and R. P. Burford, "Thermal properties and heat transfer coefficients in cryogenic cooling," *Cryogenics,* vol. 22, no. 6, pp. 283-286, 1982.

[70] E. J. Kingston, D. Stefanescu, A. H. Mahmoudi, C. E. Truman, and D. J. Smith, "Novel applications of the deep-hole drilling technique for measuring through-thickness residual stress distributions," *Journal of ASTM International,* vol. 3, no. 4, pp. 1-12, 2006.

[71] D. George, E. Kingston, and D. J. Smith, "Measurement of through-thickness stresses using small holes," *Journal of Strain Analysis,* vol. 32, no. 2, pp. 125-139, 2002.

[72] D. M. Goudar, C. E. Truman, and D. J. Smith, "Evaluating Uncertainty in Residual Stress Measured Using the Deep-Hole Drilling Technique," *Strain,* vol. 47, no. 1, pp. 62-74, 2011.

[73] D. J. Smith, "Deep Hole Drilling," in *Practical residual stress measurement methods*, G. S. Schajer, Ed. 1 ed. Chichester: John Wiley & Sons Ltd, 2013.
[74] D. B. F. George, "Determination of residual stresses in large section stainless steel welds," PhD thesis, Department of Mechanical Engineering, University of Bristol, 2000.
[75] "Abaqus v6.14," Providence, RI, USA: Dassault Systemes Simulia Corp. .
[76] "ASTM E8/E8M - 15a Standard Test Methods for Tension Testing of Metallic Materials," ASTM International, West Conshohocken, PA, 2015.
[77] S. R. Claves and W. J. Mills, "Influence of crystallographic texture on Young's modulus of various Alloy 82H welds," *Microscopy and Microanalysis,* vol. 17, no. 3, pp. 341-9, Jun 2011.
[78] R. L. Klueh and J. F. King. Elevated temperature tensile behaviour of ERNiCr-3 weld metal. *Welding Journal*. April 1980, 114-120.
[79] D. Xia *et al.*, "Mechanical Properties and Corrosion Resistance of SA508-4 Low Carbon Alloy Steel," *Electrochemistry,* vol. 81, no. 4, pp. 262-268, 2013.
[80] G. S. Schajer, "Measurement of Non-Uniform Residual-Stresses Using the Hole-Drilling Method .1. Stress Calculation Procedures," *Journal of Engineering Materials and Technology-Transactions of the Asme,* vol. 110, no. 4, pp. 338-343, Oct 1988.
[81] "ASTM E837-13a, Determining Residual Stresses by the Hole-Drilling Strain-Gage Method," ASTM International, West Conshohocken, PA, 2013.
[82] M. B. Prime, "Cross-sectional mapping of residual stresses by measuring the surface contour after a cut," *Journal of Engineering Materials and Technology-Transactions of the Asme,* vol. 123, no. 2, pp. 162-168, Apr 2001.
[83] S. Oliver, M. Mostafavi, F. Hosseinzadeh, and M. Pavier, "Redistribution of residual stress by thermal shock in reactor pressure vessel steel clad with nickel alloy," *International Journal of Pressure Vessels and Piping,* vol. 196, pp. 37-47, 2019.
[84] A. Goldsmith, T. E. Waterman, and H. J. Hirschhorn, *Handbook of thermophysical properties of solid materials, Volume II: Alloys*. New York: Macmillan, 1961.
[85] A. H. Committee, B. P. Bardes, Ed. *Metals handbook, Volume 1: Properties and selection: irons and steels*, 9 ed. Ohio: American Society for Metals, 1978.
[86] "INCONEL alloy 600," Data sheet SMC-027, Special Metals Corporation,

http://www.specialmetals.com/assets/smc/documents/alloys/inconel/inconel-alloy-600.pdf, Sept. 2008 (accessed 1 August 2016).
[87] G. Panneerselvam *et al.*, "A study on the thermal expansion characteristics of Inconel-82® filler wire by high temperature X-ray diffraction," *Materials Letters,* vol. 58, no. 1-2, pp. 216-221, 2004.
[88] B. A. Latella and S. R. Humphries, "Young's modulus of a 2.25Cr–1Mo steel at elevated temperature," *Scripta Materialia,* vol. 51, no. 7, pp. 635-639, 2004.
[89] G. V. Smith, "Evaluations of the elevated temperature tensile and creep-rupture properties of C-Mo, Mn-Mo and Mn-Mo-Ni steels," Data Series DS 47, ASTM International, West Conshohocken, PA, 1971.
[90] M. J. Marques, A. Ramasamy, A. C. Batista, J. P. Nobre, and A. Loureiro, "Effect of heat treatment on microstructure and residual stress fields of a weld multilayer austenitic steel clad," *Journal of Materials Processing Technology,* vol. 222, pp. 52-60, 2015.
[91] A. Mirzaee-Sisan, D. Smith, and C. Truman, "Characterizing residual stresses in rectangular beam specimens following thermomechanical loading," *The Journal of Strain Analysis for Engineering Design,* vol. 42, no. 2, pp. 79-93, 2007.
[92] S. Hossain, C. E. Truman, D. J. Smith, and M. R. Daymond, "Application of quenching to create highly triaxial residual stresses in type 316H stainless steels," *International Journal of Mechanical Sciences,* vol. 48, no. 3, pp. 235-243, 2006.
[93] "Manual on the use of thermocouples in temperature measurement, fourth edition, sponsored by ASTM Committee E20 on temperature measurement," MNL12-4TH-EB, ASTM International, West Conshohocken, PA, 1993.
[94] P. Withers, "Synchrotron X-ray Diffraction," in *Practical residual stress measurement methods*, G. S. Schajer, Ed. 1 ed.: John Wiley and Sons, Ltd, 2013.
[95] S. Oliver *et al.*, "Measurements of stress during thermal shock in clad reactor pressure vessel material using time-resolved in-situ synchrotron X-ray diffraction," *Proceedings of the ASME Pressure Vessels and Piping Conference, 2018,* PVP2018-84676.
[96] C. Simpson, "pyxe: XRD Strain Analysis (Version v0.8.1). Zenodo. ," 2016, http://doi.org/10.5281/zenodo.50185.
[97] R. Narasimhan and A. J. Rosakis, "Three-dimensional effects near a crack tip in a ductile three-point bend specimen: part I - a numerical investigation," *Journal of Applied Mechanics,* vol. 57, no. 3, pp. 607 - 617, 1990.

[98] G. R. Irwin, "Analysis of stresses and strains near the end of a crack traversing a plate," *Journal of Applied Mechanics,* vol. 24, pp. 361-364, 1957.
[99] M. Creager and P. C. Paris, "Elastic field equations for blunt cracks with reference to stress corrosion cracking," *International Journal of Fracture Mechanics,* vol. 3, no. 4, pp. 247-252, 1967.
[100] S. Marie, "Analytical expression of the thermal stresses in a vessel or pipe with cladding submitted to any thermal transient," *International Journal of Pressure Vessels and Piping,* vol. 81, no. 4, pp. 303-312, 2004.
[101] S. Marie, Y. Ménager, and S. Chapuliot, "Stress intensity factors for underclad and through clad defects in a reactor pressure vessel submitted to a pressurised thermal shock," *International Journal of Pressure Vessels and Piping,* vol. 82, no. 10, pp. 746-760, 2005.
[102] R. O. Ritchie, J. F. Knott, and J. R. Rice, "Relationship between Critical Tensile Stress and Fracture Toughness in Mild-Steel," (in English), *Journal of the Mechanics and Physics of Solids,* vol. 21, no. 6, pp. 395-410, 1973.
[103] V. F. González-Albuixech, G. Qian, and M. Niffenegger, "Integrity analysis of a reactor pressure vessel with quasi laminar flaws subjected to pressurized thermal shocks," *Nuclear Engineering and Design,* vol. 280, pp. 464-472, 2014.
[104] G. G. Chell, J. R. Haigh, and V. Vitek, "A Theory of Warm Prestressing - Experimental Validation and the Implications for Elastic Plastic Failure Criteria," *International Journal of Fracture,* vol. 17, no. 1, pp. 61-81, 1981.
[105] C. Garza, R. Das, A. Shterenlikht, and M. Pavier, "Measurement of assembly stress in composite structures using the deep-hole drilling technique," *Composite Structures,* 2017.
[106] S. A. Fawaz and J. J. M. de Rijck, "A Thin-Sheet, Combined Tension and Bending Specimen," *Experimental Mechanics,* vol. 39, no. 3, pp. 171-176, 1999.
[107] Z.-B. Wang, Q. Yu, and Z. Tao, "Behaviour of CFRP externally-reinforced circular CFST members under combined tension and bending," *Journal of Constructional Steel Research,* vol. 106, pp. 122-137, 2015.
[108] R. P. Johnson and C. J. Tait, "The Strength in Combined Bending and Tension of Concrete Beams with Externally Bonded Reinforcing Plates," *Building and Environment,* vol. 16, no. 4, pp. 287-299, 1981.
[109] S. Izawa *et al.*, "Combined Tension-Bend System for Large Deformation Analysis," *Experimental Techniques,* vol. 31, no. 5, pp. 42-45, 2007.

[110] C. J. Aird, M. J. Pavier, and D. J. Smith, "A fundamental study of the interaction of residual stress and applied loading on fracture," *Proceedings of the ASME Pressure Vessels and Piping Conference, 2010,* PVP2010-25943.
[111] "Abaqus Analysis User's Guide Section 6.1.3: General and linear perturbation procedures," in *Abaqus 6.14 Documentation*: Providence, RI, USA: Dassault Systemes Simulia Corp. .
[112] P. M. James, "Fracture under combined primary and secondary stresses," PhD thesis, Faculty of Engineering and Physical Sciences, University of Manchester, 2013.
[113] D. G. A. V. Gelderen, "Effects of load history on low temperature fracture of steels," PhD thesis, Department of Mechanical Engineering, University of Bristol, 2016.
[114] W. Sylwestrowicz and E. O. Hall, "The deformation and ageing of mild steel," *Proceedings of the Physical Society Section B,* vol. 64, pp. 495-502, 1951.
[115] P. Moore, "The effect of notch sharpness on the fracture toughness determined from sent specimens," *Proceedings of the ASME 2014 33rd International Conference on Ocean, Offshore and Arctic Engineering,* OMAE2014-24663.
[116] A.-H. I. Mourad and A. El-Domiaty, "Notch Radius and Specimen Size Effects on Fracture Toughness of Low Alloy Steel," *Procedia Engineering,* vol. 10, pp. 1348-1353, 2011.
[117] M. Mostafavi, "Improving the Accuracy of Fracture Assessments," PhD thesis, University of Bristol, 2009.
[118] A. G. Miller, "Review of limit loads of structures containing defects," *International Journal of Pressure Vessels and Piping,* vol. 32, pp. 197-327, 1988.
[119] G. Shen and W. R. Tyson, "Crack size evaluation using unloading compliance in single-specimen single-edge-notched tension fracture toughness testing," *Journal of Testing and Evaluation,* vol. 37, no. 4, 2009.
[120] M. A. Verstraete, S. Hertelé, R. M. Denys, K. Van Minnebruggen, and W. De Waele, "Evaluation and interpretation of ductile crack extension in SENT specimens using unloading compliance technique," *Engineering Fracture Mechanics,* vol. 115, pp. 190-203, 2014.
[121] M. A. Verstraete, W. De Waele, K. Van Minnebruggen, and S. Hertelé, "Single-specimen evaluation of tearing resistance in SENT testing," *Engineering Fracture Mechanics,* vol. 148, pp. 324-336, 2015.
[122] "MATLAB version R2014a," Natick, USA: MathWorks.

[123] P. M. James, D. G. Hooton, L. A. Higham, C. J. Madew, J. K. Sharples, and C. T. Watson, "Continuing development of a simplified method to account for the interaction of primary and secondary stresses," *Proceedings of the ASME Pressure Vessels and Piping Conference, 2008,* PVP2008-61040.
[124] D. G. Hooton, J. K. Sharples, S. F. Yellowlees, and C. T. Watson, "An alternative method to that of the R6 procedure for the treatment of combined primary and secondary loading," *Proceedings of the ASME Pressure Vessels and Piping Conference, 2006,* PVP2006-ICPVT-11-93569.
[125] P. M. James, D. G. Hooton, C. J. Madew, and A. H. Sherry, "Predictions of elastic–plastic crack driving force and redistribution under combined primary and secondary stresses – Part 1: Analytical investigation," *International Journal of Pressure Vessels and Piping,* vol. 101, pp. 101-112, 2013.
[126] H. Gu, M. Pavier, and A. Shterenlikht, "Experimental study of modulus, strength and toughness of 2D triangular lattices," *International Journal of Solids and Structures,* 2018.

Appendix A: Design of Thermal Shock Rig for In-Situ Diffraction

This section gives details about the design of the self-contained thermal shock rig used for the in-situ X-ray diffraction experiment described in Chapter 4.

Figure A 1 shows a schematic of the thermal shock rig with some key components labelled. The operating principles were given in Section 4.2.2. The tank was manufactured out of 80 x 120 mm aluminium box section with a rectangular plate welded on the bottom to make it watertight. The quench bath was manufactured out of five aluminium plates which were welded together into an open-top box. The footprint of the quench bath is 230 x 260 mm and the height is 200 mm. Square windows of size 50 x 50 mm were machined in the front and rear of the quench bath and sealed with 2 mm thick polycarbonate to allow the X-ray beam to pass through to the specimen. The whole apparatus was encased in clear polycarbonate and sealed with silicon. The thermal shock apparatus was assembled on a 12 mm thick aluminium base plate and the components were connected by an adjustable aluminium frame. A picture of the thermal shock rig is shown in Figure A 2, in which the thermal shock rig is on the right and the control box is on the left. The footprint of the thermal shock rig is 480 x 330 mm and the overall height is 450 mm. A picture of the specimen mounting arrangement is shown in Figure A 3. The specimen mounting arrangement was constructed using mild steel.

The circuit diagram of the control box is shown in Figure A 4, and key electric components are listed in Table A 1. The control box contains: power supplies for the pump and heaters; a proportional-integral-derivative (PID) temperature controller to control the temperature of the specimen; and a safety interlock circuit which cuts power to the thermal shock rig when the lid is removed (i.e. the safety switches are opened). The control box was designed so that the heaters and pump could be controlled from an external switch-box situated outside the experimental hutch in the beamline control room. The switch box provides power to the heater and pump circuits in the control box via

separate cables, which connect to the heater and pump power inputs shown in Figure A 4. The switch box is designed so that power can be supplied to either the pump or the heaters, but not both simultaneously.

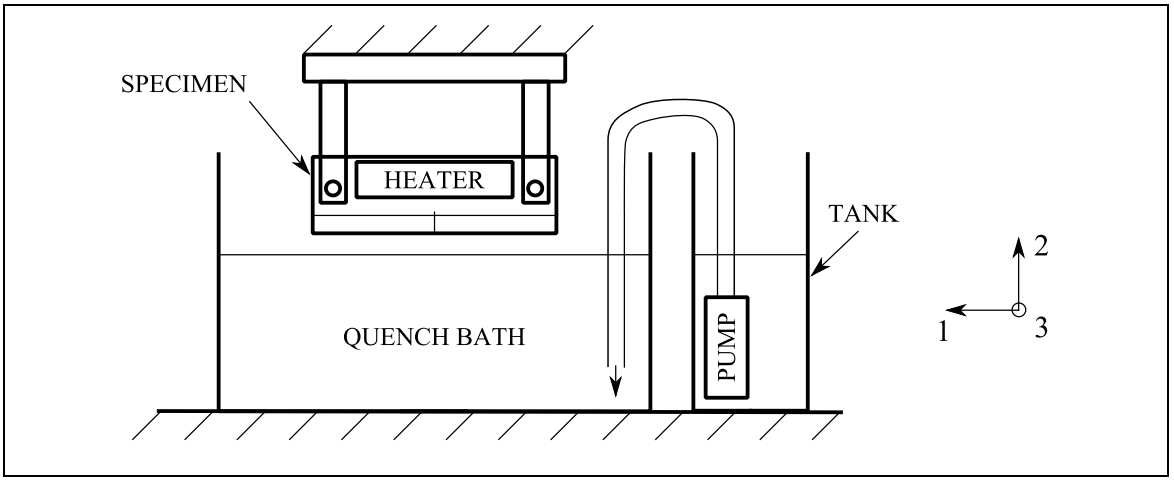

Figure A 1 **Schematic of the self-contained thermal shock rig.**

Figure A 2 **Picture of the thermal shock rig (right) and the control box (left).**

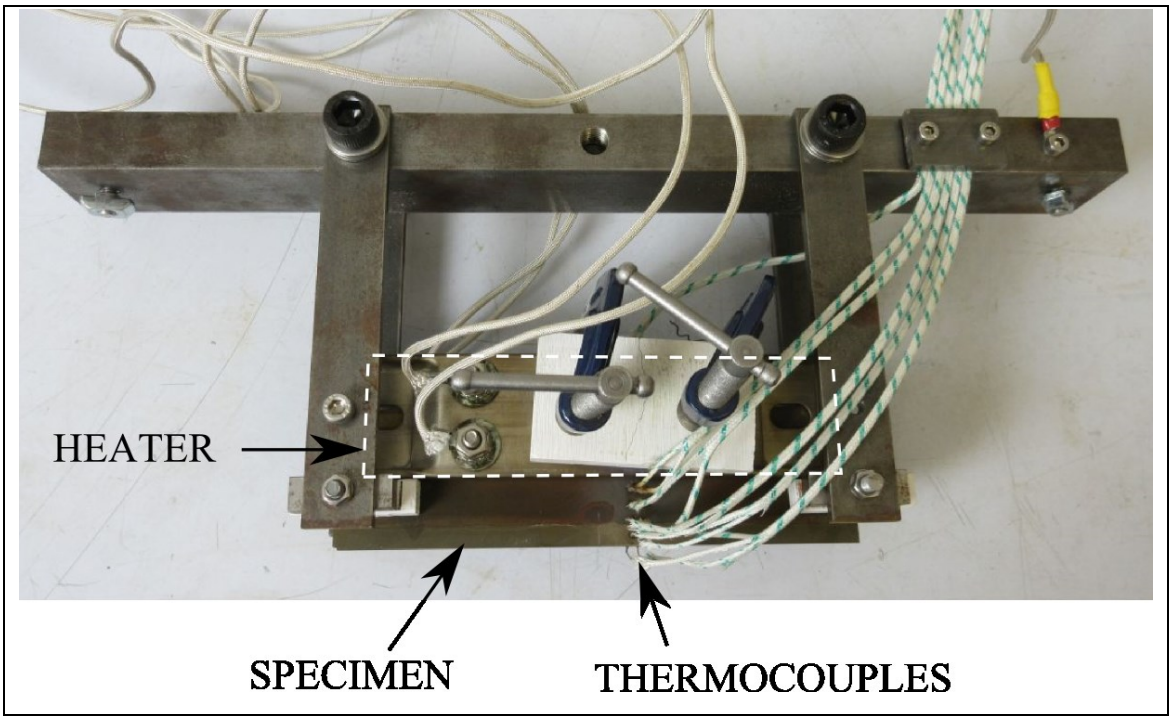

Figure A 3 **Picture of the specimen mounting arrangement.**

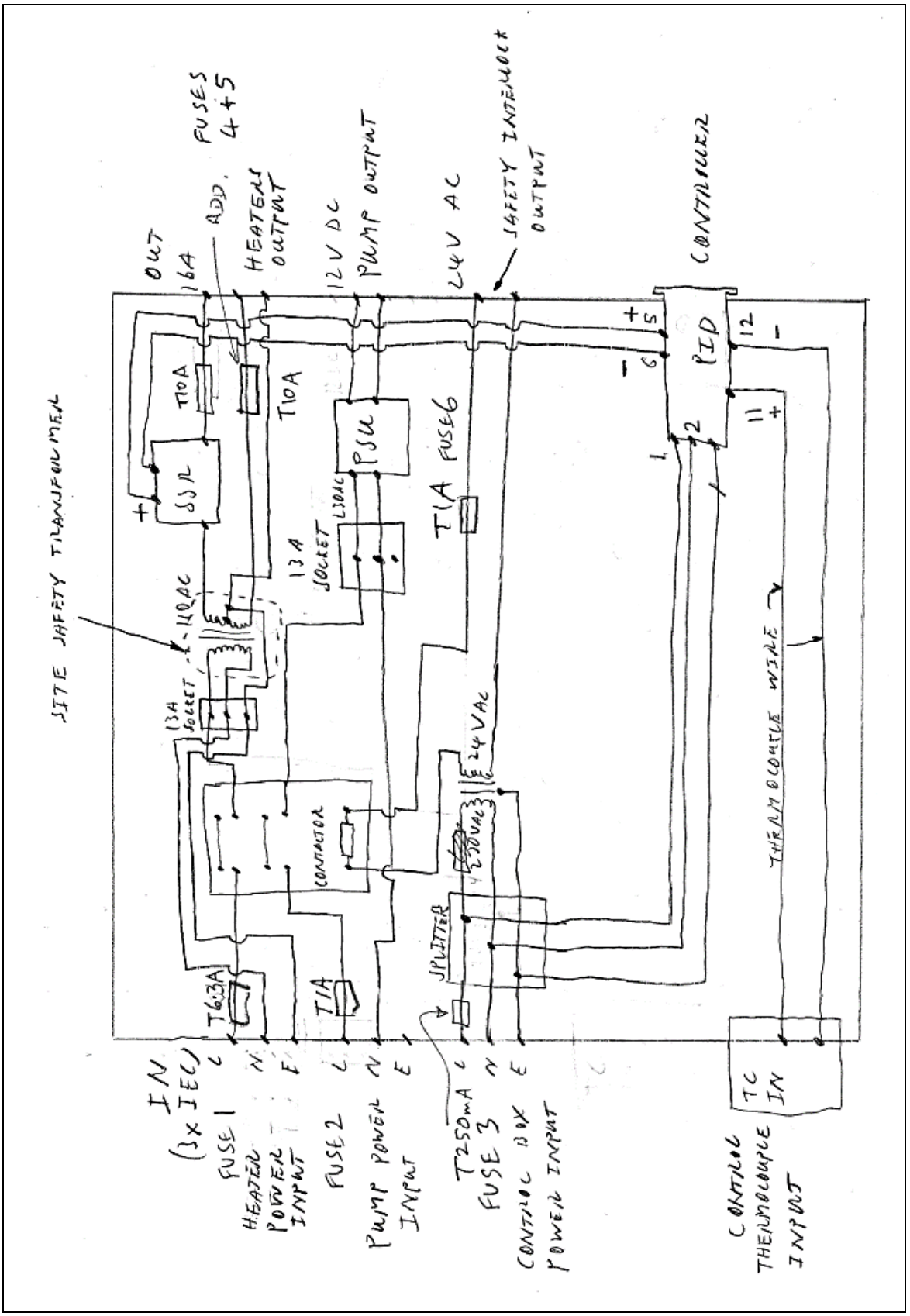

Figure A 4 **Circuit diagram of the control box for the self-contained thermal shock rig.**

Table A 1 Key electric components used in the thermal shock rig.

Part	Manufacturer	Model number	Quantity
Pump	Xylem	Rule iL280P 12VDC submersible pump	1
Heaters	Omega Engineering	CSH00163 ceramic-insulated 300 W strip-heater	2
Site safety transformer (heater power supply)	RS Pro	RS #122-6712 1.5kVA isolation transformer, 2 x 16A output	1
Pump power supply (PSU)	RS Pro	RS #816-0090 12VDC 0-5A	1
PID temperature controller	Red Lion	PXU20020	1
Relay for controller output (SSR)	RS Pro	RS #922-4987 10A 280 VAC SPNO solid state relay	1
Contactor for safety interlock circuit	Schneider Electric	LC1K0610B7	1
Safety interlock switches	Omron	D3V-163-3C5 16 A 250 VAC microswitch	2
230 VAC to 24 VAC transformer for interlock circuit	RS Pro	RS #123-5697 25VA Isolation Transformer, 15 – 400VAC primary, 2x12VAC secondary	1

Appendix B: Design of Fixed-Displacement Four-Point Bend Fixture for Representing Residual Stress

This section gives details about the design of the fixed-displacement four-point bending fixture used in work described in Chapter 5. Table B 1 lists the components which were bough-in from external manufacturers, and Table B 2 lists the parts which were manufactured at the University of Bristol. An assembly drawing is shown in Figure B 1, and a picture of the test rig is shown in Figure B 2. Engineering drawings of each part follow in Figure B 3 - Figure B 13.

The rollers are supported in the inner and outer support plates by full-compliment drawn-cup needle roller bearings. Each bearing is 20 mm wide. There are four bearings mounted in each outer support plate (two in each hole), and four bearings in total mounted in the inner support plate (one in each hole). The inner and outer rollers (the four-point bend rollers, not the needle rollers) act as the inner race (i.e. the bearing does not have an integrated inner race). Therefore, the inner and outer rollers are surface-hardened to prevent the needle rollers from indenting the surface under load. The bearing casing press-fits, and the inner and outer rollers also needed to be manufactured to special tolerances. The inner and outer rollers were ground to n6 ISO tolerance, and the casing press-fits in the inner and outer support plates were manufactured to ISO N7 using wire EDM.

Table B 1 List of bought-in components.

Part	Manufacturer	Model number	Quantity
Load cell	Novatech	F313	1
Bearings	Nadella	DL5020	12

Table B 2 List of components manufactured at the University of Bristol.

Part	Material	Drawing (figure)	Quantity
Anti-rotation nut	Bright mild steel	Figure B 3	1
Bottom spacer	5083 Aluminium alloy	Figure B 4	2
Inner rollers	Surface hardened steel shaft Ø50 (ground and polished to h6 ISO tolerance)	Figure B 5	2
Inner support plate	Bright mild steel	Figure B 6	1
Load pin	EN24 steel	Figure B 7	1
Lock nut	EN24 steel	Figure B 8	1
Locking outer roller	Surface hardened steel shaft Ø50 (ground and polished to h6 ISO tolerance)	Figure B 9	1
Outer roller	Surface hardened steel shaft Ø50 (ground and polished to h6 ISO tolerance)	Figure B 10	1
Outer support plate	EN 10025 S275 steel	Figure B 11	2
Roller locking plate	Bright mild steel	Figure B 12	1
Top spacer	6082 T6 Aluminium alloy	Figure B 13	1

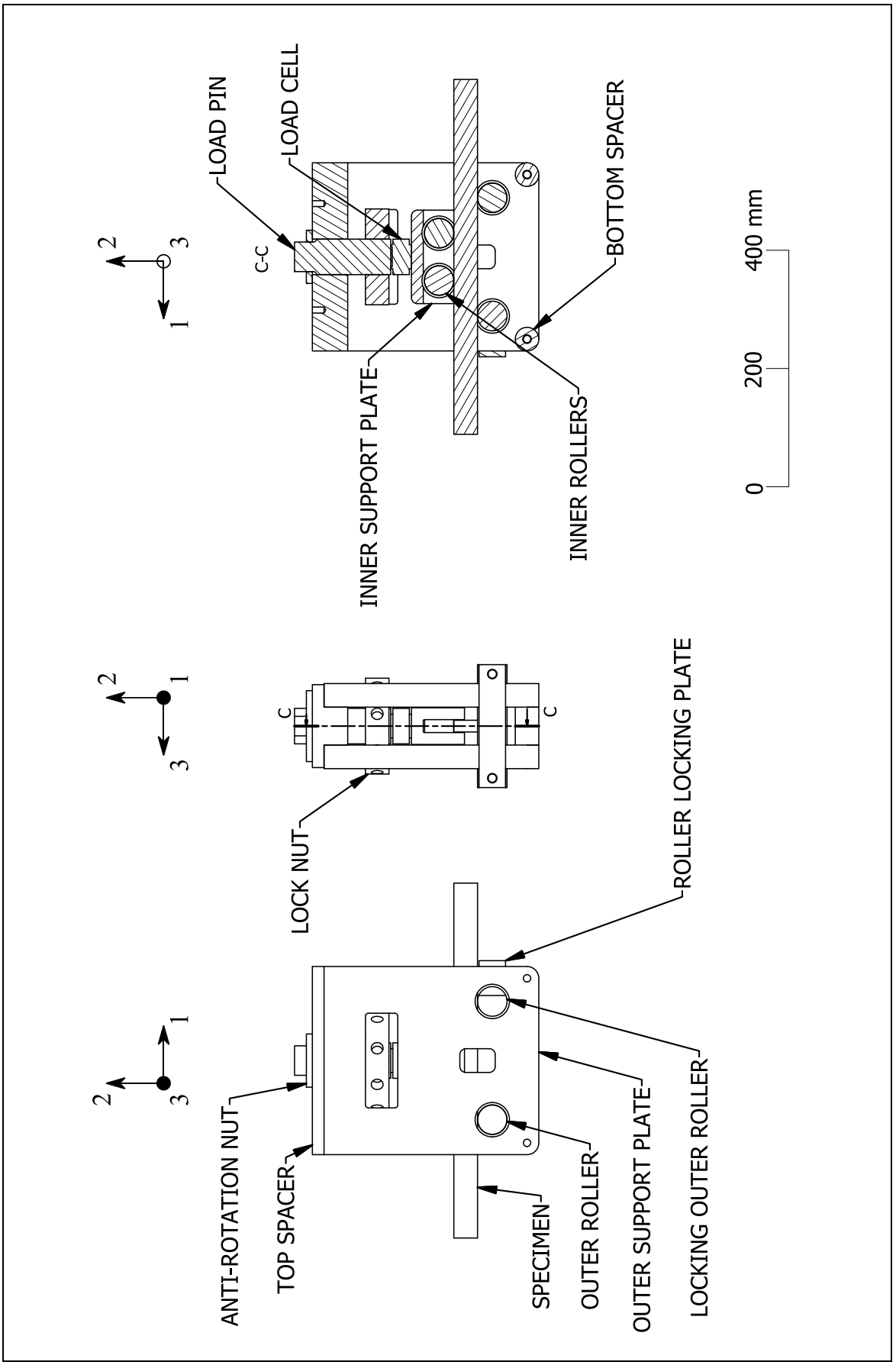

Figure B 1 **Assembly drawing of the fixed-displacement four-point bending fixture.**

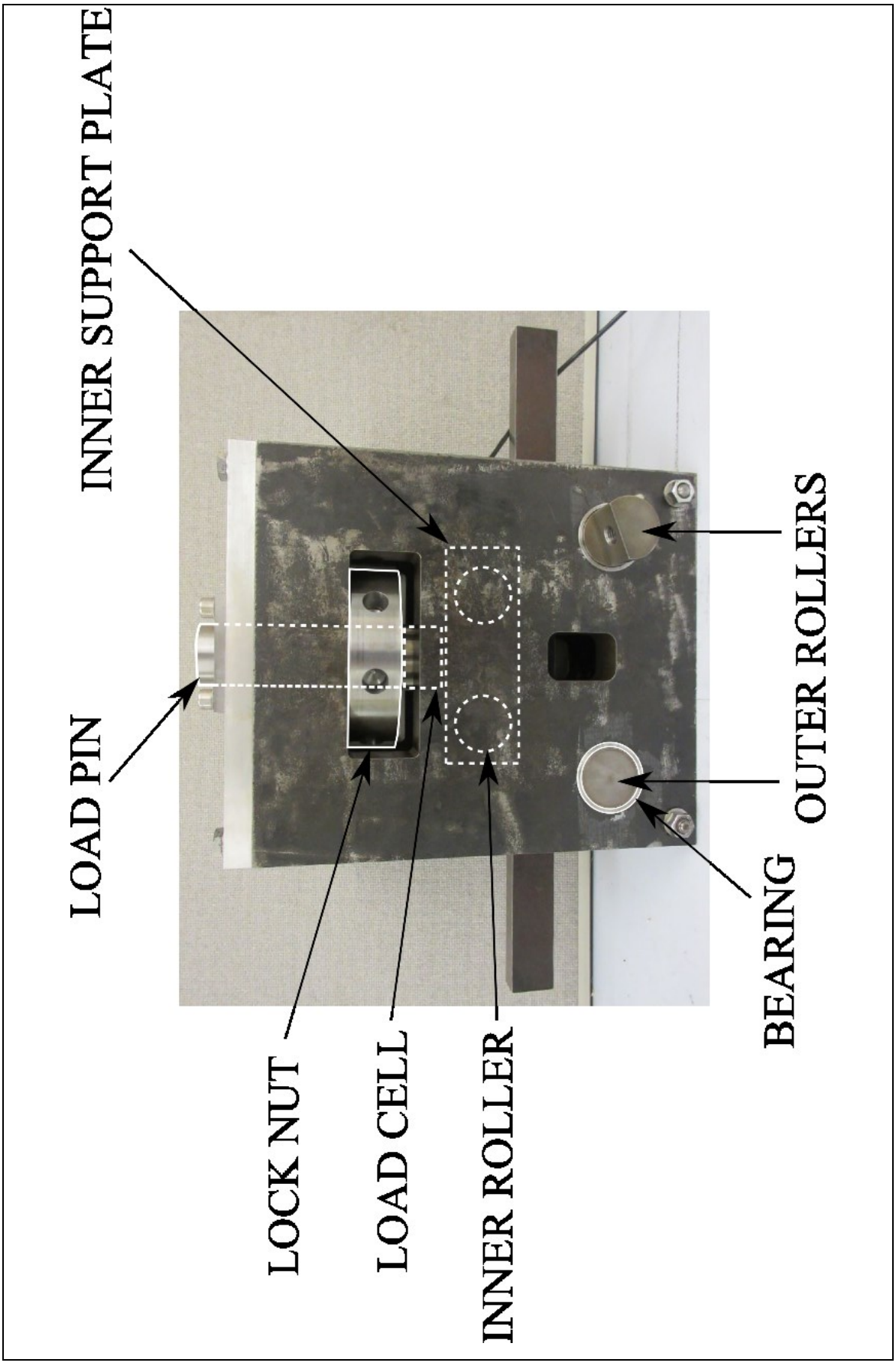

Figure B 2 **Photograph of the fixed-displacement four-point bending fixture.**

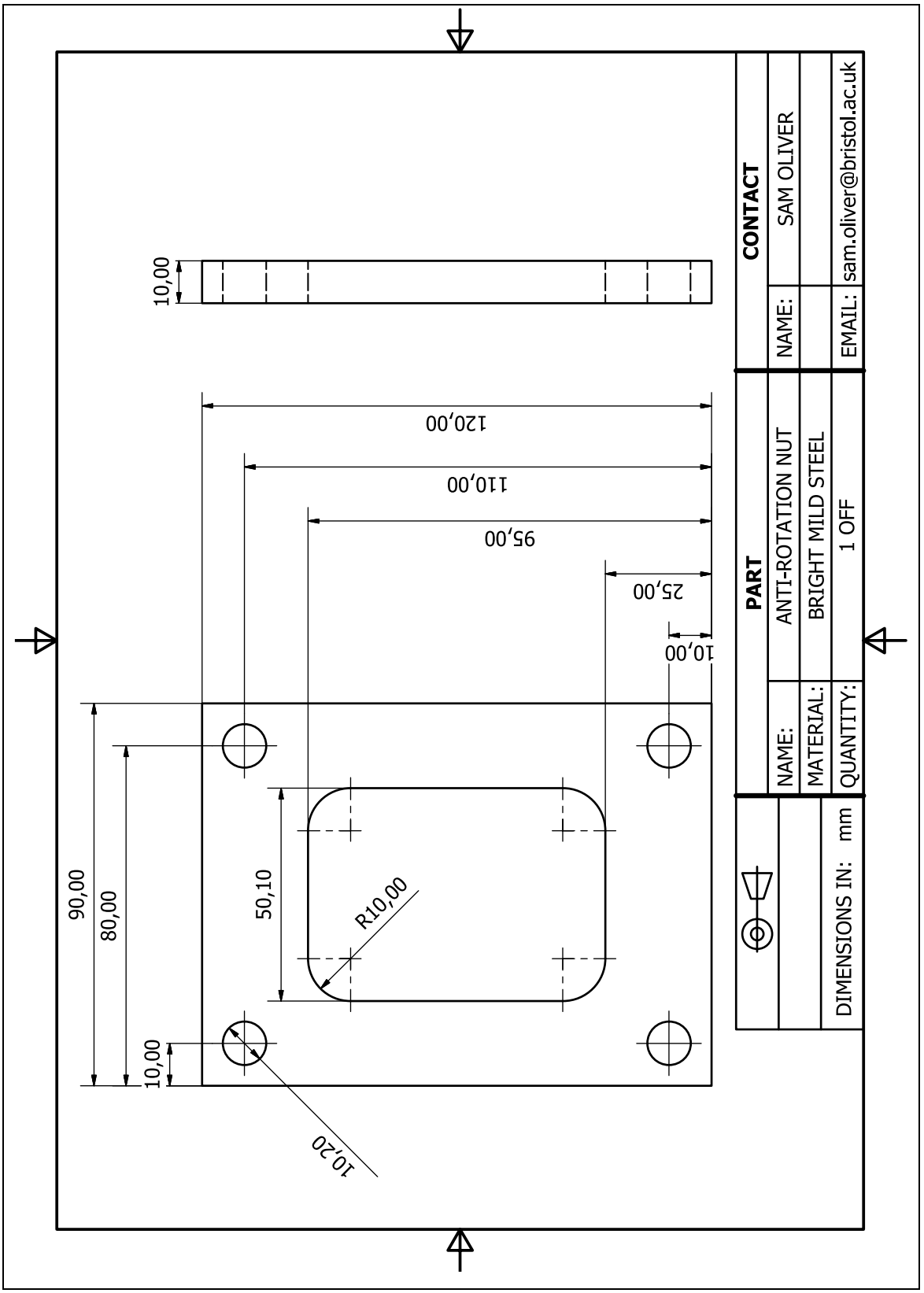

Figure B 3 **Anti-rotation nut.**

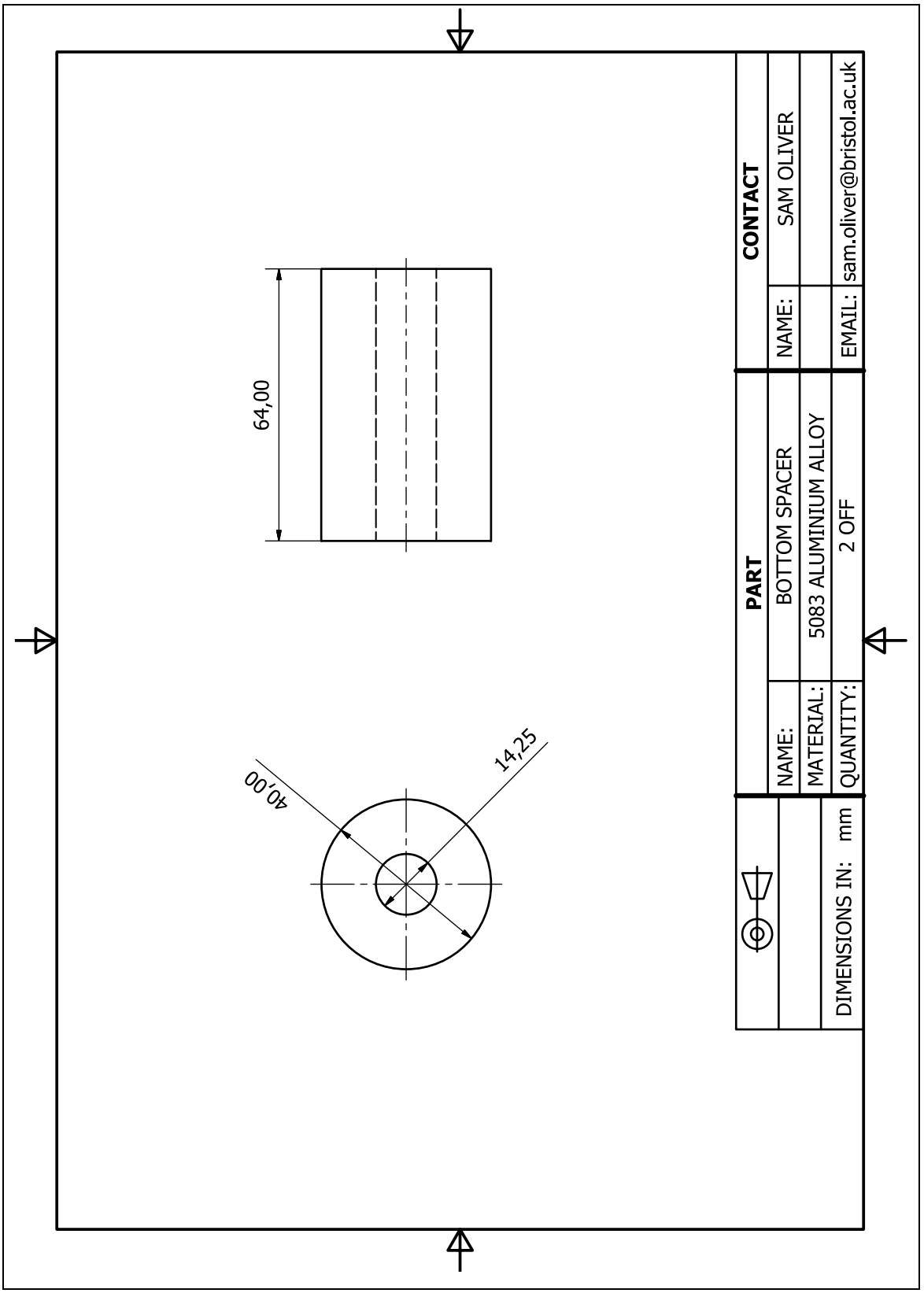

Figure B 4 **Bottom spacer.**

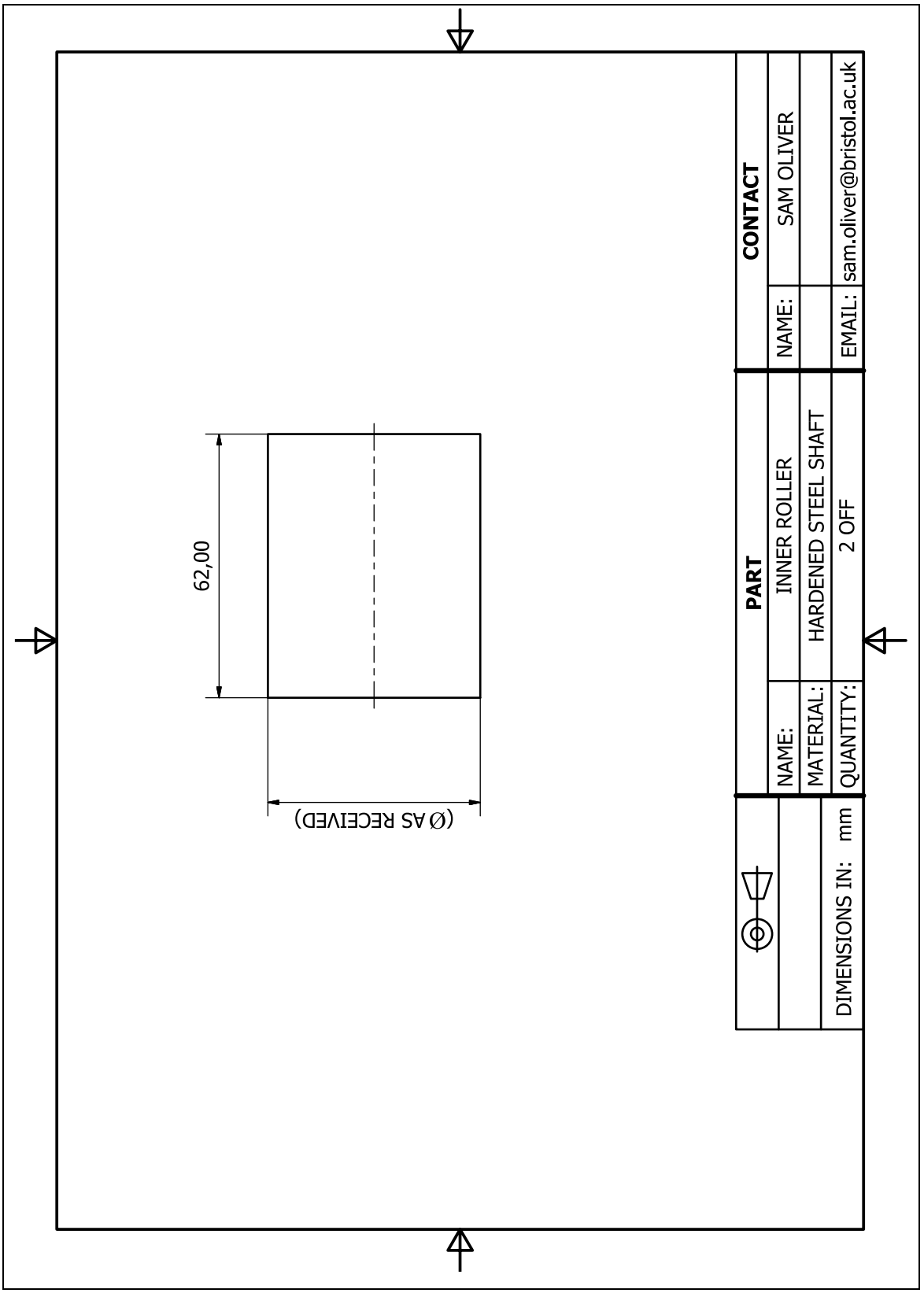

Figure B 5 **Inner roller.**

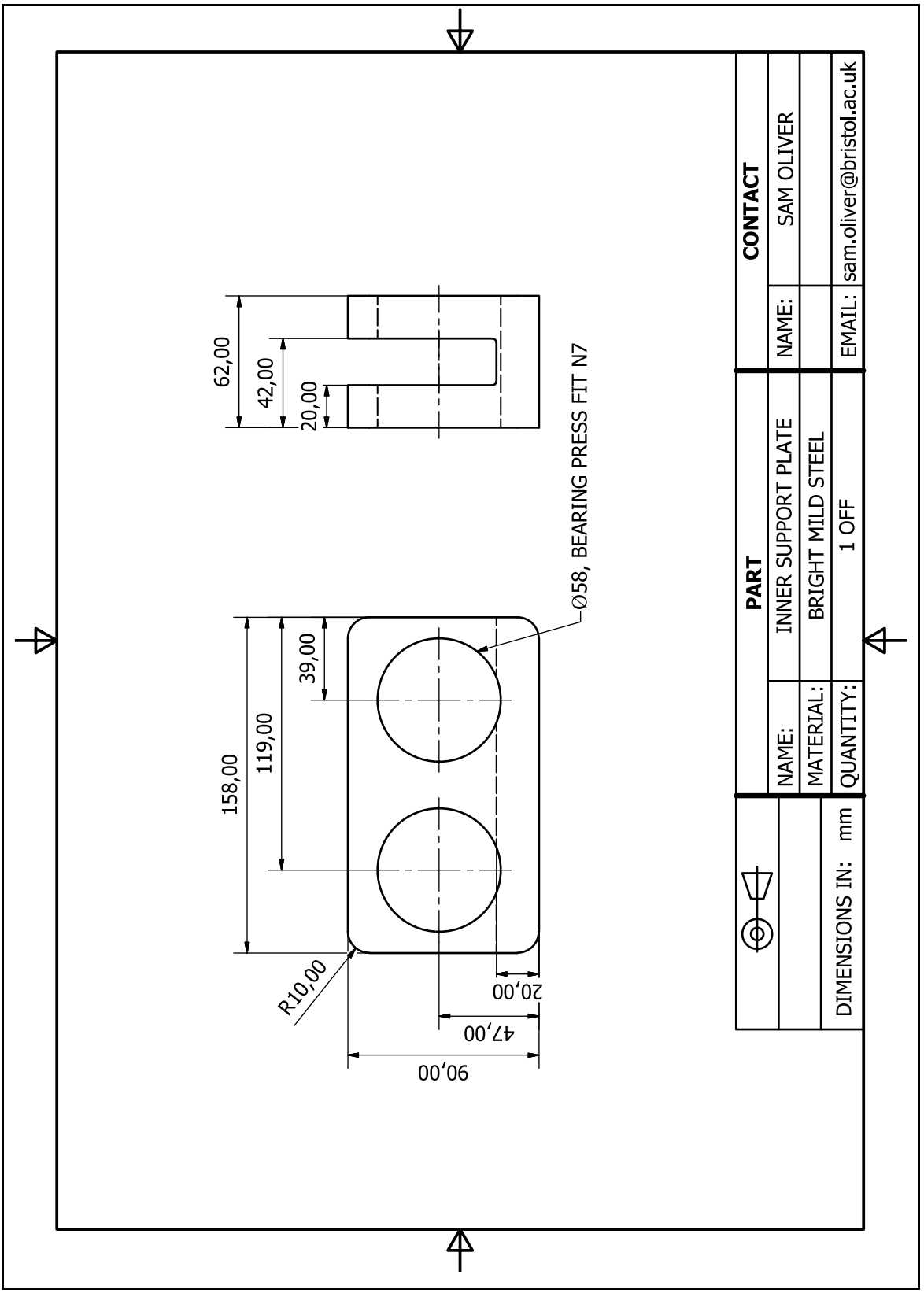

Figure B 6 **Inner support plate.**

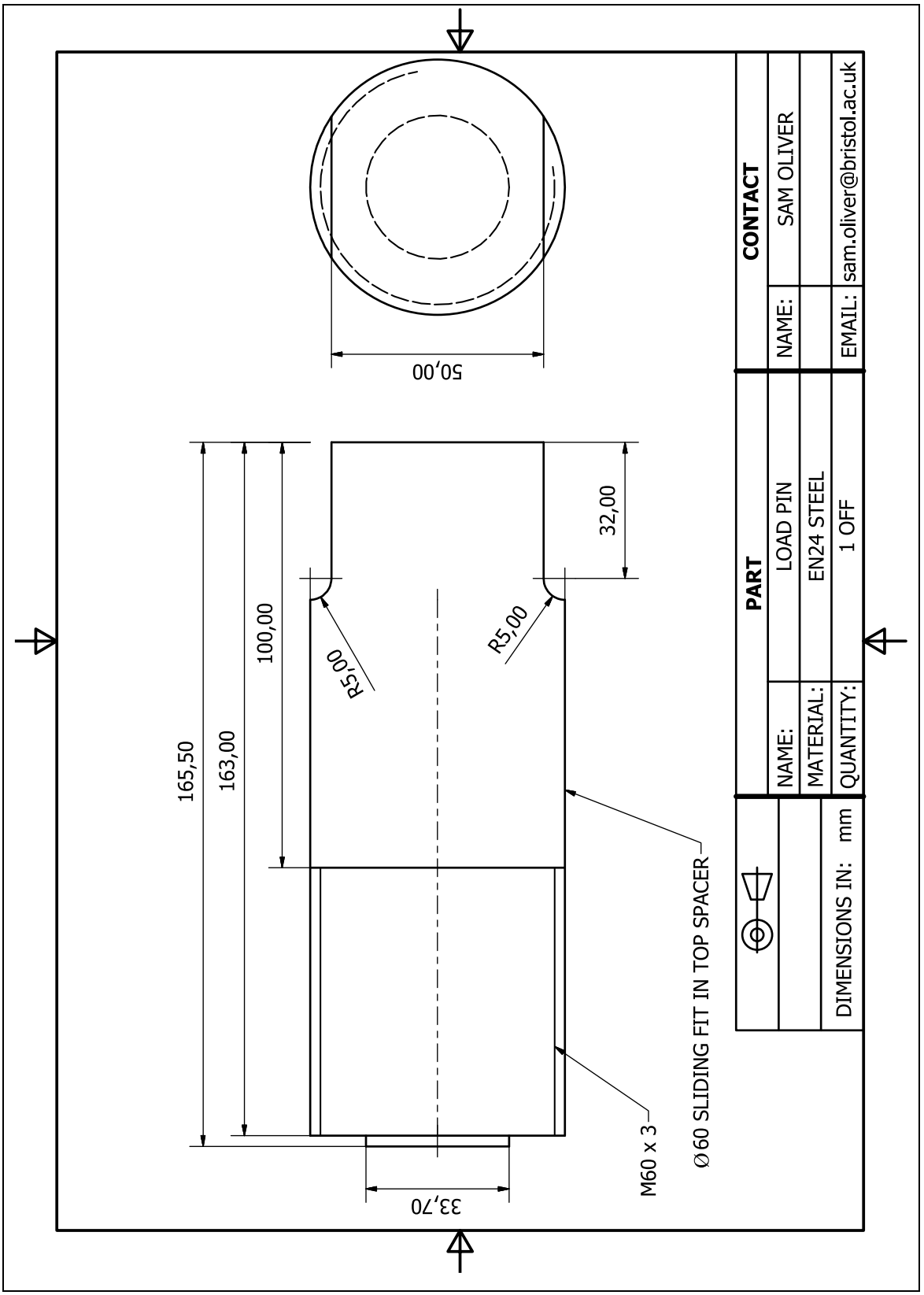

Figure B 7 Load pin.

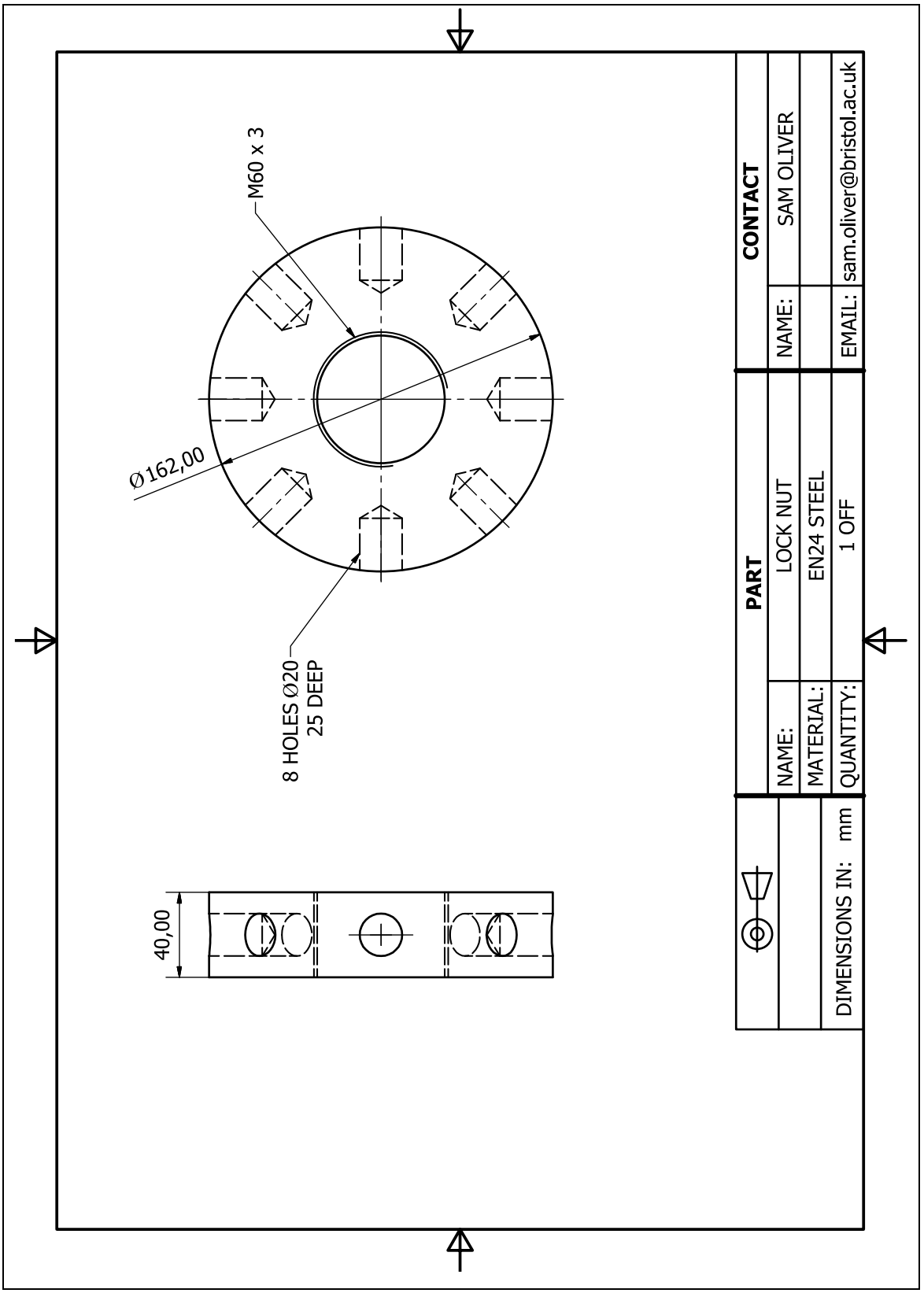

Figure B 8 **Lock nut. The eight axial holes were reamed for a sliding fit with 20 mm silver steel bar.**

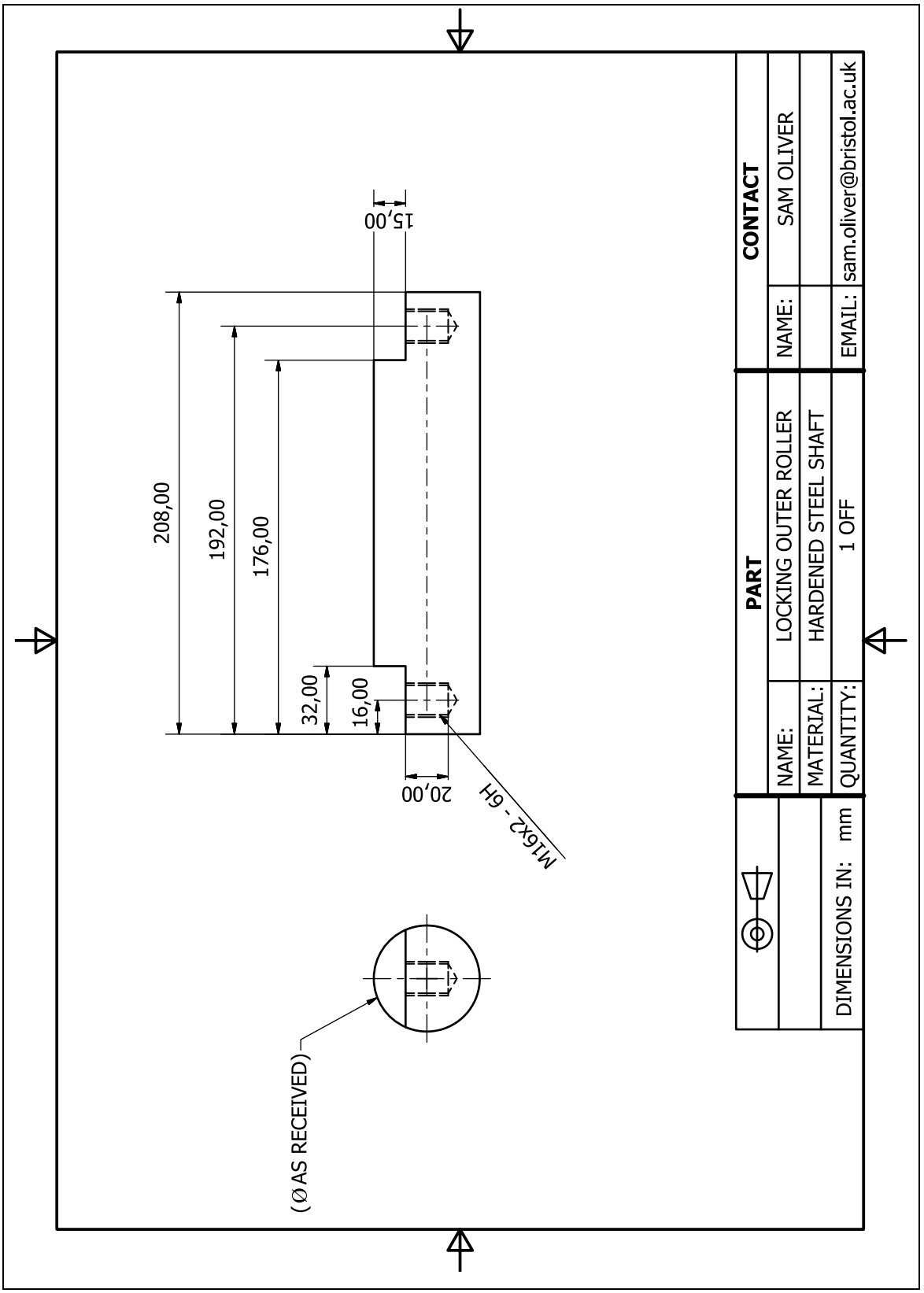

Figure B 9 **Locking outer roller.**

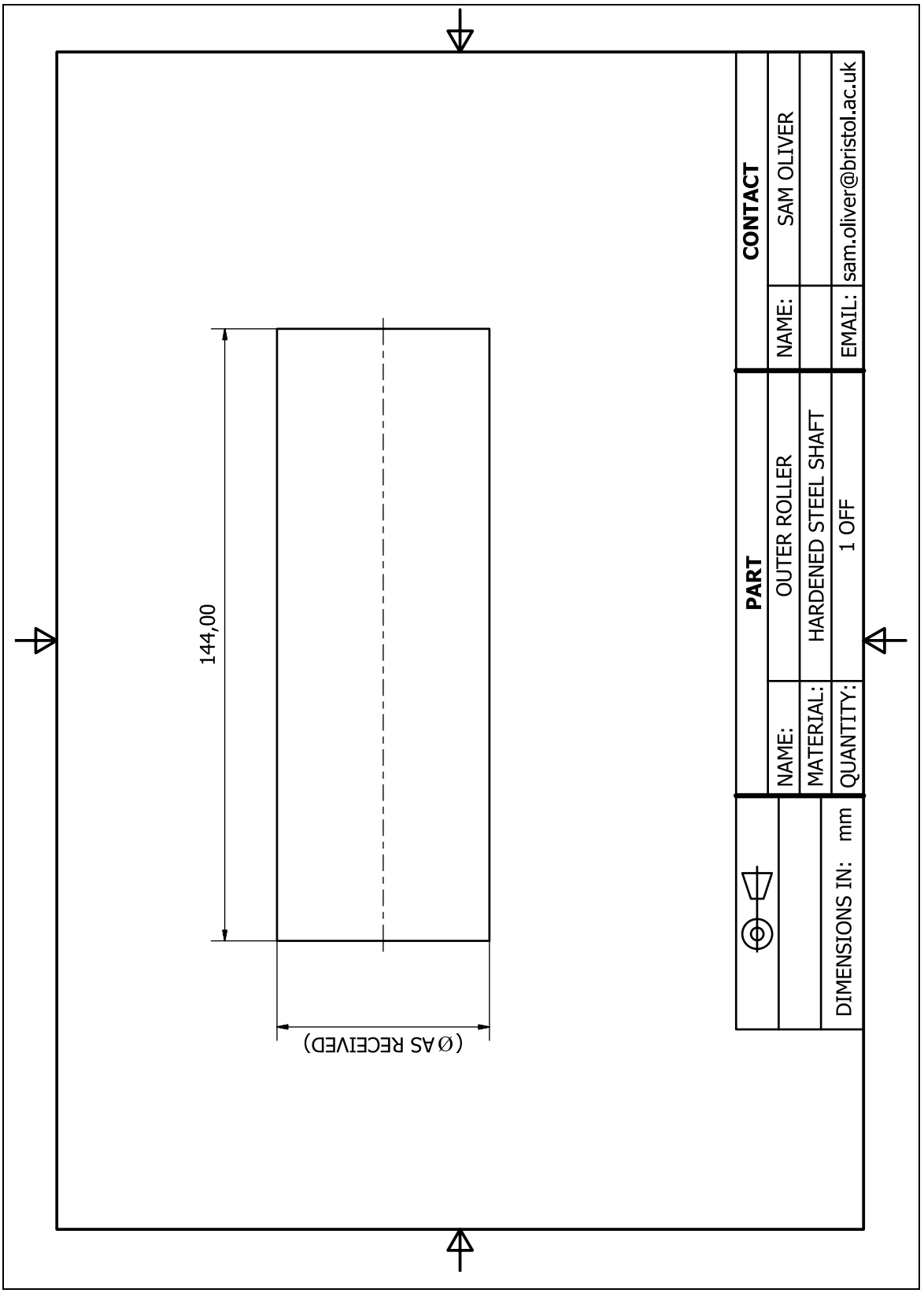

Figure B 10 Outer roller.

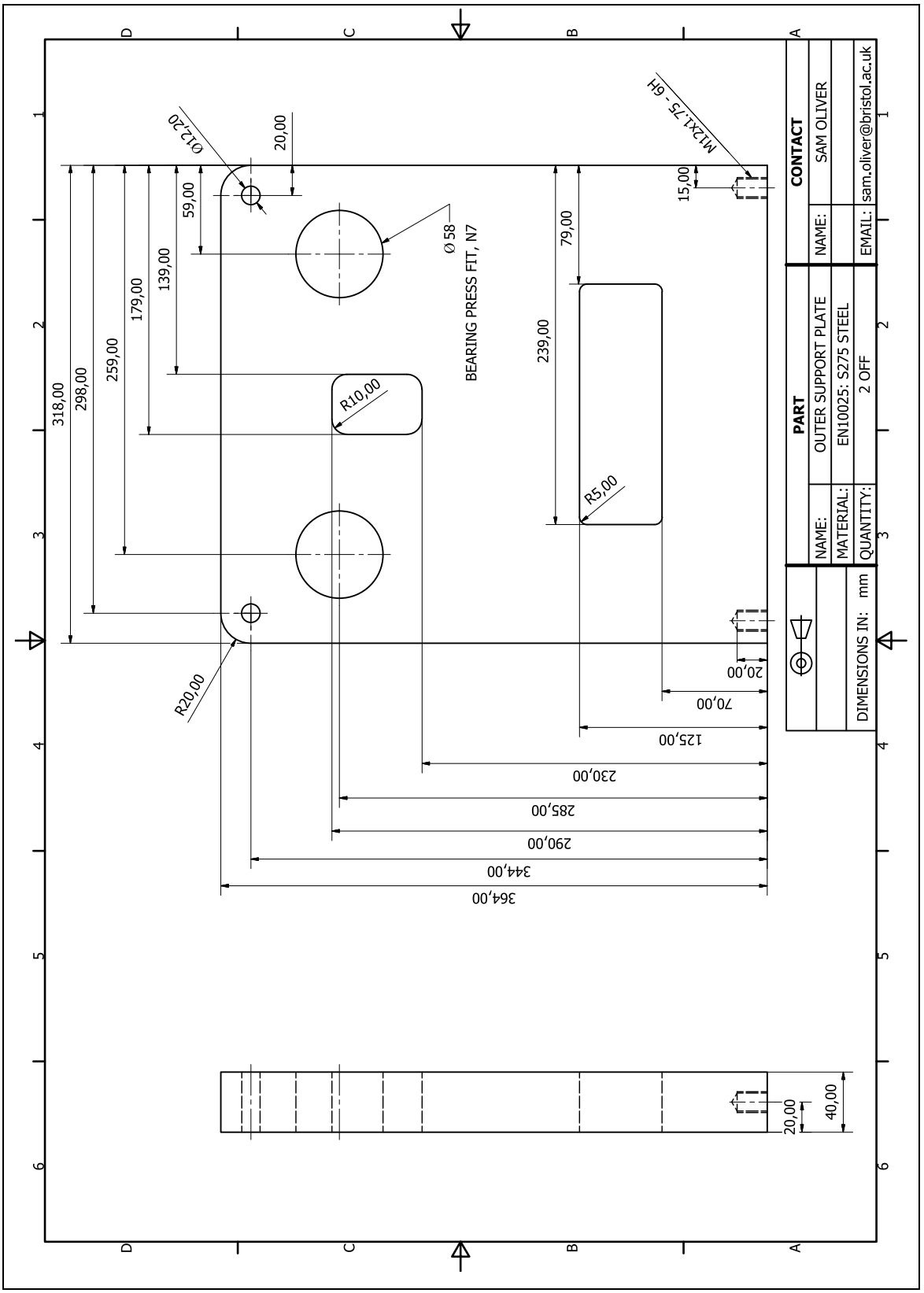

Figure B 11 Outer support plate.

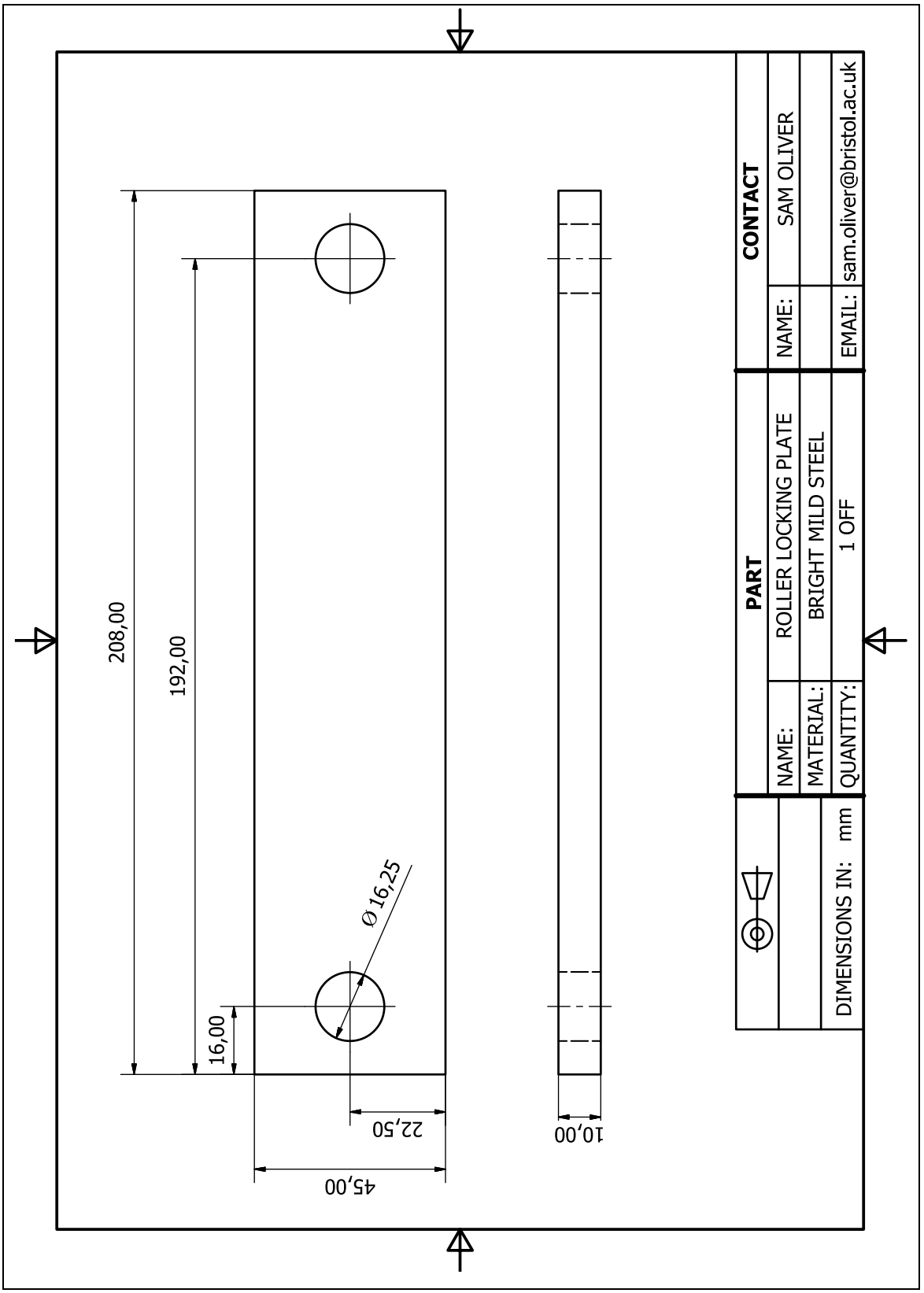

Figure B 12 Roller locking plate.

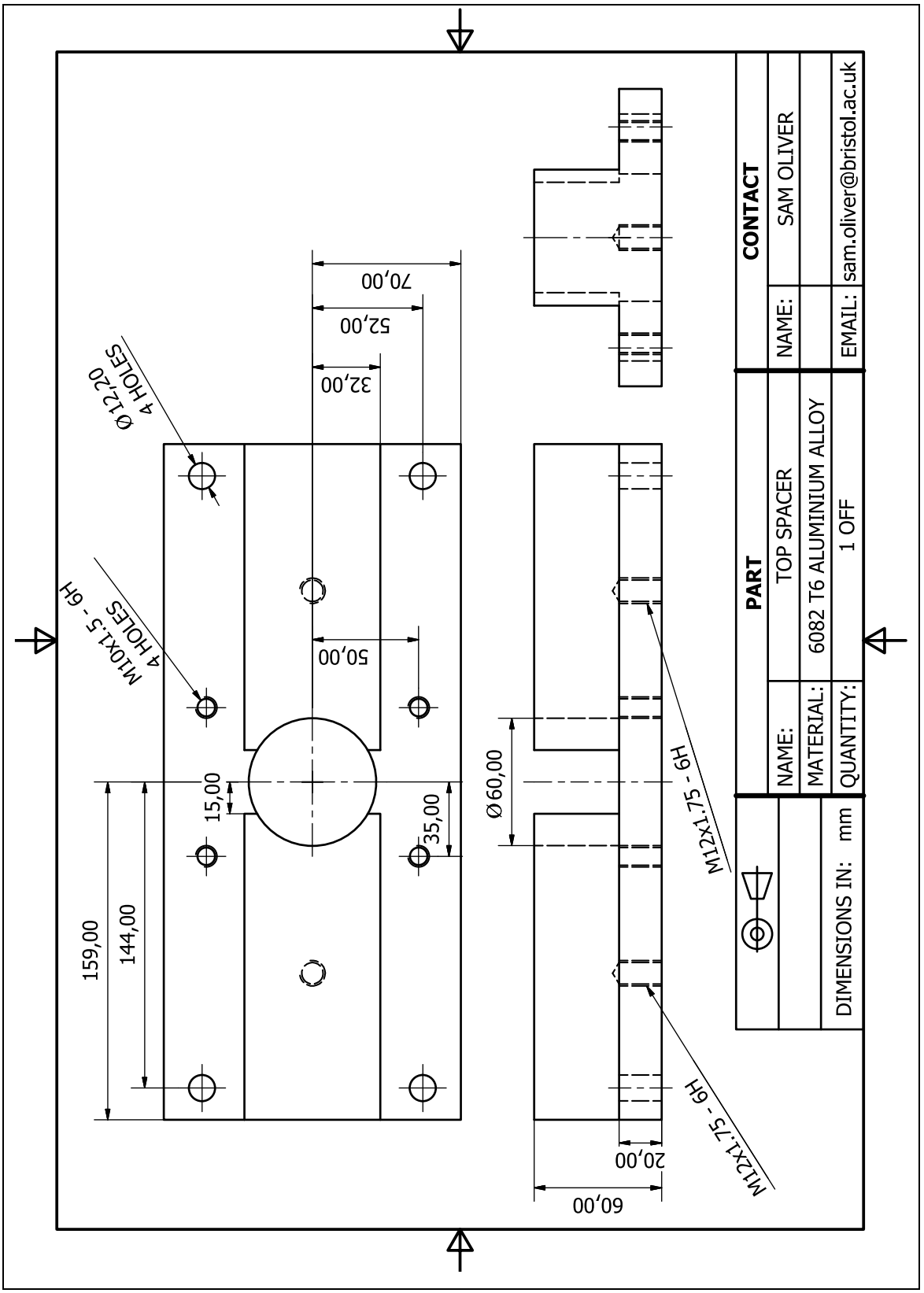

Figure B 13 Top spacer.